PEOPLE'S DEMOCRATIC REPUBLIC OF ALGERIA

MINISTRY OF HIGHER EDUCATION AND SCIENTIFIC RESEARCH

UNIVERSITY OF KASDI MERBAH – OUARGLA

Faculty of Hydrocarbons, Renewable Energies and Earth and Universe Sciences

Department of Earth and Universe Sciences

THESIS

Presented by: **Mr. DEKMOUCHE Riad Imededdine**

Domain: *Earth and Universe Sciences* ***Field:*** *Geology*

Option: *Petroleum Geology*

In order to obtain the

Doctorate degree in Petroleum Geology

Geochemical assessment of the Paleozoic hot shale in Ahnet Basin Algeria, and its implications in unconventional resource development.

Publicly defended on: 08/04/2026 before the following committee:

- ***Mr. HACINI Messouad (President)*** ***Univ. Ouargla***
- ***Mr. KADRI Mohamed Mehdi (Supervisor)*** ***Univ. Ouargla***
- ***Mr. ZATOUT Merzouk (Examiner)*** ***Univ. Sétif 01***
- ***Mr. MECIBAH Ilyes (Examiner)*** ***Univ. Ouargla***
- ***Mr. HADJ KOUIDER Mohammed (Examiner)*** ***Univ. Adrar***
- ***Mr. DJARFOUR Nouredine (Examiner)*** ***Univ. Adrar***

Academic year: 2025/2026

Dedication

To my Father's Soul "Ali DEKMOUCHE"

Acknowledgements

First and foremost, I would like to thank Allah, the Most Gracious and Merciful, for granting us the strength and patience to successfully complete this research. I would like to express my deep gratitude to my supervisor, Professor KADRI Mohamed Mehdi, for his valuable advice, continuous support, and patience throughout my PhD studies.

Taking this occasion, I would like to thank the jury members for their willingness to evaluate this modest work:

Prof. HACINI Messaoud for the honour of chairing the thesis jury, along with the jury members: Prof. HADJ KOUIDER Mohammed, Prof. ZATOUT Merzouk, Prof. DJARFOUR Nouredine and Dr. MECIBAH Ilyes for taking the time to review my thesis despite their hectic duties.

I would also like to extend my gratitude to the Sonatrach team and company for sharing their knowledge, expertise, and experience, as well as their exceptional support and collaboration.

My appreciation goes to Dr. MEZZAR Abdelkamel and Dr. BOULASSEL Abdelbasset. Their assistance was very fruitful.

A special greeting will be directed to Mr. MEKERRI Kamel for his precious contributions in many areas.

Finally, my heartfelt gratitude extends to all those who have contributed, directly or indirectly, to the success of this research, which has required a significant amount of time and effort.

Thanks to all of you.

الملخـــص

تقدم هذه الدراسة تقييمًا جيوكيميائيًا وجيوميكانيكيًا شاملاً للصخر الزيتي الفراسني من ثلاث آبار تقع في حوض أحنات، جنوب غرب الجزائر. من خلال تحليل تقييم الصخور وفحص السحنات البالينية، وتقنية نسبة الغاز، والخصائص الميكانيكية المرنة للصخر، والخصائص المعدنية. يستكشف البحث النضج الحراري والثراء العضوي وإمكانات الهيدروكربون للصخر الزيتي، مع تسليط الضوء أيضًا على البيئة الترسيبية ومصادر المادة العضوية وظروف الحفظ. في الوقت نفسه، يتم تأكيد هذه النتائج من خلال تحديد ميل وأنواع وتماسات السوائل الهيدروكربونية. كما يسلط الضوء على مؤشرات الهشاشة من خلال عدة طرق. تقدم النتائج فهمًا شاملاً للمادة العضوية داخل الصخر الزيتي Frasnian، مما قد يعزز بشكل كبير استكشاف واستغلال الموارد غير التقليدية في المنطقة.

في البئر الأولى، أظهرت معظم العينات محتوىً متوسطًا إلى ممتازًا من الكربون العضوي الكلي (TOC)، ولكن مع وجود هيدروكربونات محتملة محدودة، مما يشير إلى مراحل متفاوتة من نضج الطور الغازي. على العكس من ذلك، أظهرت البئر الثانية محتوىً جيدًا إلى ممتاز من الكربون العضوي الكلي (TOC) مع هيدروكربونات محتملة منخفضة، مما يشير إلى مرحلة متقدمة من النضج، وخاصةً في طور الغاز الجاف. في المقابل، تُظهر البئر الثالثة عيناتٍ غنية بالمواد العضوية. ومع ذلك، فإن كلاً من إمكانات الهيدروكربونات الحرة والمتبقية منخفضة، مما يشير إلى إمكانية وجود غاز أو غاز جاف. وقد أكد التحليل المجهري أيضًا مستويات نضج الآبار، حيث أن المواد العضوية مصدرها الرئيسي مصادر بحرية مختلطة من النوع الثاني.

من الناحية الجيوميكانيكية، أظهرت البئر الأولى أعلى درجات الهشاشة بين الآبار الثلاثة، تلتها البئر الثانية، بينما أظهرت البئر الثالثة أدنى القيم. تُعد هذه المعلومات بالغة الأهمية لتقييم إمكانات الهيدروكربون ومراحل النضج في حوض أحنات، بالإضافة إلى إمكانية هشاشة الصخور للتكسير الهيدروليكي، وتحديد مناطق الإنجاز المثلى، أو "المناطق المثالية"، مما يجعلها أساسية لتقييم الموارد واستغلالها عمليًا.

وخلصت نتائج تقييم الآبار X1 وX2 وX3 إلى أن البئرينX1 وX2 تتمتع بإمكانات بترولية وملاءمة أفضل للتكسير الهيدروليكي من البئرX3.

الكلمات المفتاحية: حوض أحنات؛ صخر Frasnian؛ إمكانات الهيدروكربون؛ الكربون العضوي الكلي TOC؛ تحليل تقييم الصخور؛ فحص الطبقات الحبيبية؛ تقنية نسب الغاز؛ مؤشرات الهشاشة؛ الموارد غير التقليدية.

Abstract

This study presents a comprehensive geochemical and geomechanical assessment of Frasnian shale from three wells situated in the Ahnet Basin, southwestern Algeria. Through Rock-Eval analysis and palynofacies examination, the Gas Ratio technique, the rock's mechanical elastic properties, and mineralogical properties. The research explores the thermal maturity, organic richness, and hydrocarbon potential of the shale, while also shedding light on the depositional environment, sources of organic matter, and preservation conditions. At the same time, confirming these results by identifying the tendency, types, and contacts of hydrocarbon fluids. Also illuminating Brittleness indices through several methods. The findings offer a comprehensive understanding of the organic matter within the Frasnian shale, which could significantly boost the exploration and exploitation of unconventional resources in the region.

In the first well, most samples revealed medium to excellent total organic carbon (TOC) content, but with limited potential hydrocarbons, indicating varying stages of gas-phase maturation. Conversely, the second well showed good to excellent TOC content with low hydrocarbons potential, indicating a more advanced stage of maturation, particularly within the dry gas phase. In contrast, the third well displays core samples rich in organic matter. However, both free and residual hydrocarbon potentials are low, suggesting potential for gas or dry gas. Microscopic analysis further confirmed the wells' maturity levels, with the organic material primarily originating from mixed marine Type II sources.

Geomechanically, the first well exhibited the highest brittleness among the three wells, followed by the second well, while the third well showed the lowest values. These insights are crucial for assessing the hydrocarbon potential and maturation stages in the Ahnet Basin, as well as the rock brittleness potential for hydrofracturing and identifying optimal completion areas, or "sweet spots," making them essential for practical resource evaluation and exploitation.

The evaluation results of wells X1, X2, and X3 concluded that X1 and X2 have better petroleum potential and fracking suitability than X3.

Keywords: Ahnet Basin; Frasnian shale; Hydrocarbon potential; TOC; Rock-Eval analysis; palynofacies examination; Gas Ratios Technique; Brittleness indices; Unconventional resources.

Résumé

Cette étude propose une évaluation géochimique et géomécanique des schistes frasniens à partir de trois puits du bassin d'Ahnet (sud-ouest de l'Algérie). Les analyses Rock-Eval, palynofaciès, Gas Ratio, ainsi que les propriétés mécaniques, élastiques et minéralogiques, ont permis d'examiner la maturité thermique, la richesse organique, le potentiel en hydrocarbures, l'environnement de dépôt, les sources de matière organique et leur préservation. L'identification des types, tendances et contacts des fluides hydrocarbonés confirme ces résultats. L'étude met aussi en évidence des indices de fragilité, offrant ainsi une vision approfondie du potentiel des ressources non conventionnelles de la région.

Dans le premier puits, la plupart des échantillons ont révélé une teneur en carbone organique total (COT) moyenne à excellente, mais avec un potentiel limité d'hydrocarbures, indiquant différents stades de maturation en phase gazeuse. À l'inverse, le deuxième puits a montré une teneur en COT bonne à excellente avec un faible potentiel d'hydrocarbures, indiquant un stade de maturation plus avancé, en particulier dans la phase gazeuse sèche. En revanche, le troisième puits présente des carottes riches en matière organique. Cependant, les potentiels d'hydrocarbures libres et résiduels sont faibles, suggérant un potentiel gazeux ou gazeux sec. L'analyse microscopique a confirmé les niveaux de maturité des puits, la matière organique provenant principalement de sources marines mixtes de type II.

D'un point de vue géomécanique, le premier puits a présenté la fragilité la plus élevée des trois puits, suivi du deuxième puits, tandis que le troisième puits a affiché les valeurs les plus faibles. Ces informations sont cruciales pour évaluer le potentiel en hydrocarbures et les stades de maturation du bassin d'Ahnet, ainsi que le potentiel de fragilité des roches pour la fracturation hydraulique et pour identifier les zones de complétion optimales, ou « sweet spots », ce qui les rend essentielles à l'évaluation et à l'exploitation pratiques des ressources.

Les résultats de l'évaluation des puits X1, X2 et X3 ont conclu que X1 et X2 ont un meilleur potentiel pétrolier et une meilleure aptitude à la fracturation que X3.

Mots clés : Bassin d'Ahnet ; Schiste frasnien ; Potentiel en hydrocarbures ; COT ; Analyse Rock-Eval ; Examen des palynofaciès ; Technique des rapports de gaz ; Indices de fragilité ; Ressources non conventionnelles.

Table of contents

Dedication ---------- I

Acknowledgements ---------- II

الملخـــص ---------- III

Abstract ---------- IV

Résumé ---------- V

Table of contents ---------- VI

List of Figures ---------- VII

List of Tables ---------- VIII

GENERAL INTRODUCTION ---------- 1

Chapter I: Geological context of the study area ---------- 4

Introduction ---------- 4

1. Geographical location ---------- 4

2. Geological framework ---------- 4

3. History of geological and geophysical research in the Ahnet basin ---------- 5

4. Stratigraphy ---------- 6

4.1. Substratum ---------- 7

4.1.1. Basement ---------- 7

4.1.2. Intermediate series of Ahnet ---------- 7

4.1.3. Paleozoic cover ---------- 7

4.1.4. Mesozoic ---------- 12

5. Tectonics ---------- 15

5.1. Eastern Ahnet ---------- 15

5.2. Central Ahnet ---------- 15

5.3. Occidental Ahnet ---------- 15

5.4. Fault systems ---------- 15

5.5. Folded structures ---------- 18

6. General sedimentation context ---------- 19

7. Paleostructural evolution of the Ahnet basin ----------22

7.1. Pan-African phase ---------- 22
7.2. Cambro-Ordovician phase ---------- 22
7.3. Taconic phase (Caradoc) ---------- 22
7.4. Silurian phase ---------- 22
7.5. Caledonian phase ---------- 22
7.6. Devonian phase ---------- 23
7.7. Famennian post phase ---------- 23
7.8. Hercynian movements ---------- 23
7.9. Triassic phase ---------- 23
7.10. Jurassic phase ---------- 23
7.11. Cretaceous phase ---------- 23
8. Maps interpretation ---------- 24
8.1. Cambrian ---------- 25
8.2. Ordovician ---------- 26
8.3 Silurian ---------- 27
8.4. Devonian ---------- 29
8.4.1 Lower Devonian ---------- 30
8.4.2 Middle Devonian ---------- 33
8.4.3 Upper Devonian (Frasnian, Famennian) ---------- 36
9. Petroleum aspect ---------- 38
9.1. Source rocks ---------- 38
9.2. Reservoir rocks ---------- 38
9.3. Seal rocks ---------- 39
9. Maturation history ---------- 39
Conclusion ---------- 40
Chapter II: Geochemical characterization of Frasnian Hot shales ---------- 41
Introduction ---------- 41
1. Methods ---------- 41
1.1. Determination of total organic carbon (TOC) ---------- 41
1.2. Rock-Eval Pyrolysis VI ---------- 42

1.3. Determination of palynofacies and maturity estimation ---------- 43
2. Results and Discussion ---------- 44
2.1. Determination of total organic carbon (TOC) ---------- 44
2.2. Rock-Eval Pyrolysis VI ---------- 47
2.3. Determination of palynofacies and maturity estimation ---------- 54
Conclusion ---------- 60
Chapter III: Geochemical evaluation of Frasnian Hot shales ---------- 61
Introduction ---------- 61
1. Methods ---------- 62
1.1. Gas Ratio technique ---------- 63
1.1.1. Wetness Ratio (Wh) ---------- 64
1.1.2. Balance Ratio (Bh) ---------- 64
1.1.3. Character Ratio (Ch) ---------- 66
2. Results and Discussion ---------- 67
2.1. Well (X1) ---------- 69
2.1.1. Dry Gas interval ---------- 69
2.1.2. Gas interval ---------- 69
2.1.3. Condensate interval ---------- 69
2.2. Well (X2) ---------- 71
2.3. Well (X3) ---------- 73
2.3.1. Dry Gas interval ---------- 73
2.3.2. Gas interval ---------- 74
2.3.3. Condensate interval ---------- 74
Conclusion ---------- 76
Chapter IV: Geomechanical Approach ---------- 77
Introduction ---------- 77
1. Definition of brittle rock and brittleness ---------- 77
2. Factors influencing the Brittleness index ---------- 79
2.1. Composition (mineral contents) ---------- 79
2.2. Porosity ---------- 80

2.3. Temperature ---------- 81
2.4. Strain rate ---------- 81
3. Correlation of Brittleness and Fracability ---------- 83
3.1. In-Situ Earth Stresses ---------- 84
3.2. Temperature effects ---------- 86
3.3. Natural Fractures ---------- 87
4. Benefit of evaluating Brittleness for shale gas reservoirs ---------- 88
4.1. Texas 2 Step Frac ---------- 90
4.2. Zipper Frac ---------- 91
4.3. Modified Zipper Frac ---------- 92
5. Methods of evaluating Brittleness ---------- 93
5.1. Determination of brittleness from rock compression Stress-Strain curves ---------- 94
5.2. Determination of brittleness from Mohr's envelope, based on the angle of internal friction -------- 100
5.3. Determination of brittleness from tensile and compressive strengths ---------- 101
5.4. Determination of brittleness from rock mechanical properties ---------- 102
5.5. Determination of brittleness from mineral rock components (mineral composition) ---------- 104
5.6. Determination of brittleness by experimental method ---------- 107
Conclusion ---------- 109
Chapter V: Geomechanical characterization of Frasnian Hot shales ---------- 110
Introduction ---------- 110
1. Methods ---------- 110
1.1. Mechanical elastic properties ---------- 110
1.1.1. Gamma Ray Logging ---------- 111
1.1.2. Density Logging (gamma-gamma) ---------- 112
1.1.3. Velocity Logging (Sonic) ---------- 113
1.2. Mineralogy properties ---------- 113
1.2.1. X-ray diffractometry analysis (XRD) ---------- 114
2. Results and Discussion ---------- 115
2.1. Elastic-based Brittleness ---------- 118
2.1.4. EBI comparison of the three wells ---------- 128

2.2. Mineralogy-based Brittleness ---------- 131

3. Comparison between EBI and MBI ---------- 141

Conclusion ---------- 146

GENERAL CONCLUSION ---------- 149

1. Synthesis ---------- 149

2. Perspectives ---------- 151

3. Recommendations ---------- 157

REFERENCES ---------- 158

List of Figures

Fig. 01: Geographical Location of the Ahnet Basin ---------- 05

Fig. 02: Lith-stratigraphic column of the Ahnet Basin (Zeroug et al., 2007) ---------- 14

Fig. 03: Structural map (tectonic elements) of the Ahnet basin (Zeroug et al., 2007) ---------- 16

Fig. 04: Schematic map showing the main fault systems that affect the Ahnet basin (Haddoum,2009) --- 17

Fig. 05: Main geometries associated with the folded structures of the Ahnet ---------- 19

Fig. 06: Main facies associations observed in the Cambro-Ordovician series of the Ahnet (modified after Euzen et al., 2005) ---------- 21

Fig. 07: Positioning map of study wells in the SHALE ZONE perimeter ---------- 25

Fig. 08: Cambro-Ordovician roof Isobath map showing the structure of the study area before Silurian sedimentation ---------- 27

Fig. 09: Silurian Isopach map showing the thickness variation within the study area ---------- 28

Fig. 10: Isobath map with a Silurian roof showing the structure of the study area before the Devonian sedimentation ---------- 29

Fig. 11: Isopach map of the Emsian showing the thickness variation within the study area ---------- 30

Fig. 12: Emsian Isobath map showing the depth variation within the study area ---------- 31

Fig. 13: Isopach map of the Seginian showing the thickness variation within the study area ---------- 31

Fig. 14: Seginian Isobath map showing the depth variation within the study area ---------- 32

Fig. 15: Isopach map of the Gedinnian showing the thickness variation within the study area ---------- 32

Fig. 16: Isobath map of the Gedinnian showing the depth variation within the study area ---------- 33

Fig. 17: Isopach map of the Covinian showing the thickness variation within the study area ---------- 34

Fig. 18: Isobath map of the Covinian showing the depth variation within the study area ---------- 34

Fig. 19: Isopach map of the Gevitian showing the thickness variation within the study area ---------- 35

Fig. 20: Isobath map of the Gevitian showing the depth variation within the study area ---------- 35

Fig. 21: Isopach map of the Frasnian showing the thickness variation within the study area ---------- 36

Fig. 22: Isobath map of the Frasnian showing the depth variation within the study area ---------- 37

Fig. 23: Isopach map of the Famennian showing the thickness variation within the study area ---------- 37

Fig. 24: Isobath map of the Famennian showing the depth variation within the study area ---------- 38

Fig. 25: Heat flow in the Ahnet basin (Takherist et Hamdi, 1992) ---------- 40

Fig. 26: Analytical procedure for the Rock-Eval 6 device ---------- 43

Fig. 27: Cross-plots of total organic carbon (TOC) content versus depth (m) ---------- 46

Fig. 28: Rock-Eval pyrolysis VI of the X1 analyzed samples ---------- 49

Fig. 29: Rock-Eval pyrolysis VI of the X2 analyzed samples ---------- 51

Fig. 30: Rock-Eval pyrolysis VI of the X3 analyzed samples ---------- 53

Fig. 31: Representative palynofacies assemblages from the Frasnian Shales Formation (well X1) showing various types of organic matter in the kerogen concentrates ---------- 57

Fig. 32: Representative palynofacies assemblages from the Frasnian Shales Formation (well X2) showing various types of organic matter in the kerogen concentrates ---------- 58

Fig. 33: Representative palynofacies assemblages from the Frasnian Shales Formation (well X3) showing various types of organic matter in the kerogen concentrates ---------- 59

Fig. 34: Schematic evolution of organic matter, burial, and preservation (Peters et al., 2005) ---------- 62

Fig. 35: Mud-gas monitoring system (Fatai Anifowose et al., 2022) ---------- 63

Fig. 36: Typical fluid and contact profiles of the Wh and Bh Ratio ---------- 66

Fig. 37: Gas ratio interpretation chart (Baker Hughes, 1995) ---------- 67

Fig. 38: Gas Chromatographic peaks for well X1 ---------- 70

Fig. 39: Fluids characterization for well X1 ---------- 70

Fig. 40: Total gas variation versus depth for well X1 ---------- 71

Fig. 41: Gas Chromatographic peaks for well X2 ---------- 72

Fig. 42: Fluids characterization for well X2 ---------- 72

Fig. 43: Total gas variation versus depth for well X2 ---------- 73

Fig. 44: Gas Chromatographic peaks for well X3 ---------- 74

Fig. 45: Fluids characterization for well X3 ---------- 75

Fig. 46: Total gas variation versus depth for well X3 ---------- 75

Fig. 47: Schematic illustration resumes the 2nd chapter outcomes (Geochemical characterization) ----- 76

Fig. 48: Typical stress-strain curves (modified) showing rocks' failure behaviors and failure modes ------78

Fig. 49: Pure brittleness index of different minerals (Qian et al., 2020) ---------- 80

Fig. 50: Brittle transition temperature (Guo et al., 2021) ---------- 81

Fig. 51: Variations in dynamic strength, failure stress with strain rate (Grady, 1996) ---------- 83

Fig. 52: Influence of minimum horizontal stress (Sh) on failure mode (Tang et al., 2020) ---------- 85

Fig. 53: Various hydraulic fracture morphologies from simple and complex fracture transition to the tree fracture network concerning rock brittleness (Wang et al.,2015) ---------- 88

Fig. 54: Brittleness index versus gas production (Buller et al., 2010) ---------- 90

Fig. 55: Texas 2-step frac method (Soliman et al., 2010) ---------- 91

Fig. 56: Zipper Frac method (Soliman et al., 2010) ---------- 91

Fig. 57: Modified Zipper Frac method (Soliman et al., 2010) ---------- 92

Fig. 58: Various types of Frac methods (Jacobs, 2014) ---------- 93

Fig. 59: Typical compression stress-strain curve and associated deformation and failure characteristics for brittle rocks ---------- 95

Fig. 60: Energy at each stage of the Stress-Strain curve (Zhang et al., 2016) ---------- 96

Fig. 61: Change in the degree of brittleness represented by B1 and B2 based on the energy changes of stress-strain curves (Zhang et al., 2016) ---------- 98

Fig. 62: Stress and deformation used for BI calculation (Wong et al., 2021) ---------- 99

Fig. 63: Different types of Brittleness indices defined based on compressive loading tests (modified after Yang et al., 2013) ---------- 100

Fig. 64: Schematic diagram for determining the angle of internal friction from Mohr circle envelope. σn and τ are the normal stresses and shear strength, respectively (Zhao, 2008) ---------- 101

Fig. 65: Cross plot of Young's modulus and Poisson's ratio showing the brittleness percentage --------- 103

Fig. 66: Brittleness Vs. GR classification based on Perez and Marfurt (2013) ---------- 105

Fig. 67: Punch penetration test apparatus and sample preparation (Yagiz, 2009) ---------- 107

Fig. 68: Measurement of rock brittleness using force penetration profile (Yagiz, 2009) ---------- 108

Fig. 69: A. The NGT instrument for measuring natural gamma radioactivity. B. Detail of the detector (RABAUTE, 1998)---------- 111

Fig. 70: Compton scattering (Watfa, M. 2021) ---------- 112

Fig. 71: Schematic of the wave train detected at the receiver as a function of time (Close, D. et al.2009) ---------- 113

Fig. 72: Schematic representation of Bragg's law conditions (Stan, Camelia V., et al.2018) ---------- 115

Fig. 73: GR logs of the three wells versus depth ---------- 117

Fig. 74: Well X1; EBI versus depth ---------- 119

Fig. 75: Well X1; EBI with GR as a reference ---------- 120

Fig. 76: Well X1; Poisson ratio versus Young modulus with EBI as a reference ---------- 121

Fig. 77: Well X2; EBI versus depth ---------- 123

Fig. 78: Well X2; EBI with GR as a reference ---------- 124

Fig. 79: Well X2; Poisson ratio versus Young modulus with EBI as a reference ---------- 124

Fig. 80: Well X3; EBI versus depth ---------- 126

Fig 81: Well X3; EBI with GR as a reference ---------- 127

Fig. 82: Well X3; Poisson ratio versus Young modulus with EBI as a reference ---------- 127

Fig. 83: Only shales cross plots of Poisson ratio versus Young modulus with EBI as a reference;(a) well X1, (b) well X2, (c) well X3 ---------- 129

Fig .84: Ternary plot showing the mineralogy composition for well X1 ---------- 132

Fig .85: Well X1, MBI versus depth ---------- 133
Fig .86: Well X1, mineralogy composition versus depth ---------- 134
Fig .87: Ternary plot showing the mineralogy composition for well X2 ---------- 136
Fig .88: Well X2, MBI versus depth ---------- 137
Fig .89: Well X2, mineralogy composition versus depth ---------- 138
Fig .90: Ternary plot showing the mineralogy composition for well X3 ---------- 139
Fig .91: Well X3, MBI versus depth ---------- 140
Fig .92: Well X3, mineralogy composition versus depth ---------- 141
Fig .93: Well X1, EBI and MBI profiles comparison versus depth ---------- 143
Fig .94: Well X2, EBI and MBI profiles comparison versus depth ---------- 144
Fig .95: Well X3, EBI and MBI profiles comparison versus depth ---------- 145
Fig .96: Well X1, composite log versus depth ---------- 154
Fig .97: Well X2, composite log versus depth ---------- 155
Fig .98: Well X3, composite log versus depth ---------- 156

List of Tables

Table. 01: Source rocks classification according to TOC (Kracha, 2011) ---------- 42

Table. 02: Correlation of the main elements of thermal maturation (Kracha., 2011) ---------- 44

Table. 03: Frasnian studied intervals on each well depending on available data ---------- 44

Table. 04: The main geochemical parameters from Pyrolyse Rock-Eval (Espitalié et al., 1985; Peters and Cassa, 1994), Vinci-Technologies, (2014) ---------- 47

Table. 05: Wetness ratio relations (Baker Hughes,1995) ---------- 64

Table. 06: Fluid characterization using the wetness and balance ratios ---------- 65

Table. 07: Frasnian studied intervals on each well depending on available data ---------- 68

Table. 08: Brittleness classification based on the ratio of UCS to TS (Serdar YASAR, 2020) ---------- 102

Table. 09: Suggested rock brittleness classification based on the punch penetration test (Yagiz, 2009) ---------- 108

Table. 10: Frasnian studied intervals on each well depending on available data ---------- 116

Table. 11: Frasnian comparison intervals on both wells depending on available data ---------- 142

GENERAL INTRODUCTION

GENERAL INTRODUCTION

Frasnian shale has become an increasingly important unconventional reservoir around the globe, due to its high organic richness and potential for shale gas and shale oil production. Therefore, due to its economic value and potential as a source rock for hydrocarbons, black shales have caught the attention of researchers. For instance, Tobia and Mustafa (2022) studied the geochemical and clay Mineralogical characteristics of black shale and the constraints on Diagenesis and Maturation in the Kurdistan Region, Iraq.

The Ahnet Basin in Algeria has emerged as a promising area for exploring and producing unconventional resources. Several studies have been carried out on the organic matter in the Frasnian shale in different basins around the world, including the characterization of its type, quality, and maturity. In particular, some studies have investigated the organic matter of the Frasnian shale in the Ghadames Basin in Tunisia, Algeria, Libya (Echikh, 1998; Boote et al., 1998; Dardour et al., 2004), and Iraq (Abdula et al., 2020). Boote et al. (1998) mentioned that the Paleozoic petroleum systems of North Africa contain five large giant (> 1 billion barrels of oil equivalent) and 24 giant (> 250 million barrels of oil equivalent) oil and gas fields with total recoverable reserves discovered to date of more than 46 billion barrels of oil equivalent, while the Upper Devonian Frasnian shales are the origin of 10-15% of Paleozoic sourced hydrocarbons. On the other hand, Dardour et al. (2004) have extensively discussed the stratigraphic controls on Paleozoic petroleum systems in the Ghadames Basin, Libya.

Other than that, Echikh (1998) indicates that Ordovician and Devonian reservoirs have the best petrophysical properties in the southern basin of Ghadames, Libya. Silurian and Devonian source rocks are present across large parts of the basin. They are estimated to have generated volumes of hydrocarbon far greater than the volumes discovered in traps to date, suggesting that a great volume of oil remains to be discovered in the Ghadames Basin, as well as other basins such as the Appalachian Basin in the United States, where Ettensohn et al. (1985) find that the occurrence and distribution of delta-basin deposits (Frasnian black shales) and regional disconformities, as well as the estimated depth of basinal deposits, are used to define the Acadian Orogeny tectophases and their deltaic responses. Additionally, the Baltic Basin in Poland, as demonstrated by Racki (2005) and Pisarzowska et al. (2006) in their study of the organic matter of the Conodont-based event stratigraphy of the Early-Middle Frasnian transition on the South Polish carbonate shelf.

From an evaluation point of view, many geochemical studies carried out on this basin have demonstrated that the radioactive 'Hot Shales' clays of the upper Devonian constitute a primary source rock that supply conventional reservoirs with known hydrocarbon matter through the Algerian Saharan platform (Lüning et al., 2003; Kadri and Hacini, 2017; Boote et al., 1998; Macgregor et al., 1998). Lüning et al. (2003) have identified the Frasnian organic-rich shales in the North African region, especially their distribution and depositional model, while Macgregor et al. (1998) expanded some of their research focusing on petroleum systems and exploration maturity in Algeria, precisely on its Giant fields. On the other side, from the perspective of bibliographic resources and references, there has been no previous study on the organic matter characterization in the Frasnian shale of the Ahnet Basin (Based on our research). Therefore, this study aims to fill this knowledge gap through a bi-disciplinary characterization study, primarily based on analysing and evaluating the available composite actual data of the Ahnet basin Frasnian shale, which could be valuable and useful in the case of future field exploitation and development.

This study presents the results of different kinds of rock analyses (both, direct and indirect methods), geochemical and geomechanical approaches. For the first approach, we used the Rock-Eval analysis and palynofacies examination of Frasnian shale from three wells drilled in the Ahnet Basin, Algeria. The Rock-Eval data provide information on the shale's thermal maturity, organic richness, and hydrocarbon potential. By heating the rock and measuring the quantity and composition of the volatile products released (Mamaseni et al., 2022), Rock-Eval pyrolysis can determine parameters such as total organic carbon (TOC), the hydrogen index (HI), the oxygen index (OI), and the production index (PI), which are commonly used to evaluate the source rock potential of a shale (Espitalié et al., 1985; Peters and Cassa, 1994). while the palynofacies analysis offers insights into the depositional environment, the source of the organic matter, and the preservation conditions of the organic matter. Even in terms of the type, abundance, and preservation state of the organic matter, as well as the nature and intensity of the depositional environment (Sia and Abdullah, 2012; Hakimi et al., 2013; Mendonça Filho et al., 2010; Suárez-Ruiz et al., 2012).

Furthermore, in the geochemical approach, we confirmed organic matter maturity using an additional indirect method, the Gas Ratio technique, which employs real-time plots to identify hydrocarbon fluid types (Haworth et al., 1984). This method integrates component gases detected

during the drilling operation (C1-C8) in order to extract three functional parameters: Wetness Ratio (Wh), Balance Ratio (Bh) and Character Ratio (Ch). These parameters provide important insights into fluids' tendency, confirming the potential of production gas, validating the gas prediction, and identifying the gas-oil contact (GOC) as well as the oil-water contact (OWC).

In the geomechanical approach, the objective was to calculate the Brittleness indices for our three wells using two different methods: the Rock's mechanical elastic properties and mineralogical properties. The mechanical elastic properties serve to assess the elastic rock brittleness through the mechanical elastic parameters; Young's modulus and Poisson's ratio (Rickman et al., 2008) by using sonic Logging data such as P and S waves, slowness and velocities (compressive and shear slowness) through shale formations, gamma rays (SGR) and rock density. The Mineralogy properties serve to assess the mineralogical rock brittleness using mineral components of the studied Frasnian formation by integrating several models as well as Jarvie et al. (2007), Buller et al. (2010), and Wang and Gale (2009) using the three main known minerals in nature: quartz, clay, and carbonate plus the total organic carbon (TOC) to identify lithology.

Combining these two approaches will provide a comprehensive understanding of the organic matter in the Frasnian shale of the Ahnet Basin. The result of this study will provide us with a holistic understanding of its suitability for unconventional resource development. Based on the available data, the main studied rock properties will be characterized and evaluated such as source rock potential for petroleum interest qualification and brittleness rock potential for hydrofracturing and completion suitability (sweet spots), which can enhance relatively the assessment and the better understanding of this unconventional source rock for any possible exploration and exploitation in this region.

Chapter I

Geological context of the study area

Introduction

Algeria is part of northwestern Africa and includes two major domains: the Atlas Domain and the Saharan Domain. The Atlas domain is structured during the Alpine cycle and it is separated from the Sahara by the southern Atlas accident.

The Saharan platform is a stable to relatively rigid area. It is located south of the Atlas chain and bounded north by the Southern Atlas accident and to the south and southwest, respectively, by the Touareg and Reguibat shields. This cratonic platform is covered with a sedimentary series from the Cambrian to the Carboniferous.

The Saharan slab is subdivided into three oil-related provinces:

- ***The western province*:** includes the Bechar, Reggane, Ahnet, Mouydir, Timimoun, and Sbâa basins.
- ***The Triassic province (central):*** located in the northern part of the Saharan shelf.
- ***The eastern province (eastern syncline):*** includes the Illizi and Berkin basins separated by the Ahara mole**.**

1. Geographical location

The Ahnet Basin is located in the southwestern part of the Algerian Sahara, part of the western province of the Saharan Platform. Bounded by Easting 290,000 – 500,000 m and Northing 2,655,000 – 2,990,000 m. It spreads over nearly 75,000 km^2.

2. Geological framework

The Ahnet Basin is limited by:

- To the north, by the Tademaït tray and the Djoua seeding, which separates from the Timimoun Basin (Gourara).
- To the south, he admits the Touareg shield as the southern limit.
- To the west by the Azzel-Matti axis, the separation of the Reggane Basin and the Sbâa Bowl.
- To the east by the Arak-Idjerane pier, which is the separation of the Mouydir Basin.

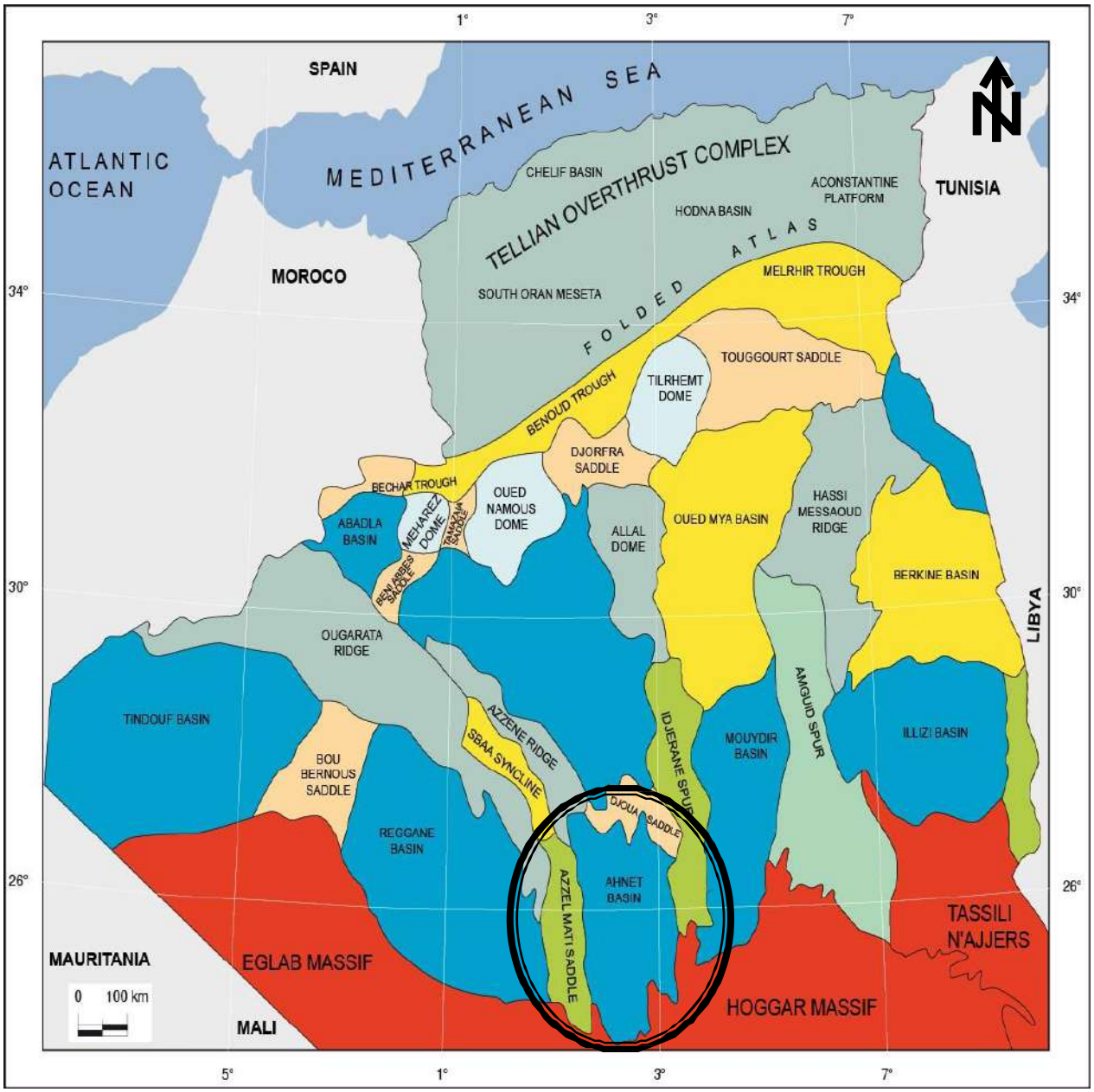

Fig. 01: *Geographical Location of the Ahnet Basin (Technical Report, Sonatrach Exploration).*

3. History of geological and geophysical research in the Ahnet basin

The Ahnet basin was the first region of the Algerian Sahara to be the subject of hydrocarbon exploration and discovery.

In 1908 GAUTIER presented the first geological sketch of the Ahnet by simple observation and collection of some clues. Several fossil studies have also been carried out by FLAMANT and HAUG, the results of which were illustrated in FLAMANT's thesis on Saharan

geology.

In 1931, BOUCART and MONOD resumed geological studies in the region. The results of their work illustrate the monograph of the Ahnet region. Thus, MONOD carried out the first topographical survey of the region. All this exploration work was completed during the 1952 International Geological Congress in Algiers, during which a thesis was presented:

- From **1952** to **1959**:

This was the period during which several companies such as CREPS, the B.R.P, C.E.P, S.N.REPAL, C.P.A. embarked on an intense exploration activity by drilling some thirty wells (BZ-1, MH-1, TH-201...), all located on surface structures. This exploration was a very encouraging success, which led to the first discovery of hydrocarbon accumulations in the Ahnet region of Jebel Berga (BG1), by the company C.R.E.P.S. in 1953. This discovery proves, for the first time, the existence of hydrocarbons in the Saharan platform.

- From **1959** to **1971**:

During this period, exploration activities slowed down in the Ahnet basin for several reasons:

- First because of the discovery of oil (1956) in the Illizi region and the giant Hassi Messaoud deposit.
- Due to the remoteness of the Ahnet and the difficulties of supplying water to the site,
- Also, the small amount of hydrocarbons obtained during the tests of the wells already drilled discourages companies from continuing their exploration and developing the fields already discovered.

- From **1971** to the present:

The nationalization of hydrocarbons has allowed Sonatrach to carry out numerous explorations in the Ahnet region based on seismic refraction and reflection that will highlight several very important anticlinal structures in the subsurface. These anticlines include Garet El Guefoul and Bahar El Hamar, which is one of the regions containing the most important structural traps. All these positive structures are at least known by a survey, and the results were satisfactory.

4. Stratigraphy

4.1. Substratum

The Paleozoic deposits of the Ahnet rest in discordance on the substrate. The latter is of Precambrian age, it could be of the same nature as that of the Eglabs (W.E.C, 1995). the base and the sub-cambrian summit part.

4.1.1. Basement

It has a volcano-metamorphic nature, formed of mica schists and amphibolite interspersed by magmatic intrusions (Boujemaa, 1987), it appears to be of the same nature and age as the western Pharusian outcropping at the Western Hoggar.

4.1.2. Intermediate series of Ahnet

This series has been described at the outcrop for tens of kilometers in the bled el Mass region; it corresponds to a conglomeratic arkose's formation with river facies or alternate clay and silt levels to intercalation of Tillites marking episodes of glaciation. The intermediate series of the Ahnet was described (Fabre et al., 1988) as part of the pan-African molasses of the Sahara, preserved at the edges of the West African Craton.

Considered partly of the Cambrian age (Caby, 1977), it corresponds to end-of-cycle orogenic accumulations showing evidence of synsedimentary tectonics and presenting the dismantling products of the Pharusian chain. The Precambrian was formed mainly by igneous rocks, associated with metamorphic rocks that were the result of attributes to the early Cambrian, and they are deformed before an erosive phase leading to the formation of a vast peneplain marking the top of the unit by Tassilian discordance.

4.1.3. Paleozoic cover:

At the Ahnet Basin, the Paleozoic terrain is entirely complete, with series ranging from the lower Cambrian to the carboniferous (Beuf, 1971). This cover is separated from the base by infra-Tassilian discordance and mesozoic deposits by Hercynian discordance. This paleozoic cover is subdivided into two distinct morphological sets:

- The Tassilian belt, or Tassilian country, comprises the Cambro-Ordovician, the Silurian, and the Lower Devonian.
- Before Tassili foreland or pre-Tassilian tray.

a. Cambro-Ordovician

a.1. Cambrian (Unit II)

The Cambrian is separated from the pre-Cambrian by sub-Tassilian discordance. This unit is formed from bottom to top by:

- From coarse to conglomerate to oblique stratification indicating the river deposition medium with a marine influence to the top.
- Above these last deposits, we encounter more fine sandstones, well-led with the presence of tigillites, and the appearance of marine fauna, indicating the mixed or transition facies.

a.2 Ordovician

The Ordovician consists of the following formations from the base to the top:

- *Lower Ordovician:* It includes units III 1, and III 2 of the formation of the Ajjers, limited to the base by the sandstones of Meribel and the roof by the quartzites of Hamra.

Unit **III_1**

Ranging from a few tens of meters to the east of the basin to more than 200m to the northwest, recording a transgression. This unit includes:

Sandstones of Meribel:

The top of the formation is a sandstone-clay complex composed of alternating green-grey quartzitic sandstones, noting the presence of glauconia and pyrite (Tidals and Deltaic deposits).

Clays of El Gassi:

Black and micaceous clay siltstones pass with the presence of glauconite, representing a major transgression (open platform and ramp).

Sandstones of El Atchane:

Formed mainly by medium-sized, light-grey to whitish coarse sandstones, moderately consolidated containing brachiopod debris, the glauconitic and silico-clay with rare indurated, silty clay pasts (shallow to deltaic).

Unit **III_2**

This unit corresponds to:

El Hamra quartzites:

These are shallow marine deposits, which are based in discordance on the sandstones of El

Atchane; they are formed mainly of quartzitic sandstones and quartzites. We also note the presence of tigilite with clay pass; they are usually cracked. The thickness of this level is estimated at 50 to 250 m. It is underlying the Arenigian (Lower Devonian) anti-discordance, marking an episode of heaving (Platform under the influence of the storm).

Unit **III3**

It was formed following another uprising, followed by a North and North-West marine transgression. This unity is based on discordance in the formation of the Ajjers.

Sandstones and clays of Ouargla:

This formation is based on discordance with the Hamra quartzites. It is represented by alternations from white to light grey sandstones, with slightly carbonated clays.

Tiferouine Clays:

It is a formation of silty, sometimes pyrite bearing, indurated black clay with quartzitic fine, varied passes, fine or very fine light grey quartzite.

Azzel's clays:

Formed generally from dark to black greys clays, indurated, silty, micaceous, sometimes carbonated with grey to light grey sandstones, fine to very fine quartzitic, compact and hard (open platform and ramp).

- *Middle Ordovician*

It includes the Unit **IV**:

Unit **IV**

These formations are installed following an uprising and on this surface have installed a vast ice cap highlighting four (04) cycles of glaciation with a large area of discordance attributed to this unit, which includes the following formations:

Oued Saret's sandstones:

They are represented by light grey to dark grey sandstones, compact, silico-clay cement with fine black clays, sometimes slightly dolomitic (river to tidal);

Sandstones of El Goléa:

This level is formed mainly by quartzites with clay and siltstones.

- *Upper Ordovician*

It includes, from bottom to top:

Micro-conglomerate clays or El Goléa clays:

These are black, indurated, micaceous pyritous clays with thick, subangular, and angular quartz grains, sometimes with fine intercalations of clay siltstones (deltaic front, glacial influence) with fine sandstone pass.

Sandstones of Ramade (Slab of M'ekratta):

They form the summit part of the Ordovician and have gregarious and quartzitic facies. These quartz sandstones are grey to white and sometimes have coarse medium ends with fine intercalations of clays. These deposits underwent rapid sedimentation under lake and river conditions just after the various periods of glaciation.

a.3. Silurian

Silurian Deposits are based on stratigraphic unconformity on Ramade's sandstones. Following the melting of the Ordovician ice, the Silurian transgression deposits black clays with graptolites rich in organic matter in the paleo glacial valleys before covering all paleo landforms. It is composed mainly of clays that are divided into three members:

- *Lower limb (*Middle Llandoverian to Upper Wenlockian): It is silty, with many black-grey clays and some limestone and sandstone benches.
- *Middle member* (Ludlovian to Upper Pridolian): Clay sedimentation with some limestone and sandstone pasts.
- *Upper limb* (end of upper Pridolien - Base of Lochkovian): Clay sedimentation with increased gregarious levels announcing the sandstone-clay deposits of the Devonian age passage zone.

a.4 Devonian

It is divided into three subsystems:

- Lower Devonian
- Middle Devonian

- Upper Devonian.

a.4.1 Lower Devonian

Compared to the two subsystems, it has a more significant geographical extension.

- *Gedinnian:*

It is a sandstone-clay group, composed mainly of more or less regular alternations of grey to dark grey clays, puffed, silt, micaceous, slightly dolomitic, and grey to white, thin-to-medium, locally coarse to silica cement, sometimes becoming quartzitic and thin passes of grey, clay, micaceous and compact hard siltstones.

- *Segenian (quartz bar):*

This massive, compact, completely azoic bar is represented by thin, sometimes coarse, light grey and brown grey bars with silica-carbonated silicas, micaceous, with rare excesses of dark grey to black, silica, micaceous and locally pyritous clays.

- *Emsian:*

It is a vast extension in the two basins that have been spared from Hercynian erosion. On the other hand, it is eroded on the high parts of the Azzene and Azzel Mati saddles. The Emsian is represented by a series of grey sandy clayey to black grey, silty, micaceous, often very fossiliferous.

a.4.2 Middle Devonian

The Middle Devonian is experiencing a return to marine conditions with deposits of clays and then limestones of The Givetian.

The floors represent it; Eifelian and Givetian.

- *Eifelian: (formerly Couvinian)*

It comprises locally carbonated dark grey clays with siltstones and clay limestone.

- *Givetian:*

It is represented predominantly by limestone with still some black clay intercalations, more or less shale.

a.4.3 Upper Devonian

It corresponds to the formations of marhouma or Temertasset clays, its thickness reaching 1400m in the most subsident parts of the Timimoun basin. It is divided into three formations: Frasnian, Famennian, and Strunian.

- *Frasnian :*

It starts with a microcrystalline limestone bank, often clay, before giving way to dark grey to black clays, sometimes interspersed with whitish limestone banks. Black and radioactive basal clays are excellent source rocks, comparable to the Hot Shales of the basal Silurian.

- *Famennian:*

It consists of dark grey to black clays, more or less charcoal, pyritous, and very fossiliferous, with some dark grey limestone benches.

The Frasnian and the Famennian (except the Strunian) are in the logic of deposits of the Middle Devonian with a frankly marine sedimentation (clays). Terrigenous Material reappears at the end of the Famennian (Strunian) associated with a regression.

a.5 Carboniferous

It is very thick in the Timimoun Basin (more than 1500m in the central part) which was at that time part of the great carbon basin of Bechar - Timimoun - Ahnet. It includes two terms:

- *Tournaisian:*

Generally, it begins with black clays, indurated, flaky, silty, pyritous, and micaceous with thin white-grey sandstones with silica cement. Towards the middle of this formation, in a tendency to see dark grey to black clays, finely micaceous, crossed in places by vertical sandstone pipes, including thin irregular lenticular or nodular intercalations from grey to greenish grey sandstones.

- *The Visean*:

It is formed of dark grey, silty, micaceous, sometimes slightly carbonated clays with centimeter films of white to light sandstone, thin, slightly micaceous. From a paleontological point of view, it is found in the clays of the Crinoids, The Debris of Lamellibranches and Brachiopods.

4.1.4. Mesozoic

Mesozoic series are little answered in the Ahnet basin; they are represented by infill continental deposits or younger tertiary rocks, based on discordance with Paleozoic deposits.

Cretaceous

a. Lower Cretaceous

It is represented by versicolor clays, with passes of microcrystalline dolomitic limestone.

b. Upper Cretaceous

It is represented by gypseous formations with saccharoidal clay gypsum, dolomite benches, and massive anhydrite with slightly carbonated red plastic clays.

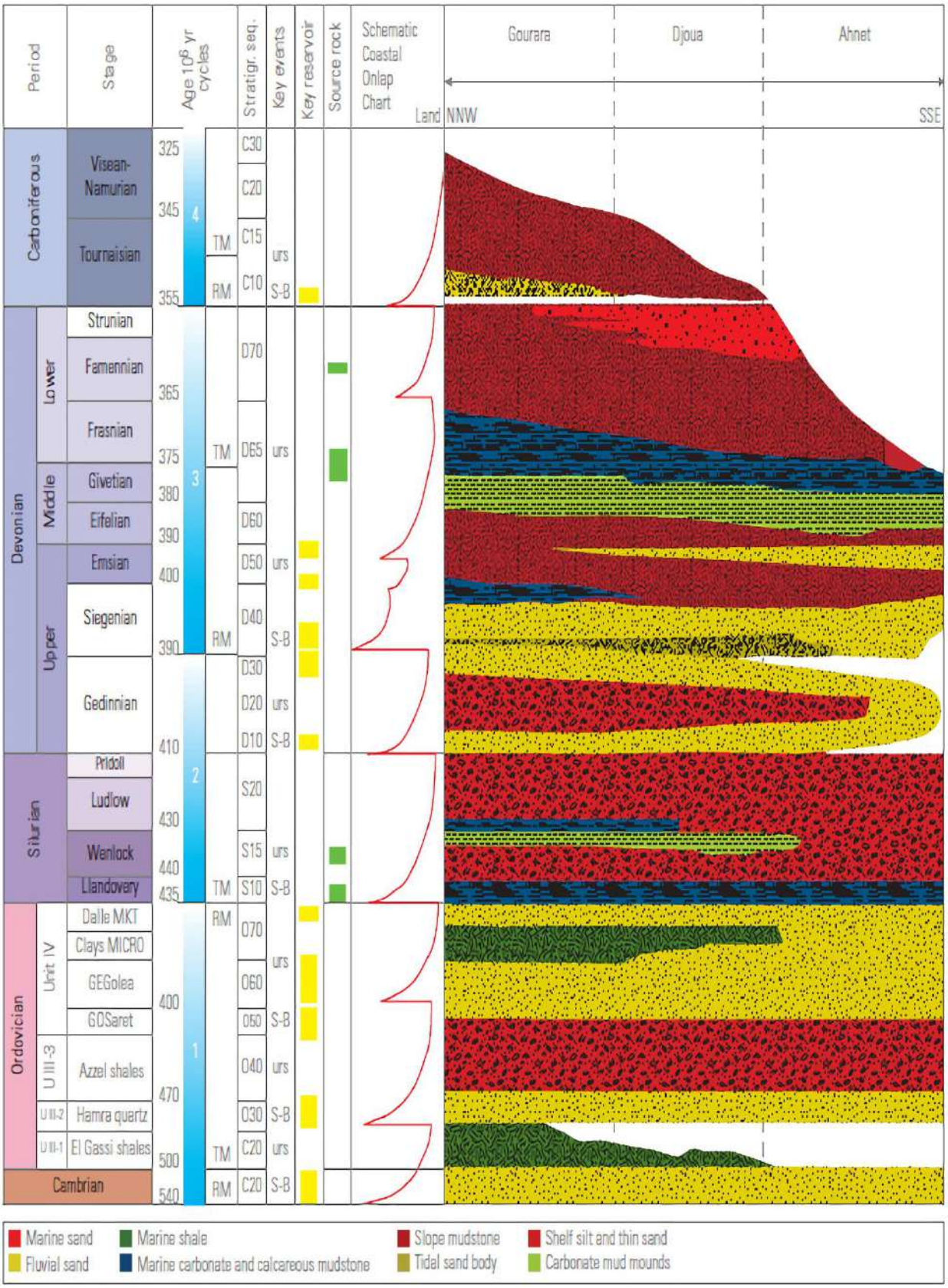

Fig. 02: *Lith-stratigraphic column of the Ahnet Basin (Zeroug et al., 2007).*

5. Tectonics

The Ahnet Basin is distinguished from other basins in the Saharan shelf by its tectonic complexity and degree of intense structuring. It is a depression with a north-south elongation axis.

By its position, the Ahnet basin is approaching the suture zone between the West African Craton stable from the Eburnean Orogeny and the Targui shield cratonized during the Pan-African cycle; their collision certainly created a brittle tectonic at the substrate.

The current structural image was mainly acquired during the Hercynian Orogeny, which ultimately shaped this basin and was strongly influenced by the tectonics inherited from the Pan-African. These events have given rise to three distinct structural areas:

5.1. Eastern Ahnet

It is a structurally high, limited area:

- To the east by the M'Zab Idjerane mole.
- To the west by the sub-meridian accident of Fogarrét Ezzoua, Foum Belrem.
- To the south via Zini and Gour Bouchreiss.

5.2. Central Ahnet

It is located between the Western Ahnet and the Eastern Ahnet. It is the deepest area of the basin, revealing slightly different structural aspects from the previous areas. It shows many large anticlinal structures such as Bahar El Hammar, Garet El Guefoul, Oued Djaret, and Tirechoumine. These structures are associated with vertical faults with significant releases for a platform considered stable.

5.3. Occidental Ahnet

It represents a mole separating the Basin of the Ahnet from that of Reggane. This area is structurally high and narrow; it is limited to the west by an accident coming from the north of Akabli and passing approximately the Adrar Morat to the south.

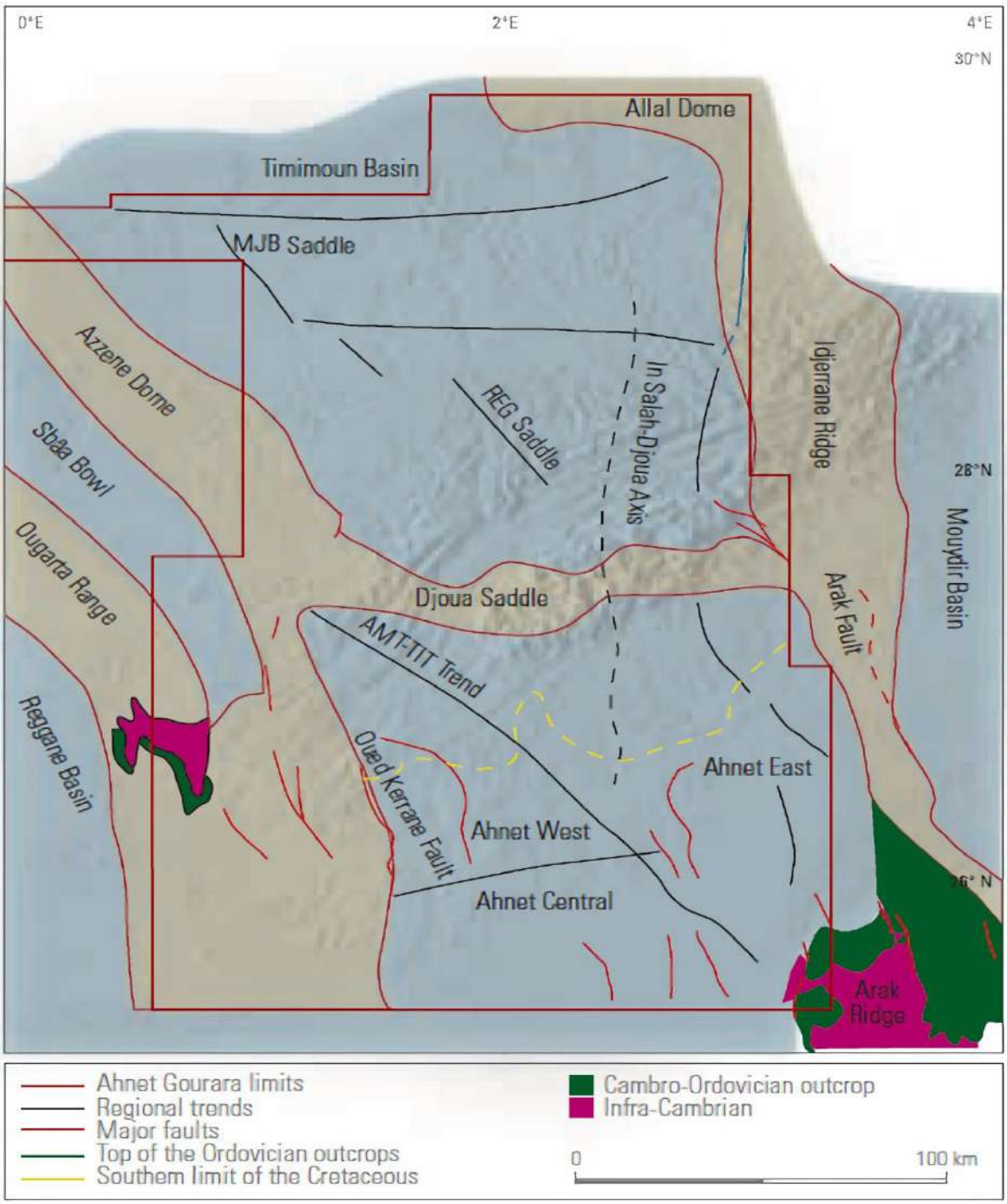

Fig. 03: *Structural map "tectonic elements" of the Ahnet basin (Zeroug et al., 2007).*

5.4. Fault systems

Faults are a crucial element in the structural configuration of the Ahnet (Fig. 04). They show two main directions, N-S to NNW-SSE and NE-SW, and play essentially in reverse components.

These faults are particularly developed in the bordering areas of the basin, where their length can reach 200 km, and their horizontal discharges exceed 1000 m. Their discontinuous character and their often sinuous and arching traces are reminiscent of those of Proterozoic zones of weakness (Donzeau et al., 1981; Haddadi, 1996; Badsi, 1998; Daoudi et al., 1999; Haddoum, 2009).

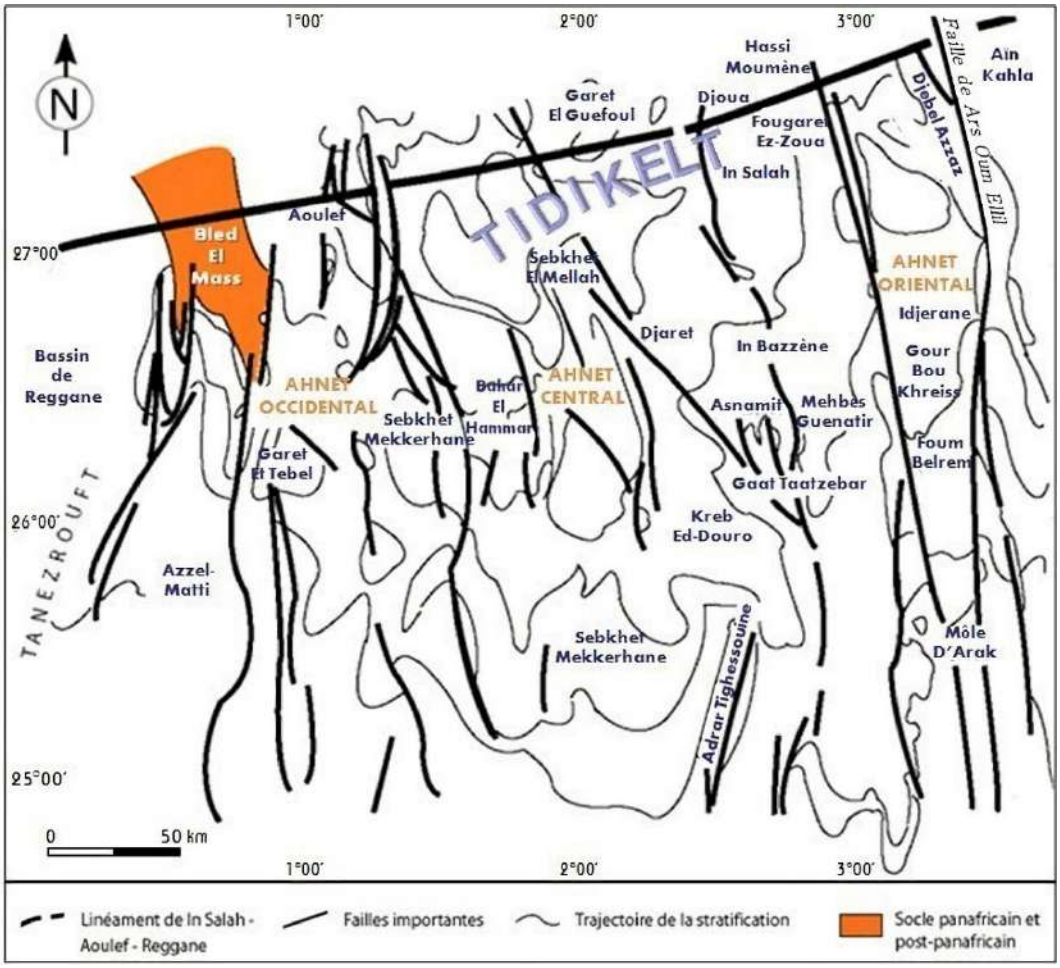

***Fig. 04*:** *Schematic map showing the main fault systems that affect the Ahnet basin (Haddoum,2009).*

The predominant N-S to NNW-SSE trending faults are well expressed in the competent Cambro-Ordovician series and generally tend to be damped in the incompetent Upper Devonian series. These faults are not continuous but arranged in relays, favoring the sliding of individualized blocks concerning one another.

They can also change orientation following a blockage (outcrop of the base), leading to the reorientation of the fold axes and their spillage in the form of unhooking structures (Haddoum, 2009).

5.5. Folded structures

The folded structures observed on the surface or in the subsurface all have NW-SE and N-S axial directions, parallel to the large Pan-African faults, and most often close against accidents with a Reverse-Thrust component. These structures are almost always anticlines.

They present very variable shapes and geometries, resulting from the diversity of the mechanisms that gave rise to them, from the nature of the material affected (mechanical contrasts between the stratigraphic units), and from the evolution of deformation over time (Mercier and Vergely, 1992; Haddoum, 2009).

These structures can be in echelons (fig. 05-A) when they overhang the base faults and parallel to them or quadrangular (fig. 05-B) when they are guided by two directions of faults: N-S and E-W, which drag the Paleozoic blanket into their movements. They can also be elliptical (fig. 05-C) when they get stuck between two NS accidents or circular (fig. 05-D) when blockages prevent the cover from moving sideways and force it to turn on itself through a peel level.

This is particularly observed in areas of intense deformation (compressive relays of crustal faults not visible on the surface). Several fault branches limit some anticlinal forms on the flanks, giving rise to "positive flower" structures, as illustrated by the structure of Oued Ouzdaf (fig. 05-E).

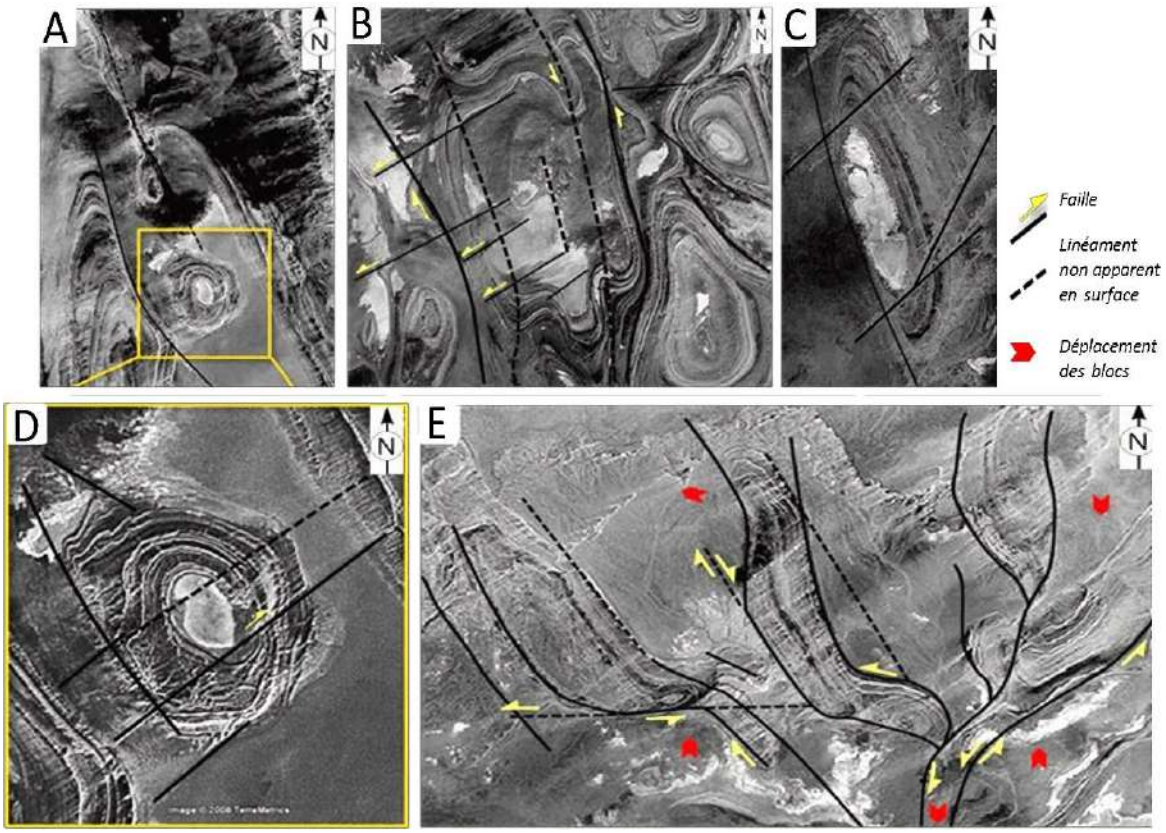

Fig. 05**:** *Main geometries associated with the folded structures of the Ahnet. (A) echelon folds, (B) quadrangular fold guided by two fault directions, NS and NE-SW, (C) elliptical fold stuck between two NS accidents, one of which is not visible on the surface, (D) circular structure overhanging base faults not very visible on the surface, (E) expression on the surface of stall structures in positive flowers (modified from Haddoum, 2009).*

6. General sedimentation context

In the Ahnet basin, the Paleozoic cover is represented by detrital sediments belonging to various environments; continental, paralic, shallow marine, and glacial. Sedimentation conditions were influenced during this period by three main factors:

6.1) The presence of very shallow epicontinental seas, subject to intense wave energy and tidal currents. The North Gondwanan platform had a very smooth topography, slightly sloping towards the NNW (Beuf et al., 1971; Boote et al., 1998; Carr, 2002), in which the high energy facies, characteristic of shallow internal environments, pass quickly towards low energy facies, typical of deeper external environments. There was no break in slope at these cratonic sites, and the continental margin was located thousands of kilometers to the NNW. The sediment redistribution power on this large ramp was very high. Tidal and storm currents played an important role in the lateral transport of sediments and their continual redistribution, thus allowing the formation and

maintenance of a shallow profile and constant slope characteristic of ramp systems.

6.2) The low rate of sedimentation and accommodation. The Ahnet, like all North-Gondwanan regions, experienced a relatively stable tectonic regime and a low rate of sedimentation (Benaacef et al., 1971; Boote et al., 1998). Indeed, the maximum thickness recorded between the Upper Cambrian and the Middle Devonian (a period of 150 MY) does not exceed 1,800 meters. Dividing the thickness by time, while assuming that the sedimentation was continuous (unlikely to be the case), the sedimentation rate would be only 12 m per million years. Such a value is extremely low and is typical of cratonic areas with a low subsidence regime (Beuf et al., 1971). The low rate of accommodation (space open to sedimentation) had significant effects: the permanent reworking of the same clastic material by tidal and marine currents and the increase in the lateral continuity of prograding systems, facilitating their correlation over great distances.

6.3) The absence of continental vegetation cover, especially root systems, known for their active role in the stability of alluvial plains (soils) by reducing the energy of precipitation and runoff, delaying erosion, and reducing the production of detrital materials. According to some authors (Cotter, 1978; 1983), almost all of the Pre-Silurian River networks are of the braided type, and it was not until the Upper Paleozoic that the meandering networks began to appear, following the development of the vegetable continental cover, the pre-vegetative systems were characterized by high migration speeds, and moved incessantly laterally, over vast alluvial plains.

Deposition sediments fell into four main categories, dominated by fluvial, tidal, marine, and glacial processes, respectively (Fig. 06).

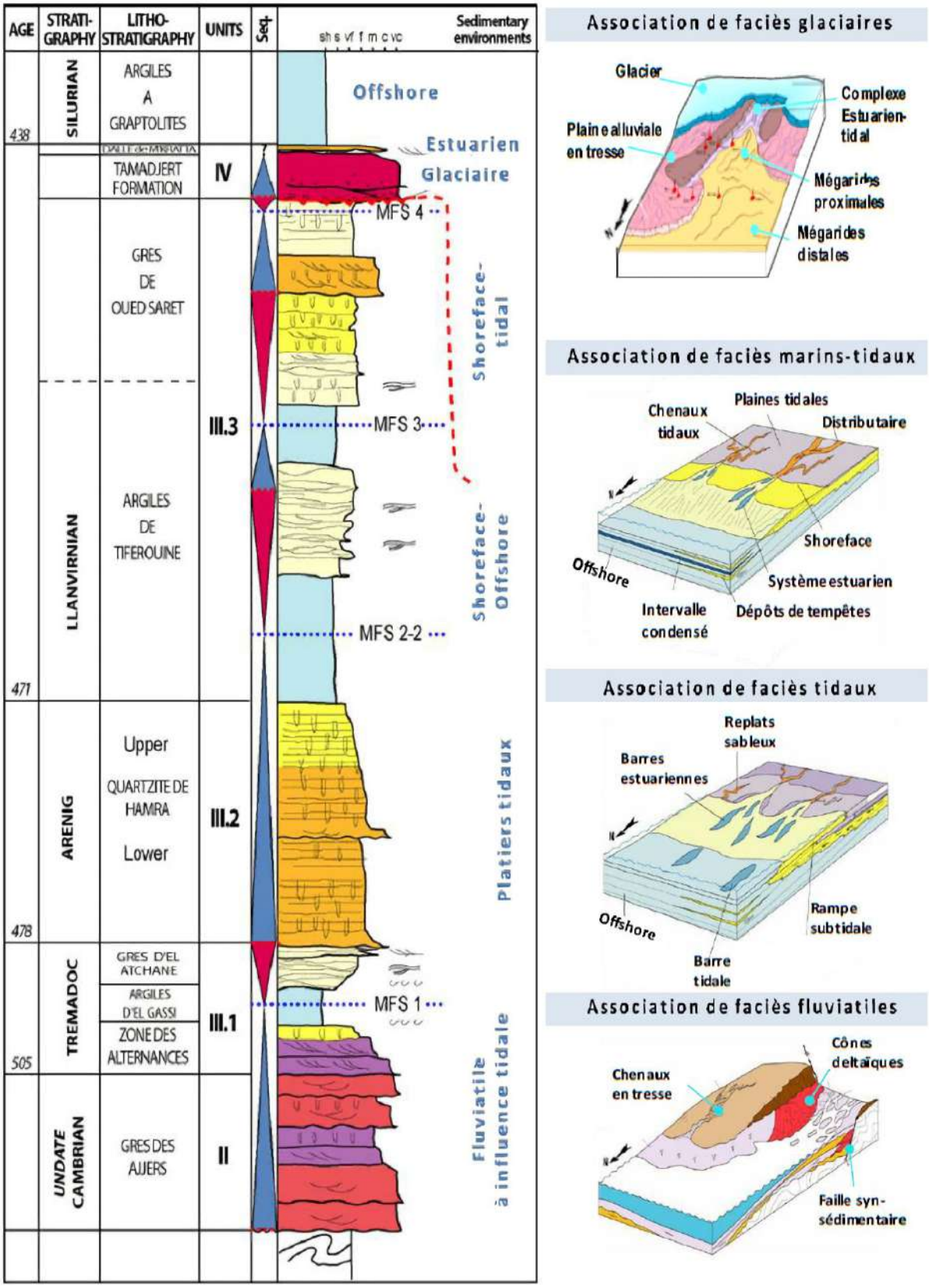

***Fig. 06*:** *Main facies associations observed in the Cambro-Ordovician series of the Ahnet (modified after Euzen et al., 2005).*

7. Paleostructural evolution of the Ahnet basin

The reconstitution of the global geodynamic framework, as well as the evolution of deposit environments and their relations with the succession of paleogeographic contexts controlled by paleoclimatology, paleo-hydrogeology, the structuring of basins and the dynamics of environments in a general framework.

7.1. Pan-African phase

Precambrian tectonics, particularly the Pan-African phase, are at the origin of a large fracturing network characterized by vertical sub-meridian accidents, underlined by mylonitic. These accidents are interpreted as stalls with horizontal discharge up to 100 km. These accidents are at least late Pan-African age and possibly older.

7.2. Cambro-Ordovician phase

The Pan-African orogenic phase, ending during the Cambrian, is followed by a period of significant erosion which levels the structures and the reliefs, forming a vast peneplain characterized by a slight dip towards the north as evidenced by the perfect homogeneity of the directions of transport observed in the overlying deposits. The Cambro-Ordovician series show, locally, that a tectonic instability accompanied their deposit.

7.3. Taconic phase (Caradoc)

The Cambro-Ordovician distension, where the broad outlines of the future basins of the Saharan Platform can already be detected, is followed by a transgression of the Arenigian-Llanvirnian age.

7.4. Silurian phase

The glacial phase follows the melting of the icecap, and eustatism engenders a generalized transgression. This reaches the southern Sahara, where black graptolite clays are deposited, which are rich in organic matter.

7.5. Caledonian phase

The Silurian is characterized by black clays gradually taking on detrital material from the South East. Several local unconformities are the harbinger of the Late Silurian and Early Devonian tectonic phases.

7.6. Devonian phase

The Lower Devonian is the seat of various tectonic-sedimentary phenomena. On the one hand, variations in thickness and facies are observed along the sub-meridian structural axes; on the other hand, in the southern and eastern parts of the Hoggar, volcanism is known in the form of basic flows interspersed and sometimes reworked in the formation of Efeimazerta (Middle and Upper Devonian Movements).

The Frasnian discordance is the superposition of two discordances. The first of these is located just above the Emsian, and the second is located at the wall of the Upper Intra-Devonian radioactive peak.

7.7. Famennian post phase

Micropaleontology highlights a gap in the Famennian. Indeed, in a fishbone arrangement, the western and northern Saharan basins show a general Carboniferous onlap on different Devonian terms.

7.8. Hercynian movements

They are divided into early (Visean) and major (late Paleozoic) movements. The microstructural analysis indicates an N40° tightening direction, compatible with North-West-South East structures.

7.9. Triassic phase

This phase is characterized by collapses marked by thickening and variations in facies and thicknesses from Southwest to Northeast, which are described. Variations in thickness are observed along the North - East - South - West faults, which are accompanied by volcanism and are related to the distension that occurred during the Hettangian.

7.10. Jurassic phase

During this phase, a collapse of the North-West border of the basin causes a variation in thickness with a maximum of deposits at the level of the axis of the Atlas furrow, located to the North-West of the Triassic basin with carbonate series at oolitic facies corresponding to a high energy environment.

7.11. Cretaceous phase

The Lower Cretaceous (Neocomian - Barremian) encountered a reactivation of the North-South faults, in reverse by East-West compression, which occurred during the Austrian phase. This has led to great variations in thickness south of the Saharan platform, followed by erosion that affects the entire Lower Cretaceous in places along the North-South faults (BEICP, 1972).

8. Maps interpretation

Eighteen maps 18 (positioning, isopach, and isobaths) were produced to illustrate the distribution and variations in thicknesses and depths of the various stages of the Paleozoic at the scale of the Ahnet basin. To do this, we examined all the "Master logs" of the boreholes we have in the Ahnet basin (24 wells). The maps were produced using the SURFER 16 software. Fourteen wells (14) were selected for the production of these maps. The rest of the wells could not be considered because they are shallow holes (core drill), so we used the wells that cut a large part of the Paleozoic stages.

The surface structure (Fig. 07) has the shape of a semi-syncline; the wells positioned in the North and South-East are practically raised compared to the wells positioned in the South and South-West.

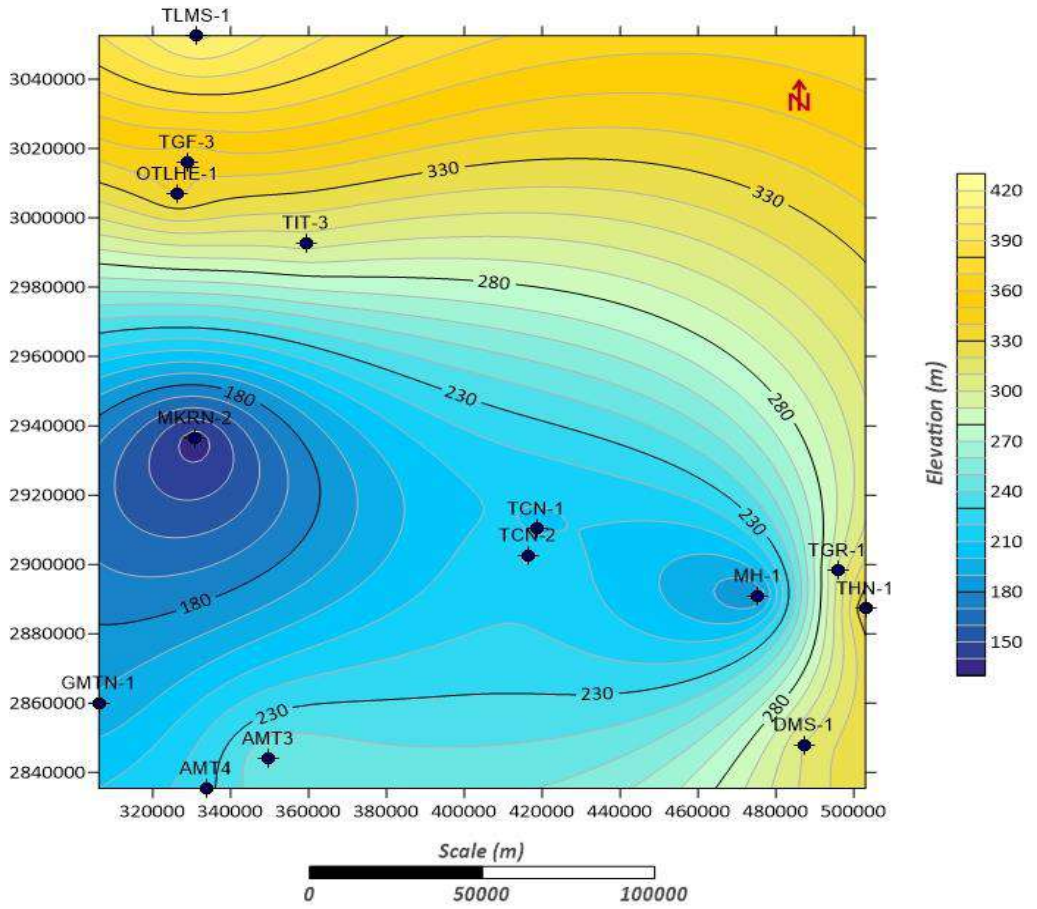

Fig. 07: *Positioning map of study wells in the SHALE ZONE perimeter.*

Reminder:

Isobath maps are used to represent the structural image in depth, visualizing the current absolute coasts of a geological horizon.

Isopach maps illustrate variations in reservoir thickness (local, regional basin). They also make it possible to locate the zones with strong subsidence and the directions of the Syn-sedimentary accidents, which control them during tectonic periods, as well as areas with intense erosion and the accidents that control them during compressive tectonic phases. These maps correspond to a formation or set of formations located between two landmark horizons; they also make it possible to indicate the local or regional extension of the stratigraphic or lithological units.

8.1. Cambrian

Post-Pan-African peneplanation extended widely across the African continent during the Cambrian. In North Africa, Cambrian sediments lie in unconformity on rocks of the Precambrian craton and all existing infra-cambrian basins. With the Cambrian, the Caledonian megacycle

begins. The Cambrian and Ordovician quartzitic sandstones in the Ahnet basin are part of a sizeable detrital sheet spanning North Africa and the Arabian Plate.

Beuf et al. (1971) speak of regular movements along the N-S faults, which initiated the development of the two basins and influenced their shapes. The associated variations in facies and thickness along the N-S faults of the "Foum Belrem" region are a telling example. The Cambrian isopach map shows a single NW-SE direction on the position of the Ahnet basin, with a maximum thickness in the basin's center (Fig. 08).

8.2. Ordovician

During the Ordovician, Africa drifted through the South Pole. Towards the end of the Ordovician (about 445 MY), glaciation occurred, and the glaciers have diverged since the Nigerian Shield and central Africa to around 60° latitude. The glaciation ceased at the end of the Ordovician as Africa drifted north. As it appears in an outcrop north of Hoggar, the upper limit of the Cambro-Ordovician sequence corresponds to a discontinuity surface formed by traces of glacial erosion and/or notched drainage valleys.

A wide range of continental clastic debris spread northward during the Ordovician. Ordovician sandstones are important gas reservoirs in the study area. Marine and continental sandy facies are deposited in the east, and more clayey facies are deposited in the west. Early movements along the Pan-African faults affect the sedimentation and development of the Ahnet basin. The maximum thickness of the Ordovician sequence in the Ahnet region does not exceed 1000 m.

The isopach map indicates two depots-centers on the Ahnet basin, one in the north with a NE-SW orientation (this is probably the first sign of the individualization of the Timimoun basin) and another in the center. The axis on the Ahnet basin remains overall N-S (Fig. 08). Between the Infracambrian and the Ordovician, we are, therefore, witnessing a slight shift towards the north of the Ahnet basin.

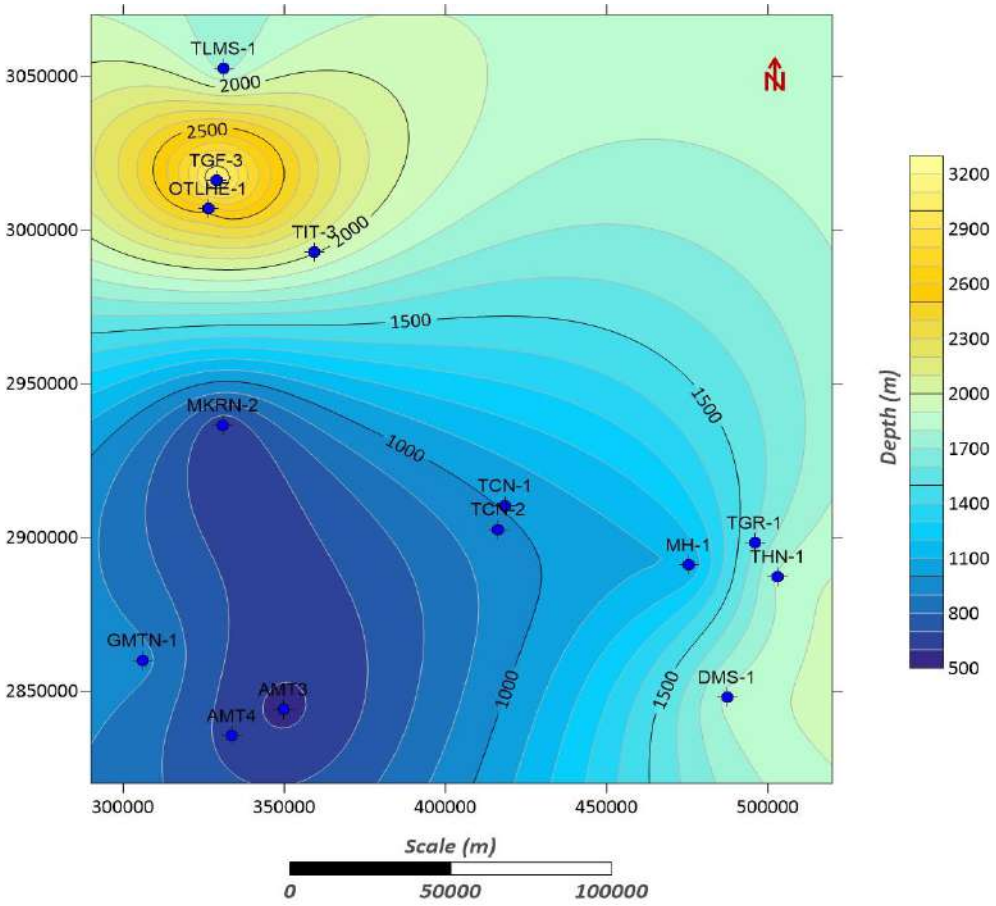

Fig. 08: *Cambro-Ordovician roof Isobath map showing the structure of the study area before Silurian sedimentation.*

8.3 Silurian

After the melting of the Ordovician glaciers, the sea level rose, and the Silurian seas invaded the Saharan platform. Black Silurian clays are the main source rock of the Algerian Sahara.

The Silurian sedimentary series materialized by grey-black to black clays, indurated, micaceous, silty, slightly flaky, carbonaceous, and pyritic with rare white sandstone passes, translucent, thin to medium, sub-rounded to subangular, siliceous to silico-clay, moderately hard a friable and white limestone, microcrystalline, moderately hard and grey-white, soft, clayey.

Silurian thicknesses are particularly important in the majority of Algerian basins, in particular in the Ahnet basin. Silurian sedimentation exceeds 1000 m of power. The Silurian's thickness variations are caused by structures causing fault movements and the filling of Ordovician topographic depressions.

The Silurian thicknesses configured in an Isopach map (Fig. 09) are critical, with a

progressive tendency from the NW to the SE; small thicknesses are observed in the extreme SW. The variations in thickness are mainly due to the topographic irregularity at the end of the Ordovician caused by the ice caps (Boudjema, 1987).

The Caledonian unconformity in the Ahnet basin is materialized by a significant discontinuity at the Silurian-Lower Devonian contact. (Boudjemâa, 1987) Furthermore, others concluded that the Silurian-Devonian discontinuity was due to E-W compression, which generated reverse motions along N-S faults.

Structurally, the Silurian isobath map shows no significant event, and the structure has kept the same model inherited from the Ordovician (Fig. 10).

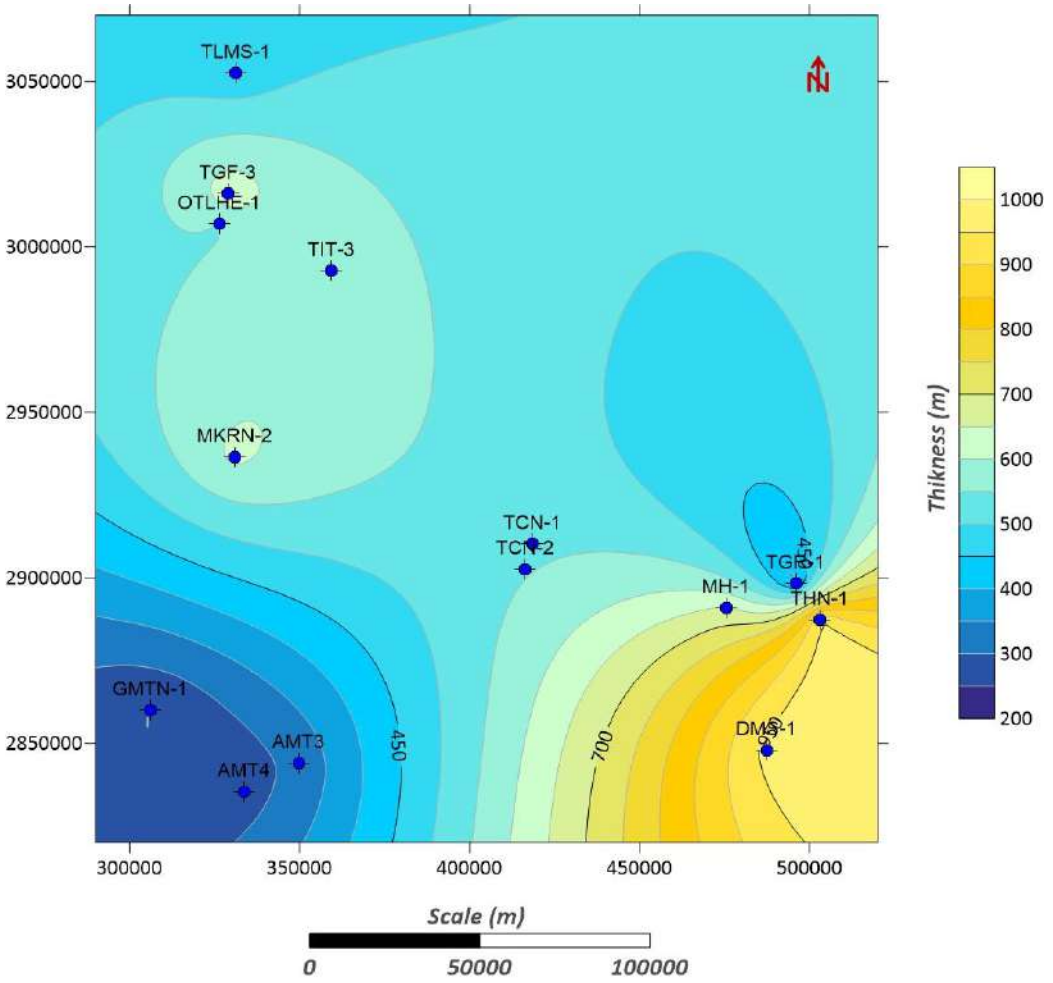

Fig. 09: *Silurian Isopach map showing the thickness variation within the study area.*

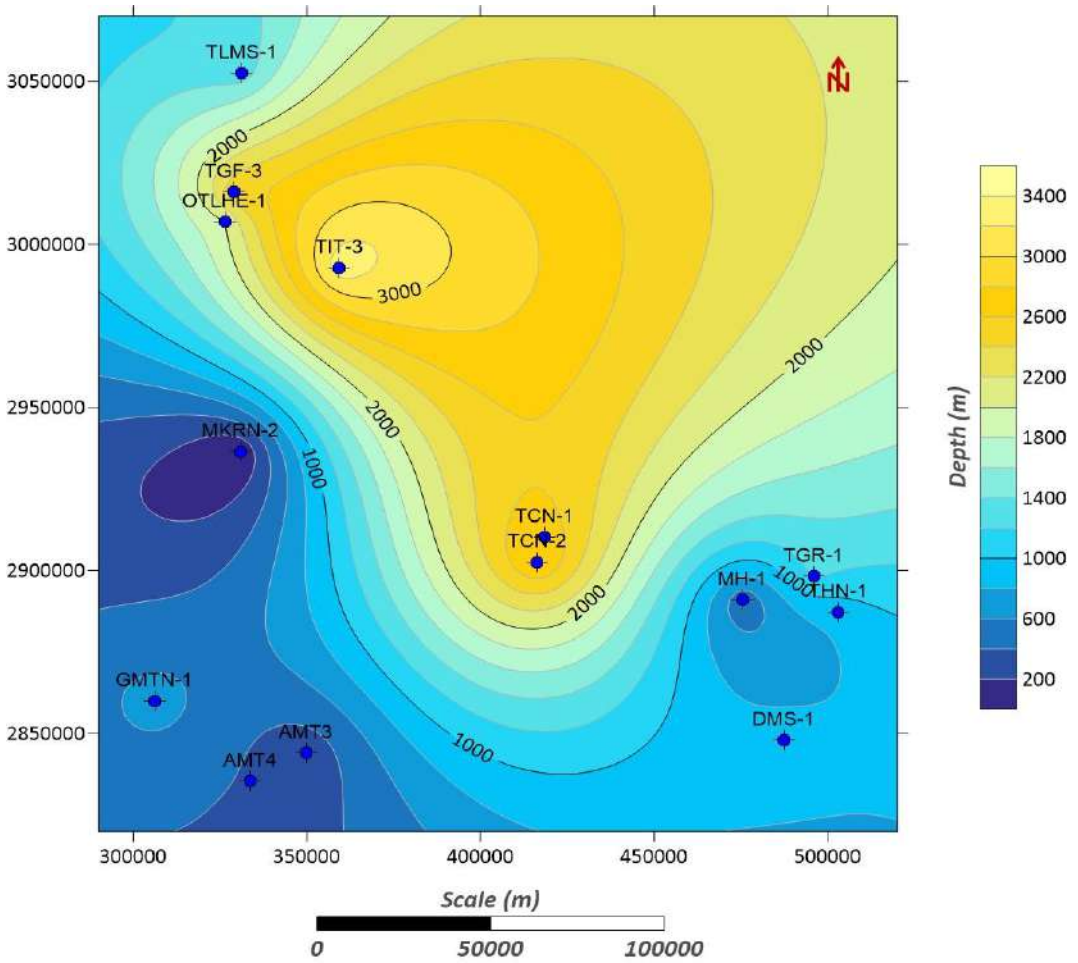

Fig. 10: *Isobath map with a Silurian roof showing the structure of the study area before the Devonian sedimentation.*

8.4. Devonian

The base of the Devonian marks the beginning of the Hercynian cycle. In the Devonian, the sedimentation is 1000 to 1500 m of power; its duration oscillates between 56 and 66 MY (estimated according to several authors).

The Devonian series in the study area have a continental and marine character at the same time, represented by intercalations of dark grey to black clay, indurated, strongly silty, micaceous, flaky, carbonate, and white sandstone, fine to medium, sub-rounded to subangular, siliceous to silico-quartzitic, hard, locally grey-white to dark grey, thin to medium, sometimes coarse, silico-clay with a pass of white, grey limestone, clayey, soft and crystalline.

8.4.1 Lower Devonian (Emsian, Seginian and Gedinnian)

The sandstone reservoirs of the Lower Devonian contain the most significant deposits discovered to date in the Ahnet and Timimoun basins.

Biostratigraphic data indicate unconformities between the Segenian and the Gedinnian and within the Emsian. The Ahnet basin appears as a large, low-relief synecise during the Lower and Middle Devonian.

The late Silurian early Devonian passage was marked by the predominance of a detrital deposit; it is the material of the Caledonian orogeny that caused the almost total uplift of the study area, which subsequently underwent an erosive period, the latter which levels the whole structure which sometimes affects the Silurian.

There are many areas of high thickness (Figs. 11-13-15); however, the regional trend is clear: the thickening is towards the north in the Ahnet basin.

The Lower Devonian is not seismically mappable, and well data indicate that its thickness is relatively constant. This suggests that many present-day structures experienced weak pre-Givetian movements and were rejuvenated in the Hercynian era.

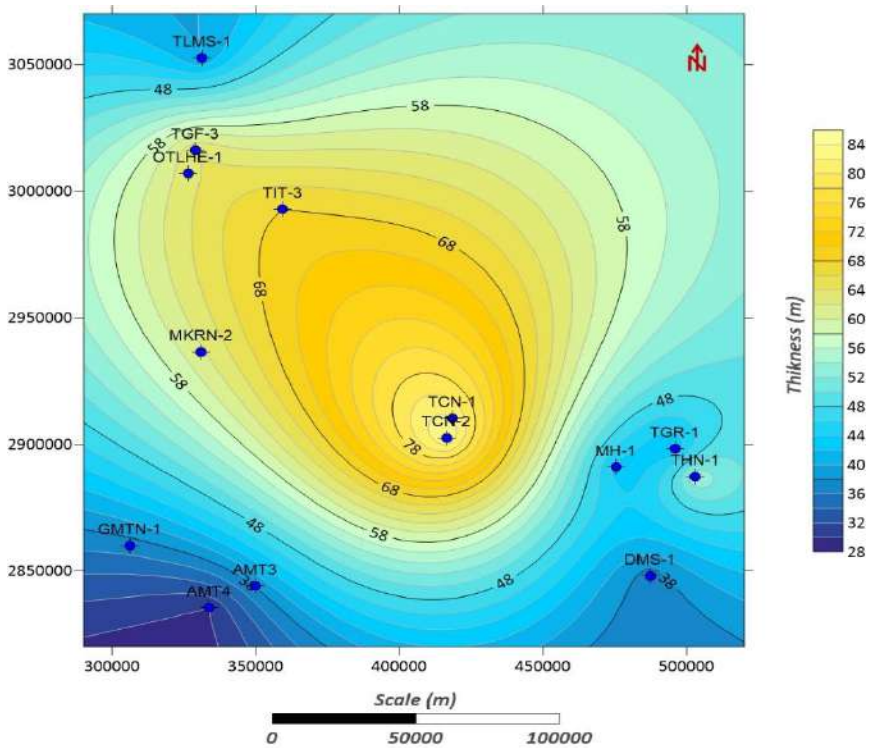

***Fig. 11**: Isopach map of the Emsian showing the thickness variation within the study area.*

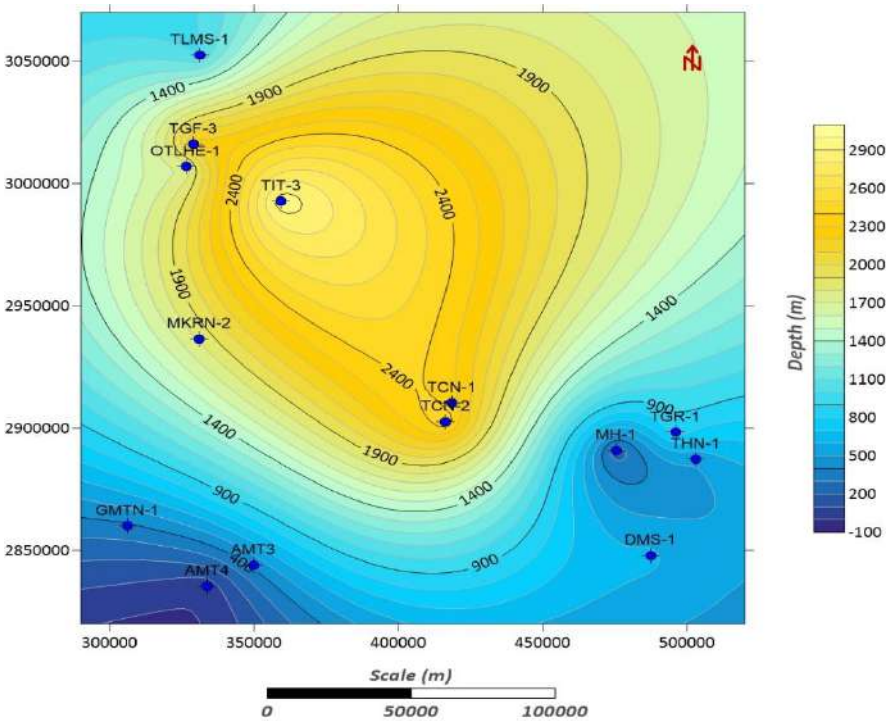

***Fig. 12**: Emsian Isobath map showing the depth variation within the study area.*

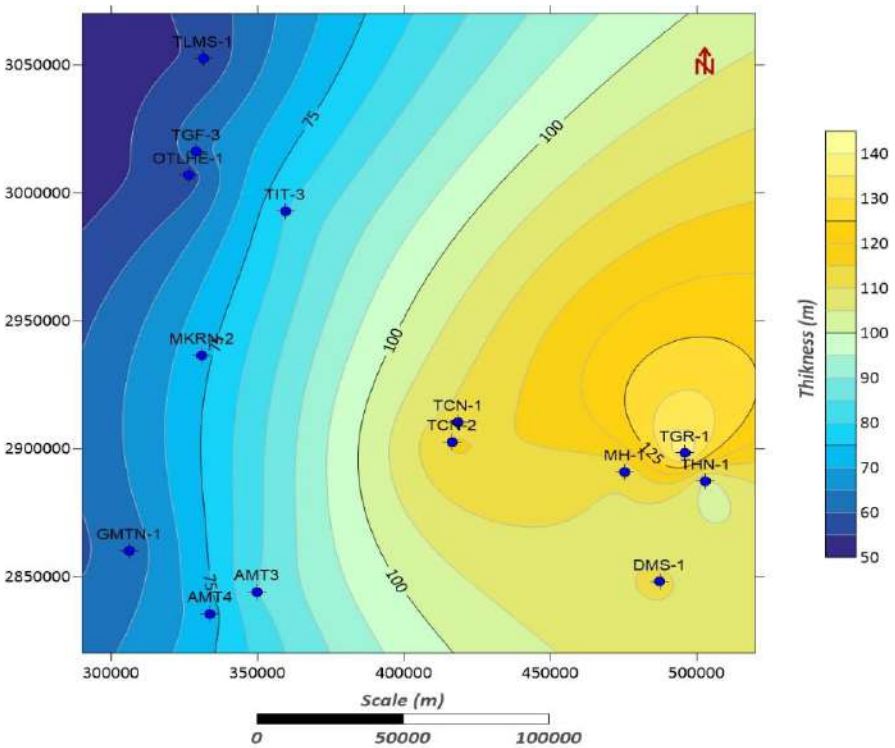

***Fig. 13**: Isopach map of the Seginian showing the thickness variation within the study area.*

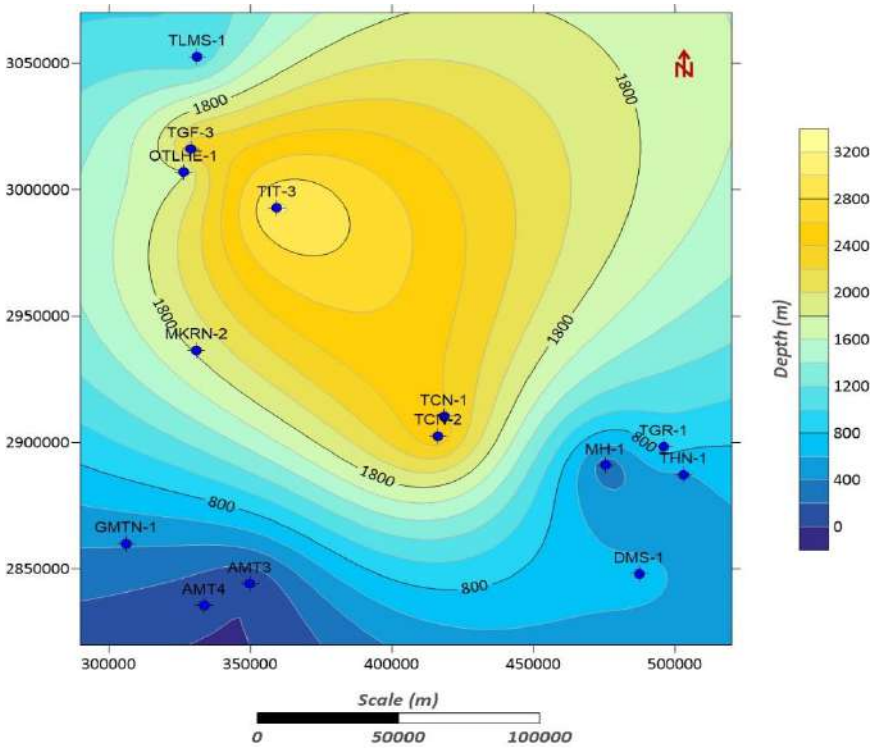

***Fig. 14**: Seginian Isobath map showing the depth variation within the study area.*

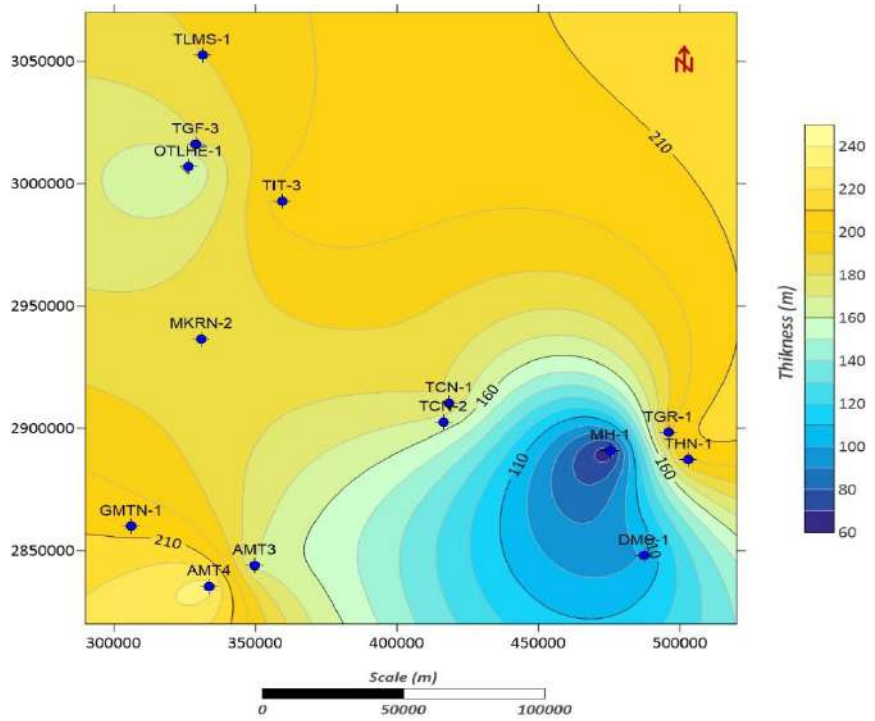

***Fig. 15:** Isopach map of the Gedinnian showing the thickness variation within the study area.*

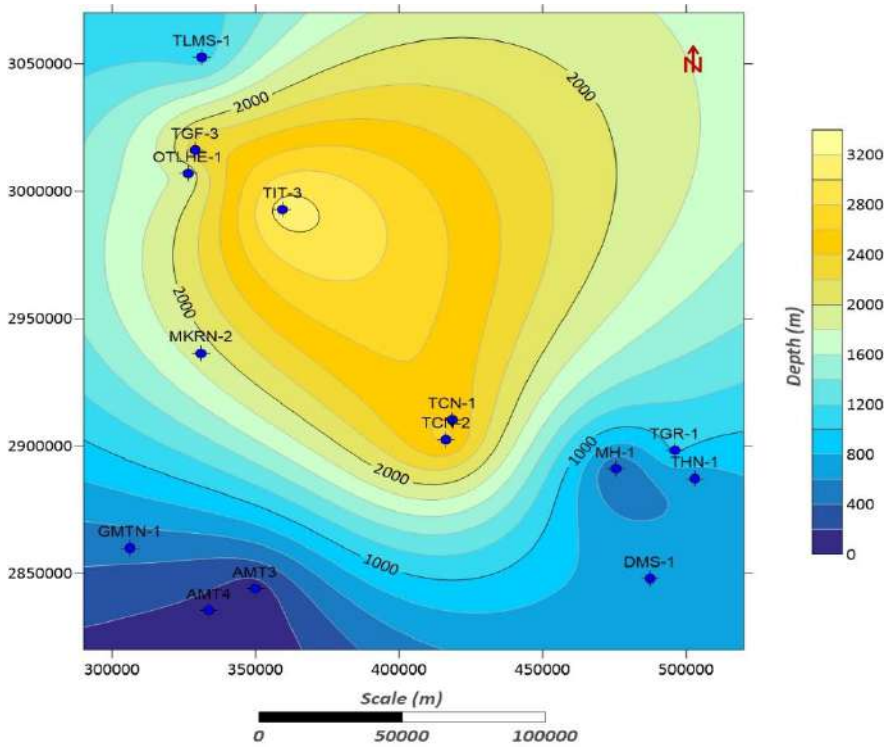

Fig. 16: *Isobath map of the Gedinnian showing the depth variation within the study area.*

8.4.2 Middle Devonian (Covinian, Gevitian)

The northern axis of the Ahnet basin is NW-SE, almost in line with what has gone before. Another axis is individualized in the N-S direction with a maximum thickness, towards the S-E for the Gevitian of 100 m (Fig. 19) and the N-W for the Covinian, 130 m (Fig. 17).

The tectonic-sedimentary events originate from epi-orogenic movements that affected Gondwana (Beuf et al., 1971; Boudjemâa, 1987). The Devonian platform emerges gradually and tilts towards the NW (direction of the Devonian paleocurrents (Beuf, 1974)).

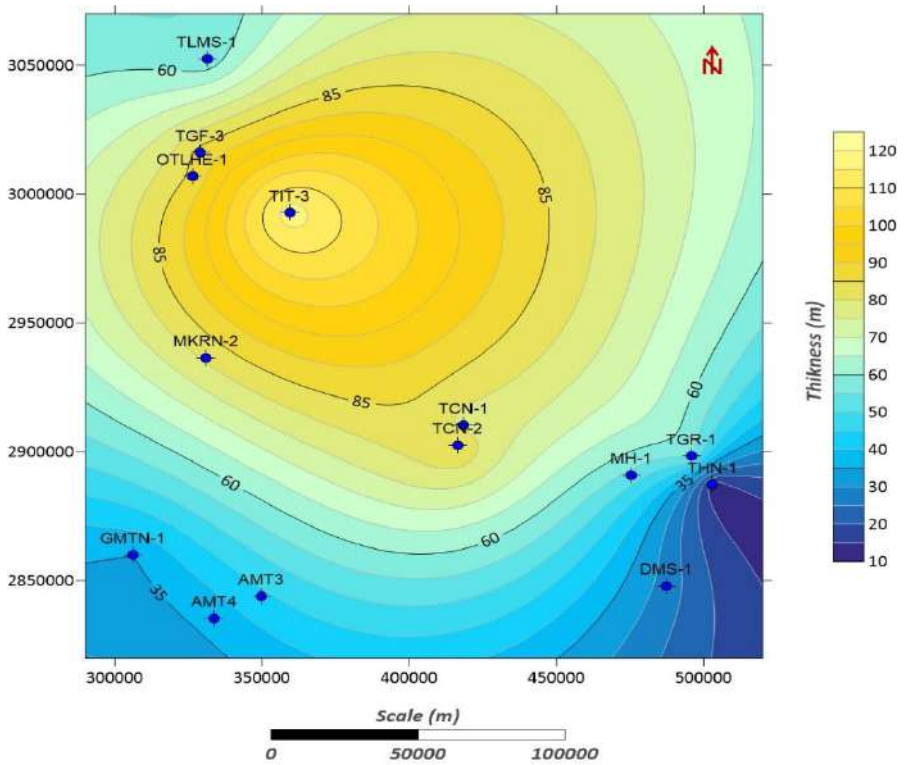

***Fig. 17**: Isopach map of the Covinian showing the thickness variation within the study area.*

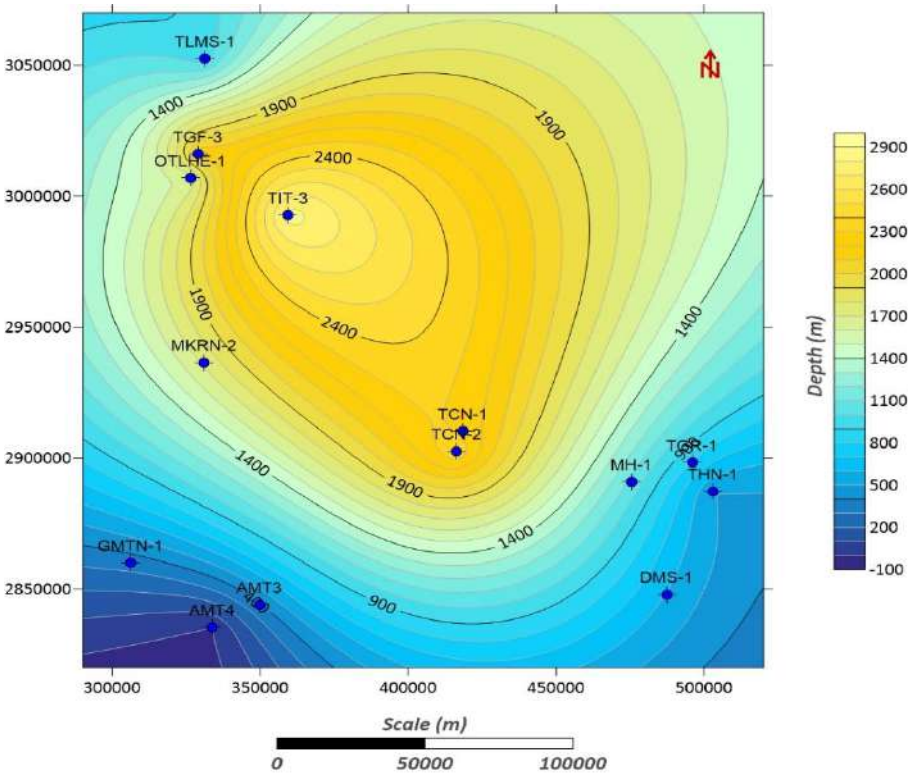

***Fig. 18:** Isobath map of the Covinian showing the depth variation within the study area.*

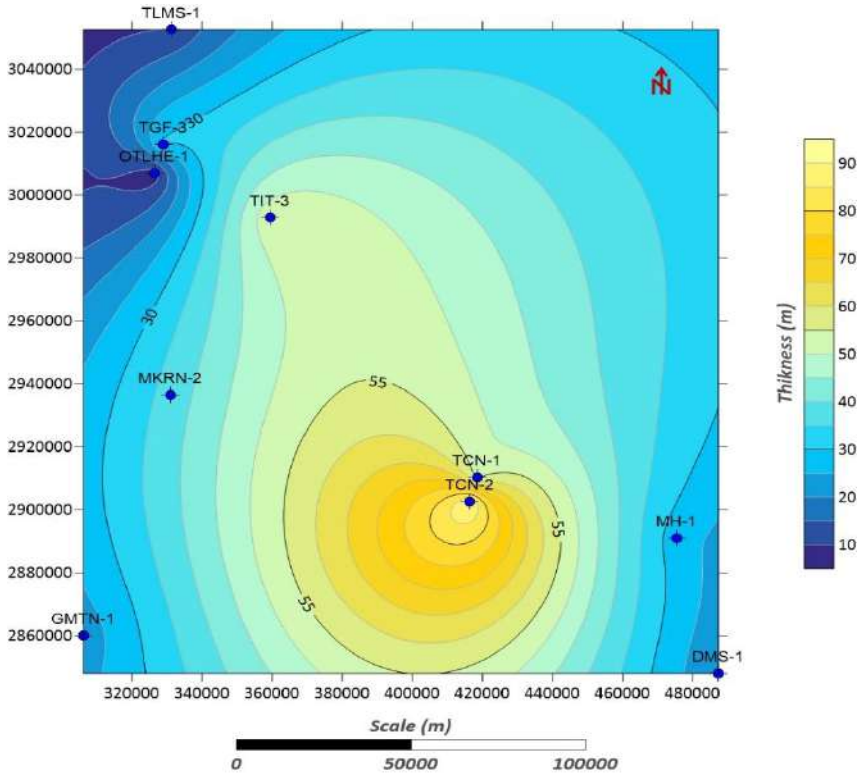

Fig. 19: *Isopach map of the Gevitian showing the thickness variation within the study area.*

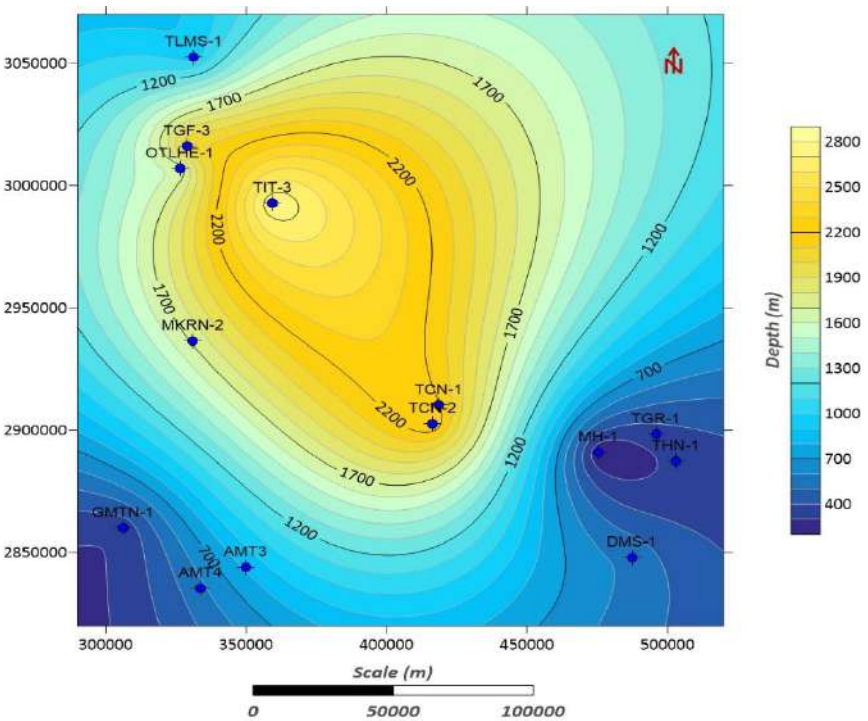

Fig. 20*: Isobath map of the Gevitian showing the depth variation within the study area.*

8.4.3 Upper Devonian (Frasnian, Famennian)

The thickness of the Upper Devonian is of the order of 2000 m (1150 m Famennian plus 850 m Frasnian). Marine deposits extend further south. Clays represent them and are also a bedrock in the region. The axes of the basin directions are preserved; the most important deposit center for the Famennian is located approximately to the south of the basin and to the north of the study region (Fig. 23). In contrast, the direction axis of the thicknesses of the East Frasnian spread towards the NW-SE (Fig. 21).

The erosion surfaces marked by the complete absence of the Devonian series in the perimeter and the structure at the end of the Devonian correlated with that of the Silurian led us to conclude that this period experienced instability on the sedimentary and structural level (rapid subsidence).

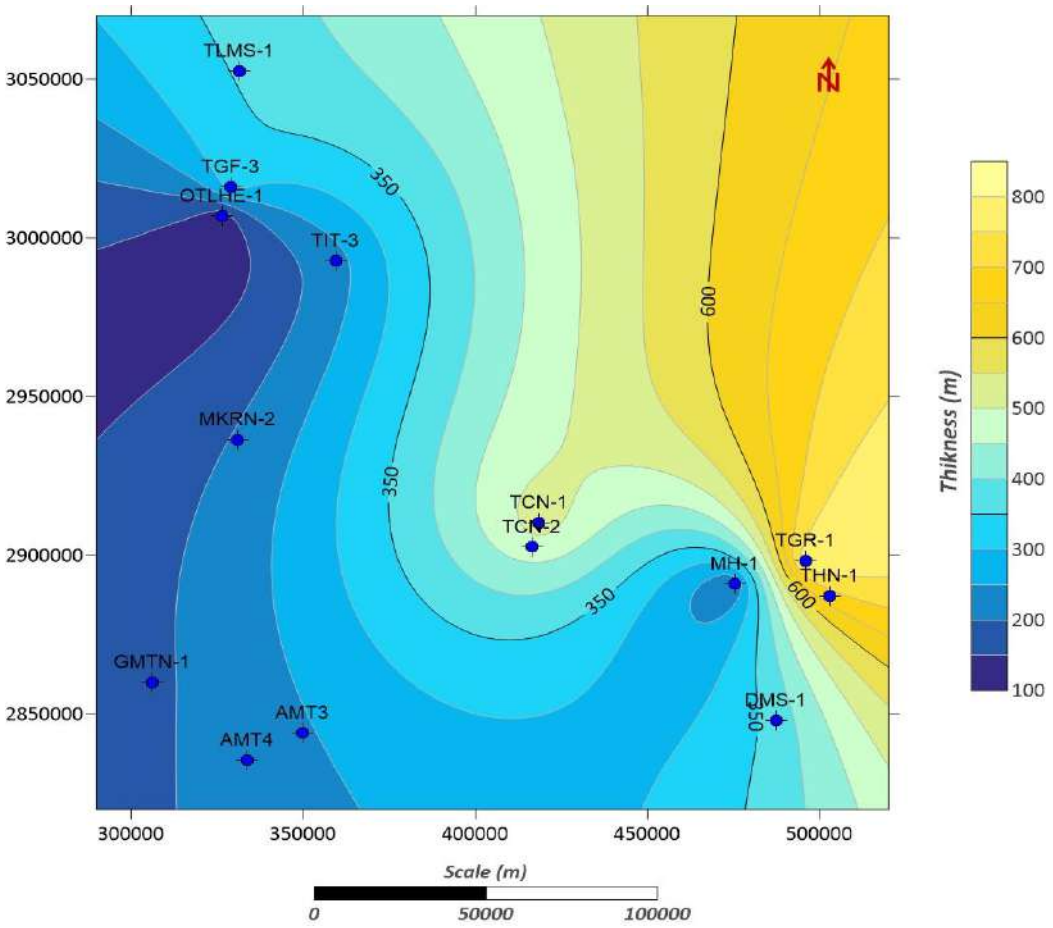

***Fig. 21**: Isopach map of the Frasnian showing the thickness variation within the study area.*

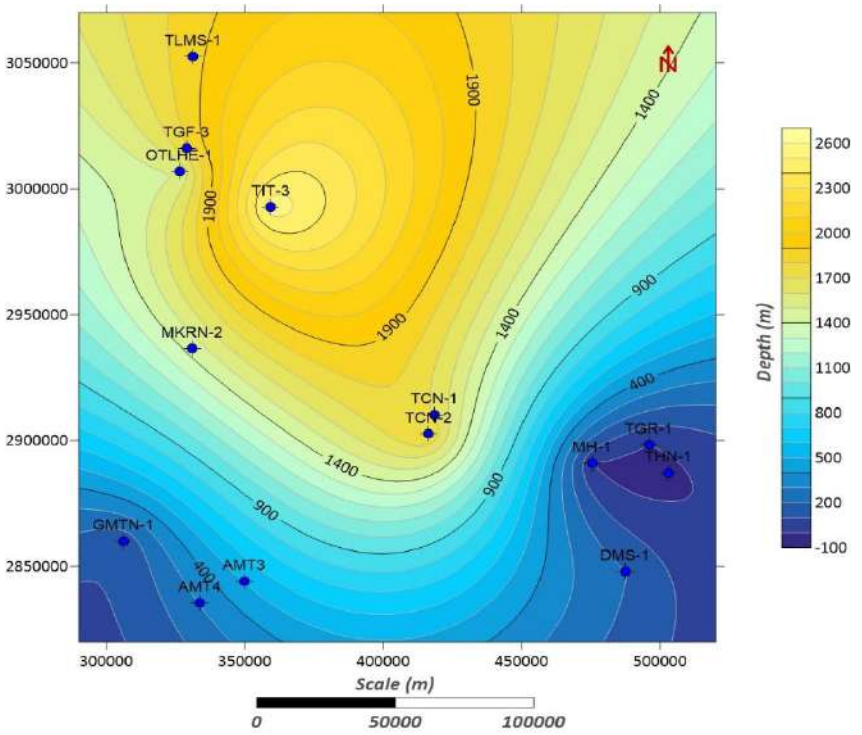

***Fig. 22**: Isobath map of the Frasnian showing the depth variation within the study area.*

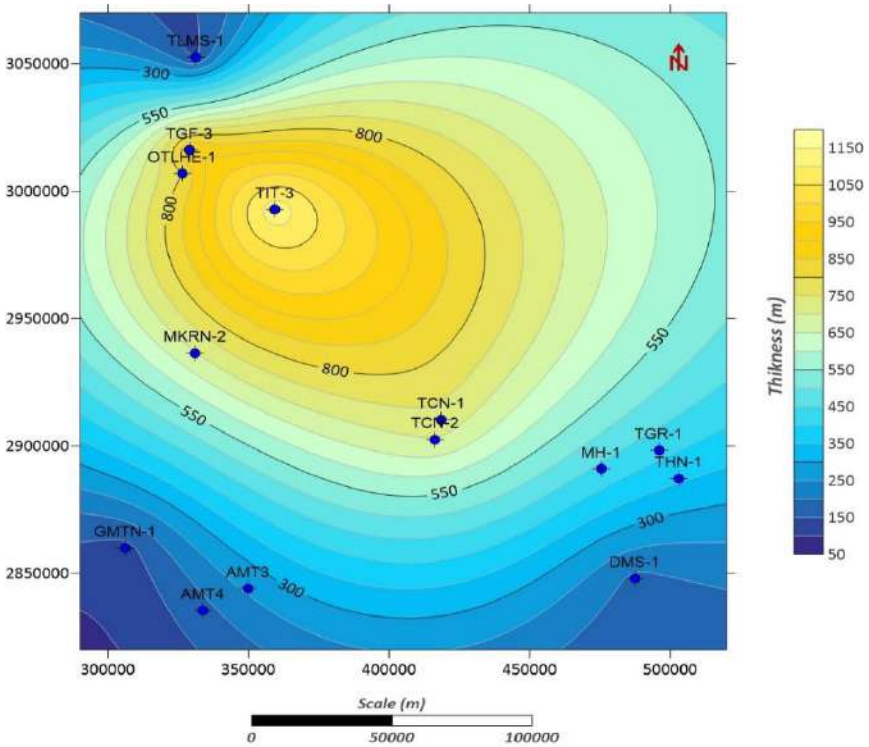

***Fig. 23**: Isopach map of the Famennian showing the thickness variation within the study area.*

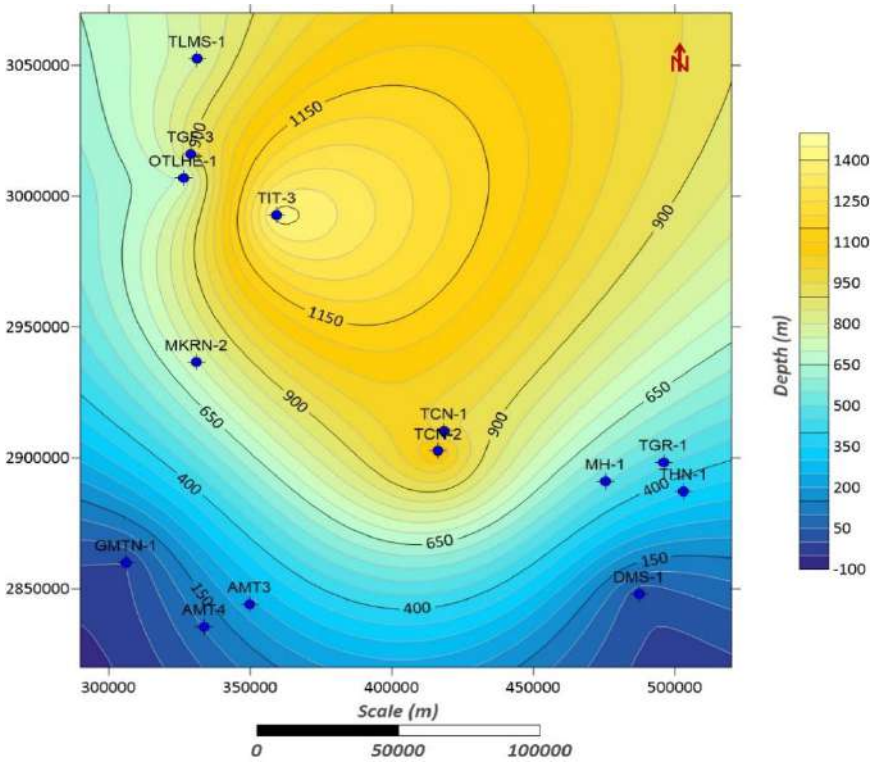

Fig. 24*: *Isobath map of the Famennian showing the depth variation within the study area.

9. Petroleum aspect

9.1. Source rocks

The potential source rocks that generate gas in the Ahnet basin are essentially radioactive clays from the base of the Silurian and Frasnian, with an immense gas potential. The thickness of radioactive Silurian clays varies from a few meters. Currently, we recognize at least two (02) gas generation phases:

The first from the Upper Devonian before the Hercynian structuring is the most important, and the second is synchronous with the Hercynian structuring and relatively less important than the previous one (Achour, 2008).

9.2. Reservoir rocks

The reservoir rocks are mainly Cambro-Ordovician and Lower Devonian sandstones. Several boreholes have also been produced in originally compact unite IV.

The few data available show that the petrophysical characteristics are often better in unit II than in the sandstone in units III and IV. The reservoirs of Unit III do not show good storage quality. Natural fracturing improves these reservoir characteristics locally.

The Tournaisian is also a suitable reservoir, often eroded in this region. The Lower Devonian can also be considered a good reservoir. The Emsian base has been produced in several holes.

9.3. Seal rocks

The thick Silurian clay series constitutes an excellent seal rock for the reservoirs of Unit IV. As for Unit III-2, it is the Ordovician clays of Unit III that form their cover. The presence of high rejection faults is likely to favor dismigration and consequently reduces the rate of filling of structures. Frasnian and Emsian clays provide the cover for the Lower Devonian reservoirs (Achour, 2008).

9. Maturation history

In the region of In Salah, a study of the heat flux was carried out (Takherist & Hamdi 1995). The heat flux map of the Ahnet region shows that the average flux level exceeds. Three areas of positive anomalies have been identified:

- In the southwestern part of the Ahnet basin, the flow reaches 120 mW / m2.

- In the Reg area in the NE, the flow exceeds 100 mW / m2.

- In the North-West, the flow exceeds 110 mW / m2.

The regional tendency of heat flux in the Ahnet is to decrease from the north (Timimoun) to the south (Ahnet), implying a decrease in the flux with the deepening of the basin. This heat flux level is very high compared to that generally measured in Paleozoic cratons, which is 45 mW / m2.

Takherist and Hamdi (1992) suggest a relationship with a probable recent rifting. Consequently, from the petroleum point of view, they ask themselves a pertinent question: "How were these deposits preserved despite the intense tectonics, particularly during the Austrian phase responsible for the operation of all the accidents and faults in the region?".

At least part of the region's gas potential may be associated with recent thermal expansion (past to present) depleting residual oil potential. This would explain the low pressure in the reservoirs, low trap filling rates, and mainly dry gas hydrocarbons (Takherist and Hamdi, (1992)).

However, the post-Hercynian deformation is much smaller than that acquired at the end of the Hercynian phase. In addition, the Silurian clayey series are sufficient for at least Cambro-Ordovician reservoirs to be preserved.

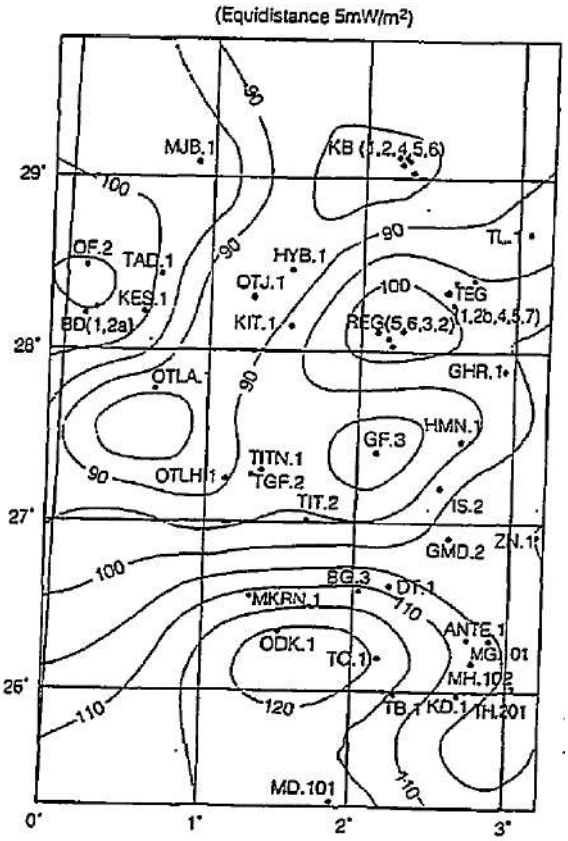

***Fig. 25**: Heat flow in the Ahnet basin (Takherist et Hamdi, 1992).*

Conclusion

The Ahnet basin is one of the most structured basins of the Saharan platform. Structures associated with reverse faults appear on the surface and are confirmed in the subsurface by seismic. The Paleozoic series of the Ahnet basin contains several reservoir levels (Lower Devonian, Silurian-Gedinnian passage zone, and Cambro-Ordovician), producing gas with more or less significant flow rates.

This synthesis indicates that the Ahnet basin shows signs of regional differentiation in its structural and thermal evolution. However, the delineation of the hydrocarbon accumulation zones requires the siting of close exploration wells to provide more detailed data for more credible thermal and geochemical simulations.

Chapter II

Geochemical characterization

Introduction

This chapter presents the results of the Rock-Eval analysis and palynofacies examination of Frasnian shale from three wells drilled in the Ahnet Basin, Algeria. The Rock-Eval data provides information on the thermal maturity, organic richness, and hydrocarbon potential of the shale; by heating the rock and measuring the quantity and composition of the volatile products released (Mamaseni et al., 2022), Rock-Eval pyrolysis can determine parameters such as total organic carbon (TOC), the hydrogen index (HI), the oxygen index (OI), and the production index (PI), which are commonly used to evaluate the source rock potential of a shale (Espitalié et al., 1985; Peters and Cassa, 1994). while the palynofacies analysis offers insights into the depositional environment, the source of the organic matter, and the preservation conditions of the organic matter. Even on the type, abundance, and preservation state of the organic matter, as well as the nature and intensity of the depositional environment (Sia and Abdullah, 2012; Hakimi et al., 2013; Mendonça Filho et al., 2010; Suárez-Ruiz et al., 2012).

1. Methods

Within the Ahnet Basin, three exploration wells (X1, X2, and X3) were drilled to the depth of the Frasnian formation. A representative set of samples was selected for this study through the shale intervals of the Frasnian Formation were collected and analyzed using geochemical and petrological methods as discussed below.

Initially, the selected samples were cleaned of impurities with distilled water and then dried in an oven (40 °C) for 24 h. The analytical approaches employed included measuring total organic carbon (TOC), performing Rock-Eval pyrolysis VI, and assessing palynofacies and maturity levels.

1.1. Determination of total organic carbon (TOC)

A sum of Two Hundred Nineteen (219) core samples taken from the X1, X2, and X3 wells (chosen for this purpose) were crushed and ground to a homogeneous powder for analysis. Total organic carbon (TOC) content measurements were conducted on the powdered shale samples. The richness in total organic carbon makes it possible to establish a classification of rocks (Tab. 1). The determination of organic carbon is an essential criterion for evaluating the

richness of rock in organic matter, without being sufficient; it is also necessary to study the type of organic matter as well as its maturation.

Table 01: *Source rocks classification according to TOC (Kracha, 2011).*

Total organic carbon (shales) %	Total Organic Carbon (carbonates) %	Classification
0.01 - 0.20	< 0.25	Very poor rock
0.21 - 0.50	0.25 - 0.50	Poor rock
0.51 - 1.00	0.50 - 1.00	Moderately rich rock
1.01 - 3.00	1.00 - 2.00	Rich rock
> 3.00	> 2.00	Very rich rock

1.2. Rock-Eval Pyrolysis VI

The powdered samples were subsequently subjected to determine basic source rock parameters and screened using a Rock-Eval VI instrument (Fig. 26) following the procedures provided by Espitalie et al. (1985). Around 100 mg of the crushed sample was subjected to pyrolysis, heating to 600 °C in an atmosphere of helium. Geochemical parameters such as S1 (amount of free hydrocarbons), S2 (amount of hydrocarbons generated by thermal cracking of non-volatile organics), S3 (CO2 released by kerogen during pyrolysis “mg CO2/g of rock”), and Tmax (temperature of maximum hydrocarbon release by kerogen cracking) were measured during pyrolysis. Subsequently, additional geochemical parameters, such as hydrogen index (HI = S2 × 100/TOC), oxygen index (OI = S3× 100/TOC), potential yield (PY = S1 + S2), and production index (PI = S1/S1 + S2), were calculated according to Emeis and Kvenvolden (1986).

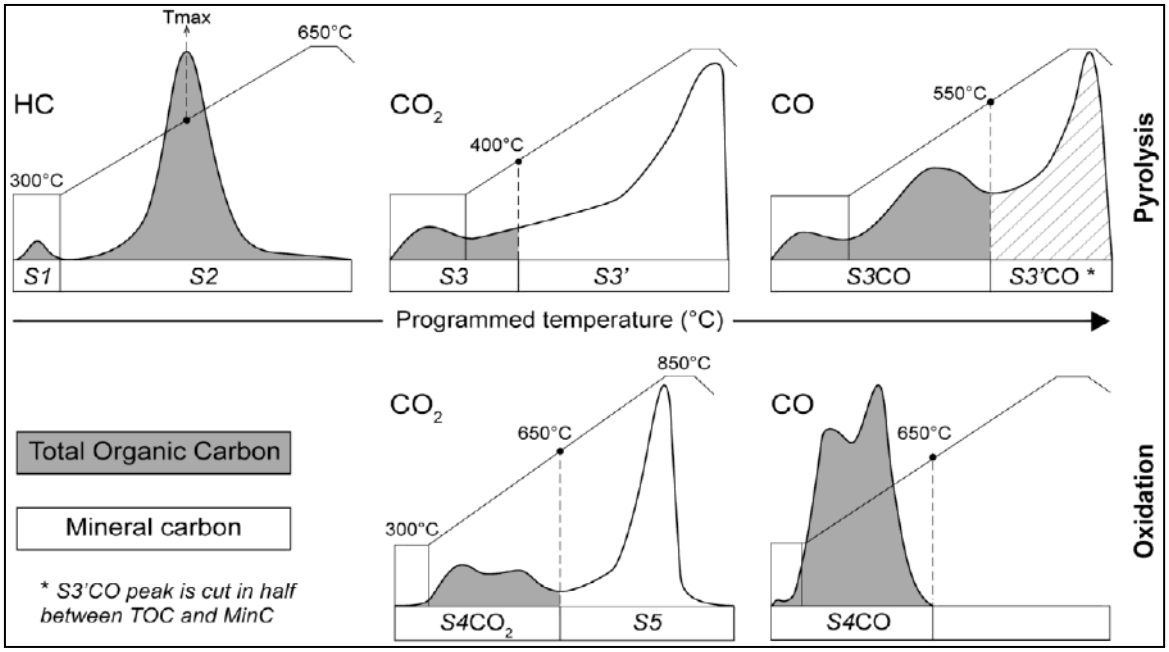

Fig. 26: *Analytical procedure for the Rock-Eval 6 device. The straight lines refer to the evolution of temperature over time. The surfaces of the different peaks are integrated to calculate TOC and Min-C. Modified from Behar et al. (2001).*

1.3. Determination of palynofacies and maturity estimation

This method involves isolating organic matter by treating a crushed rock sample with hydrochloric acid (HCl) to dissolve carbonates and hydrofluoric acid (HF) to break down silicate minerals (Mamaseni et al., 2019). The sample is then rinsed with distilled water, followed by alcohol. Subsequently, a separation using a bromoform/alcohol mixture is conducted. The organic matter, being less dense, floats on the bromoform, while the denser minerals settle at the bottom, forming a pellet. The floating organic matter is then collected in a test tube and rinsed again to remove any remaining bromoform. This residue is prepared as a thin section for examination under transmitted light.

This analysis allows us to determine the organic matter's origin and identify the palynofacies present in the sample, differentiating between amorphous and structured elements (Mamaseni et al., 2019). The color of structured elements, such as spores and pollens, indicates the maturation stage of the material. The Thermal Alteration Index (TAI) reference scale ranges from 1 to 5, progressing from pale yellow to black (Tab. 2). Lighter colors represent less mature

stages. At the same time, darker hues indicate higher degrees of thermal maturation, reflecting more mature organic matter.

Table 02: *Correlation of the main elements of thermal maturation (Kracha, 2011).*

Evolution Stages	Diagenesis	Catagenesis		Metagenesis
	Immature Zone	Oil genesis area	Condensate and wet gas genesis area	Dry gas genesis zone
VRo	0.3 – 0.5 %	0.5 – 1.35 %	1.35 – 2.0 %	2.0 – 3.0 %
TAI	1.0 – 1.5	2.0 – 3.0	3.0 – 3.5	3.5 – 5.0
Tmax	≤ 435° c	435° c – 465° c	465° c – 530° c	530° c – 550° c

2. Results and Discussion

To assess the potential for shale gas development in this region, we must examine the lateral extent of prospective zones. This assessment relies on available geochemical data, helping map the distribution of favorable reservoir characteristics across the area (Tab. 3).

Table 03: *Frasnian studied intervals on each well depending on available data.*

Wells	Frasnian Thickness
	Geochemical Data
X1	1528-1950 (422m)
X2	1561-1663 (102m)
X3	1565-1788 (223m)

2.1. Determination of total organic carbon (TOC)

The critical factors influencing shale petroleum generation include the organic matter's quantity, type, and thermal maturity (Welte, 1965; Tissot and Welte, 1978; Peters and Cassa, 1994). Welte (1965) observed that for bitumen to be expelled from a potential source rock, there must be a minimum organic carbon content of 0.5 wt.%. Below this threshold, bitumen remains

adsorbed on kerogen and clay surfaces, and no expulsion occurs until these adsorption sites are saturated. Peters and Cassa (1994) established geochemical criteria for an in-depth classification of source rocks, ranking them from poor to excellent. This classification is based on total organic carbon (TOC) content, delineated by ranges: 0–0.5 wt.%, 0.5 wt.%–1 wt.%, 1 wt.%–2 wt.%, 2 wt.%–4 wt.%, and greater than 4 wt.%, respectively.

The threshold for the minimum total organic carbon (TOC) required to initiate hydrocarbon generation in shale is still debated. Schmoker (2005) and Peters and Cassa (1994) proposed that shales with a TOC content greater than 2 wt.% possess strong hydrocarbon generation potential. In contrast, Mohamed et al. (2020) argued that shale with a TOC content exceeding 1 wt.% could sufficiently generate petroleum, making it an effective source rock. Bowker (2007) maintained that a TOC content between 2.5 wt.% and 3.0 wt.% is essential in commercial shale gas fields. Meanwhile, Burnaman and Shelton (2009) determined that the minimum TOC content for a shale reservoir should be at least 2 wt.%.

2.1.1. Well (X1)

Out of the eighteen analyzed Frasnian shale samples, except for one that exhibited low organic matter content with a total organic carbon (TOC) of approximately 0.42% at a depth of 1903.28m, the majority displayed moderate to rich TOC levels. The depth/TOC diagram (Fig. 27a) illustrates the range of TOC values between 0.71% and 4.57%, showing that the samples contain significant amounts of organic matter and are thus considered favorable source rocks (Hunt 1967, 1991).

2.1.2. Well (X2)

The fifty-two analyzed Frasnian shale samples exhibited very high total organic carbon (TOC) levels. The depth/TOC diagram (Fig. 27b) displays TOC values ranging from 3.50% to 10.08%, suggesting the presence of potentially very rich organic matter. These samples are classified from good to excellent regarding source rock potential (Peters and Cassa, 1994).

2.1.2. Well (X3)

The one hundred and forty-nine (149) analyzed Frasnian shale samples, which were assayed and revealed very good to excellent total organic carbon TOC contents ranging from 2.11 to 15.90% with an average of 7%. The depth/TOC diagram (Fig. 27b) shows that the best TOC

contents were recorded between 1734 and 1764m, (ranging from 3.19 to 15.90%), indicating a potentially very rich organic matter and classified as very good to excellent source rock potential (Peters and Cassa, 1994).

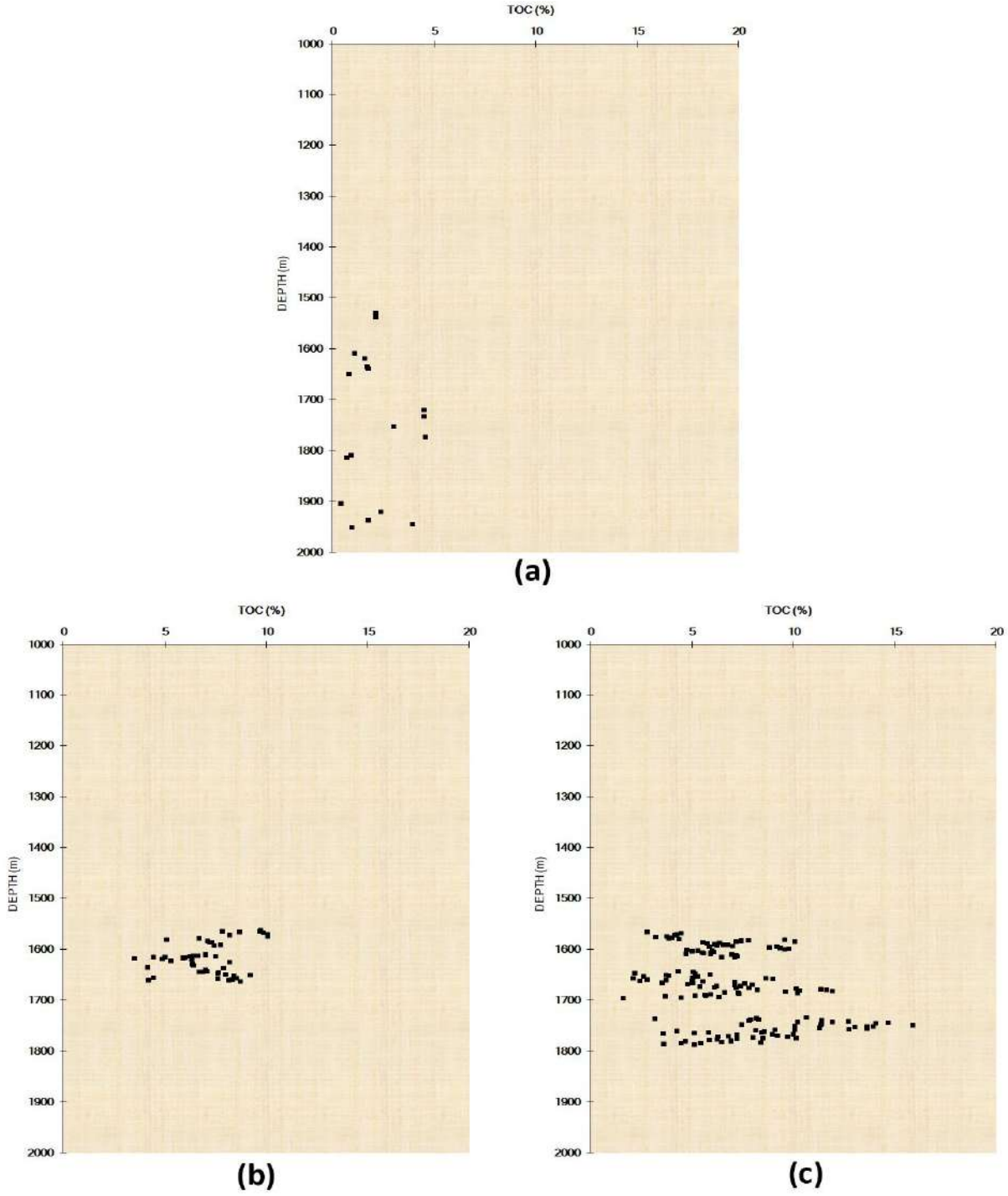

Fig. 27: *Cross-plots of total organic carbon (TOC) content versus depth (m): (a), X1 analyzed samples; (b), X2 analyzed samples; (c), X3 analyzed samples.*

2.2. Rock-Eval Pyrolysis VI

The source rock properties of the Frasnian shales were investigated in this section to characterize the organic richness, hydrocarbon potential of the organic matter, and thermal maturity level. The main parameters considered to highlight the oil potential in question are illustrated (see Table 04).

(NB: Only samples with a TOC greater than 0.50% were affected by Rock-Eval 6 pyrolysis).

Table. 04: *The main geochemical parameters from Pyrolyse Rock-Eval (Espitalié et al., 1985 ; Peters and Cassa, 1994), Vinci-Technologies, (2014).*

Parameter	Low	Medium	Good	Excellent
S1 (mg HC/g of rock)	≤ 0,5	0,5 – 1	1 – 4	≥ 4
S2 (mg HC/g of rock)	≤ 2,5	2,5 – 5	5 – 10	≥ 10
Tmax (°C)	≤ 435	435 - 460		≥ 460
Parameter	**Low**	**Medium**	**Good**	**Excellent**
HI (mg HC/g of TOC)	≤100	100 – 300 (oil –gas)	300 – 600 (oil)	≥ 600 (oil)
OI (mg CO_2/g de TOC)	≤100	100 – 200	200 – 400	≥ 400

2.2.1. Well (X1)

Seventeen (17) samples from this well, taken from depths of 1528.20 m to 1814.39 m and 1920.13 m to 1950.41 m, underwent pyrolysis Rock-Eval 6 analysis. The hydrocarbon yield (S2) released during pyrolysis is a crucial metric for assessing the generative potential of source rocks (Peters, 1986; Bordenave, 1993). The results indicated low levels of free and volatile hydrocarbons (S1) and hydrocarbon potential (S2). Specifically, free hydrocarbons (S1) ranged from 0.04 to 0.17 mg HC/g rock. The hydrocarbon potential (S2) varied from 0.09 to 0.51 mg HC/g rock (see Fig. 28a). The potential yield (PY) for all samples analyzed was below 2 mg/g, ranging from 0.14 to 0.65 mg HC/g of rock, which is considered low. Merrill (1991) and Fatma and Sadettin (2013) state that PY values less than 2 mg/g indicate a low likelihood of producing appreciable amounts of hydrocarbons.

The parameters Tmax, a chemical indicator of thermal maturity, and hydrogen index (HI) were calculated for all analyzed samples. These metrics help identify the general types of kerogens, referencing studies like Peters and Cassa (1994), Hunt (1996), and Bose et al. (2015). The HI and oxygen index (OI) values in samples from the Frasnian Formation are notably low, indicating a high level of maturity. Specifically, HI values range from 3 to 33 mg HC/g TOC, and OI values from 2 to 24 mg CO2/g TOC. Graphical representations of HI against Tmax (Fig. 28b) and HI versus OI (Fig. 28c) were utilized to classify the kerogen type in the Frasnian samples. According to the modified Van Krevelen diagram, these samples predominantly fall within the Type III kerogen zone, suggesting an origin from terrestrial organic matter, as supported by literature such as Tissot and Welte (1978), Peters and Cassa (1994), and Sykes and Snowdon (2002).

Values of Tmax are influenced not only by maturity but also by kerogen type (Espitalié, 1986). The pyrolysis temperatures (Tmax) taken at the top of the S2 peaks are between 486°C and 605°C, making it possible to distinguish two stages of thermal maturity. The first stage at the end of wet gas condensate generation concerns samples between 1528.20m and 1720.37m depth. The second stage in the dry gas phase concerns samples between 1773.20m and 1950.41m depth (Fig. 28b).

(NB: only temperatures for which the S2 is greater than 0.20 mg HC/g of rock are considered.).

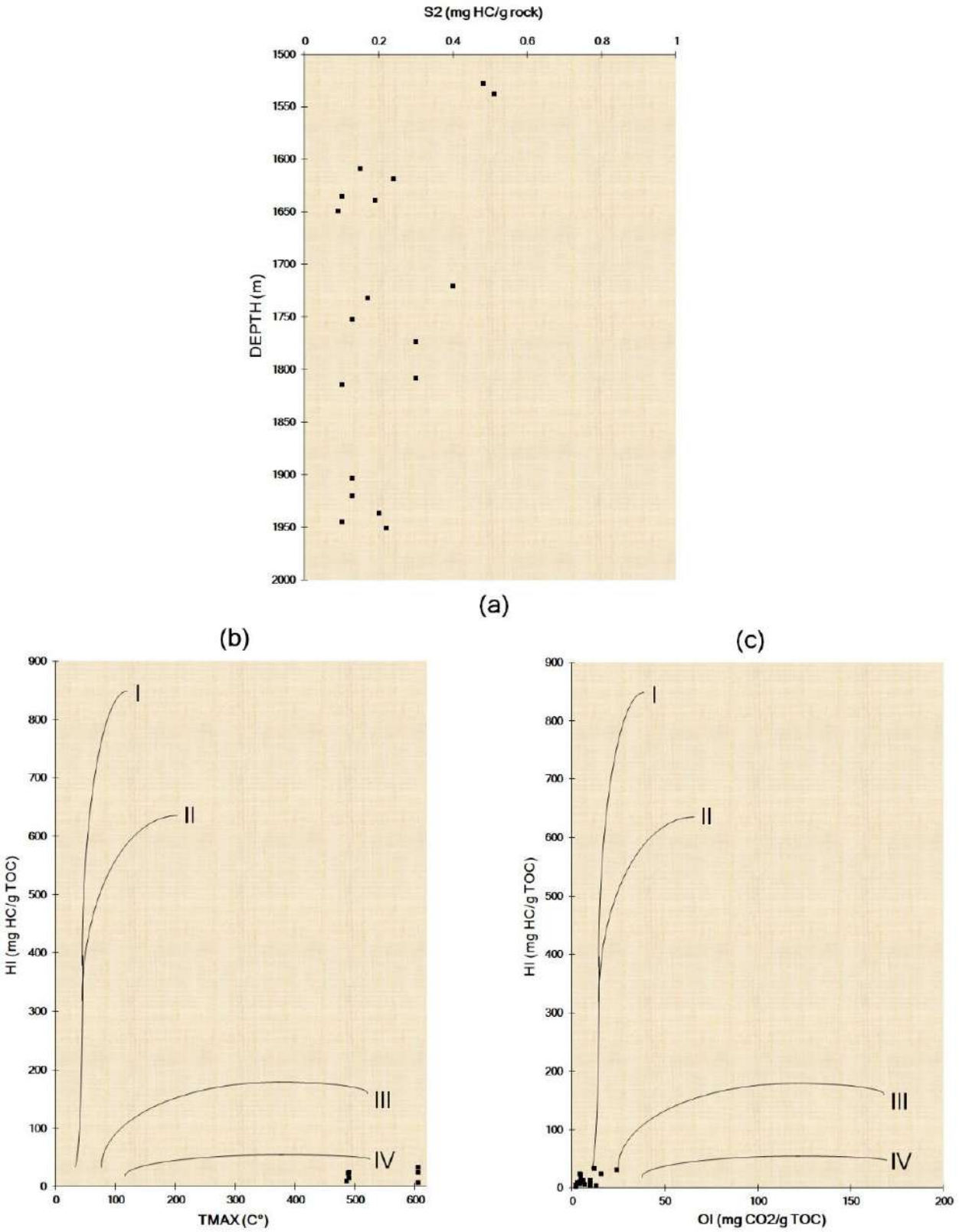

Fig. 28: *Rock-Eval pyrolysis VI of the X1 analyzed samples: (a), diagram of Rock-Eval S2 yield versus depth; (b), plot of hydrogen index (HI) versus Tmax for the Frasnian shales, showing kerogen quality and thermal maturity stages; (c), a modified van Krevelen diagram (HI-OI) showing kerogen concentration.*

2.2.2. Well (X2)

A total of fifty-two (52) samples, taken from depths ranging from 1561.86 m to 1662.71 m within the well, underwent pyrolysis Rock-Eval 6 analysis. The hydrocarbon yield (S2) released during pyrolysis serves as an indicator of the generative potential of source rocks, as noted by Peters (1986) and Bordenave et al. (1993). The results indicate that both the free and volatile hydrocarbons (S1) and the potential hydrocarbons (S2) were low, with S1 values varying from 0.06 to 0.14 mg HC/g rock and S2 values from 0.32 to 0.76 mg HC/g rock (Fig. 29a). The combined potential yield (PY) did not exceed 2 mg/g in any of the analyzed samples, ranging only from 0.39 to 0.89 mg HC/g rock, indicating limited potential for significant hydrocarbon production, as supported by Merrill (1991) and Fatma and Sadettin (2013).

Additionally, the pyrolysis parameter (Tmax), a chemical indicator of thermal maturity, and the hydrogen index (HI), a geochemical parameter, were determined for all samples. These parameters are critical for classifying the overall kerogen types, as referenced in studies by Peters and Cassa (1994), Hunt (1996), and Bose et al. (2015). The Frasnian Formation samples revealed very low HI and oxygen index (OI) values, signifying a high degree of maturity; HI ranged from 5 to 13 mg HC/g TOC and OI from 2 to 7 mg CO2/g TOC. Graphical analyses of HI versus Tmax (Fig. 29b) and HI versus OI (Fig. 29c) helped identify the kerogen types present in the Frasnian samples. According to the modified Van Krevelen diagram, these samples predominantly fall within the Type III kerogen zone, indicative of terrestrial organic inputs, as discussed in the literature by Tissot and Welte (1978), Peters and Cassa (1994), and Sykes and Snowdon (2002).

Values of Tmax are influenced not only by maturity but also by kerogen type (Espitalié, 1986). The pyrolysis temperatures (Tmax) taken at the top of the S2 peaks are between 570°C and 599°C, which leads us to locate one stage in the dry gas phase that concerns samples between 1561.86 m and 1662.71 m deep (Fig. 29b).

(NB: only temperatures for which the S2 is greater than 0.20 mg HC/g of rock are taken into consideration).

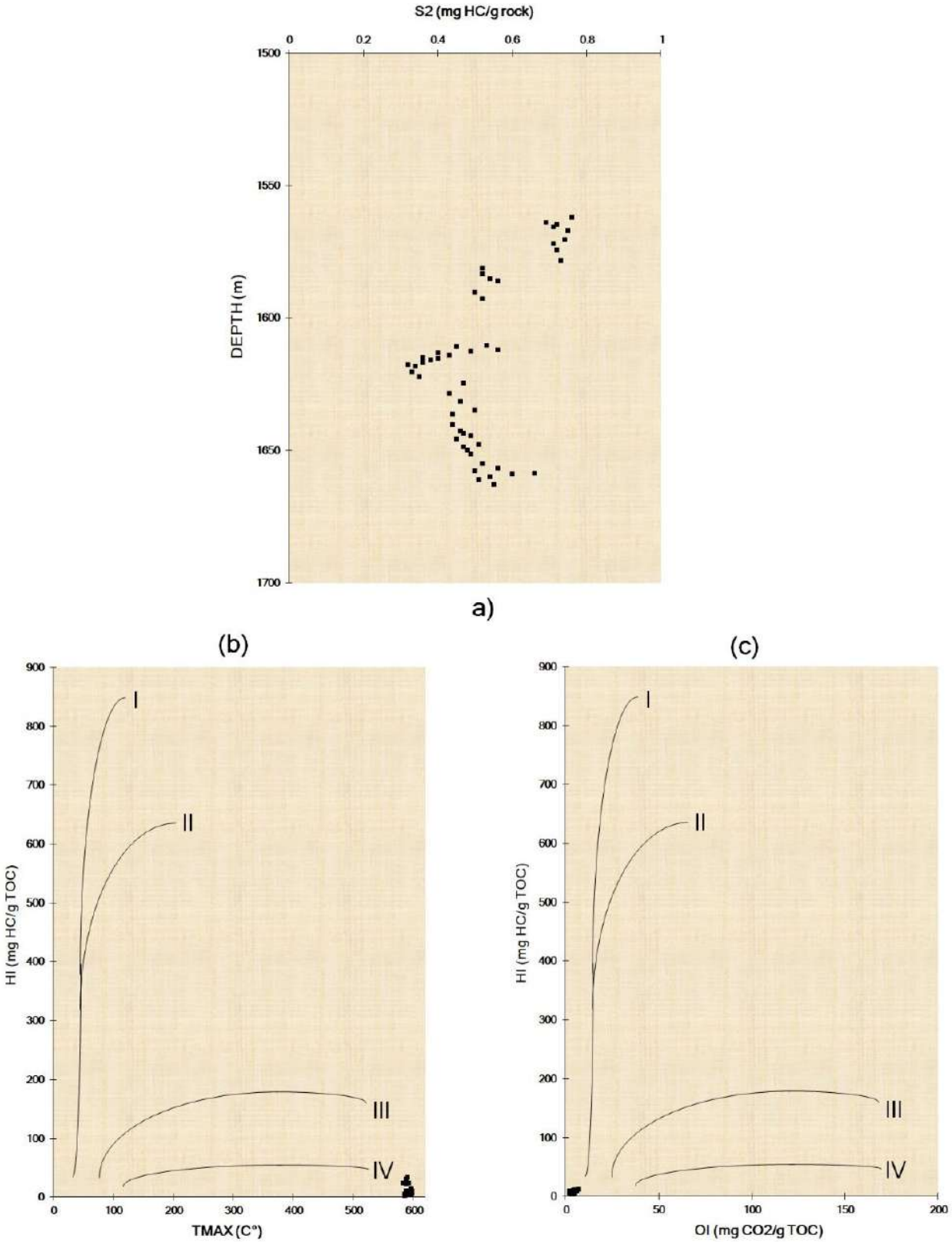

Fig. 29: *Rock-Eval pyrolysis VI of the X2 analyzed samples: (a), diagram of Rock-Eval S2 yield versus depth; (b), plot of hydrogen index (HI) versus Tmax for the Frasnian shales, showing kerogen quality and thermal maturity stages; (c), a modified van Krevelen diagram (HI-OI) showing kerogen concentration.*

2.2.3. Well (X3)

One hundred and forty-nine (149) samples from this well, corresponding to depths ranging from 1565.25 m to 1787.70 m, were the subject of a Pyrolysis Rock-Eval 6 analysis. The amount of hydrocarbon yield (S2) expelled during pyrolysis is a valuable measurement to evaluate the generative potential of source rocks (Peters, 1986; Bordenave, 1993). The results indicate that both the free and volatile hydrocarbons (S1) and the potential hydrocarbons (S2) were low to medium, with S1 values varying from 0.03 to 3.63 mg HC/g rock and S2 values from 0.06 to 2.58 mg HC/g rock (Fig. 30a). Except for the sample from depth 1750.20 m, which recorded an average value of around 3.63 mg HC/g rock. The average value of S2 is around 0.61 mg HC/g rock. The combined potential yield (PY) slightly exceeded 2 mg/g in the analyzed samples, ranging from 0.16 to 3.88 mg HC/g rock, indicating low to medium potential for significant hydrocarbon production, as supported by Merrill (1991), Fatma and Sadettin (2013) and Peters and Cassa, (1994).

The pyrolysis parameter (Tmax), a chemical indicator of thermal maturity, and the geochemical parameter hydrogen index (HI) were also calculated for all analyzed samples. These parameters assess the bulk kerogen types (e.g., Peters and Cassa, 1994; Hunt, 1996; Arora et al., 2015). Samples from the Frasnian Formation show that HI and OI values are very low, confirming the very advanced maturity. The HI is between 1 and 36 mg HC/g TOC. The OI is almost nil except for rare values not exceeding 83 mg CO2/g TOC. Plots of S2 versus CO2 (Langford and Blanc, 1990) (Fig. 30b) and HI versus OI (Fig. 30c) were used to identify the kerogen type of organic matter in the Frasnian samples. The Van Krevelen diagram shows that the samples are clustered in the Type III kerogen zones. Such kerogen type is interpreted as input from terrestrial organic sources (Tissot and Welte, 1978; Peters and Cassa, 1994; Sykes and Snowdon, 2002).

Values of Tmax are influenced not only by maturity but also by kerogen type (Espitalié, 1986). The pyrolysis temperatures (Tmax) taken at the top of the S2 peaks are between 305°C and 606°C, and given the low oil potential measured, this clarifies why they will not be taken into account as a maturity parameter for the organic matter. Therefore, the use of optical observation is essential to confirm maturity.

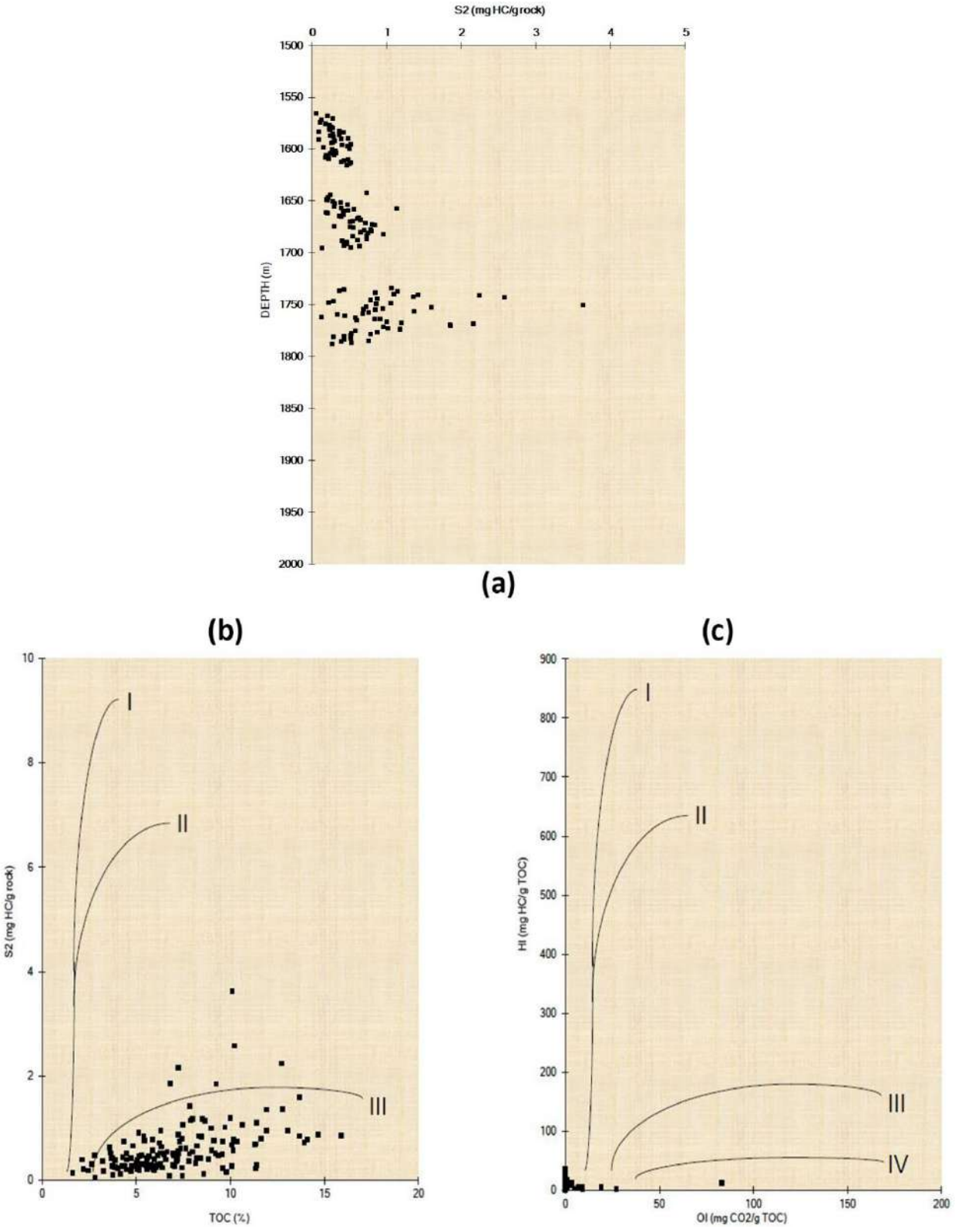

Fig. 30: *Rock-Eval pyrolysis VI of the X3 analyzed samples: (a), diagram of Rock-Eval S2 yield versus depth; (b), plot of (S2) versus TOC for (Langford and Blanc, 1990), showing Frasnian kerogen types; (c), a modified van Krevelen diagram (HI-OI) showing kerogen concentration.*

2.3. Determination of palynofacies and maturity estimation

Palynofacies analysis was used to determine the organic facies and types of kerogens, the depositional environments, and to reconstruct relative sea-level and sequence stratigraphic framework (e.g., Tyson,1993, 1995, 1996; Mansour et al., 2018; Mohamed et al., 2018). The Frasnian shale's high total organic matter content (TOC) provides enough kerogen residues to be optically studied. Based on the richness of organic matter and the oil potential, a total of sixteen (16) samples were selected to determine the type of organic matter and the degree of thermal evolution achieved. Figs; 31, 32, and 33 provide examples of photomicrographs relevant to the kerogen assemblages of the analyzed samples.

The samples concerned by the optical analysis are distributed as follows:

- Well X1: five (05) samples were taken at depths: 1537.80m, 1638.85m, 1732.38m, 1808.15m, and 1950.41m.

- Well X2: five (05) samples were taken at depths: 1570.63m, 1614.21m, 1624.57m, 1649.75m, and 1661.00m.

- Well X3: six (06) samples were taken at depths: 1568.18m, 1595.10m, 1642.20m, 1679.10m, 1743.10m, and 1770.20m.

The crude kerogen previously isolated from its mineral matrix by acid attacks (HCl and HF) was mounted between a slide and coverslip and then observed in natural transmitted light using a Zeiss MPM 400 photometric microscope. Amorphous organic matter (AOM) was identified by its structure and fluorescence, which derives from phytoplankton or terrestrial organic components after intensive degradation (Mendonça Filho et al., 2010).

2.3.1. Well (X1)

The five (05) samples revealed a very abundant organic material of marine origin consisting of a flaky and granular amorphous organic fraction, algae, Acritarchs and Chitinozoan associated with a continental component represented by spores and woody fragments. It was also observed, unidentifiable organic fragments, a fragment of Scolecodents as well as some probable fragments of Graptolite sicles (Fig. 31). This organic balance is of mixed marine type II (proximal) (Baudin et al., 2007). The coloring of the figured elements (algae) made it possible to distinguish two stages of thermal maturity (Peters and Cassa, 1994):

- The first concerns the interval comprising the samples 1537.80m, 1638.85m, and 1732.38m, whose state of maturity is at the end of the generation of wet gas condensate with Thermal Alteration Indices (TAI) of the order of 3.5 (Figs. 31-a to 31-c).

- The second, where the state of evolution is more advanced, is in the dry gas phase, which concerns depths of 1808.15m and 1950.41m. These carbonized palynofacies made it possible to estimate the Thermal Alteration Indices (TAI) around 4 (Figs. 31-e, 31-f). These states confirm the results obtained by pyrolysis.

2.3.2. Well (X2)

The five (05) samples revealed abundant organic material of marine origin composed of a flocculent and granular amorphous organic fraction, algae, Acritarchs, and Chitinozoan. This organic balance is associated with a continental component, i.e., spores and woody fragments. Unidentifiable organic fragments were observed (Fig. 32). This kerogen is type II, mixed marine (proximal) (Baudin et al., 2007).

The coloring of the figured elements (algae and spores) made it possible to locate the stage of thermal maturity in the dry gas phase with a Thermal Alteration Index (TAI) between 3.5 and 4 (Peters and Cassa, 1994) (Fig. 32). This state corroborates the results of Tmax obtained during the rock eval pyrolysis.

2.3.3. Well (X3)

The six (06) samples revealed a very abundant organic material of marine origin consisting of a flaky and granular amorphous organic fraction, Tasmanaceous algae, Acritarchs, and Chitinozoan. It was also observed, unidentifiable organic fragments, a fragment of Graptolite sicles (Fig. 33). This organic balance is of mixed marine type II (proximal) (Baudin et al., 2007). The coloring of the palynomorphs (dark brown to blackish) made it possible to distinguish two stages of thermal maturity (Peters and Cassa, 1994):

- The first concerns the first sample, 1568.18m, whose state of maturity is at the end of the generation of wet gas condensate (gas window) with Thermal Alteration Indices (TAI) of the order of 3.5 (Fig. 33-a).

- The second, where the state of evolution is more advanced, in the dry gas phase, concerns depths: 1595.10m, 1642.20m, 1679.10m, 1743.10m, and 1770.20m. These carbonized palynofacies made it possible to estimate the Thermal Alteration Indices (TAI) around 4.5 (Figs. 33-b/f). These states confirm the results obtained by pyrolysis.

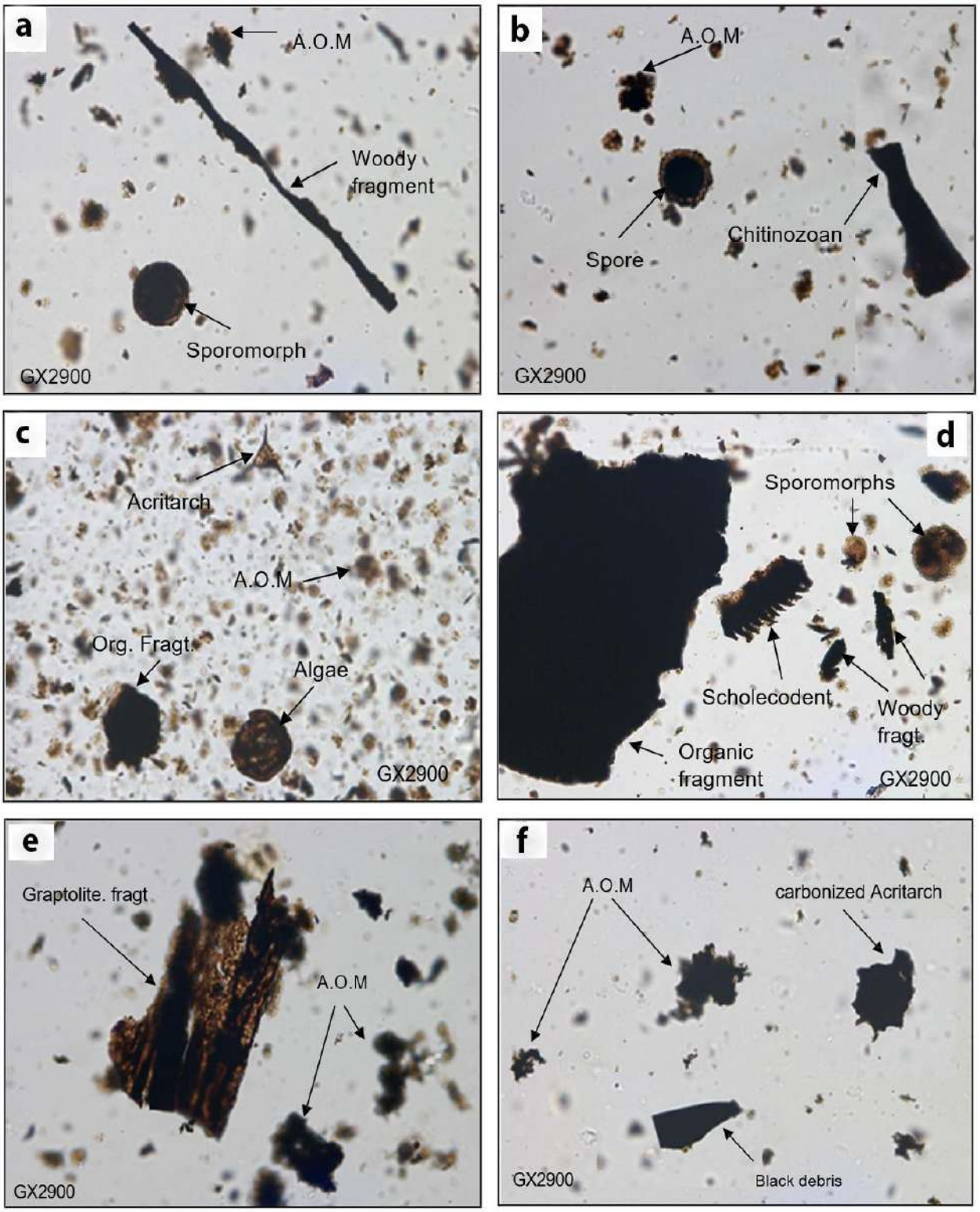

Fig. 31: *Representative palynofacies assemblages from the Frasnian Shales Formation (well X1) showing various types of organic matter in the kerogen concentrates. Key to labels: AOM=amorph organic matter, Acrit=acritarch, Fragt=fragment, Org=organic, GX=magnification. Fig (31-a); Depth = 1537,80 m; TAI = 3,5. Fig (31-b); Depth = 1638,85 m; TAI = 3,5. Fig (31-c); Depth = 1732,38 m; TAI = 3,5. Fig (31-d); Depth = 1808,15 m; TAI = 4. Fig (31-e/f); Depth = 1950,41 m; TAI = 4.*

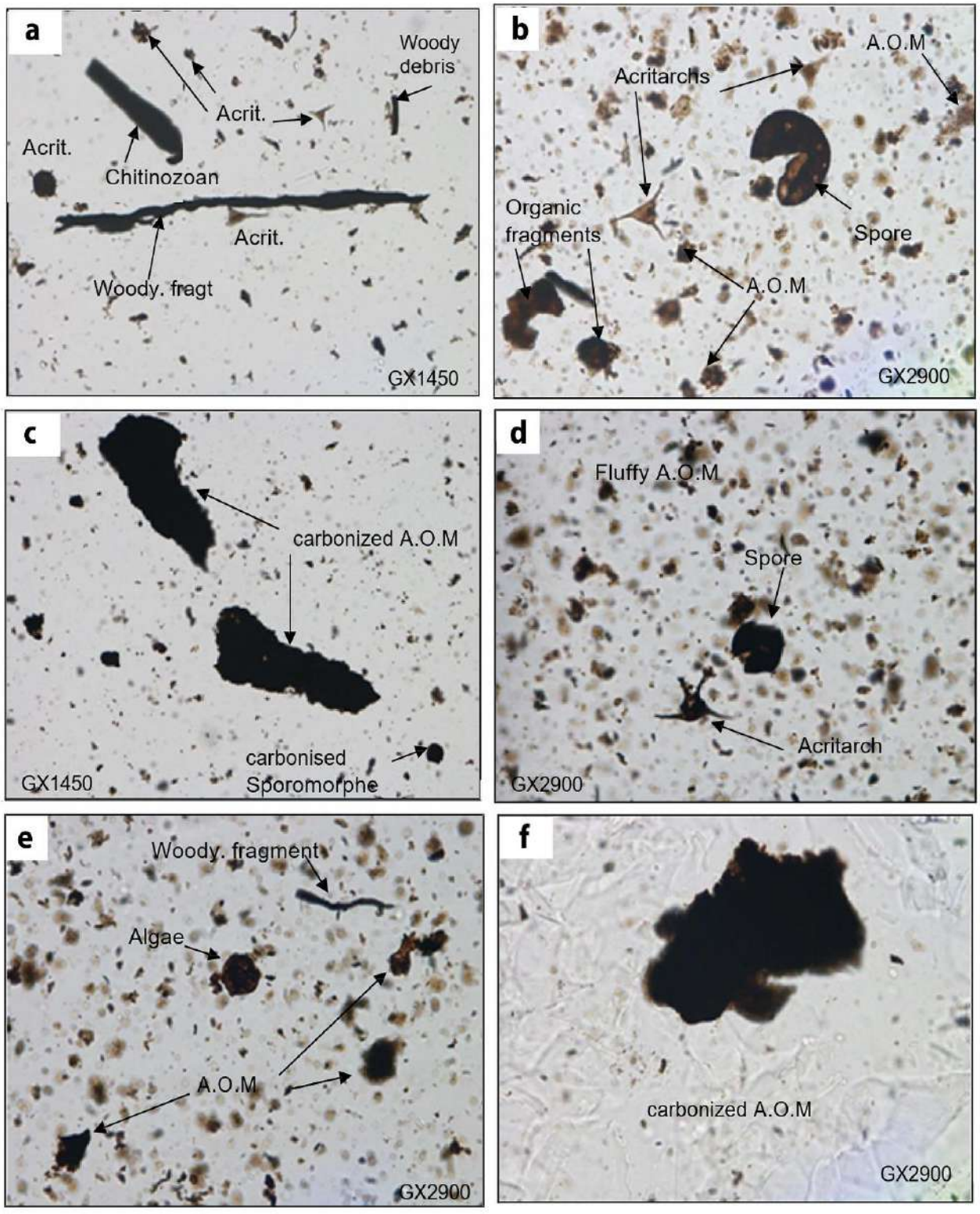

Fig. 32: *Representative palynofacies assemblages from the Frasnian Shales Formation (well X2) showing various types of organic matter in the kerogen concentrates. Key to labels: AOM=amorph organic matter, Acrit=acritarch, Fragt=fragment, Org=organic, GX=magnification. Fig (32-a); Depth = 1570,63 m; TAI = 3,5-4. Fig (32-b); Depth = 1614,21 m; TAI = 3,5-4. Fig (32-c/d); Depth = 1624,57 m; TAI =4. Fig (32-e); Depth = 1649,75 m; TAI =4. Fig (32-f); Depth = 1661,00 m; TAI =4.*

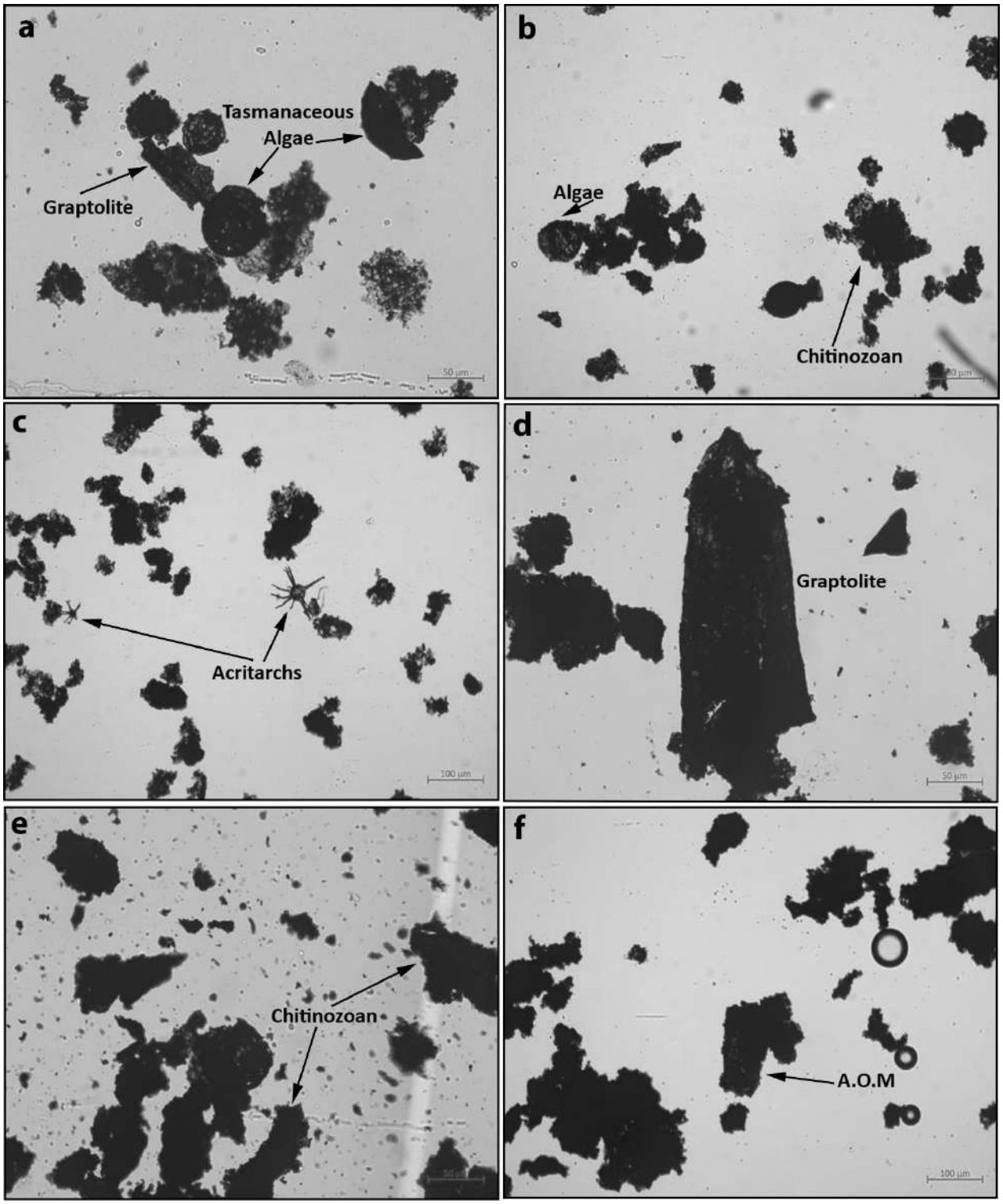

Fig. 33: *Representative palynofacies assemblages from the Frasnian Shales Formation (well X3) showing various types of organic matter in the kerogen concentrates. Key to labels: AOM=amorph organic matter, Fig (33-a); Depth = 1568,18 m; TAI = 3,5-4. Fig (33-b); Depth = 1595,10 m; TAI = 4,5. Fig (33-c); Depth = 1642,20 m; TAI =4,5. Fig (33-d); Depth = 1679,10 m; TAI =4,5. Fig (33-e); Depth = 1743,10 m; TAI =4,5. Fig (33-f); Depth = 1770,20 m; TAI =4,5.*

Conclusion

Based on the laboratory geochemical analysis of the core samples from wells X1, X2, and X3 in the Ahnet basin, the Frasnian hydrocarbon potential of these three wells can be evaluated as follows:

Starting with well X1, the core samples indicate a presence of moderate to excellent Total Organic Carbon (TOC) contents, suggesting potential as a hydrocarbon source. However, the absence of free hydrocarbons and low quantities of potential hydrocarbons pose limitations. The recorded maturity indicators point towards the production of wet gas condensate, with hints of more advanced stages in the dry gas phase.

Turning to well X2, the core samples reveal good to excellent TOC contents, highlighting a significant organic presence with hydrocarbon generation potential. Similar to well (X1), there are no free hydrocarbons, and potential hydrocarbon quantities are low. However, the maturity indicators suggest an advanced state, particularly in the dry gas phase. This positions well X2 as having greater potential for dry gas resource production compared to well X1. The abundance of organic material and advanced maturity suggest a more favorable hydrocarbon potential in the well X2.

In contrast, well X3 presents core samples with an impressive richness in organic matter, showcasing TOC contents with an average of 7%. Despite this organic abundance, its petroleum potential is relatively low due to low free and residual hydrocarbon potential. The organic composition is mainly marine (type II). Maturity analysis places the organic matter in an advanced stage, indicating gas or dry gas potential, characterized by a thermal alteration index (TAI) between 3.5 and 4.5. Despite the promising richness, the organic matter's potential as a source rock is limited due to its decayed state, likely caused by elevated heat flux generated by deep magmatic activity (Takherist and Hamdi, 1995).

Chapter III

Geochemical evaluation

Introduction

Thermal maturity, as defined, is the state of degradation of organic matter depending on the depth of burial with the increase in lithostratigraphic pressure and the geothermal gradient. It has a primordial role in forming hydrocarbons (Hood et al., 1975). The maturity in our study is already determined by laboratory geochemical methods (see Chapter II), but in this chapter, we will use the gas ratio technique (Haworth et al., 1985) using the gas analysis records by chromatograph during drilling; these fluids come from the crossed geological formations.

The idea of using this technique is to achieve two main objectives, which are first to confirm the results of direct laboratory analysis by an indirect method and second, to affirm the value and usefulness of this technique (Gas ratios), mainly since this latter serves to minimize cost and save time of moving samples to the laboratory for heavy, expensive analyzes such as vitrinite and thermal alteration, noting that the use seems very useful especially with the launch of shale gas projects across the world, knows that maturity is a key parameter in the evaluation of shale.

Previously, this technique was used in conventional reservoirs to characterize the reservoir fluids and determine the contact zones. Always in the same logic, we will try to use the parameters of the contained fluid to have an idea about the maturity state of the organic matter, which is the source of these fluids, which can generally be described by five successive stages (Hood et al., 1975):

- The burial of organic matter in typical sedimentary formations ensures better confinement and reduction, which will activate bacterial (anaerobic) activity, so it's the stage of biogenic degradation.
- With underground burial, moving to the stage of thermal degradation governed by the lithological pressure and the geothermal gradient, petroleum molecules are formed, in addition to the progressive increase in temperature (oil window).
- Hydrocarbon migration towards a porous and permeable reservoir rock.
- Alongside the increase of the aforementioned parameters by going deeper, the formation of gas window is observed.
- Carbonization is the progressive transformation of organic matter into coal.

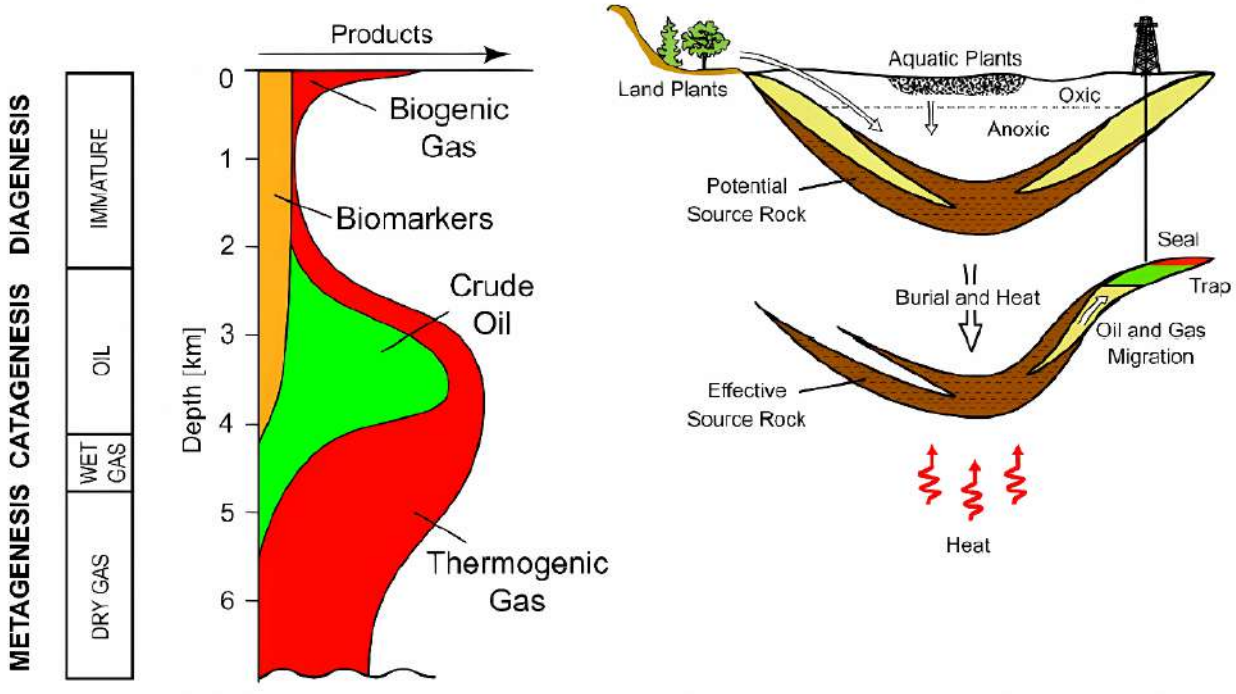

Fig. 34: *Schematic evolution of organic matter, burial, and preservation (Peters et al., 2005).*

1. Methods

The gas chromatography ratios (readings) are particularly useful for identifying fluid types in real time during analysis. These ratios are calculated and plotted in real time to offer immediate insights into the formation fluid parameters while drilling. The values, relationships, and separation of these ratio curves help determine the hydrocarbon fluid type, changes in oil gravity, gas wetness, as well as the gas/oil, and oil/water contacts. By comparing the relative concentrations of various hydrocarbon species in the chromatograph, it becomes possible to estimate the quality of the hydrocarbon reservoir. Additionally, the data from gas ratio analysis is valuable for stratigraphic correlation, using the distinctive characteristics of hydrocarbons to identify reservoir boundaries, even when no lithological facies boundary is visible (Haworth et al., 1984).

Mud logging companies such as "Geoservices," "Weatherford," and "Baker Hughes" utilize advanced equipment like high-speed gas chromatographs, mass spectrometer analyzers, and gas systems such as FLAIR and GC TRACER to record gases with greater accuracy (Fig. 35). These systems continuously analyze hydrocarbons extracted from drilling mud, providing a quantitative

evaluation of component gases (C1-C5) as well as qualitative information on heavier components (C6-C8).

There are various methods for using component gases with different algorithms to plot various types of diagrams to interpret the formation fluid response. However, the gas ratio analysis method outlined below is the most effective for identifying fluid types and fluid contacts.

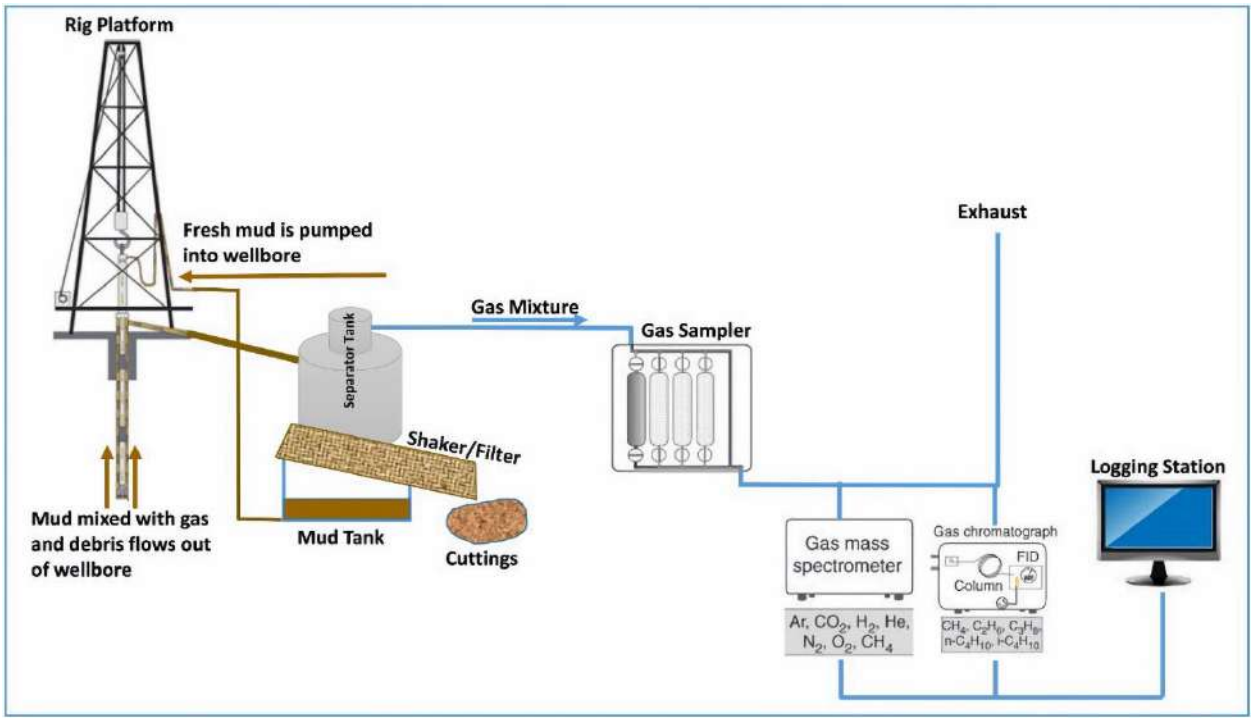

Fig. 35: *Mud-gas monitoring system (Fatai Anifowose et al., 2022).*

1.1. Gas Ratio technique

It is a technique based on three equations that link the gases detected during the drilling from methane (C1) to pentane (C5). The recorded gases manifest as a continuous sequence governed by two poles: C1 dry gas and C5 light liquid.

The gas ratio method combines three ratios that, when plotted together, indicates the fluid character. These ratios are intended to be plotted on a depth log, providing interpretive results. They were specifically designed for ditch (possum belly) gas values rather than steam-still or DST values.

1.1.1. Wetness Ratio (Wh)

It is the ratio of the sum of gases without methane (C1) to the same sum with C1 expressed in %. This parameter will give us an idea of the fluid type, whether it tends towards dry gases or condensates and oils.

$$Wh = (C2+C3+C4+C5) \,/\, (C1+C2+C3+C4+C5) \times 100$$

When this parameter is plotted (Tab. 05), it will increase with an increase in both gas and oil densities.

Table. 05: *Wetness ratio relations (Baker Hughes, 1995).*

Wh (%)	Fluid potential
< 0.5	Non-productive, non-associated dry gas
0.5 - 17.5	Potential gas–Increasing density with increasing Wh (%)
17.5 - 40	Potential oil–Increasing density with increasing Wh (%)
> 40	Residual oil / low gravity

1.1.2. Balance Ratio (Bh)

The balance ratio directly compares light to heavy hydrocarbons, and it's used together with the wetness ratio for interpretative purposes (Haworth et al., 1984).

$$\mathrm{Bh} = (C1+C2) \,/\, (C3+C4+C5)$$

"*Bh*" reacts inversely to "*Wh*" so that it decreases as the fluid density increases. It is used to determine or confirm gas production potential. The value will be very high with very dry methane for example, and then fall rapidly as soon as there is a trace of the heavy hydrocarbons associated with a productive source (Haworth et al., 1985). Table 06 shows precisely how the two ratios are used numerically to determine these zones.

Practically, a straightforward "egg-timer" type profile (Fig. 36), or relationship between the wetness and balance ratios is used to determine changing fluid type and contact points. If the balance ratio exceeds the wetness ratio, gas is predicted. The closer the curves are to each other, the denser the gas and the more likely it is to be productive (Haworth et al., 1984).

Table. 06: *Fluid characterization using the wetness and balance ratios.*

Balance Ratio	Wetness Ratio	Reservoir Fluid and Production Potential
> 100		Very light, dry gas Typically, non-associated and non-productive such as the occurrence of high-pressured methane, metagenic cracking below the oil window, bacterial methane etc
< 100	< 0.5	Possible production of light, dry gas
Wh < Bh < 100	0.5 – 17.5	Productive gas, increasing in wetness as the curves are closer together
< Wh	0.5 – 17.5	Productive, very wet gas or condensate or high gravity oil with high GOR (*Bh<Wh* indicates liquid, but *Wh* still indicates gas)
< Wh	17.5 – 40	Productive oil with decreasing gravity as the curve separation increases
<< Wh	17.5 – 40	Lower production potential of low gravity, low gas saturation oil
	> 40	Very low gravity or residual oil

Oil is predicted if the wetness ratio is greater than the balance ratio. The closer the curves are to each other, the lighter the oil. The greater the separation of the curves, the heavier the oil and the more likely it is to be unproductive or residual (Haworth et al., 1984).

The gas-oil contact (GOC) is defined by the point where the two curves intersect. The oil-water contact (OWC) is typically identified when there is a sharp increase in the wetness ratio, along with a wider separation between the two curves, indicating a higher proportion of heavier hydrocarbons associated with residual oil traces (Haworth et al., 1984).

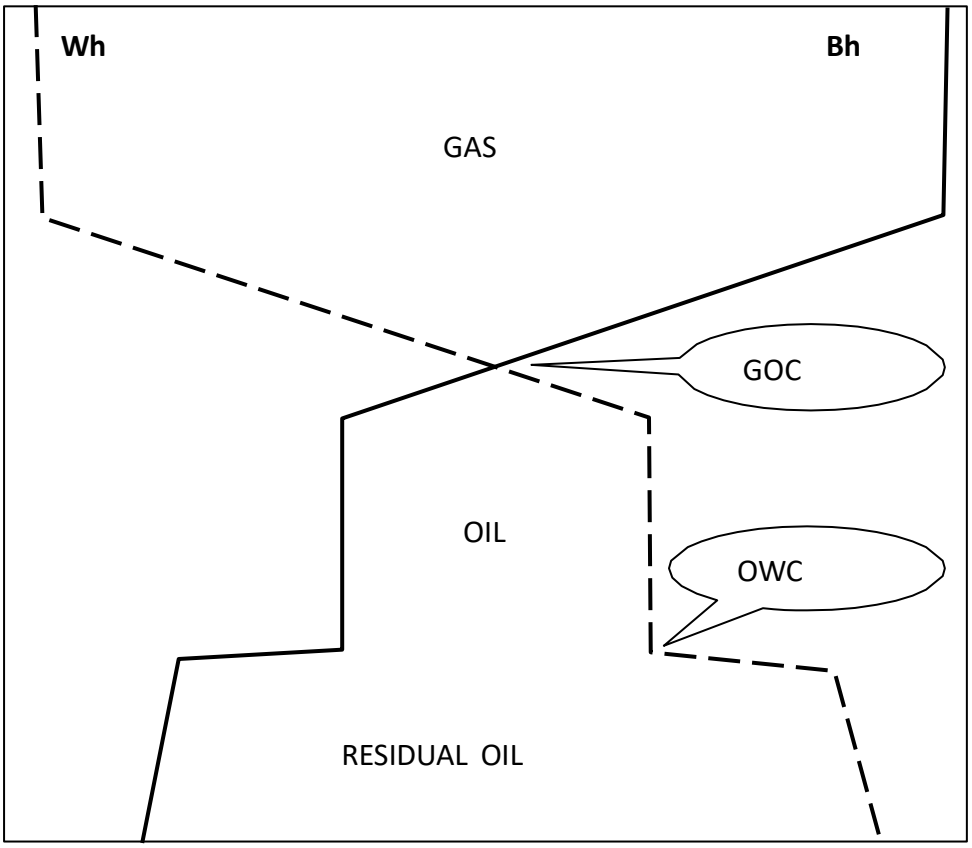

Fig. 36: *Typical fluid and contact profiles of the Wh and Bh Ratio.*

1.1.3. Character Ratio (Ch)

By comparing the heavier compounds (propane to pentane), the character ratio is used to validate a gas prediction based on the wetness/balance ratios. The character ratio helps confirm whether a gas prediction corresponds to a gas zone or if the gas is associated with oil (Fig. 37). The importance of comparing these three compounds lies in the fact that C3 is typically more dominant in a gas reservoir, with lower amounts of C4 and C5. As fluid density increases, all heavier components also rise, but C4 and C5 will increase proportionally in the case of light oils (Haworth et al., 1985).

$$Ch = (C4+C5)/C3$$

If $Ch < 0.5$ With C3 as the significant component, a productive gas phase is confirmed, indicating either wet gas or gas condensate.

If $Ch > 0.5$, a productive liquid phase is confirmed so that the gas indicated by the wetness ratio is associated with light oil (Haworth et al., 1984).

The character ratio should be used to qualify all "*Wh/Bh"* ratio gas predictions, but it is most useful in a particular situation. When the wetness and balance ratio curves are close together, it is not easy to be specific about the fluid type. A wet gas, gas condensate, and light oil can be similar compositionally to yield similar ratio values. By only considering the heavy components, the character ratio helps to determine whether the productive phase is gas or oil (Haworth et al., 1984).

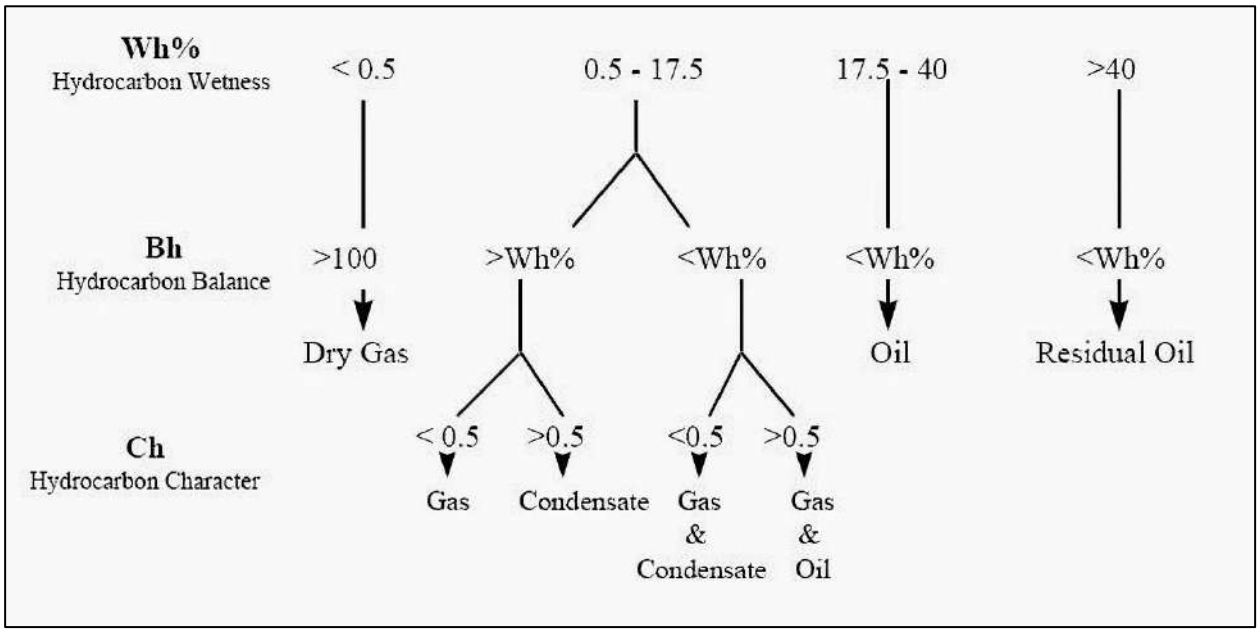

Fig. 37: *Gas ratio interpretation chart (Baker Hughes, 1995).*

2. Results and Discussion.

For the evaluation of unconventional reservoirs (such as shales in our case), we will focus on our three wells (X1, X2, and X3) located within the Ahnet basin; the logic of choice depends essentially on the availability of mud-logging data thus the positioning of wells in our study area (for reasons of confidentiality required by the company provider of data, we will not mention the coordinates of the wells, but it is allowed to say that these wells located within a perimeter of 5 km).

The objective is to determine the petroleum potential stages by integrating the indirect rig-site technique (instantaneous evaluation) and then comparing it with the direct laboratory method

(which we already have). Moreover, for a better evaluation of shale-type reservoirs, it is advisable to:

- Clean the well after each lift-up.
- Daily maintenance and calibration of the gas system.
- Evacuate the bottom plug after each gas peak.

The recording of gas chromatographic analyses during drilling allowed us to interpret and determine the three basic parameters involved in the gas ratio such as wetness, balance, and character.

In the typical case, we would first include several logging data, such as gamma rays, resistivity, sonic waves, and others, to help us indicate the favorable interval, but that is not the case here, seeing that we do not need them as a result of defining the petroleum potential via laboratory analysis (the direct and precise way), so we can name it as a direct comparison between two different methods.

The lateral extent of the prospective zones must be examined to evaluate the potential for shale gas development in this region. This evaluation is based on available Real-time gas data (Mudlogging data), which aids in mapping the distribution of favorable reservoir characteristics throughout the area (Tab. 07).

Table 07: *Frasnian studied intervals on each well depending on available data.*

Wells	**Frasnian Thickness**
	Real-time Gas Data
X1	1521-1900 (379m)
X2	1550-1730 (180m)
X3	1550-1800 (250m)

2.1. Well (X1)

Well X1 occupies the central part of the perimeter. The thickness of the Frasnian is about 432 m, and the crossed sedimentary series is represented by Mesozoic and Paleozoic formations. The gas ratios recorded crossing this well indicate that the wetness of the fluids trapped in the shales is between 1% and 14%, while the balance values range from 60 to 40000. For the character, almost all values are less than 0.5.

The tendency of the chromatographic gases refers to the type of a light hydrocarbon with a remarkable difference between C1 (Methane) and the other gases (Fig. 38). The interpretation of the mentioned results above indicates the coexistence of two types of fluid (Haworth et al., 1984): wet gas and dry gas (Fig. 39);

2.1.1. Dry Gas interval

From 1680 to 1860m, we note the predominance of dry gas, with an average wetness of 0.25% and an average balance of 3500, with a progressive trend.

2.1.2. Gas interval

From 1521 to 1628 m, with an order thickness of 107 m, the wetness showed a regressive trend contrary to the balance, with Averages around 1.03% and 1407.37, respectively, and a character less than 0.5.

2.1.3. Condensate interval

It is divided into two sub-intervals: the first from 1628 to 1680 m and the second between 1858 and 1900m.

For the first interval, the wetness is about 2.34%, the balance 1834, and a character of 0.74 as an average. The second interval includes a wetness of about 4.48% and a balance of 300; the character is 0.8 as an average.

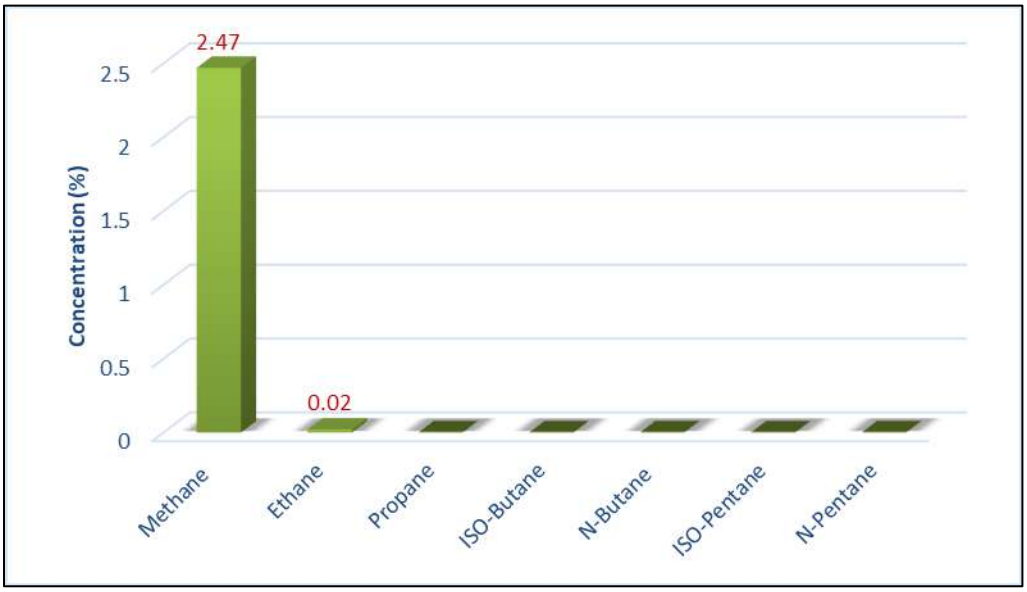

Fig. 38: *Gas Chromatographic peaks for well X1.*

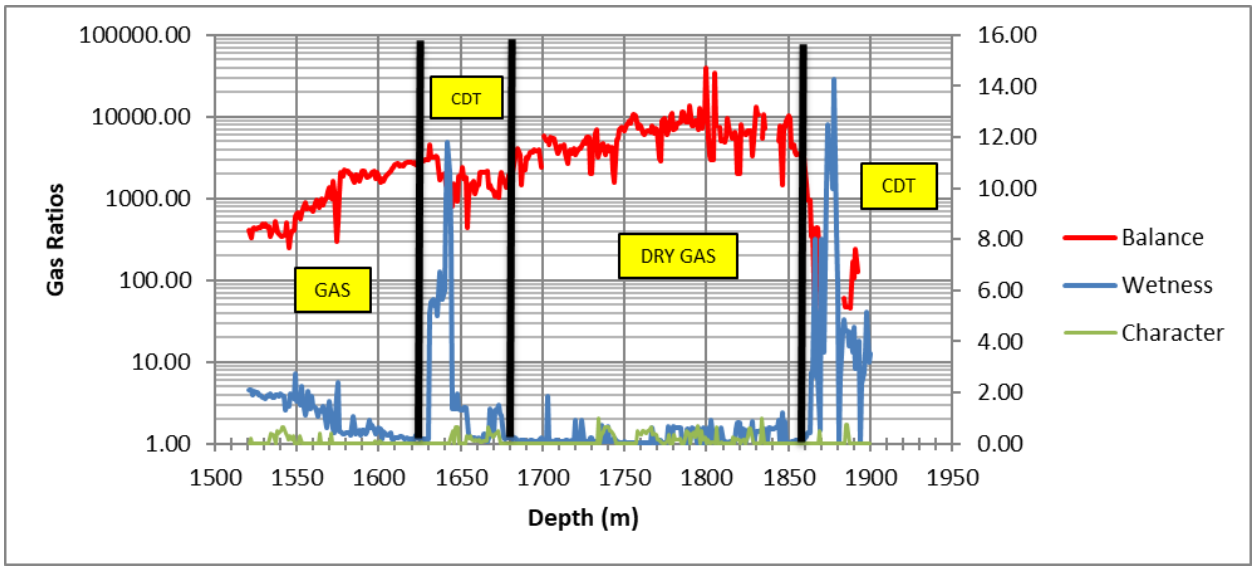

Fig. 39: *Fluids characterization for well X1.*

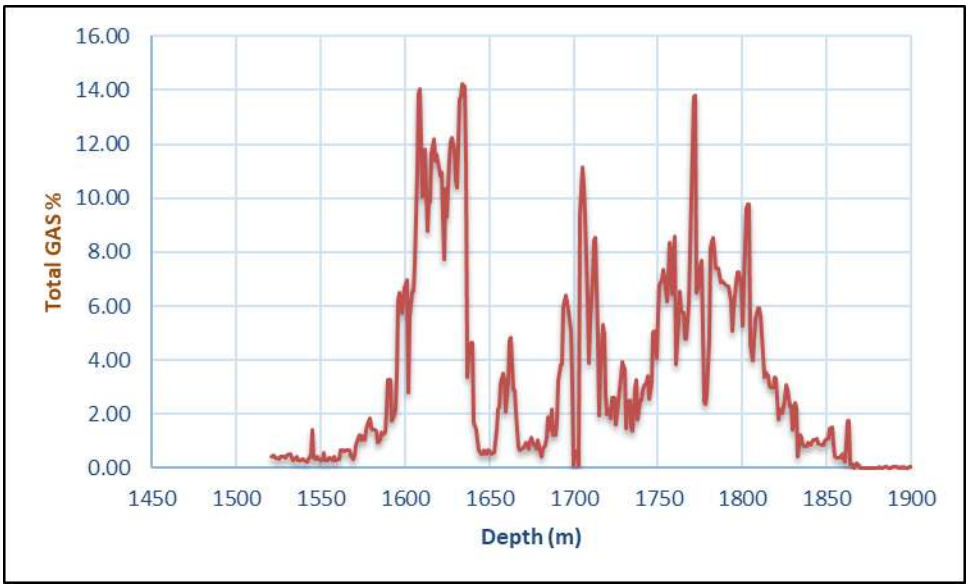

Fig. 40: *Total gas variation versus depth for well X1.*

2.2. Well (X2)

The X2 well is located in the northwestern part of the perimeter (3 km away from X1), and the Frasnian formation is topped at a depth of 1556 m. Mesozoic and Paleozoic formations represent the crossed sedimentary series. The Gas chromatographic values tend to indicate a light hydrocarbon type, with a big difference between C1 (Methane) and the other gases (Fig. 41).

According to the characterization chart of reservoir fluids, it can be seen that Frasnian contains dry gases (Fig. 42), with a character which is less than 0.5 throughout the interval, and the wetness varies from 3.04% to 12.06%, far below the balance which oscillates from 106.06 to 614.90 into the Frasnian interval and this confirms the type of the determined fluid (Haworth et al., 1984).

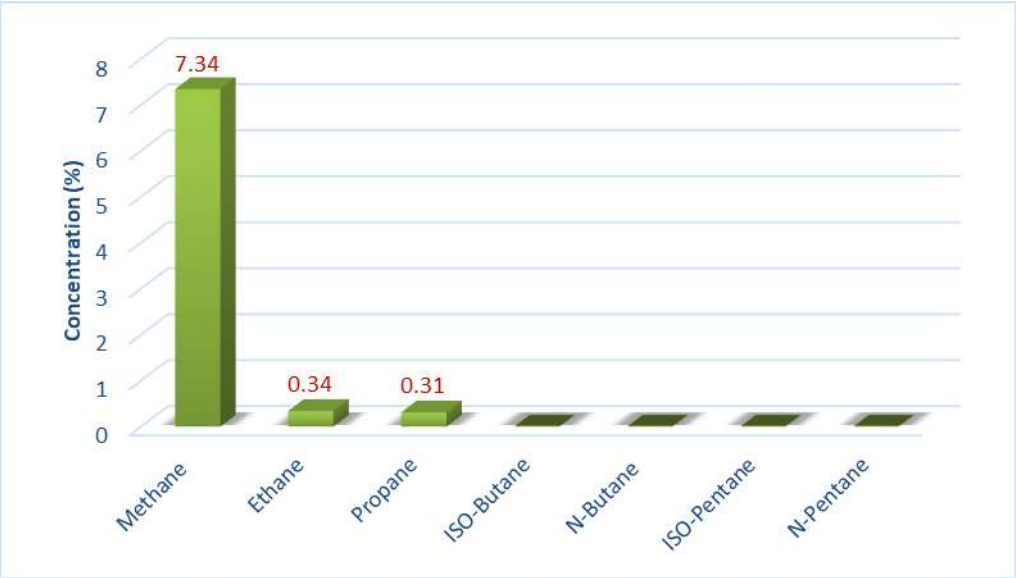

Fig. 41: *Gas Chromatographic peaks for well X2.*

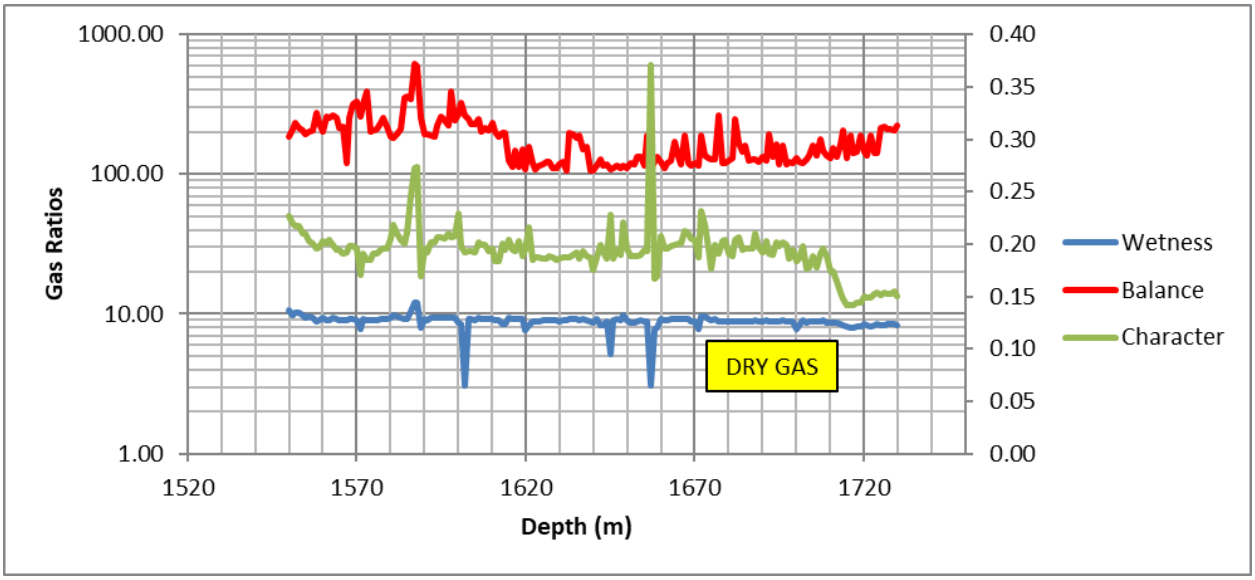

Fig. 42: *Fluids characterization for well X2.*

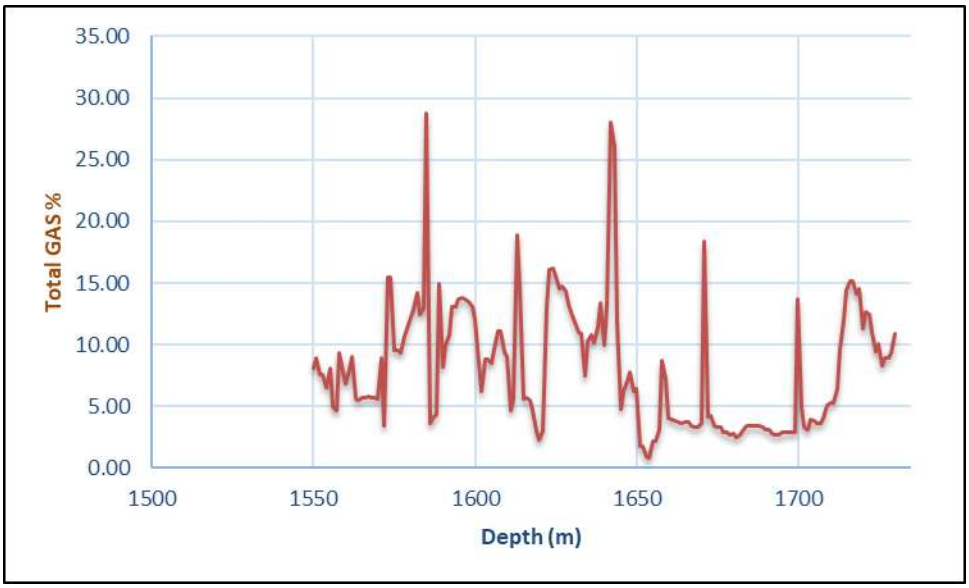

Fig. 43: *Total gas variation versus depth for well X2.*

2.3. Well (X3)

The location of well X3 throughout the studied perimeter is in the southeastern part (2 km away from well X1 and 5 km away from well X2), while the top of the Frasnian formation is about 1560 m in depth. Mesozoic and Paleozoic formations represent the crossed sedimentary series. The tendency of the chromatographic gases suggests a light hydrocarbon type with a massive difference between C1 (Methane) and the other gases (Fig. 44).

The real-time interpretation of the gas ratios allowed us to determine that the fluids trapped in this well are gas and condensate (Haworth et al., 1984), with wetness values ranging from 0.27% to 12.39%, while the balance presents an average of 540.41 maintained consistently higher than the wetness in the whole interval. The character that gave the condensate aspect to the fluid oscillates from 0.1 to 0.5 (Fig. 45). So, from the Frasnian interval, we distinguish:

2.3.1. Dry Gas interval

It's subdivided into two intervals, the first between 1573 and 1660 m and the second from 1690 to the bottom.

For the first interval, the wetness is 1.61%, the balance is 557.47, and the character is 0.18 as an average. The second interval includes a wetness of around 1.39% and a balance of 702.29; the character is 0.32 as an average.

2.3.2. Gas interval

Spreads from the Top to 1573 m, as a 23 m of thickness, this zone is characterized by a wetness of 3.62% as an average, much lower than the balance, which is in the order of 121.03, the character maintained lower than 0.5.

2.3.3. Condensate interval

From depth 1660 to 1690m, representing the peak of flexure for the wetness, which takes an intensive cadency, the recorded value is in the order of 3.38%, the balance marked by values which exceed 100, for the character is always less than 0.5.

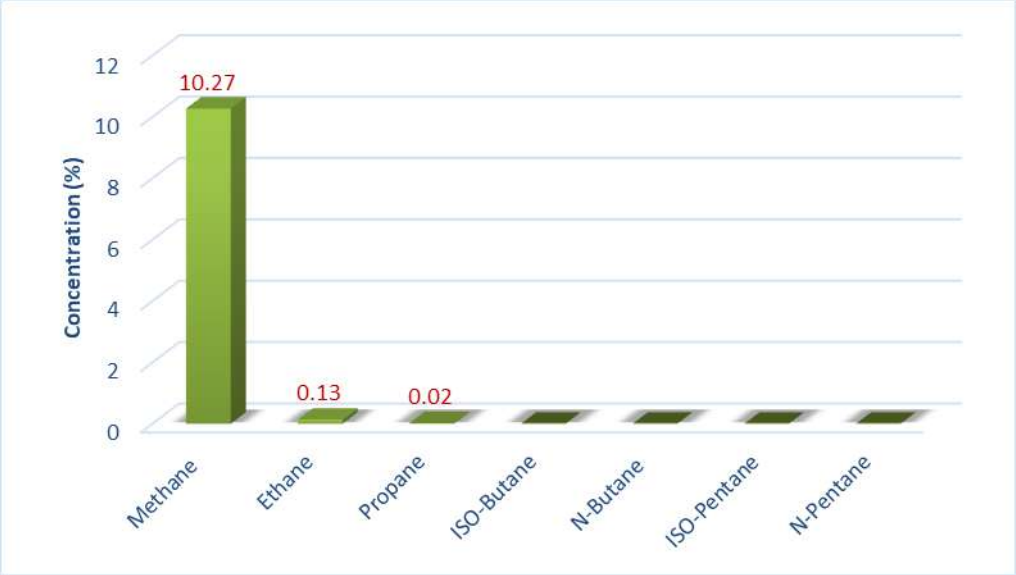

Fig. 44: *Gas Chromatographic peaks for well X3.*

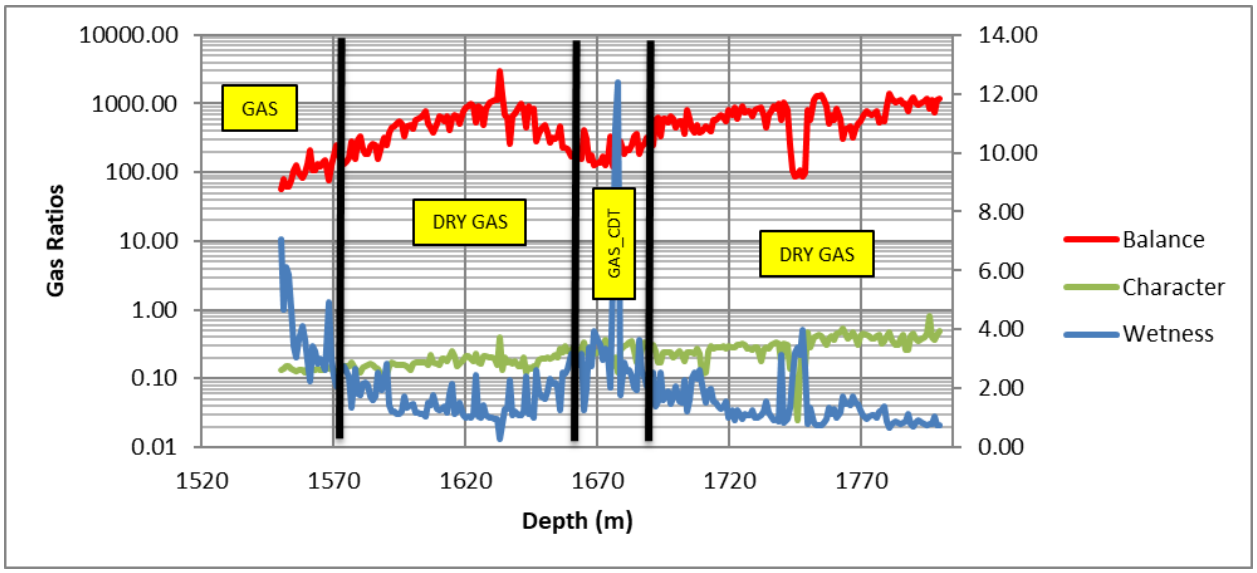

Fig. 45: *Fluids characterization for well X3.*

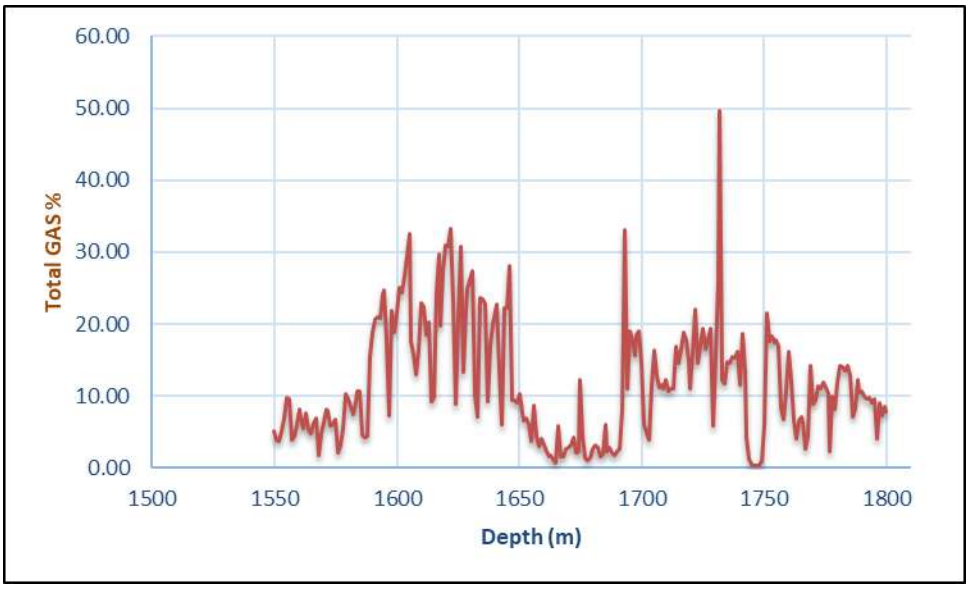

Fig. 46: *Total gas variation versus depth for well X3.*

Conclusion

Depending on the Mud-logging chromatography technique, the gas ratio method applied to wells X1, X2, and X3 have been disclosed a substantial deduction:

Based on the interpretation of Haworth et al. (1984) and considering the gas phase as a transitional state between the dry gas phase and wet gas phase (condensate), well X1 reveals the existence of two types of fluids (wet gas and dry gas), while the X2 well have only one fluid kind which is dry gas. Well X3 contains two fluid intervals, the same as Well X1: wet and dry gas.

These results above correspond by 92% with the results of the second chapter (Fig. 47), which leads us to say that the Gas ratio method is the best way to define the maturity stages of the Ahnet Frasnian shales after laboratory analysis and its use is highly recommended, especially for gaining Time as well as Money.

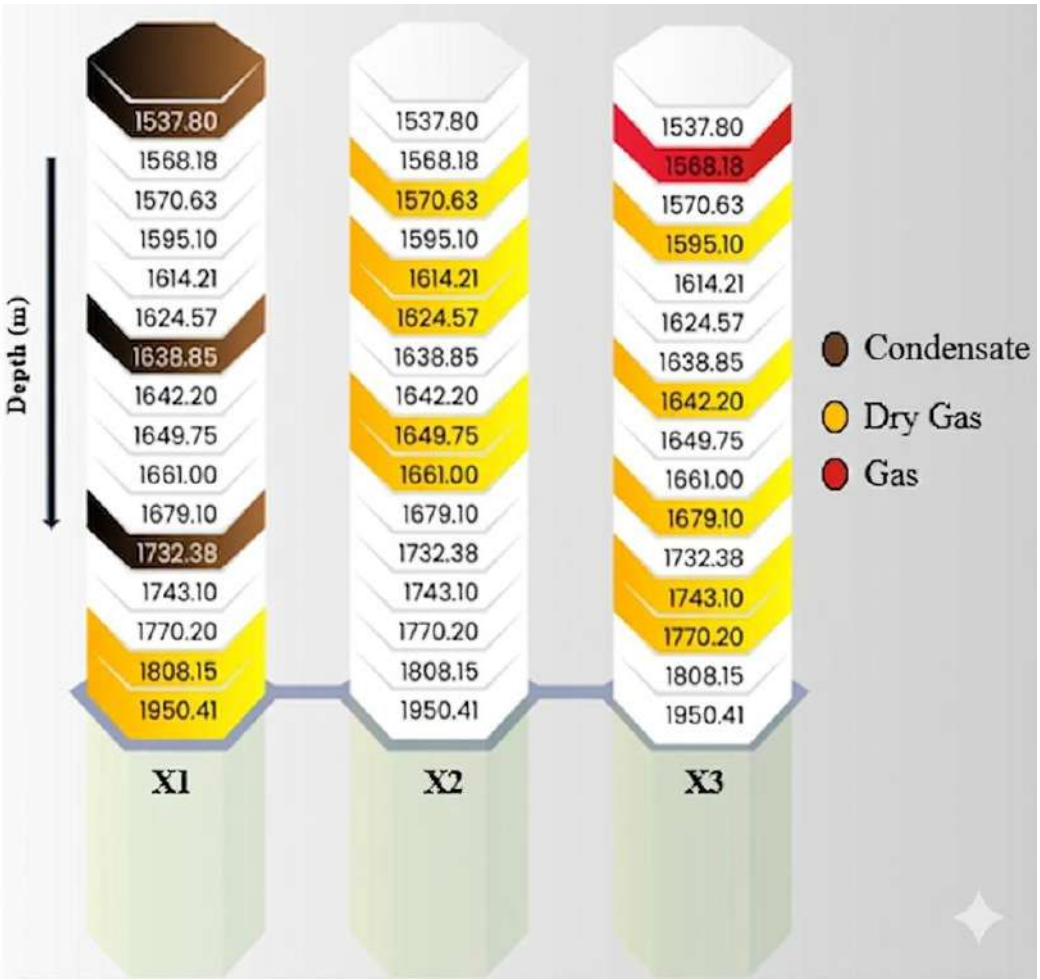

Fig. 47: *Schematic illustration resumes the 2nd chapter outcomes (Geochemical characterization).*

Chapter IV

Geomechanical Approach

Introduction

This chapter discusses one of the most important sweet spots and the most crucial properties of rock, "rock brittleness", as it plays an important role not only in the rock failure process but also in the reaction of the rock mass (reservoir) to any stress change conditions or destabilization state conducting to rock failure. Brittle rocks are more likely to be naturally fractured and respond well to hydraulic fracturing. On the contrary, ductile rocks are more plastic and absorb the energy that slows down or stops fracture propagation. It is considered a combination of rock properties, and no universally proven concept or method exists to define it.

For unconventional resources, brittleness has been used as a safety risk index and basic parameter for oil and gas reservoir evaluation. It is also used to assess rock stability and drill-ability and as a key parameter for the fracturing process.

1. Definition of brittle rock and brittleness

One of the most important behaviors of the rock under any change of conditions is mechanical behavior. This latter can be related to many factors and conditions, external efforts, rock material composition, rock strength, discontinuities or defaults, isotropy (or anisotropy), homogeneity (or heterogeneity) aspects, and temperature. All these factors may have a dominant role or part in controlling how the rock will behave, even how the rock will fail. When discussing failure or fracture, we must consider many factors related to the rock itself, external conditions, and the failing process. One could characterize the brittleness as either hard but prone to breaking readily or fragile and easily broken. That means any dictionary does not provide brittleness, it's explained.

Brittleness is the capacity of a rock to break under stress and form a fracture. (Rickman et al., 2008). The definitions of brittleness are, however, still ambiguous. There is no unique definition of brittleness which could be summarized as follows (Weibull, 1951):

- (a) Low deformation has occurred upon load application;
- (b) Brittle rock has prominent fracture surfaces upon fracturing;
- (c) The more cohesiveness a rock has, the more easily fractures can occur under load;
- (d) The compressive strength is far greater than the tensile strength, and the tensile-compressive ratio is minimal;

- (e) The more significant the internal friction angle, the greater the brittleness of the rock; the greater the Young's modulus, the greater the brittleness of the rock; the smaller the Poisson's ratio, the greater the brittleness of the rock;
- (f) The brittleness of rock is controlled mainly by its mineral composition;
- (j) When brittle rock fractures, residual strength appears after peak strength;
- (h) When the load increases to the peak strength of the rock specimen, the internal fracture of the rock specimen is localized, and the whole specimen collapses.

Many brittleness definitions have been proposed, but there is no consensus as to which definition is the most suitable, and its concept in rock mechanics is yet to be precisely defined. Perhaps the best definition of rock brittleness was offered by Bieniawski (1979): "brittle fracture defined as a fracture that exhibits no or little permanent (plastic) deformation." This definition contrasts ductile fracture, in which, before the fracture, significant plastic deformations occur.

The graph below gives a clear and simple graphic representation (stress-strain curve) of the meaningful of the Brittle and ductile process in typical rock materials:

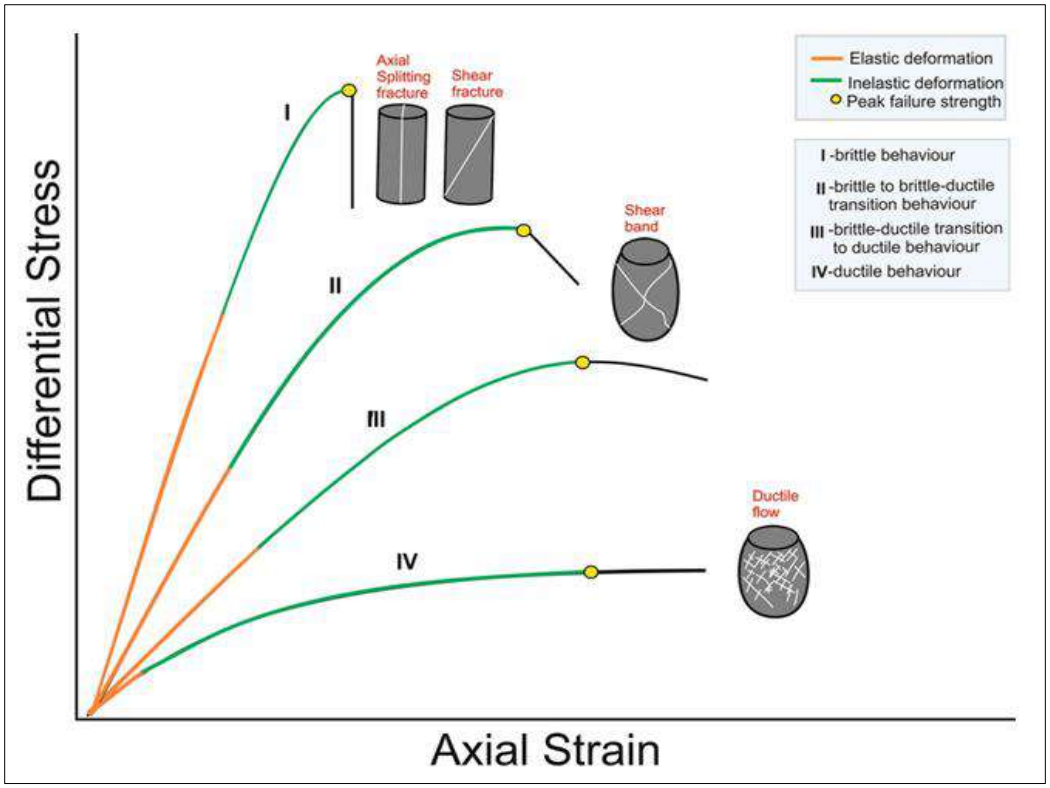

Fig. 48: *Typical stress-strain curves (modified) showing rocks' failure behaviors and failure modes (Technical Report, Sonatrach Laboratories).*

Independent of Brittleness definitions, Brittleness as a property of rock has a significant impact on the failure process. Furthermore, in shale gas extraction by hydraulic fracturing, brittleness plays a major role in the amount produced. In fact, the degree of fracturing is controlled not only by the injection pressure but also by the brittleness of shales (Meng et al., 2015; Kahraman et al., 2018).

2. Factors influencing the Brittleness index

Numerous factors influence rock brittleness, including mineral composition, Young's modulus, Poisson's ratio, compressive strength, tensile strength, porosity, temperature…etc.

Most rocks exhibit brittle behavior once they exceed the yield stress slightly. (Heidari et al., 2014). Concerning the productivity of shale gas, in petroleum science, the mechanical behavior of shales is often classified into high and low 'brittleness' rock types, sometimes referred to as 'fracability' (Rybacky et al., 2016).

Brittleness encompasses a rock's overall mechanical characteristics. Factors influencing rock brittleness are classified as internal and external factors. The key elements primarily consist of composition. (e.g., total organic carbon (TOC), minerals, water/gas/oil content), texture, and rock porosity. The external factors include ambient pressure and temperature (Tang et al., 2020). Numerous quantification methods for evaluating rock brittleness have been proposed considering different affecting factors. The main of these latters will be discussed below:

2.1. Composition (mineral contents)

The mineral composition dramatically affects the mechanical properties of rock materials, establishing a direct link between mineral content and brittleness. For instance, Jarvie et al. (2007) posited that the quartz proportion in rock material could influence its brittleness. Rickman et al. (2008) studied the mineral composition of the Barnett Shale through X-ray diffraction and laser-induced breakdown spectroscopy (LIBS). Their findings demonstrated that rock brittleness is positively correlated with quartz content and negatively correlated with clay content (Fig. 49). Additionally, brittleness exhibited moderate variations with increasing carbonate content. Buller et al. (2010) recommended using the ratio of brittle minerals to the total mineral content to measure rock brittleness.

Nonetheless, assessing the brittleness index through the lens of brittle mineral composition overlooks the impact of rock diagenesis, which significantly affects brittleness. The brittleness observed in rock materials with analogous mineral compositions can vary markedly if they have undergone different diagenetic processes. Additionally, a universal standard for weighing each brittle mineral remains absent. While utilizing the brittleness index derived from mineral composition offers simplicity and convenience, it lacks a robust physical foundation and may produce inconsistent results (Zhang et al., 2016).

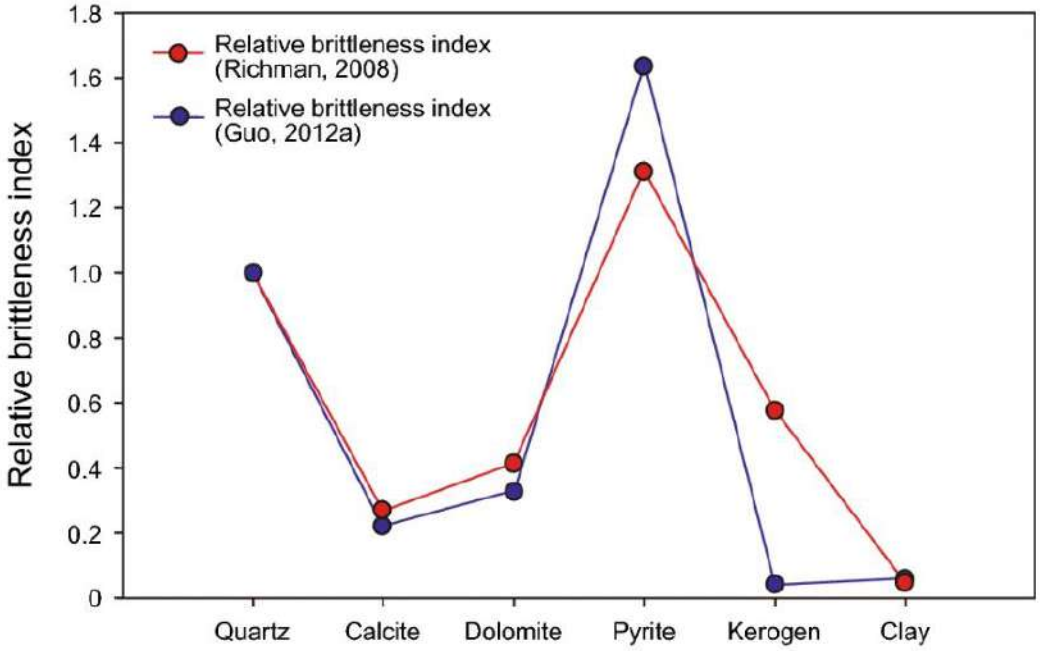

Fig. 49: *Pure brittleness index of different minerals (Qian et al., 2020).*

2.2. Porosity

Porosity has a significant effect on rocks' mechanical properties, especially brittleness, it represents one of the governing factors on rock strain. An increase in rock porosity leads to increased strain at failure and decreased brittleness. This fact may not be the only reason for reducing brittleness in rocks. The mechanical behavior of rocks cannot be directly related to their porosity because brittleness depends on porosity and other parameters (Tapponier and Brace, 1976). Practically, there is no direct correlation between the brittleness index and porosity. Brittleness variance for many rock types can be attributed to their porosity, but it likely depends

on other effects for other rocks. Regardless, based on previous experiences, rock brittleness depends on rock properties and may change as a function of rock type (Heidari et al., 2014).

2.3. Temperature

Temperature is crucial in influencing the mechanical rocks' properties, including brittleness. Geomechanics studies take into account the effect of temperature on stress magnitude. The rock strength characteristics are very different from normal to high-temperature conditions; for example, sandstone and shale produce thermally induced cracks, which affect their strength and integrity and may even cause significant damage to wells (Yang et al., 2021). The lower temperature results in a more brittle fracture manner (Fig. 50).

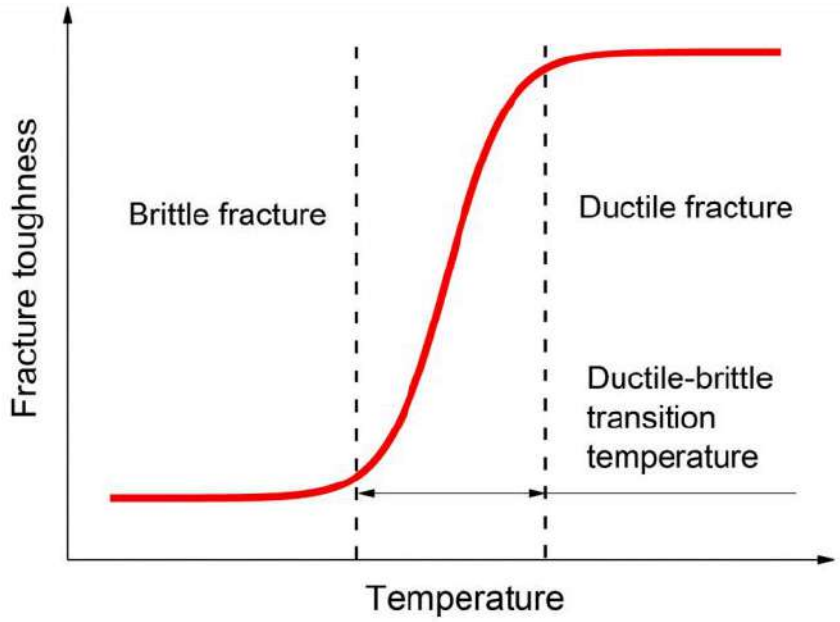

Fig. 50: *Brittle transition temperature (Guo et al., 2021).*

2.4. Strain rate

There is no clear pattern or sense of how strain rate affects brittleness. Occasionally, the brittleness index rises as the strain rate does. Brittleness increases slowly when the strain rate is lower than a specific limit. When the strain rate is between certain lower and higher limits, brittleness increases rapidly. Sometimes, brittleness decreases with the increase in the strain rate. At a higher strain rate, with the increase in the strain rate, some Brittleness indices increased slowly, and others decreased rapidly.

According to previous studies (Mishra et al., 2018; Blanton, 1981; Zheng et al., 2017), the variation in failure stress with a strain rate of brittle materials is roughly divided into three stages: I, II, and III (Fig 51).

- During stage I, in regions of low strain, a quasistatic fracture predominantly develops in rocks. As the strain rate rises, the initial pore closures and microcracks within sandstone and shale become compressed and compacted, gradually increasing rock strength and brittleness (Cai et al., 2008).
- In stage II, as the strain rate continues to rise, fracture damage influenced by rock dynamics progressively increases (Grady, 1996; Kipp et al., 1980), alongside an increase in energy consumption (M. Li, 2014; Zhu et al., 2013). The energy needed for initiating cracks surpasses that required for their expansion (Wang and Hu, 2002). The brief impact loading duration in rock dynamics experiments prevents the specimen from sufficiently accumulating energy (J.Z. Liu et al., 2009; X.B. Li et al., 2005).
- As the shock compression process reaches the upper yield, specifically at stage III, the growth in rock strength in response to the strain rate begins to decelerate. With ongoing strain rate escalation, the rock moves into a high-strain zone, where defects of various sizes develop. This transition results in permanent damage to the rock and a shift from brittleness to ductility. (Yang et al., 2021).

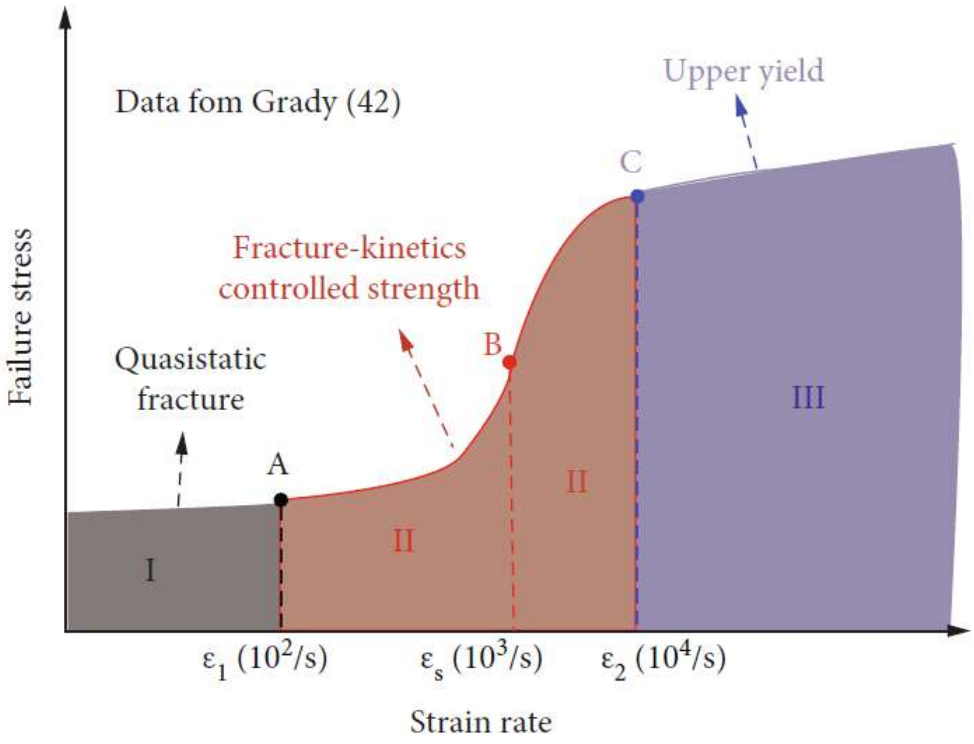

Fig. 51: *Variations in dynamic strength, failure stress with strain rate (Grady, 1996). Point A is the end of stage I, and the corresponding strain ε_1 is 10^2 s^{-1}; point B is the inflection point of the stage II curve, and the corresponding strain ε_s is 10^3 s-1; and point C is the starting point of stage III, and the corresponding strain ε_2 is 10^4 s-1.*

3. Correlation of Brittleness and Fracability

The 'fracability index (FI)' measures how effectively shale gas and oil reservoirs can be fractured (Jin.X et al., 2015). Several methods for quantifying the fracability of unconventional oil and gas reservoirs have been suggested (J.J. Wu et al., 2018; H.J. Fu et al., 2015).

In addition to the Brittleness index, several key factors influence fracability, including fracture toughness, diagenesis, natural crack density, and differential horizontal stress. These elements must be considered when selecting fracture layers, as evaluating criteria beyond just brittleness is important.

- Developing an effective method to quantify fracability is challenging when employing random calculation parameters.
- Secondly, formation fracability depends on a complex interplay of different rock compositional, textural, physical, and mechanical properties influenced by specific in-situ temperatures and pressures. Additionally, other factors must also be taken into account.

- Third, the factors related to fracability are interdependent and can influence fracturing behavior. For instance, the elastic parameters of rocks closely relate to their mineral composition and the in-situ stresses they experience.

Thus, these methods continuously compute how rock mineral content affects fracability, which is unreasonable. Therefore, to establish the right relationship between brittleness and fracability, we must scientifically analyze formation fracability by evaluating the brittleness index.

A thorough evaluation of scientific fracability should integrate all relevant factors based on rock failure mechanisms. Fracability is influenced not only by the rock's petrophysical characteristics but also by geological conditions, such as ambient pressure, temperature, and existing natural fractures (Tang et al., 2020).

3.1. In-Situ Earth Stresses

In the context of the principal stresses in three directions, the minimum horizontal stress (Sh) is crucial in designing fracturing treatments (Willis et al., 2005). The simulated fractures tend to develop perpendicular to Sh, which causes the induced fracture to close. Furthermore, as Sh rises, the rock failure mode shifts from tensile to shear failure (Fig. 52), restricting the vertical expansion of fractures (Economides et al., 2000).

Thus, in formations with more excellent Sh, fractures find it challenging to extend vertically and link to existing fractures.

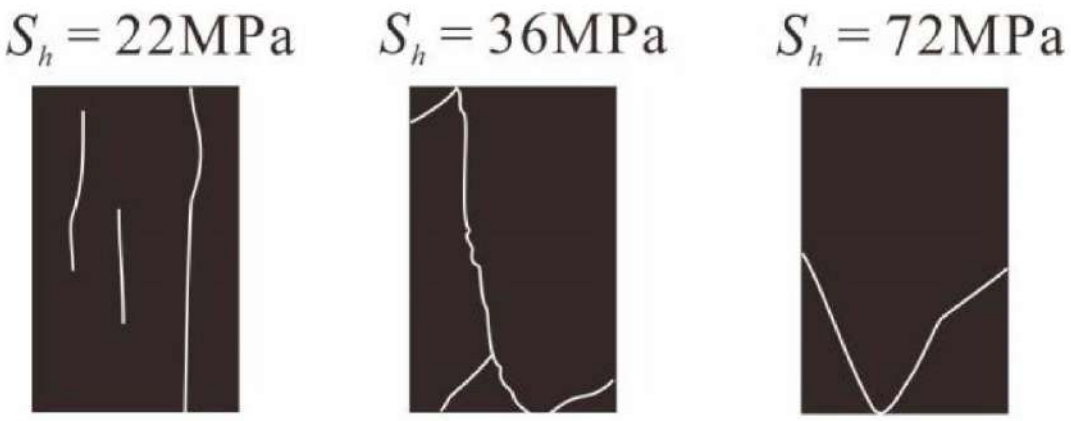

Fig. 52: *Influence of minimum horizontal stress (Sh) on failure mode (Tang et al., 2020).*

The minimum horizontal stress can be estimated using the following equation:

$$S_h = \frac{v}{1-v} \times \left(S_V - \alpha P_p\right) + \alpha P_p + \frac{Ev\varepsilon}{1-v^2} \qquad (01)$$

Where ν is Poisson's ratio; S_V is the vertical stress (psi); α is the Biot's constant, and is a dimensionless value; ε is the tectonic strain parameter (psi); PP is pore pressure (psi); *E* is Young modulus.

The minimum horizontal stress is then an essential parameter for fracability. Therefore, Tang et al. (2020) proposed the following method for fracability evaluation:

$$FI = \frac{(BI_n + S_{h-n})}{2} \qquad (02)$$

$$BI_n = \frac{(BI - BI_{min})}{(BI_{max} - BI_{min})} \qquad (03)$$

$$\mathrm{S_{h-n}} = \frac{(S_{h-\max} - S_h)}{(S_{h-\max} - S_{h-\min})} \qquad (04)$$

.

In this context, BIn and Sh_n represent normalized brittleness and normalized minimum

horizontal stresses. Meanwhile, Max and Min indicate the maximum and minimum values of the relevant variables within the studied formation, respectively.

FI ranges from 0 to 1. A formation with an FI of 1 represents the ideal candidate for hydraulic fracturing, while an FI of 0 indicates the least favorable candidate. Within this context, the optimal fracturing layers exhibit a high brittleness index combined with low minimum horizontal stress.

A fracture barrier is a formation exhibiting lower BI and higher Sh in relation to surrounding formations. Fracture design's primary goal encompasses identifying potential layers and recognizing fracture barriers (Economides et al., 2000). These barriers not only restrict the vertical expansion of hydraulic fractures but also prevent them from encroaching on water-bearing layers or fault zones (Tang et al., 2020).

Sh's formula in “Equation (01)” indicates that the minimum horizontal stress rises as Poisson’s ratio, which ranges from 0.1 to 0.45, increases. Additionally, even minor variations in Poisson’s ratio can significantly change the minimum horizontal stress. Consequently, Poisson’s ratio plays an indirect role in fracability by influencing the minimum horizontal stress, with the fracability index decreasing as Poisson’s ratio increases (Tang et al., 2020).

The foundation of fracability evaluation involves precise measurement of rock brittleness. Besides the brittleness index, the minimum horizontal principal stress is another crucial factor in identifying potential fracturing layers. Ideal fracturing layers have a high brittleness index and low minimum horizontal stress. There is a positive correlation between Poisson’s ratio and minimum horizontal stress. As Poisson’s ratio increases, the minimum horizontal stress also rises, decreasing the fracability index (Tang et al., 2020).

3.2. Temperature effects

Thermally activated deformation mechanisms, such as the dislocation slide of clay minerals, mean that temperature affects the brittleness of shales. Typically, shales transition from brittle to more ductile only when temperatures rise significantly, usually by several tens of degrees (Rybacki et al., 2016; Rybacki et al., 2015). However, the vertical thickness of a region's target interval is often insufficient (<100 m). With a geothermal gradient of 25 ◦C/km (with an uncertainty of less than 30%), temperature changes are minimal in the target layers, resulting in

no substantial alteration of rock mechanics. Thus, the impact of temperature on formation fracturing can be disregarded (Tang et al., 2020).

3.3. Natural Fractures

In hydraulic fracturing, natural fractures can allow fracturing fluid to leak into reservoirs, creating a complex network of hydraulic fractures that serve as a fast pathway for shale gas extraction (X.M.Ni et al., 2008; Tang et al., 2011). Thus, formations with a higher density of natural fractures are, to some degree, viewed as more fracable. While natural cracks are often excluded from fracability quantification models, they are not overlooked in hydraulic fracturing processes; instead, formations with greater natural fracture density are considered distinctly. The rationale behind this distinction is outlined below:

- Initially, quantitatively assessing the impact of crack density on fracability proves to be quite challenging. (Jin.X et al, 2015; Tang et al., 2018).
- Secondly, engineering methods like tiltmeters, well logging, and micro-seismic events can identify fractured strata. It is important not to view these layers as potentially favorable fractures; instead, they must be assessed on their connections to aquifer formations and faults to avoid the upward movement of shale gas.
- Third, in the same crustal stress conditions, brittle rocks typically exhibit a higher density of fractures than ductile rocks (Li.Z et al, 2018). Throughout the history of structural geology, when there is no significant difference in tectonic stress across different layers, the extent of fracture formation is influenced by the rock's brittleness. In this context, the brittleness of a rock somewhat indicates the extent of natural fracture development.

Fracability is affected by rock brittleness and natural fractures, diagenesis, and other factors. Many shale fracability indices have been established based on ‘’soundless crack agents’’, ‘’brittleness index, fracture toughness, and rock mechanical properties’’, ‘’brittleness and energy dissipation’’ during hydraulic fracturing (Wang et al.,2015). Heterogeneities in shale fracability indices also play an important role in optimizing the hydraulic fracture parameter (Jahandideh and Jafarpour, 2016). It is difficult and time-consuming to define a uniform formula for fracability index considering all the factors. Investigations of fracability index have mainly concentrated on shale gas reservoirs.

It has been proven that the formation with the higher fracability index is considered to be the better fracturing candidate (Wang et al.,2015). The geometry and complexity of hydraulic fracture stimulation treatments are primarily controlled by rocks' heterogeneous and anisotropic nature (Mullen and Enderlin, 2012). Rock brittleness is a key parameter that drives hydraulic fracture treatment to the complex state, which is the point in shale gas stimulation treatment.

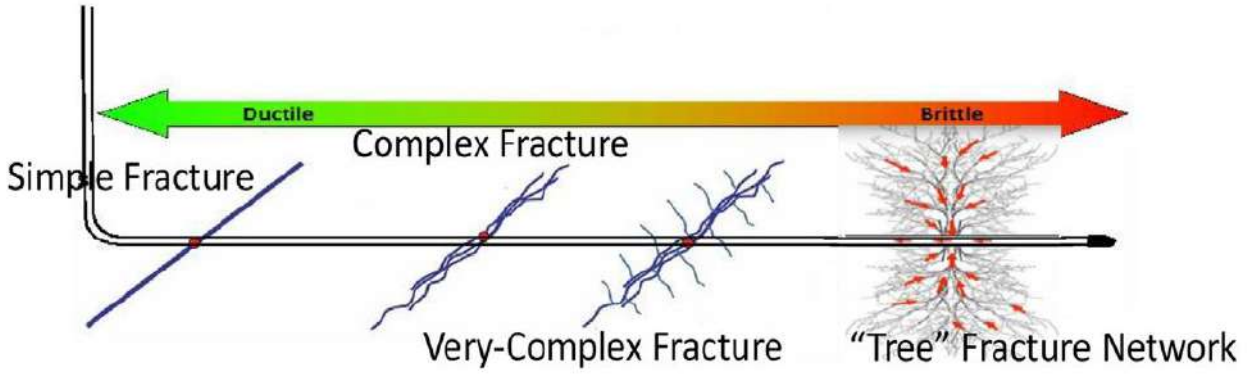

Fig. 53: *Various hydraulic fracture morphologies from simple and complex fracture transition to the tree fracture network concerning rock brittleness (Wang et al.,2015).*

4. Benefit of evaluating Brittleness for shale gas reservoirs

Over decades, fracturing and horizontal wells have become viable and important techniques for shale gas exploitation. There are many options, processes, and methods to be considered for drilling and fracturing treatment, especially for completion. Optimization of the completion process, including the location, the number, and the size of fractures, is still a challenge, especially for horizontal wells. This latter has unique aspects that require special techniques to ensure successful fracturing treatments. These elements influence the optimization process for effectively placing treatments and achieving optimal asset performance. Also, the fracturing treatment is still the best way to produce the hydrocarbons trapped in complex formations such as shale reservoirs.

Horizontal drilling combined with multiple fracture completions of these wells is today's most prevalent method of enhancing reservoir contact and extracting hydrocarbons economically. (Soliman et al., 2010).

The various fracturing methods employed to enhance production aim to create far-field fracture complexity that leads to secondary fractures. Known as fracture networks or branch fractures, secondary fractures are particularly valuable in nano-Darcy rock (<0.001 md) (Soliman et al., 2010). Techniques such as simultaneous fracturing promote the formation of secondary fractures. Simultaneous fracturing aims to induce stress interference between the fractures created during treatments, thereby altering their orientation. This approach also results in a complex fractured rock system, further increasing hydrocarbon production (Soliman et al., 2010).

Various crucial factors contribute to the successful completion of a fractured well, especially those related to geomechanics. According to Soliman et al. (2010), to deal with fracture complexity and production issue challenges, the brittleness index is one of the crucial parameters to improve the design of the created fracture and enhance fracture complexity. Kundert and Mullen (2009) propose that brittle rock is the most suitable option for forming a complex hydraulic fracture system. In the same perspective, Buller et al. (2010) have shown, based on actual data, that shale gas production is strongly related to the rock brittleness index (Fig. 54).

The comparison between gas production and Brittleness index profiles shows that the gas production profile has relatively the same trend where the high production is located in front of the rock intervals with a high brittleness index. When the brittleness index exceeds 40%, the gas flows at a low production rate, and as the BI increases, the production becomes higher; notably, when the BI exceeds 50%, the gas production rate increases drastically. This conclusion leads to the reflection that brittleness is one of the most helpful parameters that can be used to target promising production zones or intervals by improving the design of hydraulic fracturing operation, enhancing fracture complexity, and increasing the SRV (Stimulated Reservoir Volume).

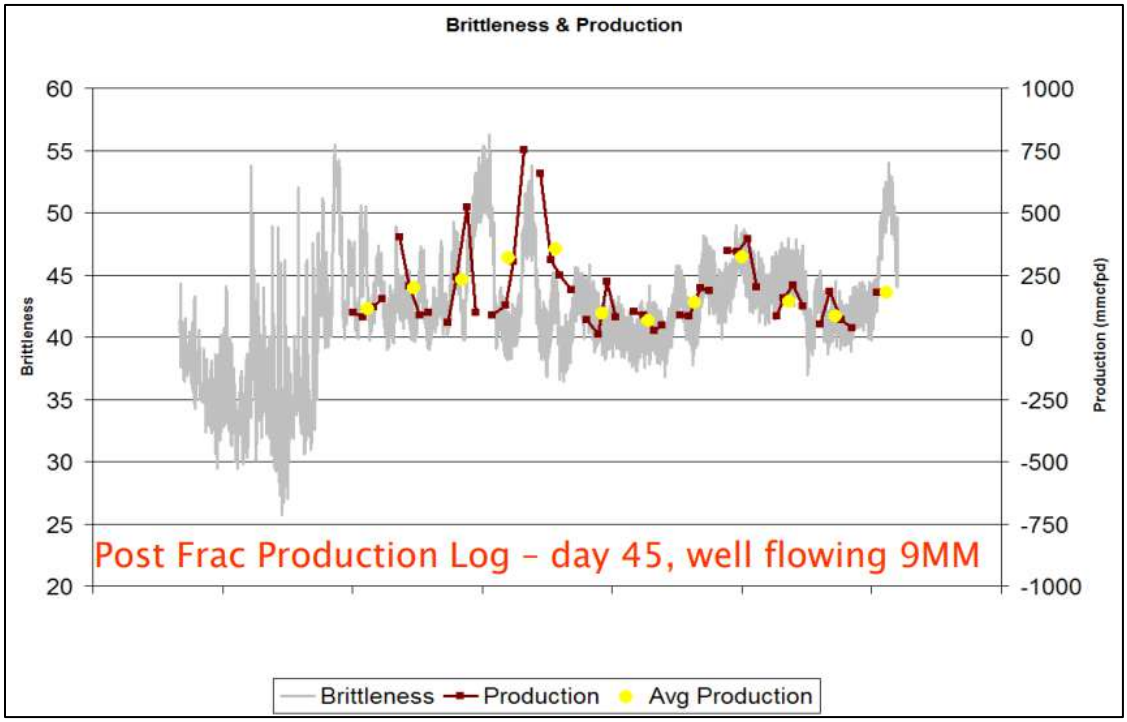

Fig. 54: *Brittleness index versus gas production (Buller et al., 2010).*

Gas production increases in the section where the brittleness is higher; otherwise, it is higher in the brittle portion of the reservoir where the complex fracturing occurred. Based on this, the brittleness index has an important impact on improving the design of created fractures to enhance fracture complexity and the gas production of shale gas reservoirs.

Stimulation treatments often focus on operational efficiency and the speed of pumping out one Frac-job moving on to the next. So, based on the horizontal well completion/stimulation techniques, Brittleness index consideration, and other features of unconventional reservoirs, the fracturing fluids are pumped out with targeted injection intervals in order to maximize the stimulated reservoir volume (SRV) and improve connectivity by creating the most complex fracture network possible. To do so, the following frac methods have been used in practice:

4.1. Texas 2 Step frac

The principle of this frac method is to fracture the horizontal well with a multitude of transverse fractures, starting from the end of the horizontal section of the borehole until its beginning (Fig. 55). This technique consists of fracturing between two injection points (stages), and then adding an intermediate fracture in order to make the stresses governing the rock closer.

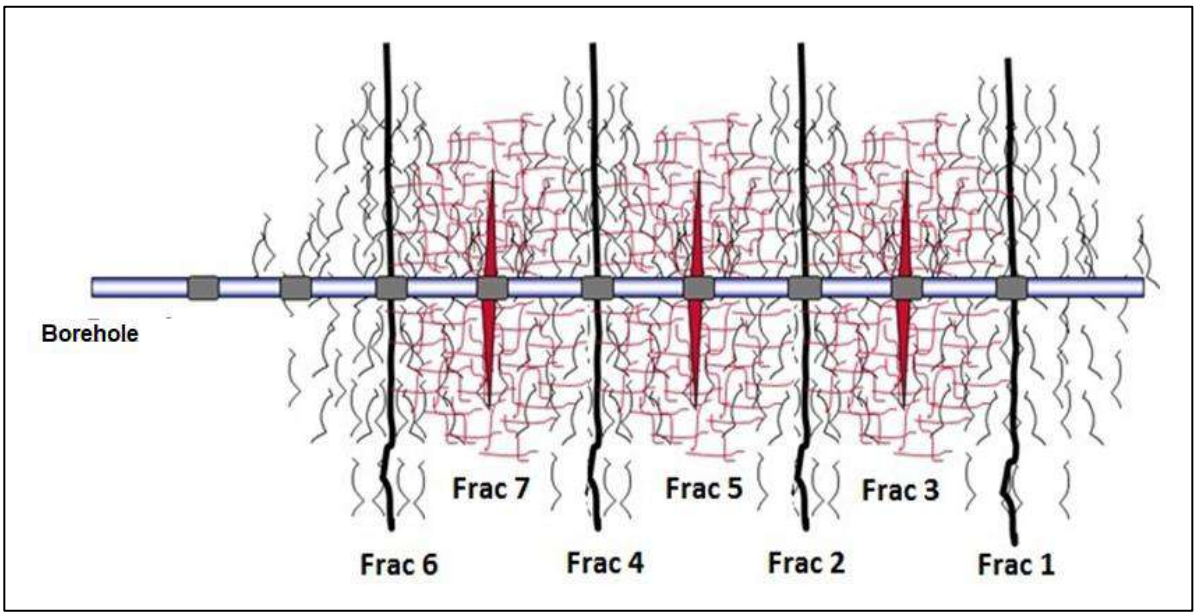

Fig. 55: *Texas 2 step frac method (Soliman et al., 2010).*

4.2. Zipper Frac

The goal of applying this fracturing method to Well-Pads with multiple horizontal boreholes is to produce equidistant fractures that follow the increasing order along the boreholes, which are assumed to be parallel. Every fracture adheres to the first borehole's alignment (Fig. 56).

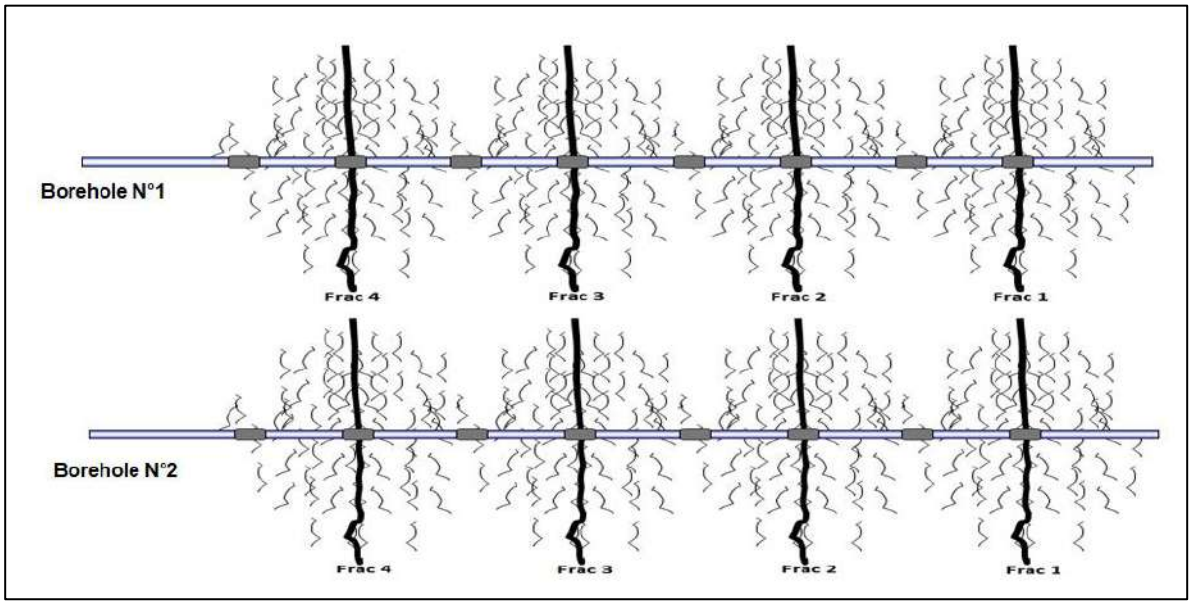

Fig. 56*: Zipper Frac method (Soliman et al., 2010).*

4.3. Modified Zipper Frac

This frac method has the same principle as the Zipper Frac method, except that the fractures of two successive boreholes are parallel and overlapped to maximize the stimulated reservoir volume (SRV) and create therefore more complexity in the rock (Fig. 57).

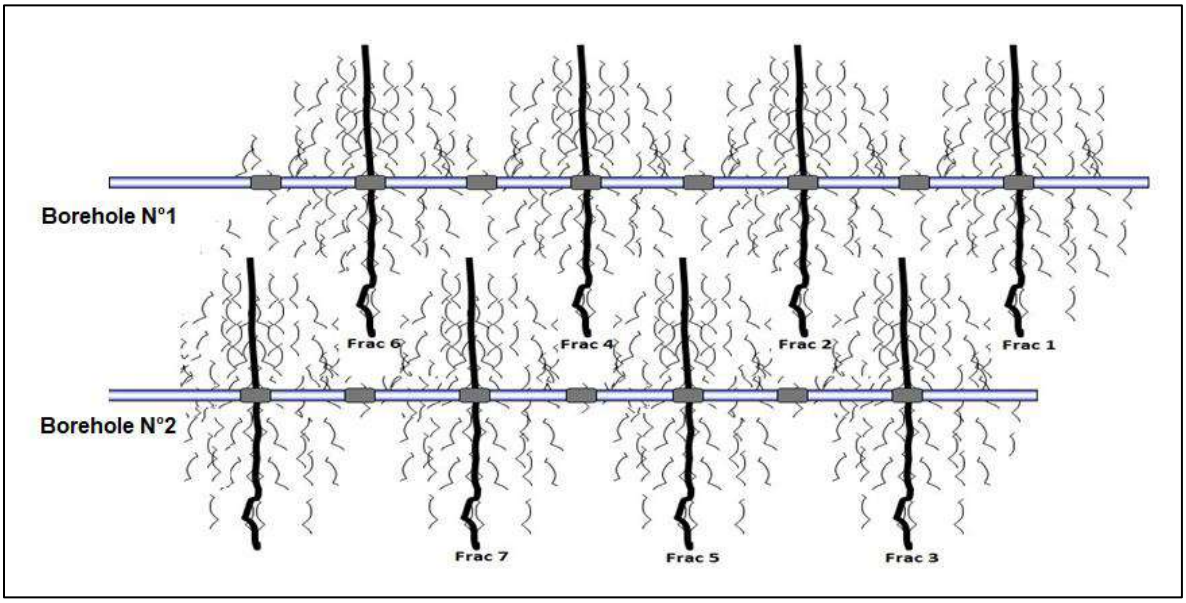

***Fig. 57**: Modified Zipper Frac method (Soliman et al., 2010).*

As seen in Figure 58, different completion methods are employed to develop shale formations. Modified zipper fracturing (MZF) represents the most recent advancement in the industry, offering greater production than traditional zipper fracturing, and the "Texas Two Step" involves stimulating stages in a non-sequential manner.

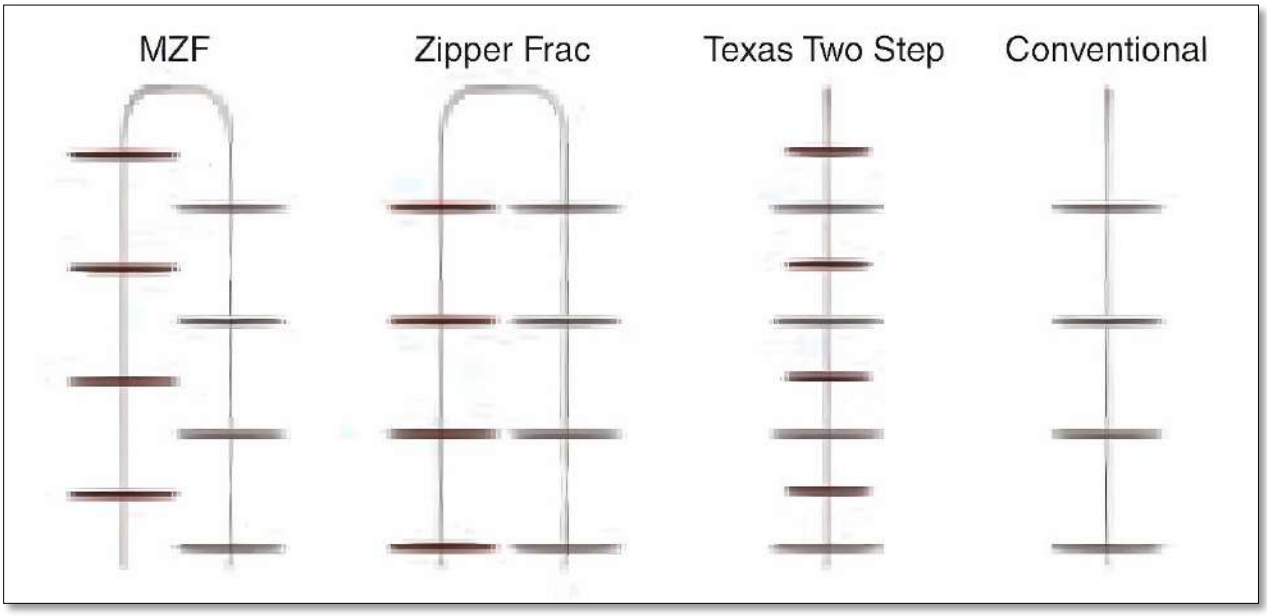

***Fig. 58**: Various types of Frac methods (Jacobs, 2014).*

5. Methods of evaluating Brittleness

Unconventional reservoirs, such as shale, with low porosity and permeability, require hydraulic fracturing to enhance productivity. A crucial characteristic that influences the hydraulic fracturing process is rock brittleness, which assesses the rock's responsiveness to fracturing. Various properties have been utilized to represent and evaluate rock brittleness, typically categorized into three main groups:

- Hardness and strength;
- Brittle minerals weight fraction;
- Elastic moduli.

Analyzing hardness and strength reveals specific brittleness properties, which must be assessed in laboratory experiments (Honda & Sanada, 1956; Hucka & Das, 1974; Altindag & Guney, 2010; Jin et al., 2014; Zhang et al., 2015). In contrast, the other two categories can be monitored and quantified using well logging or surface seismic methods, making them more widely applicable in the field.

Jarvie et al. (2007) and Wang and Gale (2009) introduced a brittleness index based on mineralogy (MBI). This index highlights that rock brittleness correlates closely with quartz and dolomite content, while ductility is associated with clay and other mineral contents. Mineralogy

data can be sourced from core analyses and well logs. A key advantage of the mineralogy-based brittleness index is its straightforward connection between brittleness and lithology, allowing for brittleness evaluation through lithological interpretation when the mineralogy of the target formation is uncomplicated. Nevertheless, factors like the presence and arrangement of voids and pore fluids can also significantly impact rock brittleness (Zhang et al., 2015).

Different elastic moduli serve to characterize brittleness. Rickman et al. (2008) introduced a brittleness index based on the average of normalized Young's modulus and normalized Poisson's ratio. A high index indicates a high Young's modulus coupled with a low Poisson's ratio (EBI). The benefit of using the elastic moduli-based EBI index is that it can be derived from both well logs and seismic data, making it more relevant than the mineral-based brittleness index (Rickman et al., 2008). Additionally, EBI captures the combined influences of mineral composition, microstructures, and pore fluids on rock brittleness. However, it can be challenging to identify lithological changes using the EBI, as different formations with varying lithologies may exhibit comparable elastic properties.

Shales' intricate components and unique microstructural characteristics significantly influence their mechanical and elastic properties, impacting rock brittleness, fluid flow, and seismic-wave transmission (Guo et al., 2012). Given that rock brittleness is vital for effective hydraulic fracturing in shale gas extraction, assessing the feasibility of estimating rock brittleness using well log, seismic, laboratory, and other relevant data is crucial. This section outlines the most recognized, reliable, and applicable methods for evaluating brittleness indices as documented in existing literature:

5.1. Determination of brittleness from rock compression Stress-Strain curves

The full stress-strain curves of a rock specimen subjected to external loads reveal its deformation and failure traits. (Fig. 59) depicts the internal micromechanical processes involved in rock deformation and failure behaviors under compressive load (Tang et al., 2020). The overall failure process can be categorized into five stages:

- 1. oa: Pre-existing micro-cracks and micro-pores close; this stage is terminated at crack closure stress (σcc).

- 2. ab: Linear elastic deformation of rock occurs with the tangent modulus of Young's modulus until the crack initiation stress (σci) is reached. σci is the turning point of the rock from elasticity to plasticity, also known as the yield point.
- 3. bc: Micro-cracks stably propagate before crack damage stress (σcd).
- 4. cd: Cracks propagate in an unstable manner until the limit strength of the rock is reached at a stress level known as failure stress (σf).
- 5. de: At the peak stress (σf), the rock is unsteady with high energy. The internal cracked surfaces of the rock intersect then form one or several macro-fracture surfaces. Subsequently, the rock mass slides along the macro-fracture surfaces and the sample's bearing capacity rapidly decreases until the residual strength (σr) is reached.

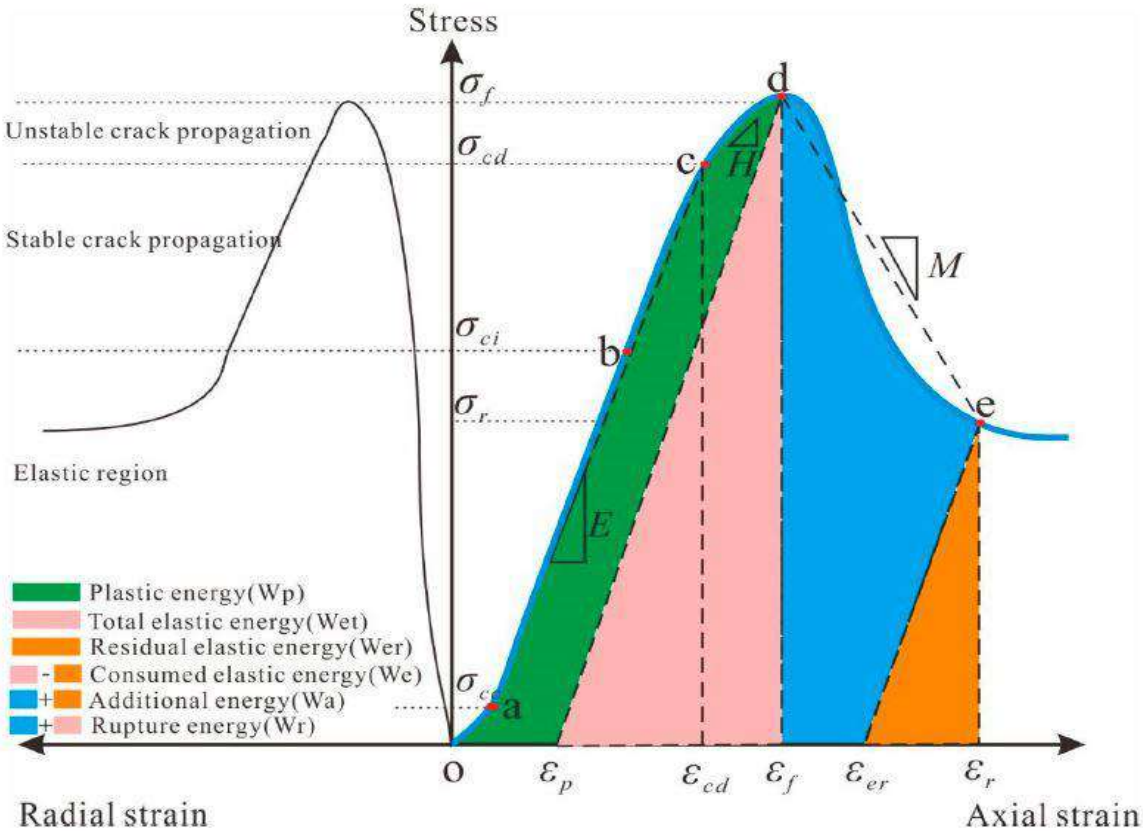

Fig. 59: *Typical compression stress-strain curve and associated deformation and failure characteristics for brittle rocks. σcc: crack closure stress; σci: crack initiation stress; σcd: crack damage stress; σf: failure stress; σr: residual stress; εp: plastic strain; εcd: strain at crack damage threshold; εf: failure strain; εr: residual strain; E: Young's modulus; H: hardening modulus and M: drop modulus (modified from Rahimzadeh et al., 2018).*

Rock failure is fundamentally a process of balancing energy absorption and release (Rahimzadeh et al., 2018; Paulding et al., 1966; Ranjith et al., 2017). In the pre-peak stage, the rock experiences both elastic and plastic deformation. The total elastic energy (Wet) built up during elastic deformation enhances the internal energy of the rock. Additionally, plastic energy (Wp) dissipates during plastic deformation due to crack closure and frictional sliding. Brittle rocks can convert a more significant portion of the absorbed external energy into elastic energy rather than plastic energy, and the increased elastic energy stored during loading promotes rock rupture and the extension of fractures (Tang et al., 2020).

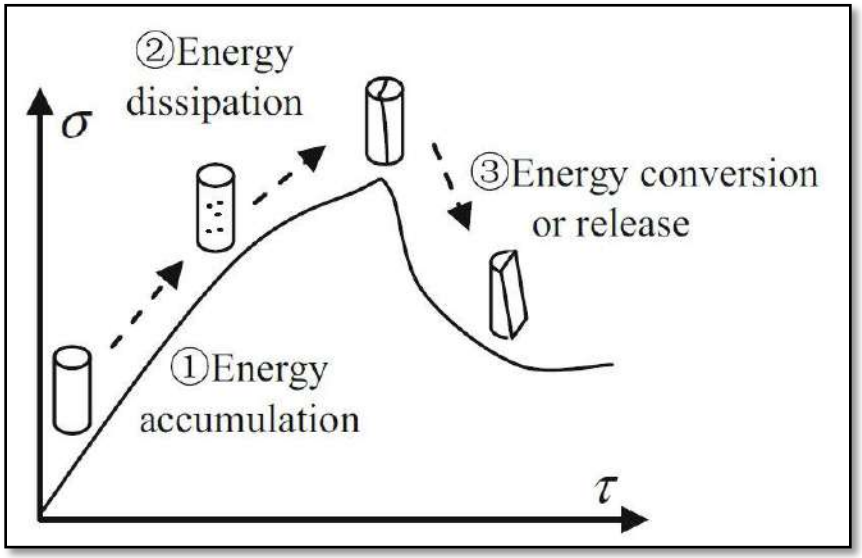

Fig. 60: *Energy at each stage of the Stress-Strain curve (Zhang et al., 2016).*

The BI based on the energy is defined as follows (Rahimzadeh et al., 2018):

$$BI = \frac{1}{2}(BI1 + BI2) = \frac{1}{2}\left(\frac{We}{Wr} + \frac{We}{Wet + Wp}\right) \quad (05)$$

$$Wet = \frac{1}{2E}\,\sigma_f^2 \quad (06)$$

$$We = Wet - Wer = \frac{1}{2E}(\sigma_f^2 - \sigma_r^2) \quad (07)$$

$$Wr = Wet + Wa - Wer = \frac{1}{2E}\left(\sigma_f^2 - \sigma_r^2\right) + \int_{\varepsilon f}^{\varepsilon r} \sigma d\varepsilon \quad (08)$$

$$Wp = Wt - Wet = \int_0^{\varepsilon f} \sigma d\varepsilon - \frac{1}{2E}\,\sigma_f^2 \qquad (09)$$

Figure 59 illustrates the definitions of the calculation parameters. Here, (We) stands for consumed elastic energy, reflecting the difference between total elastic energy (Wet) and residual elastic energy (Wer). Wt denotes the total energy consumed during the pre-peak stage. Wr indicates the rupture energy, the sum of total elastic energy (Wet), and the extra energy expended due to rock failure during system loading (shown as the blue area in Figure 59). Wp signifies the dissipation of plastic energy within the pre-peak region.

In this model, BI1 assesses how much the fracturing process happens independently. BI2 indicates the proportion of total absorbed energy during the pre-peak phase released in the post-peak rupture phase. Both of these values range from 0 to 1. As a result, the value of BI transitions smoothly from 0 to 1, and the level of brittleness shifts from complete ductility to total brittleness.

Figure 61 illustrates that the stress-strain curve for absolute brittle rock exhibits these characteristics (Zhang et al., 2016):

- (1) Before reaching the peak stress, there is almost no yield platform in the stress-strain curve;
- (2) The elastic energy stored in the rock sample is minimally converted into fracture energy during the post-peak stage, resulting in a specimen that is entirely self-sustaining fracturing.

From this, we can obtain the corresponding definition of absolute ductility and its characteristics:

- (1) The dissipation energy during the pre-peak stage and the fracture energy during the post-peak stage become infinite;
- (2) The yield platform and the post-peak curve join together to become one straight horizontal line;
- (3) There is no failure point in the curve, i.e., the material remains in a deformation state with increasing loading.

The complete stress-strain curve's variation (Fig. 61) serves to illustrate changes in rock brittleness.

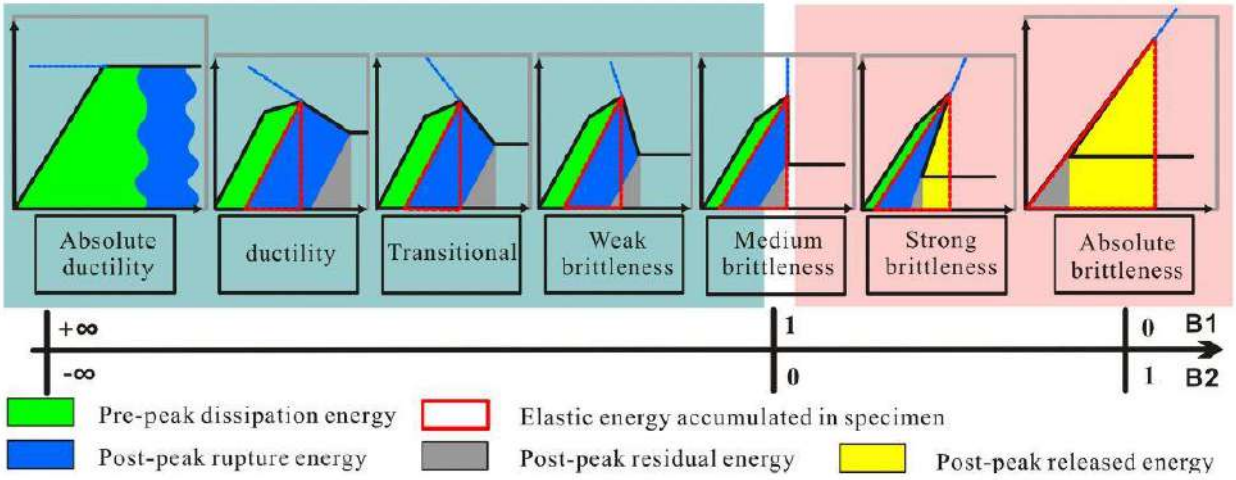

Fig. 61: *Change in the degree of brittleness represented by B1 and B2 based on the energy changes of stress-strain curves (Zhang et al., 2016).*

The stress-strain curves generated from rock loading provide a clear insight into rock properties. Consequently, the subsequent brittleness indicators (BI) have been formulated based on the shapes of the uniaxial and triaxial compressive stress-strain curves. The deformation, stress, and energy retrieved or calculated from either pre, or post-peak stress-strain curves often indicate the rock's brittleness when subjected to uniaxial or triaxial compressive stress (Wong et al., 2021). These BIs are closely associated with the strain preceding peak strength as follows:

$$BI = \frac{\sigma_c}{\varepsilon_p} \qquad (09)$$

This equation is especially used for shale, where: BI < 10: Low, 10 < BI < 20: Middle, 20 < BI< 30: Brittle, 30 < BI < 40: High, BI > 40: Extreme (Liang et al., 2017).

$$BI = \varepsilon_{1i} \times 100\ \% \qquad (10)$$

Where BI < 3% : Brittle, BI > 5% : Ductile (Andreev, 1995).

$$BI = \frac{\varepsilon_e}{\varepsilon_p} \qquad (11)$$

BI represents the reversible or elastic strain ratio to the total strain at fracture. This is important because, in brittle rock, most of the strain tends to be reversible, whereas ductile rock experiences a significant amount of inelastic deformation (Hucka and Das, 1974).

$$BI = \frac{1}{\varepsilon_e} \qquad (12)$$

In this context, the brittleness index (BI) was established under the premise that lower elastic strain signifies increased brittleness. However, this BI does not accurately represent rock brittleness, as a reduced elastic strain could coexist with considerable irreversible strain, reflecting a rock's significant ductility. An unloading test must also be performed to evaluate the elastic and inelastic strains before reaching peak strength. The selected unloading point significantly affects how these two strains are measured. The irreversible axial strain will be inaccurately low if the unloading point is too far from the peak strength (Gong and Sun, 2015).

In this regard, εp and εe represent the peak strain and the elastic strain at peak strength, respectively. Additionally, ε1i denotes the absolute irreversible longitudinal strain (aligned with σ1) leading up to failure. The peak strength is denoted by σc (see Fig. 62). Furthermore, the second, third, and fourth degrees of brittleness highlight the importance of elastic strain prior to reaching peak strength in assessing rock brittleness.

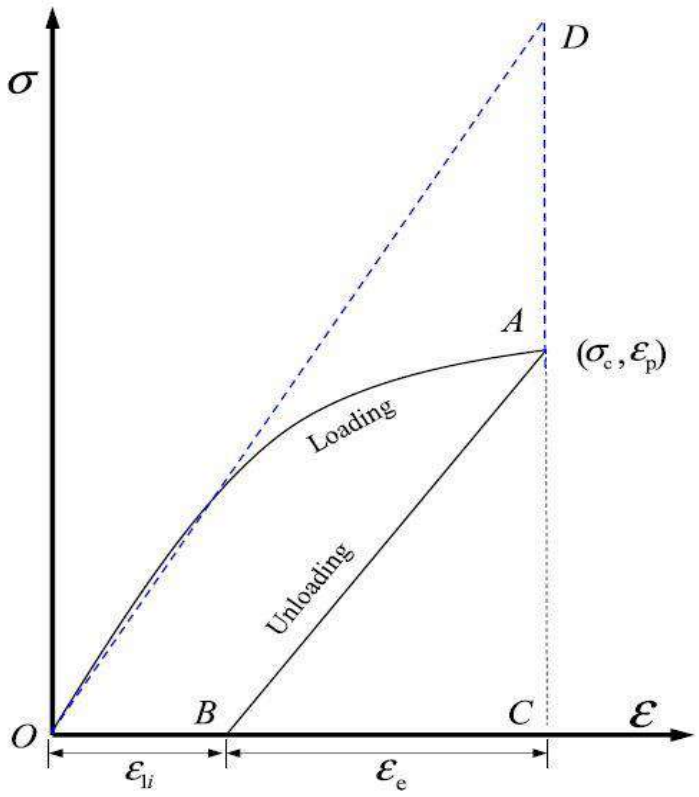

Fig. 62: *Stress and deformation used for BI calculation (Wong et al., 2021).*

Yang et al. (2013) (Fig. 63), developed other different BIs based on stress-strain curves before and after peak strength.

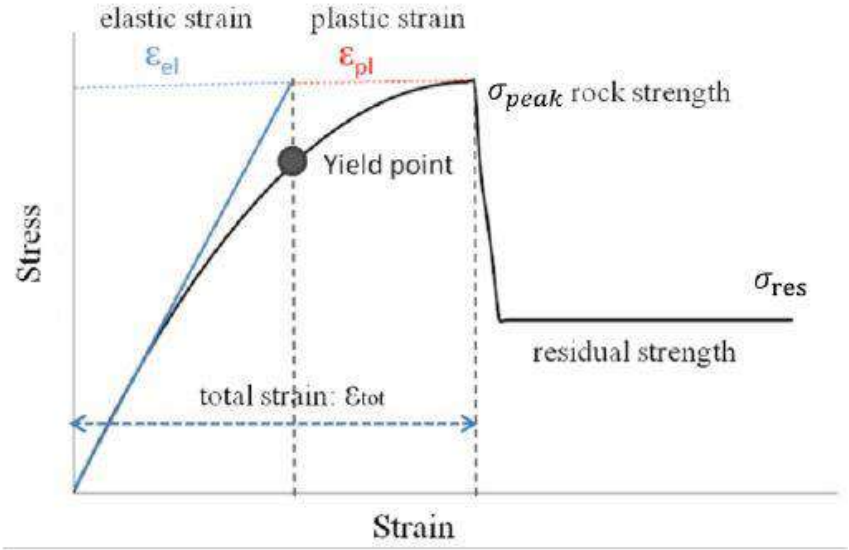

Brittleness Index	Parameters
$B = \frac{\varepsilon_{el}}{\varepsilon_{tot}}$	ε_{el}: elastic strain ε_{tot}: total strain
$B = \frac{W_{el}}{W_{tot}}$	W_{el}: elastic energy W_{tot}: total energy
$B = \frac{\sigma_{peak} - \sigma_{res}}{\sigma_{peak}}$	σ_{peak}: peak strength σ_{res}: residual strength

Fig. 63: *Different types of Brittleness indices defined based on compressive loading tests (modified after Yang et al., 2013)*

5.2. Determination of brittleness from Mohr's envelope, based on the angle of internal friction

The brittleness indices outlined in equations 13 and 14 are solely linked to the angle of internal friction. The slope of Mohr's envelope defines this angle at zero normal stress (see Fig. 64). This slope is determined by measuring the fracture plane angle αf, which is the angle between the fracture plane and the specimen's axis (cylindrical plug sample) (Hucka and Das,

1974). It is thought that rocks exhibiting greater brittleness tend to have a higher angle of internal friction Φ (Hucka and Das, 1974; Chang et al., 2006; Jin et al., 2014a, b; Zhang et al., 2016).

$$BI = \sin_{\varphi} \quad (13)$$

$$BI = 45° + \frac{\varphi}{2} \quad (14)$$

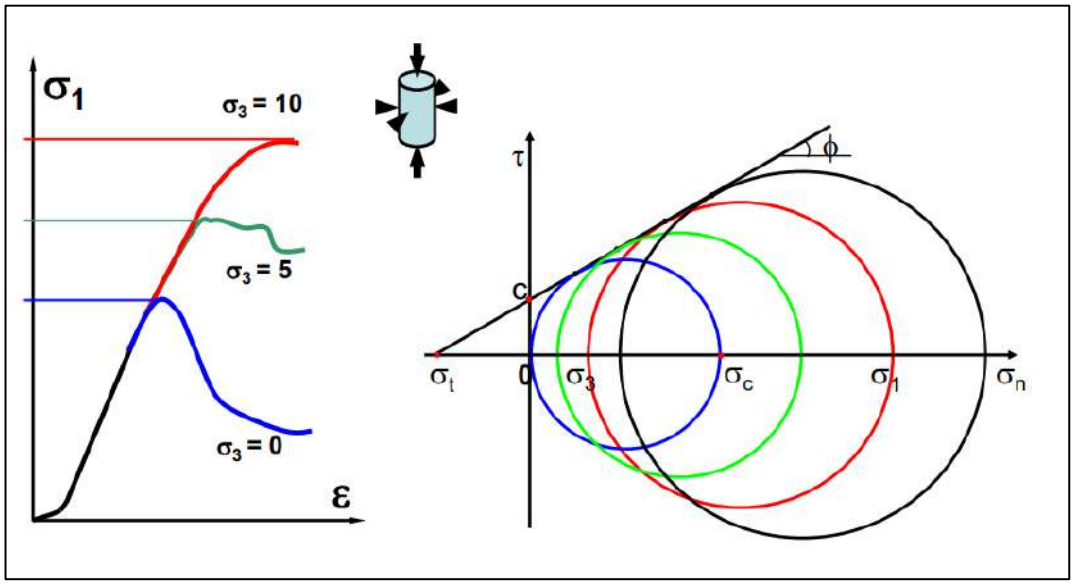

Fig. 64: *Schematic diagram for determining the angle of internal friction from Mohr circle envelope. σn and τ are the normal stresses and shear strength, respectively (Zhao, 2008).*

5.3. Determination of brittleness from tensile and compressive strengths

Among a pool of brittleness indices, for the sake of simplicity and availability of testing equipment about the strength of materials, strength-based brittleness indices have been widely utilized in a wide range of research. Parameters in these indices include uniaxial compressive strength (UCS) and Brazilian tensile strength (BTS). The literature review revealed four widely used strength-based brittleness indices as follows (Nejati et al., 2017):

$$BI = \left(\frac{\sigma_c}{\sigma_t}\right) \quad (15)\ Hucka\ and\ Das\ (1974)$$

$$BI = \left(\frac{\sigma_c - \sigma_t}{\sigma_c + \sigma_t}\right) \quad (16)\ Hucka\ and\ Das\ (1974)$$

$$BI = \left(\frac{\sigma_c \times \sigma_t}{2}\right) \quad (17)\ Altindag\ (2002)$$

$$BI = (\sigma_c \times \sigma_t)^{0.72} \quad (18)\ Yarali\ and\ Soyer\ (2011)$$

Here, σc and σt represent the rock's Uniaxial Compressive Strength (UCS) and tensile strength (TS), respectively. Yasar (2020) categorized rocks based on their brittleness, which is calculated as the ratio of UCS to TS, as shown in Table 08.

Table 08: *Brittleness classification based on the ratio of UCS to TS (Serdar YASAR, 2020).*

Brittleness ratio (UCS/TS)	Classification / Failure mode
<9	Ductile
9-15	Average
>15	Brittle

5.4. Determination of brittleness from rock mechanical properties

Rickman et al. (2008) introduced an index for assessing rock brittleness, derived from elastic properties such as Young's modulus and Poisson's ratio, demonstrating significant field applicability. This index is among the most commonly utilized measures of brittleness in shale gas extraction.

Elastic properties are derived from geophysical methods, specifically through analyzing the velocities of P and S waves in shale formations. Rocks exhibiting a high Young's modulus paired with a low Poisson's ratio tend to be more brittle, promoting the formation of complex fracture networks during hydraulic fracturing (Rickman et al., 2008; Wang et al., 2015).

$$BI = \frac{1}{2}\left(\frac{E - E_{min}}{E_{max} - E_{min}} + \frac{\nu - \nu_{min}}{\nu_{min} - \nu_{max}}\right) \quad (19)$$

E_{max} and E_{min} are the maximum and minimum static Young's moduli, respectively, and ν_{max} and ν_{min} are the maximum and minimum static Poisson's ratios of the shale formation, respectively (Rickman et al., 2008).

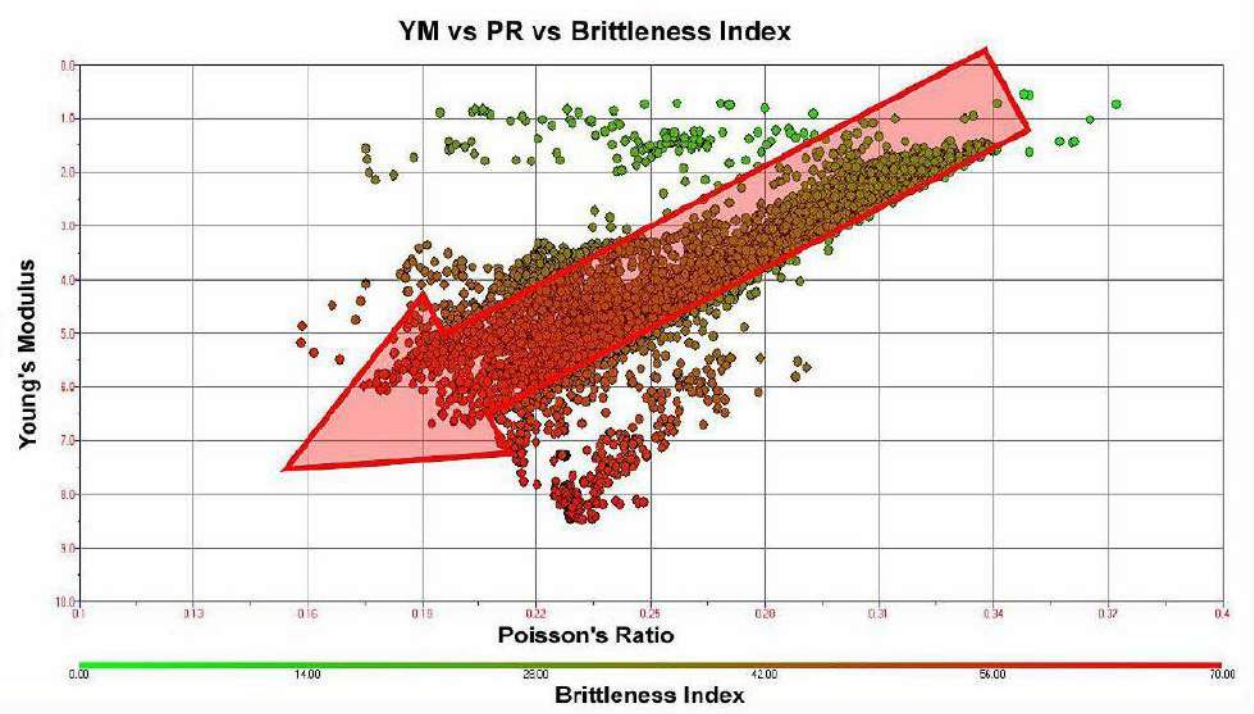

Fig. 65: *Cross plot of Young's modulus and Poisson's ratio showing the brittleness percentage increasing to the southwest corner of the plot, where the unit of Young's modulus is mpsi, and 1 mpsi = 6.8947573 GPa* (*Rickman et al., 2008).*

This model estimates the static Young's modulus and Poisson's ratio from dynamic values, which can be obtained through direct calculations using compressive and shear slowness (Mullen et al., 2007).

$$E_d = \rho\left(\frac{4 - 3\Delta t_s^2/\Delta t_c^2}{\Delta t_s^2\left(1 - \frac{\Delta t_s^2}{\Delta t_c^2}\right)}\right) \qquad (20)$$

$$\nu_d = \left(\frac{2 - \Delta t_s^2/\Delta t_c^2}{2\left(1 - \frac{\Delta t_s^2}{\Delta t_c^2}\right)}\right) \qquad (21)$$

E_d is the dynamic Young's modulus, ν_d is the dynamic Poisson's ratio, Δtc is the compressive slowness (µs/ft), Δts is the shear slowness (µs/ft), and ρ is the rock density.

The same dynamic Young's modulus and Poisson's ratio (same model) are calculated with the compressive and shear velocities:

$$E_d = \rho V_s^2 \left(\frac{3V_p^2 - 4V_s^2}{V_p^2 - V_s^2} \right) \quad (22)$$

$$\nu_d = \frac{V_p^2 - 2V_s^2}{2\left(V_p^2 - V_s^2\right)} \quad (23)$$

E_d is the dynamic Young's modulus, ν_d is the dynamic Poisson's ratio, Vc is the compressive velocity (ft/μs), Δts is the shear velocity (ft/μs), and ρ is the rock density.

5.5. Determination of brittleness from mineral rock components (mineral composition)

The mechanical properties of rock materials are greatly affected by their mineral composition, indicating a direct correlation between mineral composition and brittleness (Zhang et al., 2016). Jarvie et al. (2007) posited that quartz content influences rock brittleness, thus defining the Brittleness Index (BI) as the quartz content in rock to calculate brittleness.

$$BI = \frac{V_{Quartz}}{V_{Quartz} + V_{Carbonate} + V_{Clay}} \quad (24)$$

$$BI = \frac{\sum_{i=1}^{m} a_i M_i}{\sum_{j=1}^{m} a_j M_j} \quad (25)$$

V_{Quartz}, $V_{Carbonate,}$ and V_{Clay} are the contents of quartz, carbonate, and clay, respectively; a is the weight coefficient of each mineral; i denotes the type of brittle mineral; j denotes all minerals; and M is the mineral content (volume fraction).

Rickman et al. (2008) conducted an analysis of the mineral composition in the Barnett Shale through X-ray diffraction and laser-induced breakdown spectroscopy (LIBS). Their findings indicated that rock brittleness increases with higher quartz content and decreases with higher clay content (Zhang et al., 2016).

Brittleness varied moderately with increased carbonate levels. Buller et al. (2010) recommended using the ratio of brittle minerals to the total mineral content to assess rock brittleness. However, indices assessing brittle mineral composition overlook the impact of rock diagenesis on brittleness, leading to significant variations in brittleness among rock materials with similar mineral compositions that have undergone different diagenetic processes.

Furthermore, a universal standard for weighting each brittle mineral remains absent (Zhang et al., 2016).

$$BI = \frac{V_{Qtz+Cb}}{V_{Qtz+Cb+Toc+Cl}} \quad (26)$$

Qtz, Cl, Cb, and Toc are the quartz, clay, carbonates, and total organic carbon, respectively.

$$BI = \frac{Qz + Dol}{Qz + Dol + Ca + Cly + TOC} \quad (27) \quad \text{(Wang and Gale, 2009)}$$

Qz, Dol, Ca, Cly, and TOC are the quartz, dolomite, calcite, clay, and total organic carbon, respectively.

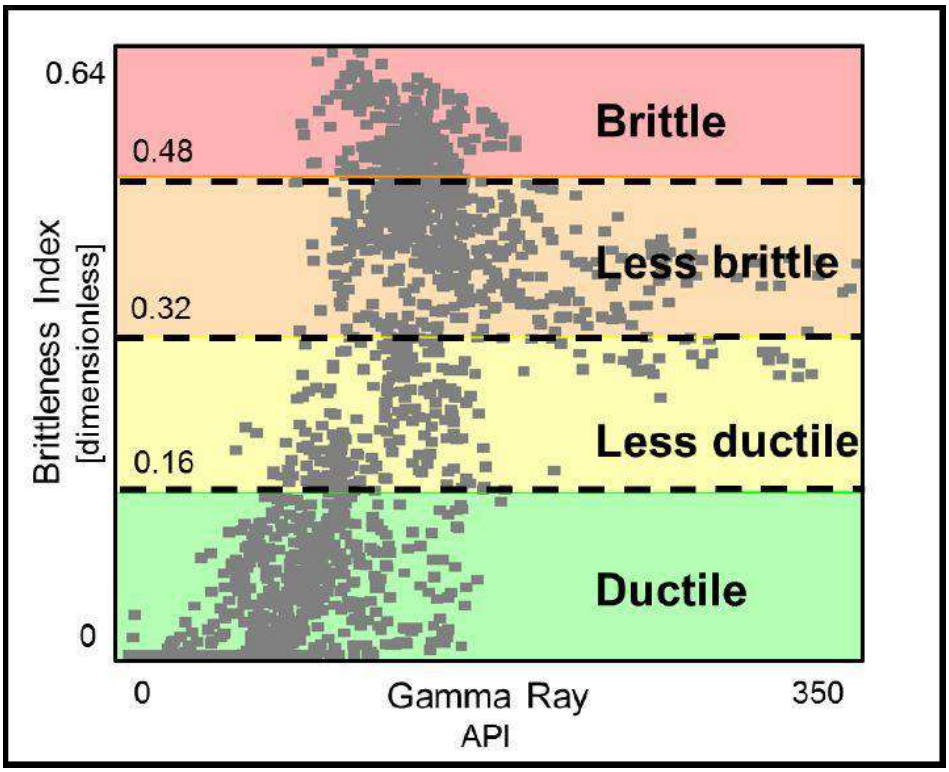

Fig. 66: *Brittleness Vs GR classification based on Perez and Marfurt (2013).*

Various brittleness indices utilized for selecting and designing hydraulic fracturing in shale gas reservoirs focus on different components of rock composition, specifically the presence of brittle or ductile minerals. These indices are derived from the ratios of the weight or volume fractions of minerals that are prone to promote brittle failure compared to those less likely to

cause such failure. These measurements can be obtained through mineralogical logging tools or laboratory X-ray diffraction (XRD) tests (Wong et al., 2021).

$$BI = \frac{W_{qtz} + W_{dol}}{W_{qtz} + W_{toc} + W_{clay} + W_{lm} + W_{dol}} \quad (28)$$

$$BI = \frac{W_{qfm} + W_{dol} + W_{cal}}{W_{tot}} \quad (29)$$

Wqtz, Wdol, Wlm, Wqfm, Wcal, Wfsp, Wclay, Wtoc and Wtot are the weights of quartz, dolomite, limestone, the weighted sum of quartz, feldspar, and mica, calcite, feldspar, clay, total organic content, and total minerals, respectively.

Shale brittleness is known to rise with higher concentrations of brittle minerals like quartz (Jarvie et al., 2007; Wang and Gale, 2009; Jin et al., 2014b; Liu and Sun, 2015). The various mineral-based brittleness indices vary based on the specific brittle minerals considered.

Two additional methods were typically used to determine the mineral-based brittleness index of oil and gas reservoirs (Sondergeld et al., 2010; Wang et al., 2015a). These models operate on the principle of calculating the brittleness index based on the ratio of brittle minerals, such as quartz and carbonate. The brittleness index is articulated through equations (29 and 30), given that feldspar is not classified alongside quartz and carbonate as a brittle mineral.

$$BI = \frac{Qz + Car + Fels}{Qz + Car + Fels + Clay} \times 100\% \quad (30)$$

$$BI = \frac{Qz + Car}{Qz + Car + Fels + Clay} \times 100\% \quad (31)$$

Qz refers to the quartz content, Fels indicates the feldspar (comprising plagioclase and K-feldspar) content, Car denotes the carbonate content, and Clay represents the total clay content by weight. A BI greater than 40% indicates brittleness, while a BI above 60% signifies high brittleness (Guo et al., 2015).

5.6. Determination of brittleness by experimental method

Over the years, various researchers have proposed numerous methods to measure rock brittleness. One of the most commonly utilized methods for direct measurement of rock brittleness has been developed by Yagiz (2009), who defined rock brittleness as the ratio of the maximum applied force on the rock sample to the corresponding penetration at that force in PPT "Punch Penetration Test" (Nejati et al., 2017).

The process of the PPT and sample preparation is shown in Figure 67. For further description of the apparatus utilized in the test procedure, refer to Yagiz (2009). He stated that the rock brittleness can be determined using the slope of the obtained force-penetration profile in the PPT. An example of such a force-penetration profile is illustrated in Figure 68. As it's shown, the slope was determined by drawing a line from the origin of the force penetration profile to the maximum applied force. In other words, the measured rock brittleness is defined as the ratio of the maximum applied force on a specimen to the corresponding penetration (Nejati et al., 2017).

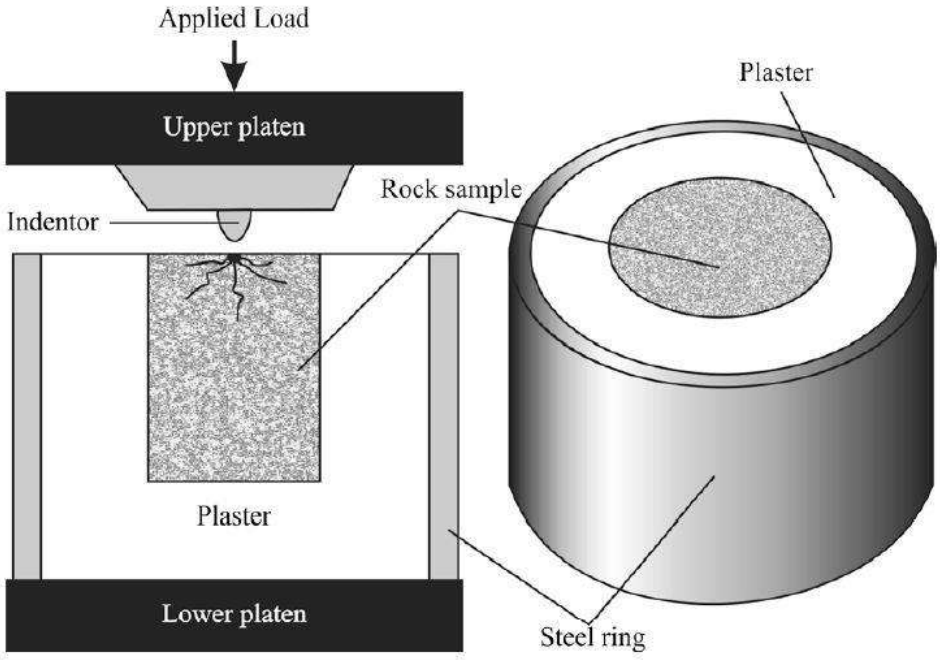

Fig. 67: *Punch penetration test apparatus and sample preparation (Yagiz, 2009).*

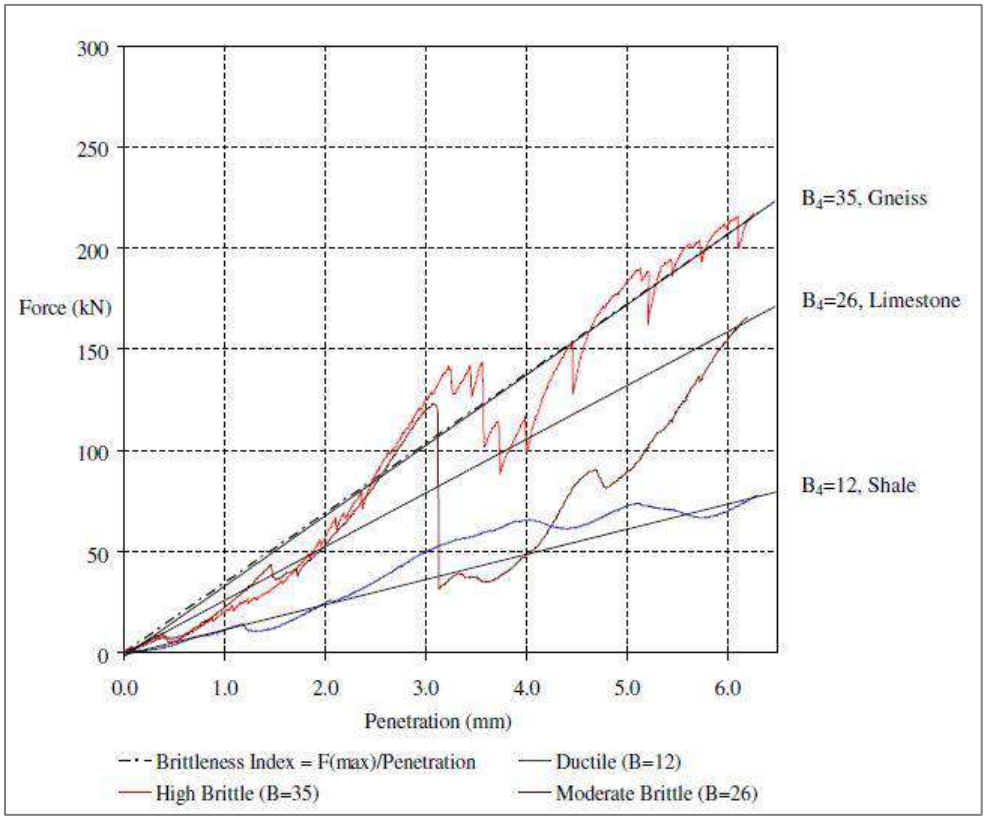

Fig. 68: *Measurement of rock brittleness using force penetration profile (Yagiz, 2009).*

$$BI = \frac{F_{max}}{P} \qquad (32)$$

BI is measured rock brittleness in kN/mm, F_{max} is the maximum applied force on a rock sample in kN, and P is the corresponding penetration at maximum force in mm. The classification of the measured BI with the punch penetration test is tabulated below (Tab. 09).

Table 09: *Suggested rock brittleness classification based on the punch penetration test (Yagiz, 2009).*

Brittleness Index (kN/mm)	Brittleness class
≥ 40	Very high brittle
35-39	High brittle
30-34	Medium brittle
25-29	Moderate brittle
20-24	Low brittle
≤ 19	No-brittle (ductile)

Conclusion

The practical implications of evaluating brittleness for shale gas reservoirs extend far beyond theoretical understanding, directly impacting extraction efficiency and operational success. Engineers can use fracturing techniques such as the Texas 2 Step frac, Zipper Frac, and Modified Zipper Frac to optimize shale gas recovery by assessing brittleness. These methods are crucial in enhancing fracture propagation and ensuring maximum reservoir contact, thereby boosting overall production yields.

Furthermore, this chapter outlines the most known methodologies for evaluating rock brittleness. These include a detailed analysis of stress-strain curves and Mohr's envelope, assessments of tensile and compressive strengths, examination of mineral composition, rock mechanical properties, and finally experimental techniques. Each method provides unique insights into the brittleness characteristics of shale formations, equipping reservoir engineers with critical data to make informed decisions on fracturing designs and operational strategies.

Overall, we aimed to comprehensively explore the significance of brittleness in shale gas reservoirs, from its definition and influencing factors to practical evaluation methods and its implications for reservoir engineering and extraction techniques.

Chapter V

Geomechanical characterization

Introduction

In this chapter, we will present the results obtained by analyzing and evaluating the different BI using two targeted calculation methods based on the available data. These results concern data analysis and characterization, as well as BI evaluation, qualification, and comparison to assess the coherence of the two evaluated Brittleness indices.

The objective is to show the two BI calculation methods' interest in shale gas characterization and evaluation, and to explore their limits related to the used data, the initial calculation equation, and the strength of the final calculation equations. The calculation methods already presented (see Chapter 04) will be applied, and this part will examine actual cases.

1. Methods

The available and existing data for the three studied wells will serve as an essential source for evaluating the rock brittleness intervals of interest along the targeted wells. These data can be analyzed and used to calculate the rock's mechanical elastic properties, EBI, and Mineralogy properties, MBI, then compare them. The data analysis was carried out to identify the shale sweet spots from the geomechanical and mineralogy point of view.

The database of the three studied wells has been used to evaluate the Brittleness index using the mechanical elastic, and mineralogy properties. This database contains wireline logs and laboratory data containing Gamma Ray, density, sonic, mineralogy, and geochemistry (see Chapter 02). The purpose is to obtain all the properties needed to evaluate the brittleness indices (EBI and MBI) along the rock intervals of interest of the three studied wells.

1.1. Mechanical elastic properties

Far from Gamma Ray data, which is highly delicate in indicating lithologies and deposit environments, equations (19), (20), and (21) for Rickman et al. (2008) are used to determine rock brittleness based on the elastic properties, Young modulus, and Poisson’s ratio (see Chapter 04). These two parameters need to be calculated based on compressive slowness (P wave), shear slowness (S wave), and rock density.

1.1.1. Gamma Ray Logging

Gamma rays are very energetic packets of electromagnetic energy (photons). In an atomic nucleus, they correspond to the transition from one quantum state to another, which is lower. This state change manifests as a photon whose energy is equal to the difference between the energies of the two quantum states. The energies of gamma rays are of the order of keV (103 eV) or MeV (106 eV). Unlike α and β radiation, gamma rays have a much wider range. The presence of radioactive elements in geological formations is often directly related to mineralogy or lithology, where the presence of Uranium indicates the presence of organic matter.

The SGR is mainly used for depth calibration of log profiles with each other, with cores, or for well-to-well correlation. The spectral information is used to calculate the CGR "non-uranium" signal by considering only the contributions of K and Th. This parameter gives more accurate information on the volume of clay present in the formations because the presence of uranium is not necessarily correlated with the clayiness (Fig. 69).

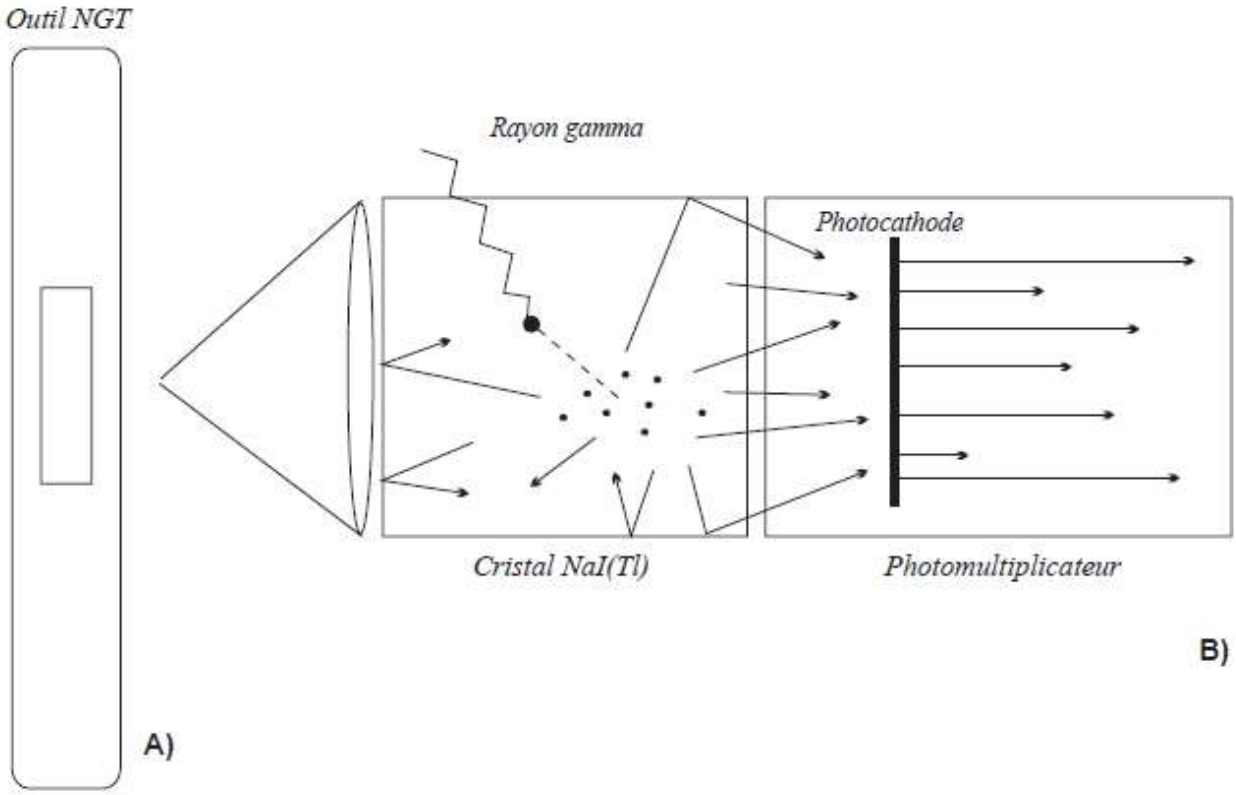

Fig. 69: *A. The NGT instrument for measuring natural gamma radioactivity. B. Detail of the detector (RABAUTE, 1998).*

1.1.2. Density Logging (gamma-gamma)

It is used to measure the density of rocks by sending gamma rays into the formation. The absorption of these rays depends on the number of electrons struck by the gamma rays (Compton scattering). The denser the formation, the more gamma rays are absorbed. It is used with Sonic to determine acoustic impedance. The measured electron density is proportional to the formation density, which depends on the density of the matrix, the porosity, and the density of the fluids filling the pores (Fig. 70).

The density of shale is usually less than 2.7g/cm3. Hydrocarbons, especially gas, have a lower density than water, which makes a formation filled with gas appear much lighter than if it were saturated with water.

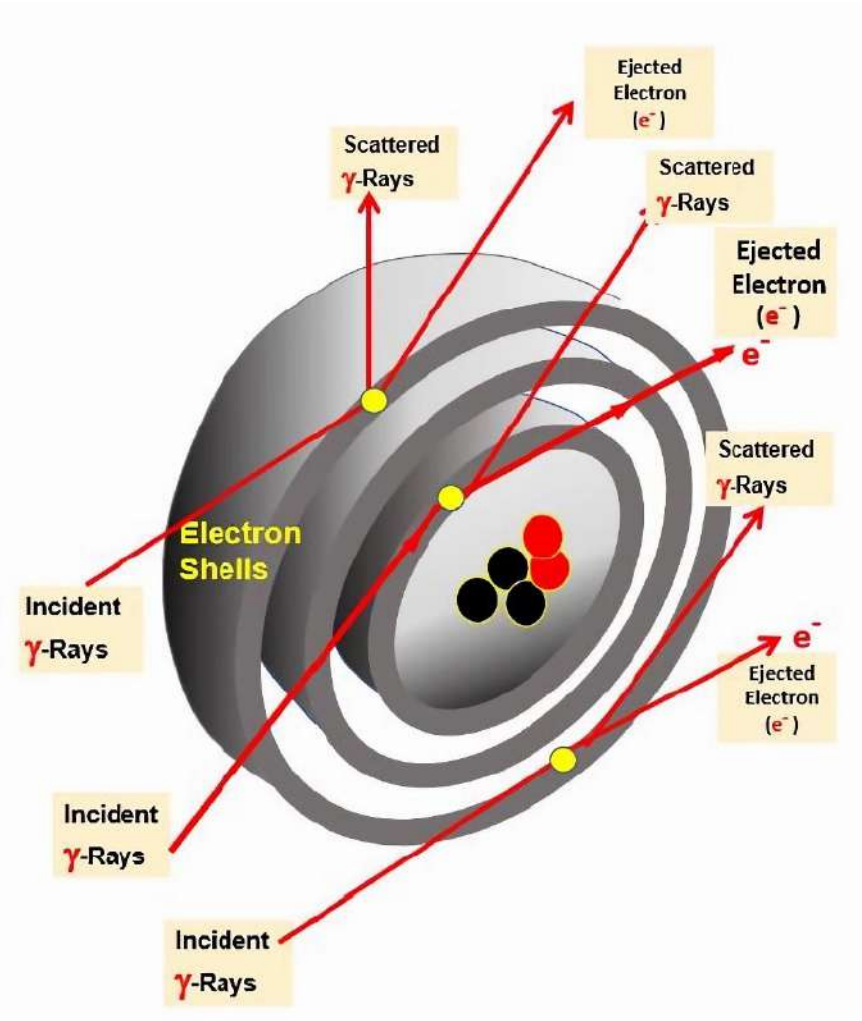

Fig. 70: *Compton scattering (Watfa, M. 2021).*

1.1.3. Velocity Logging (Sonic)

These logs are essentially based on measuring the propagation time of an acoustic wave along the walls of the well to calculate the transmitter-receiver distance. This time depends on the lithology, porosity, and the fluids in place.

In order to perform a good measurement, the sonic tool with compensation emits a wave train with an average frequency of 20 to 40 kHz. The speed of sound depends on the lithological matrix, the distribution of primary porosity, and the type of fluid in the well. Porosity slows down the sound wave, increasing the transit time Δt. However, the curve has the unit μs/foot. The measured parameter Δt is used to locate zones with abnormal pressures; given its good vertical resolution (60 cm), it is used to determine the thickness of the geological beds (Fig. 71).

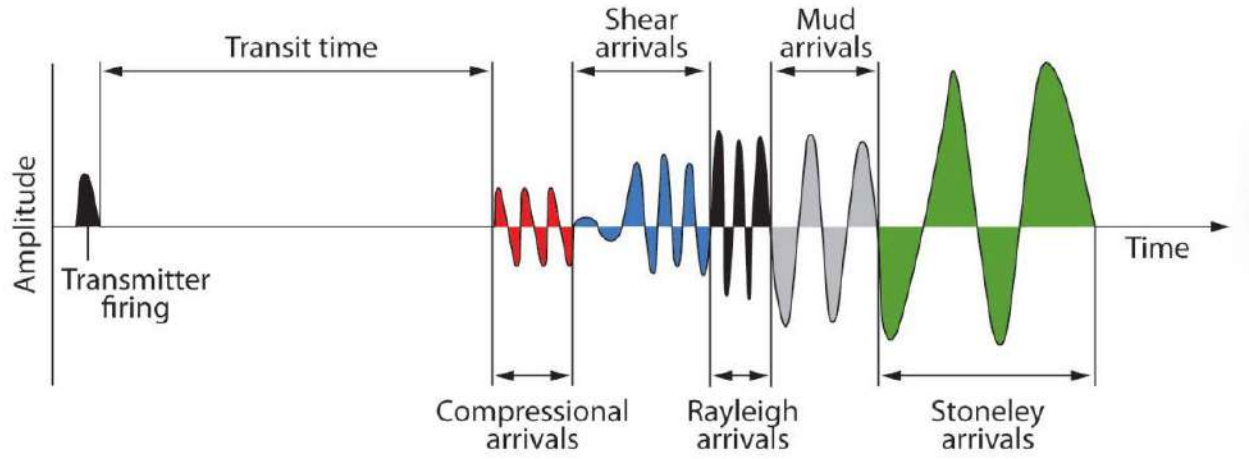

Fig. 71: *Schematic of the wave train detected at the receiver in function of time (Close, D. et al.2009).*

1.2. Mineralogy properties

After measuring the TOC (see Chapter 2), equations (24), (26), and (27) for Jarvie et al. (2007), Buller et al. (2010), and Wang & Gale (2009), respectively, are used to determine rock brittleness based on the mineral rock components (see Chapter 04). Before that, the mineralogy section should be measured by the following method:

1.2.1. X-ray diffractometry analysis (XRD)

Radio-crystallography or X-ray diffraction is the basic method that allows both the identification and quantitative description of clayey paragenesis (often present in complex mixtures of species) and the characterization of major mineralogical transitions, particularly those of the smectite-illite sequence. The equipment developed is varied, from portable diffractometers or those with easily interchangeable elements to heavy, highly stabilized sets equipped with computerized signal processing systems. X-ray diffraction is a basic method used daily. It is accepted that any crystallized body can be analyzed by X-ray diffraction because its atoms are arranged according to specific crystal planes. The finely ground solid sample (<60µm) is mounted on a suitable sample holder and then subjected to an X-ray beam to be diffracted by the reticular planes of the crystalline phases present. Indeed, there is a relationship between the angle of the diffracted beam and the reticular distance separating the planes of atoms within a crystal lattice. Bragg's law governs this:

$$\lambda = 2d\ sin\theta \qquad (31)$$

λ = wavelength of the source.

d = spacing between two successive parallel planes of the crystal lattice.

θ = angle between the incident beam and the plane's lattice.

The diffractograms, thus obtained using an X-ray diffractometer, are interpreted. The positions and intensities of the observed peaks are compared to PDF-2 and ICSD (Powder Diffraction File - Inorganic Crystal Structure Database) reference files to identify the mineralogical phases present. The quantitative analysis is carried out using the “Rietveld” method, based on a mathematical refinement of the crystallographic parameters of the minerals present in the sample. The measurement uncertainty varies from plus or minus 1 to 5% depending on the degree of crystallinity or the degradation of the structure, in particular those of clay minerals and isomorphic series (Fig. 72).

The XRD analysis conditions are cited as follows:

- *PANalytical diffractometer: EMPYREAN*, ceramic X-ray tube with copper anticathode, X-ray generator power: 40 mA, 45 kV.

- Software for data acquisition: *Data-Collector* from *PANalytical.* Software for data processing: *High-Score Plus* from *PANalytical*
- Wavelength CuKα [Å]: 1.5418.
- Start angle [°2Th.]: 2.90.
- End angle [°2Th.]: 70.0000.
- Step size [°2Th.]: 0.0130.
- Step time [s]: 122.1450.

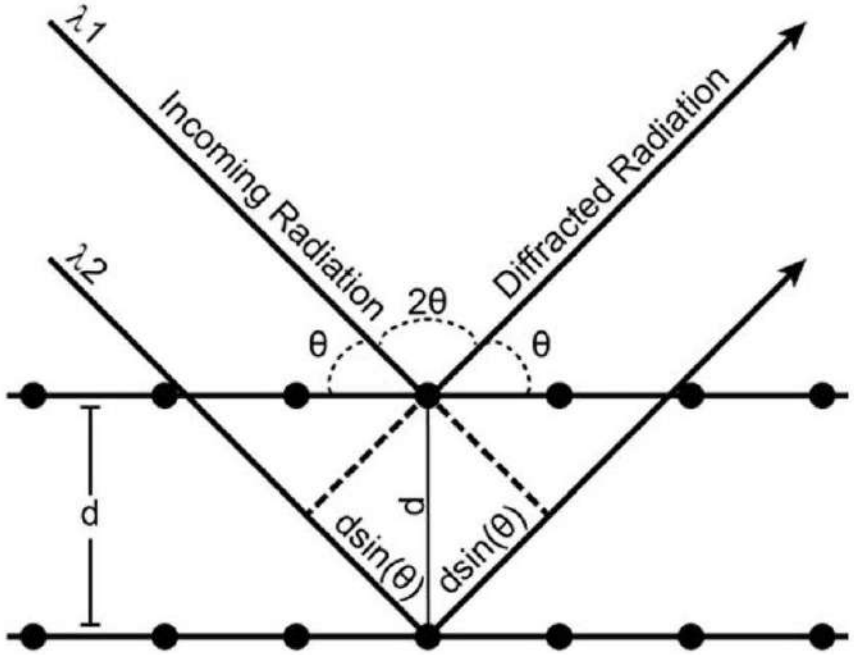

Fig. 72: *Schematic representation of Bragg's law conditions (Stan, Camelia V., et al.2018).*

2. Results and Discussion

As mentioned, a data set has been used for rock characterization and BI evaluation. A detailed initial data analysis is presented to characterize the Frasnian rock interval for each well. First, the essential log data will be used to identify the nature of the studied formation along the three wells and analyze some aspects related to the purpose of this study.

For a regional assessment in the interest of shale gas exploitation, the lateral extension of these potential areas must be perceived, depending on the availability of static and dynamic data (Tab 10).

Table 10: *Frasnian studied intervals on each well depending on available data.*

Wells	Frasnian Thickness	
	EBI Data	**MBI Data**
X1	1315-1651 (336m)	1520-1975 (455m)
X2	1501-1845 (344m)	1561-1662 (101m)
X3	1378-1724 (346m)	1572-1786 (214m)

The same data set from the three wells was used to carry out this study. It came from a large rock interval in each well. By analyzing the GR logs of the three wells presented in Figure 73, the following details have been concluded:

- Overall, the GR log of well X1 shows a stable variation compared to the other wells, X2 and X3.
- The GR values of well X1 oscillate between 116 and 230 API, which indicates a hot shale interval.
- Regarding well X2, the GR stays stable and has less than 75 API (non-shale rock) from 1500 m to 1560 m. Beyond 1560 m and until 1830 m, a significant increase in GR values is noted, which exceeds 100 API and oscillates between 125 and 775 API.
- For well X3, the GR log is stable from 1380 to 1485 m around 75 API (non-shale rock); after that, it increases to above 100 API. Two intervals, 1560-1600 m and 1625-1660 m, successively showed a GR above 200 API. The highest GR reached 340 API around a depth of 1645 m. For the depth intervals 1485-1560 m, 1600-1625 m, and 1660-1700 m, the GR oscillates between 100 and 200 API.

The GR indicates that the shale rock prone is spread in terms of depth as follows:

- Well, X1: 1315-1651 m, GR>100 API,
- Well, X2: 1560-1830 m, GR>100 API,
- Well, X3: 1485 -1730 m, GR>100 API,

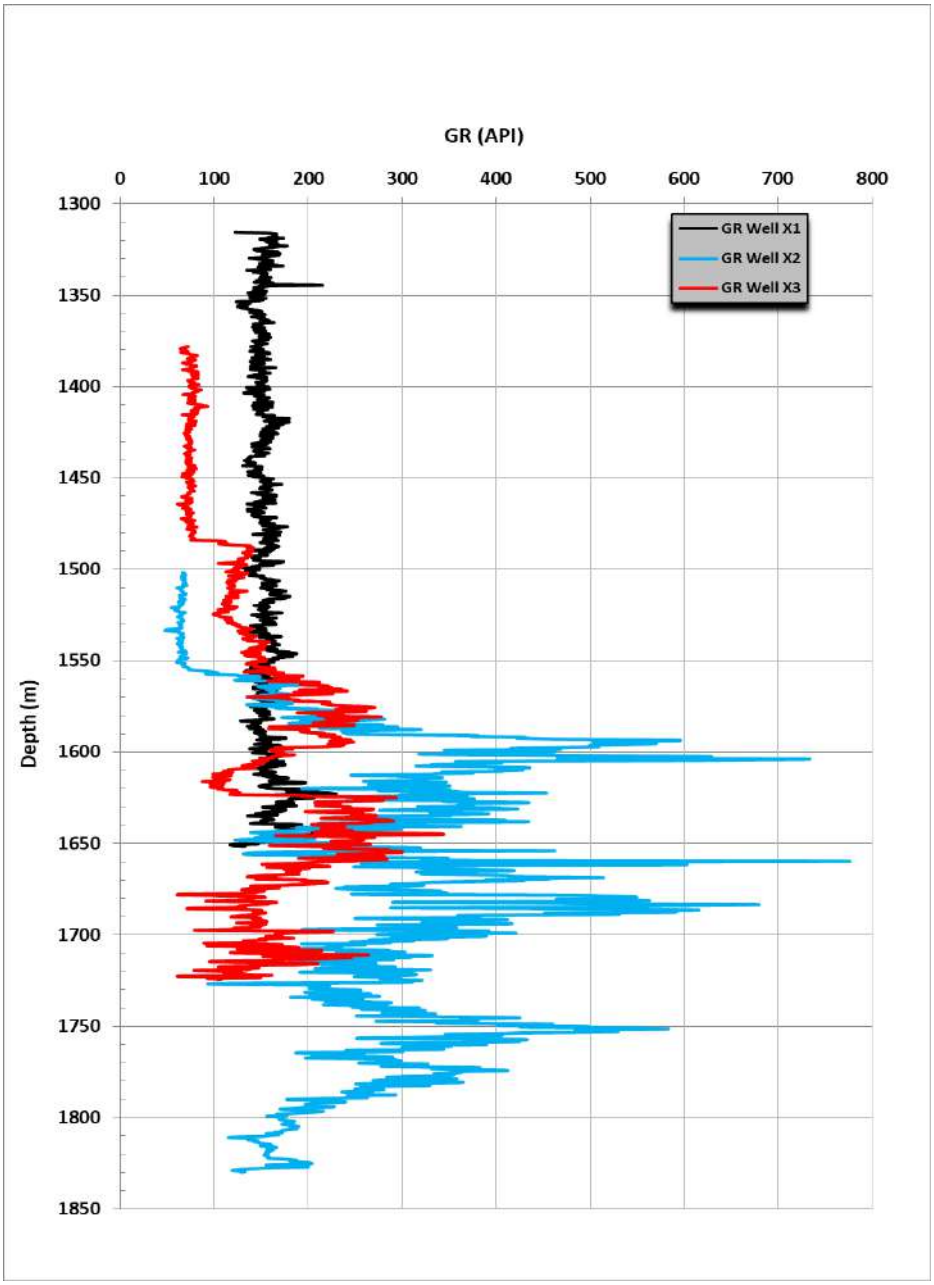

Fig. 73: *GR logs of the three wells versus depth.*

The well X1 is characterized by high GR, which remains above 140 API for the entire depth interval. The GR profile of well X1 oscillates between 140 and 200 API, and it seems more stable than wells X2 and X3. For well X2, the GR profile shows a stable tendency from the depth of 1500 to 1560 m, where the GR is slightly less than 75 API. Still, after a depth of 1560 m, the GR profile increases drastically with a considerable variation until a depth of 1830 m. This

variation of the GR profile ranges relatively between 120 and 780 API. The rock interval between 1590 and 1780 m of well X2 seems to be the most enormous GR response over the three wells.

Regarding the GR profile of well X3, from the depth of 1380 to 1485 m, the GR profile shows the same stability as well X2 in terms of GR magnitude and variation. Below the depth of 1485 m, a significant variation of GR is noted, with a considerable variation evaluated between 100 and 300 API.

According to the GR profiles shown in Figure 73, the high Gamma Ray reading varies along different layers for the three wells; the higher values potentially indicate shale-rich zones, and the lower values suggest cleaner formations, possibly sandstones or carbonates.

2.1. Elastic-based Brittleness

Several cross-plots and data comparison approaches have been established to better analyze and understand the available and calculated data. The EBI has been compared to different parameters along the studied rock interval. The parameters involved are Young's modulus, Poisson ratio, and GR.

Firstly, the data analysis will focus on EBI variation along the studied rock interval and separately in function of GR, Young's modulus, and Poisson's Ratio. Secondly, the calculated EBI will be correlated to Young's modulus and Poisson's Ratio in the GR function. Finally, the cross-plot of Young's modulus versus Poisson's Ratio will be built in the function of EBI. All these data analyses and comparisons will be applied to the obtained outcomes of the three studied wells and subsequently give a general insight into the EBI behavior.

2.1.1. Well (X1)

The EBI obtained from the data of well X1 showed basically two levels of magnitude; the first and the higher one are spread over two interval depths, from 1340 to 1420 m and from 1500 to 1600 m. The EBI of these intervals was evaluated above 85%. The second EBI magnitude level distinguished on the well X1 belongs to two rock interval depths, 1420 to 1500 m and 1660 m, at which the EBI was estimated to be between 80 and 85%. The graphs EBI versus depth are presented in Figure 74.

The main result distinguished for well X1 is that the EBI is higher even for those depth intervals where the EBI is lower. Overall, EBI ranges between 80 and 85%.

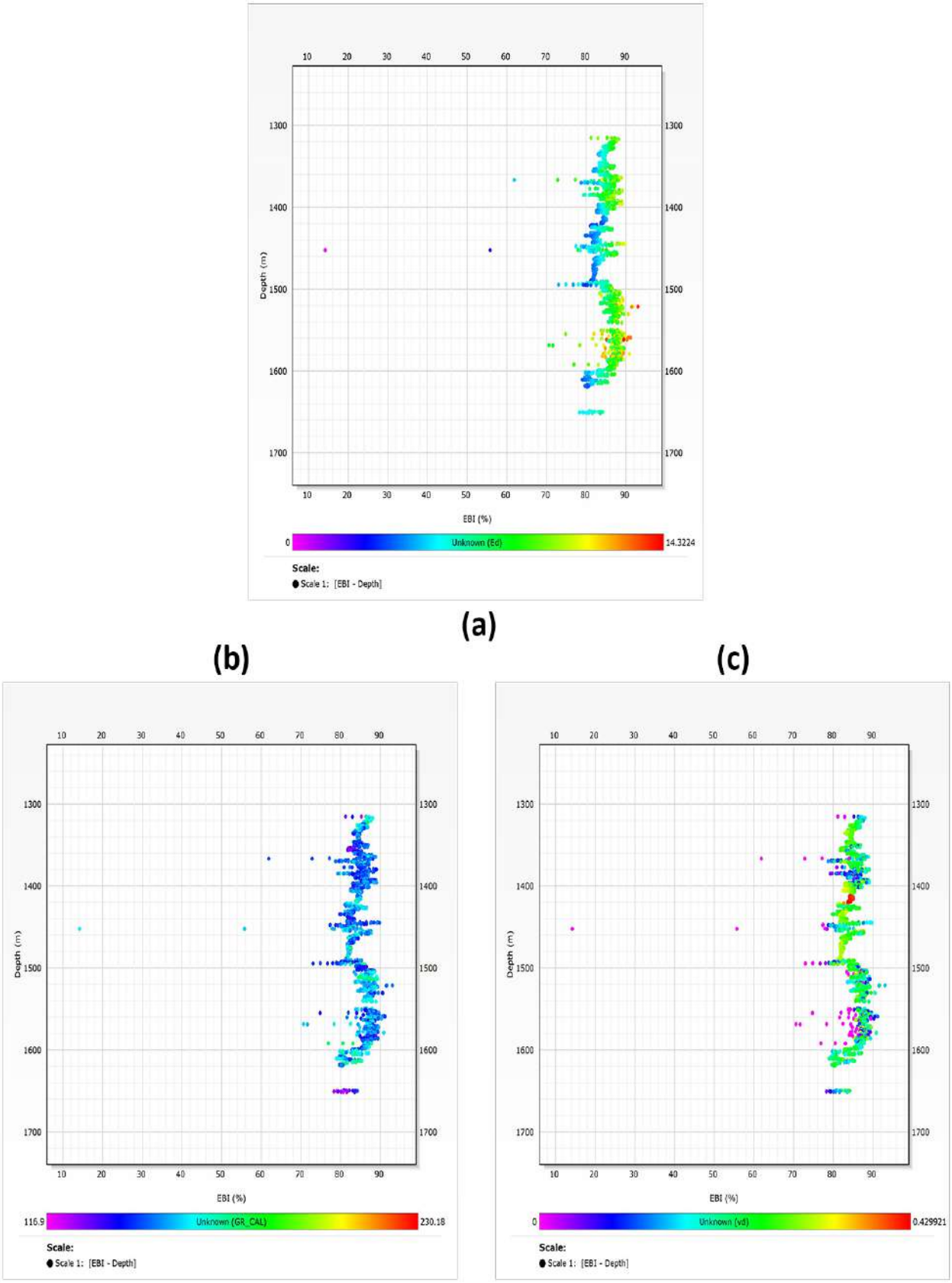

Fig. 74: *Well X1; EBI versus depth: (a), Young modulus as a reference. (b), GR as a reference. (c), Poisson ratio as a reference.*

Based on Figure 74a, the variation of EBI along the depth has shown a proportional intensity with Young's modulus. The higher EBI contained a higher Young's modulus, and the lower EBI, where Young's modulus was low. Correlating even with Poisson ratio, EBI variation has shown inverse proportional intensity with Poisson ratio; EBI is higher where Poisson ratio is lower, and it's lower where Poisson ratio is higher (Fig. 74c). The Young's modulus is estimated to range between 4 and 12 MPsi, corresponding to the Poisson ratio of 0.1 and 0.4. Based on the color spectrum shown in Figures 74a and 74c, the green, yellow, and red colors indicate the higher values of Young's modulus and Poisson ratio.

The GR was also correlated to EBI variation along the entire rock depth interval from 1315 to 1660 m; the same trend and variation noted on the Poisson ratio against EBI were noticed; the higher EBI, the lower GR, and vice versa. This trend is illustrated in Figure 74b.

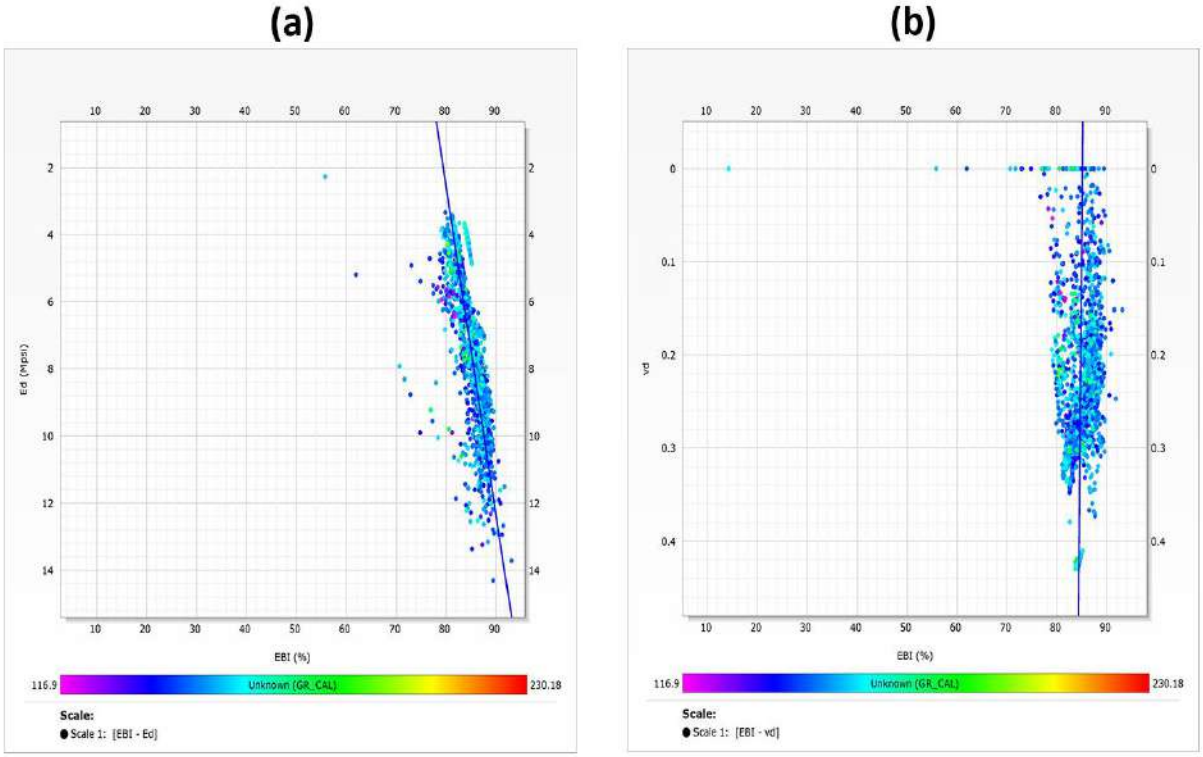

Fig. 75: *Well X1; EBI with GR as a reference: (a), depending on Young modulus. (b), depending on Poisson ratio.*

To go deeply into the data analysis, the EBI was directly correlated to Young's modulus and Poisson's ratio. The result is shown in Figure 75, where Figure 75a shows the relationship between EBI and Young's modulus, where it's distinguished that the higher Young's modulus,

the more EBI increases. This trend is also supported by the relatively low GR values (blue color). The same data cross-plot has been established on the Poisson ratio. As shown in Figure 75b, the EBI versus Poisson ratio trend is slightly inversely proportional in terms of magnitude. Still, the cross-plot is unclear due to the narrow dominance window of EBI, which is mainly between 80 and 90%. Regarding the GR, the same GR color contrast is observed in Figure 75a.

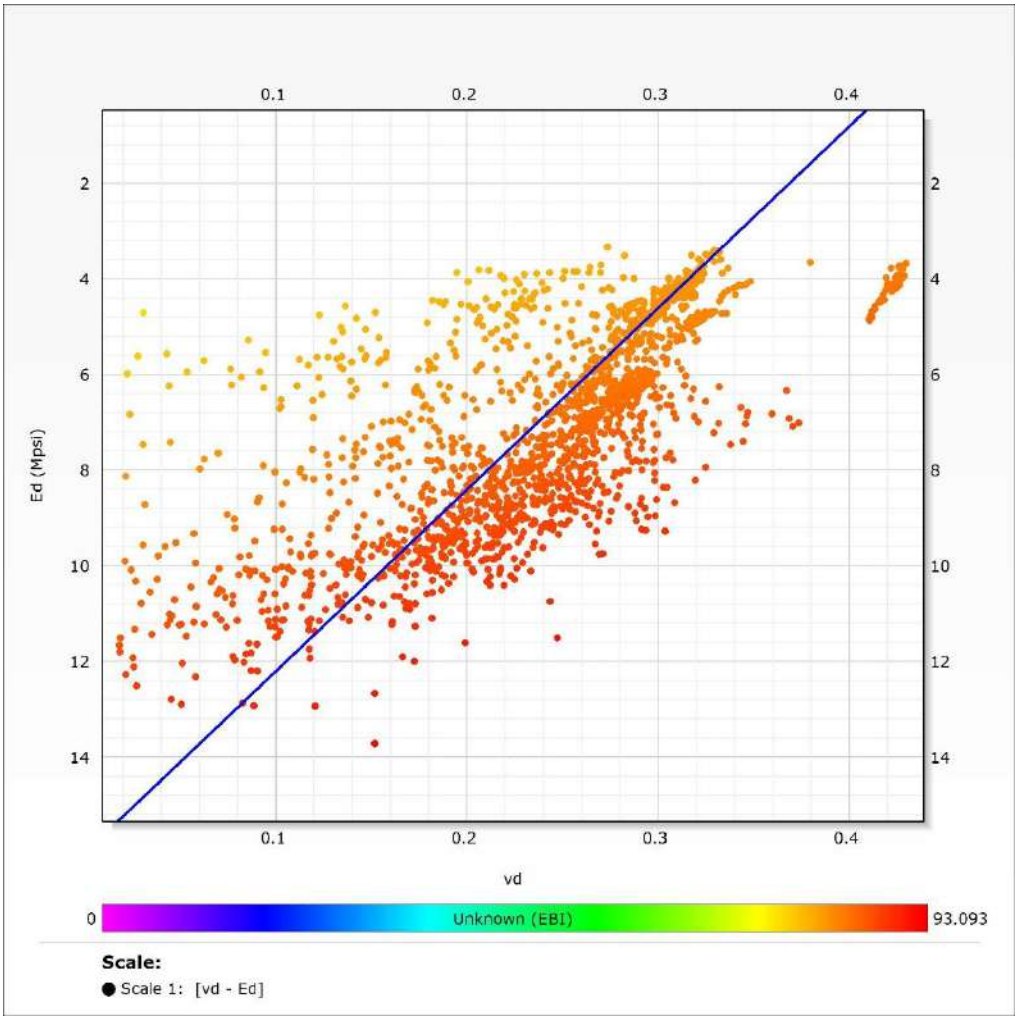

Fig. 76: *Well X1; Poisson ratio versus Young modulus with EBI as a reference.*

The consequential cross plot gathering all the data of Young's modulus, Poisson ratio, and EBI has been shown in Figure 76. A very logical trend links Young's modulus and Poisson ratio, indicating that the EBI increases from the side where Young's modulus is lower, and Poisson ratio is higher toward the side where Young's modulus is higher, and Poisson ratio is lower. A wide range of Young's modulus and Poisson ratio was obtained. On the other hand, the range of

EBI was very narrow. The more the scattering points get reddish, the more the EBI increases to higher values.

2.1.2. Well (X2)

By using the available data of well X2 to calculate EBI, the result obtained shows a wide range of EBI along the rock interval depth of the used data. Basically, the EBI ranged between 40 to 70%. The data used belong to the depth range between 1500 and 1830 m.

Along this formation depth and especially from 1500 to 1700 m, EBI is relatively found ranging between 40 and 70 %. The majority of EBI values are comprised between 50 and 60 %. Regarding the depth of 1700 to 1830 m, the EBI was mainly found between 45 and 70%, where most values are contained between 45 and 65%.

The EBI obtained from well X2 generally varies between 45 and 65%. A few EBI values go less and over these limits compared to the set of points. This spectrum of EBI could be classified as a medium EBI category.

Regarding the trend of EBI towards the Young modulus, Poisson ratio, and GR response (Fig. 77), it's clearly shown that EBI becomes higher when Young's modulus increases and Poisson ratio and GR decrease.

The cross-plot shown in Figure 77a illustrates a dominant trend where the EBI values increase with the increase of Young's modulus; this trend has an opposite variation compared to the GR response. The same cross-plot is built with the Poisson ratio (Fig. 77c); the trend between EBI and both Poisson ratio and GR has a unique dominance, leading to observe more EBI getting higher, more Poisson ratio, and GR getting lower. The same observation is noted when EBI gets lower, the Poisson ratio and GR get higher.

To strengthen the data analysis, all the calculated data of Young's modulus and Poisson ratio have been gathered in the same cross-plot and plotted in function of EBI (Fig. 79). Indeed, Young's modulus ranges between 4 and 10 MPsi, corresponding to the Poisson ratio, which varies between 0.1 and 0.35. From the EBI point of view, the scatter points show that the overall trend seems to go from the side where the Poisson ratio is bigger, and Young's modulus is lower, to the side where the Poisson ratio is lower, and Young's modulus is higher. This trend sounds reasonable for such data.

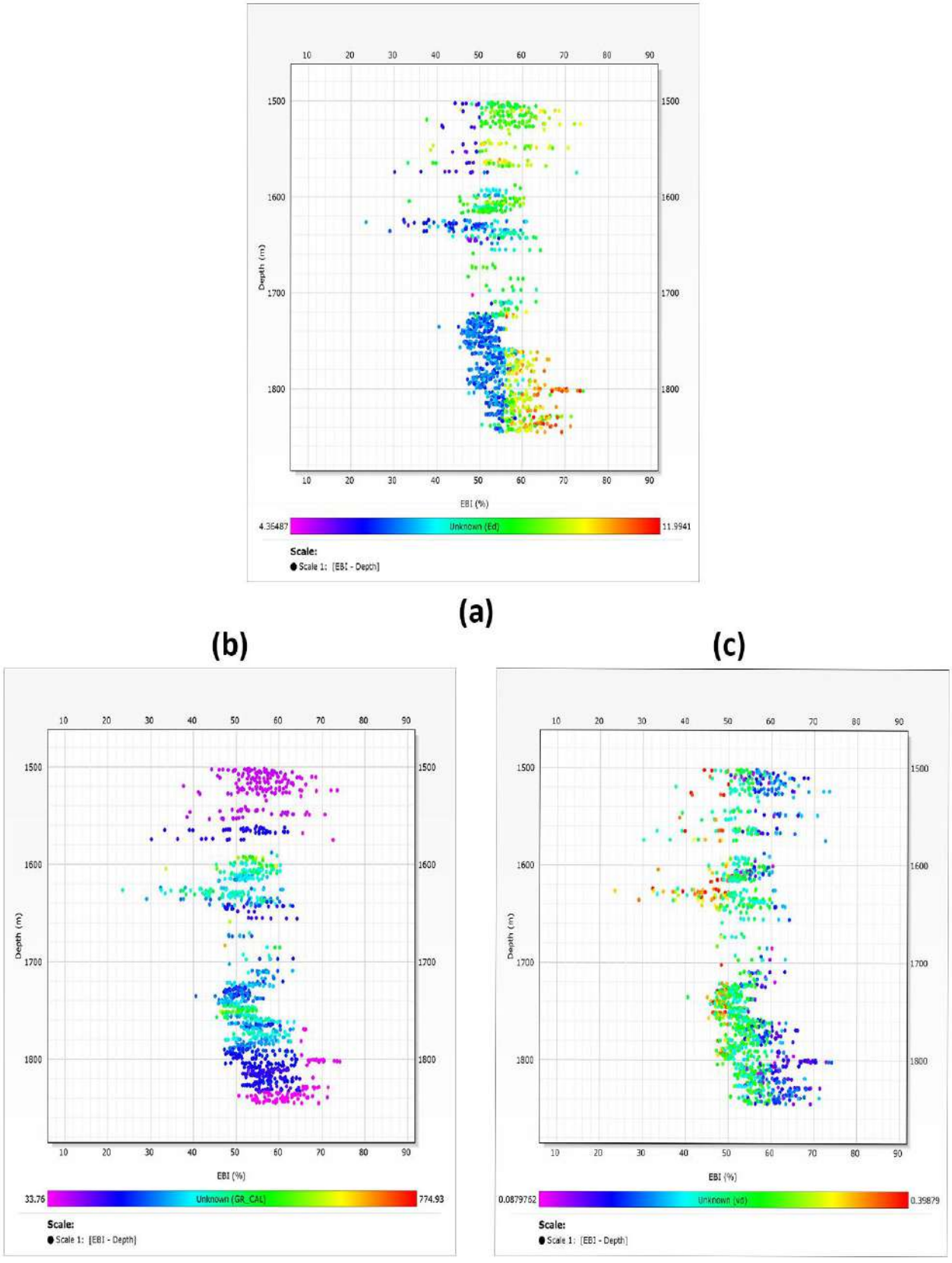

Fig. 77: *Well X2; EBI versus depth: (a), Young modulus as a reference. (b), GR as a reference. (c), Poisson ratio as a reference.*

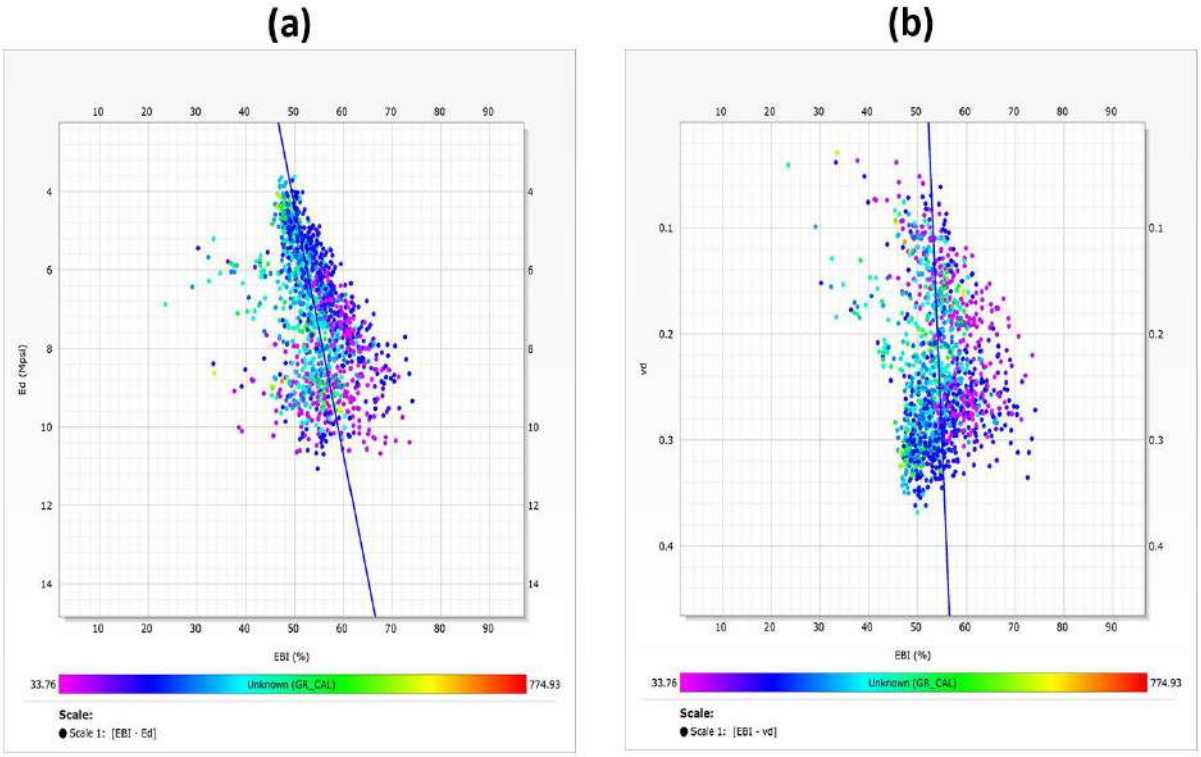

Fig. 78: *Well X2; EBI with GR as a reference: (a), depending on Young modulus. (b), depending on Poisson ratio.*

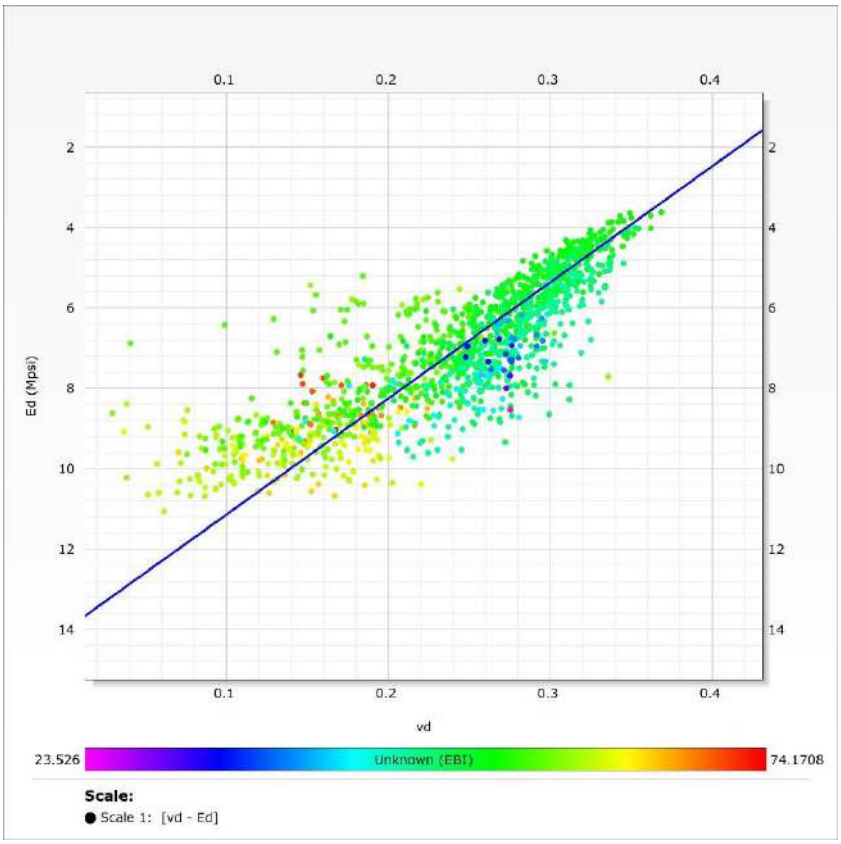

Fig. 79: *Well X2; Poisson ratio versus Young modulus with EBI as a reference.*

2.1.3. Well (X3)

Several EBI magnitude levels have been obtained on the entire evaluated rock intervals of the well X3, comprising low and high EBI. From the depth of 1380 to 1395 m, the EBI is estimated at a medium level, between 40 and 50%. The highest EBI was found between the depths 1395 and 1480 m, where the most EBI values are between 50 and 60%, with some points reaching 70%. Another medium EBI level has been found along the depth of this well, which ranges between 40 and 50% along the depth interval 1480 to 1685 m. The last part of the evaluated depth interval of the well X3 showed low EBI, which reached less than 30% for some depths. This low EBI interval belongs to the depth of 1685m to 1730 m.

The EBI of well X3 could be classified as a medium magnitude because most EBI values are between 40 and 50%.

Over the evaluated depth, Young's modulus variation has shown a good match with a corresponding EBI; the higher Young's modulus gets, the more EBI response there is. A low Poisson ratio and GR reflect this EBI evolution. The higher these are, the lower Young's modulus and EBI are. Figure 80 gives more details about the variation of EBI.

When correlating EBI to Young's modulus, the EBI tends to be higher when Young's modulus increases; simultaneously, the GR decreases. Figure 80a perfectly shows this trend, where Young's modulus ranges between 2 and 10 MPsi.

The Poisson ratio is mainly obtained between 0.2 and 0.4. This range of Poisson ratio has shown an opposite trend with EBI; nevertheless, it is the same trend with GR (Fig. 80c).

To synthesize all these data and calculated properties, Figure 82 shows an established cross plot of Young's modulus and Poisson ratio in function of EBI. The highest EBI could be classified when Young's modulus exceeds 6 MPsi, and the Poisson ratio becomes less than 0.25. The upright side of this cross-plot seems to gather the lower values of the EBI where the Poisson ratio is high and the Young modulus is low.

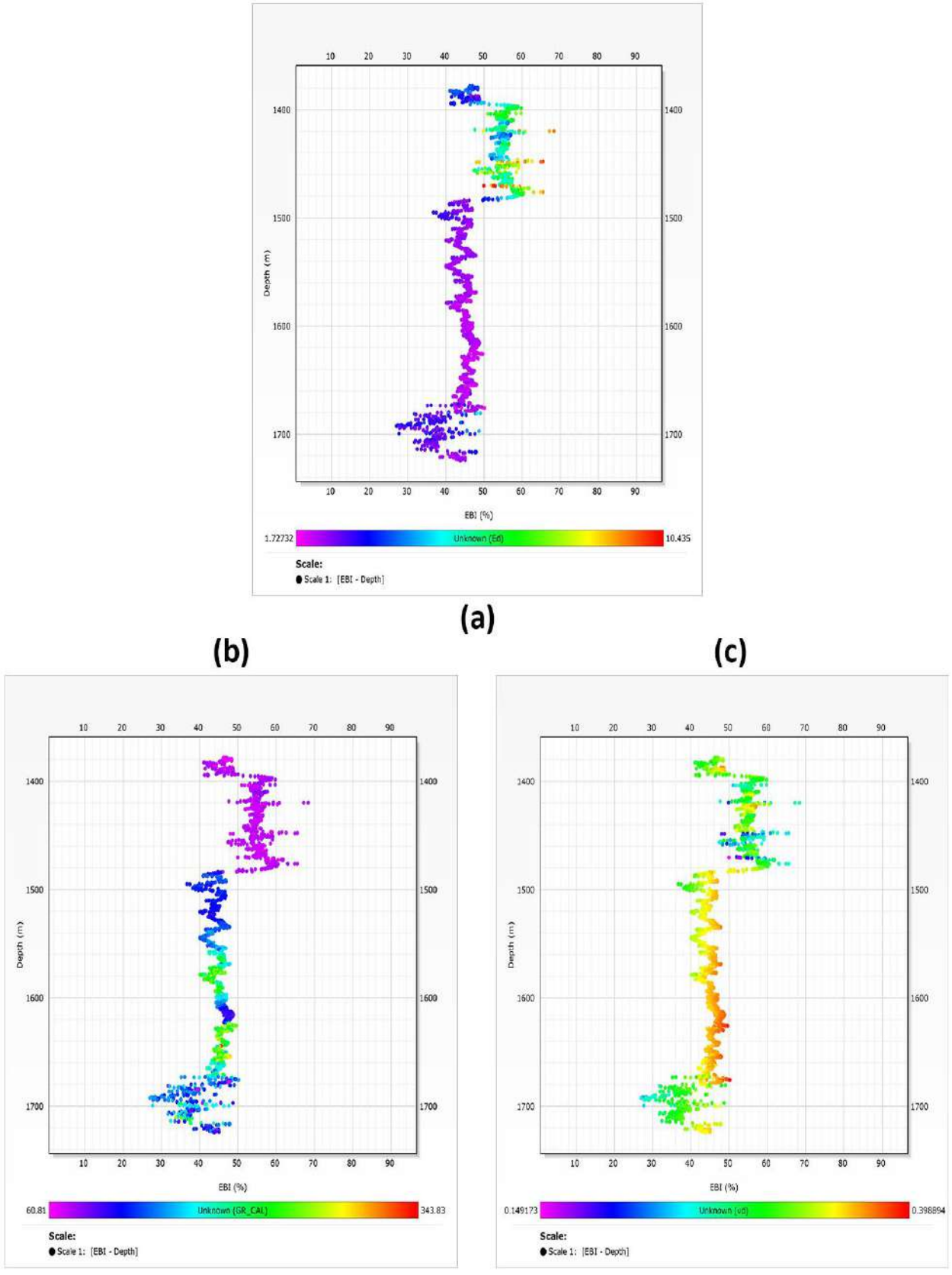

Fig. 80: *Well X3; EBI versus depth: (a), Young modulus as a reference. (b), GR as a reference. (c), Poisson ratio as a reference.*

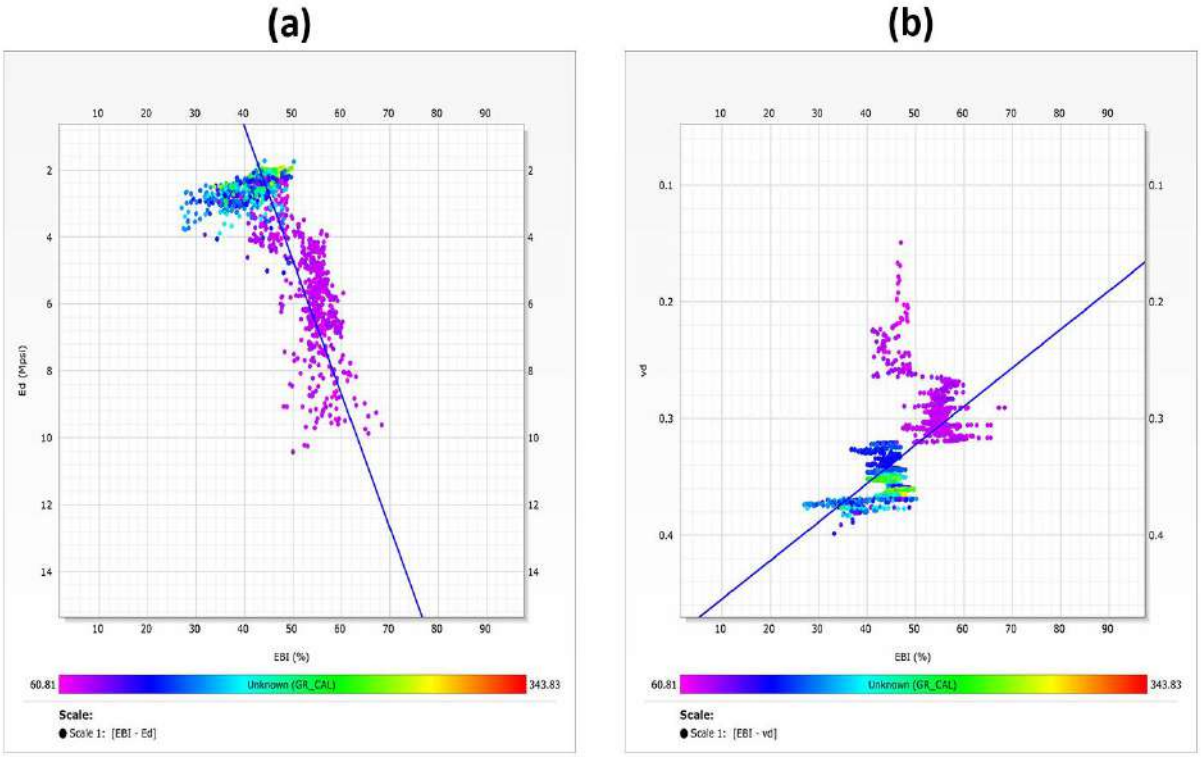

Fig 81: *Well X3; EBI with GR as a reference: (a), depending on Young modulus. (b), depending on Poisson ratio.*

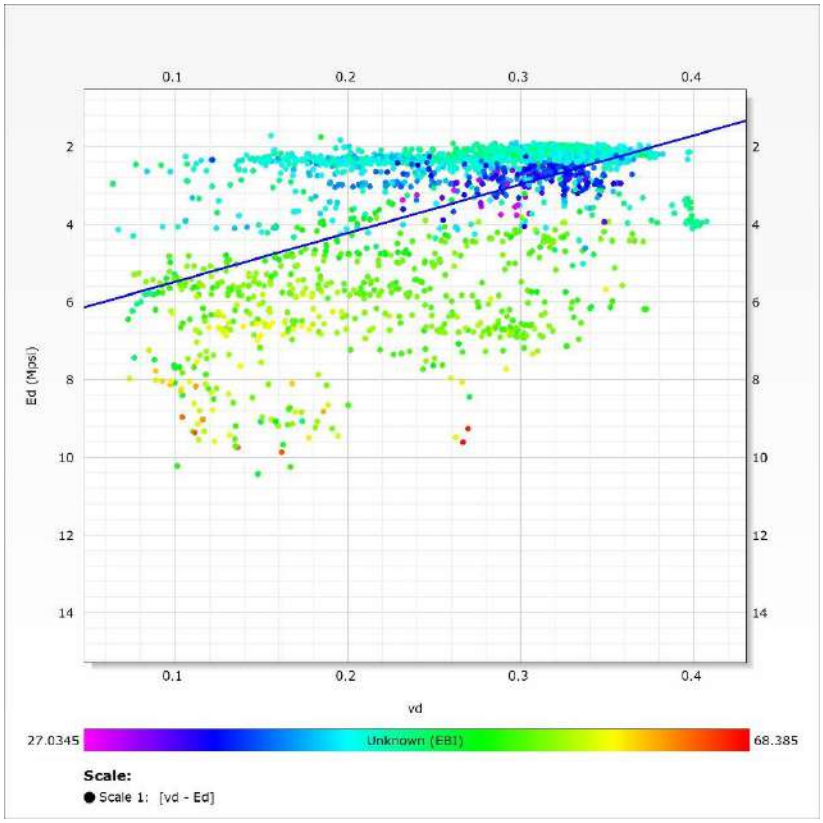

Fig. 82: *Well X3; Poisson ratio versus Young modulus with EBI as a reference.*

2.1.4. EBI comparison of the three wells

Coming to compare the EBI of the three studied wells, it's worthwhile to put the data on the same scale. To do so, the GR response was used as a data guide to select the shale rock prone to focus this approach's application only on shale layers.

Figures 83 (only shale) show the cross plots of Young's modulus versus Poisson ratio in function of EBI of the three studied wells. These cross-plots concern only the data belonging to shale rock prone, which has been distinguished based on the GR response. The shale rock has been identified based on the GR cut-off of 100 API; therefore, all rock intervals having a GR above 100 API are considered shale rock. As mentioned previously, the rock layers, including the shale rock prone (GR > 100 API), are presented as follows:

- Well X1: 1315-1651 m,
- Well X2: 1560-1830 m,
- Well X3: 1485 -1730 m.

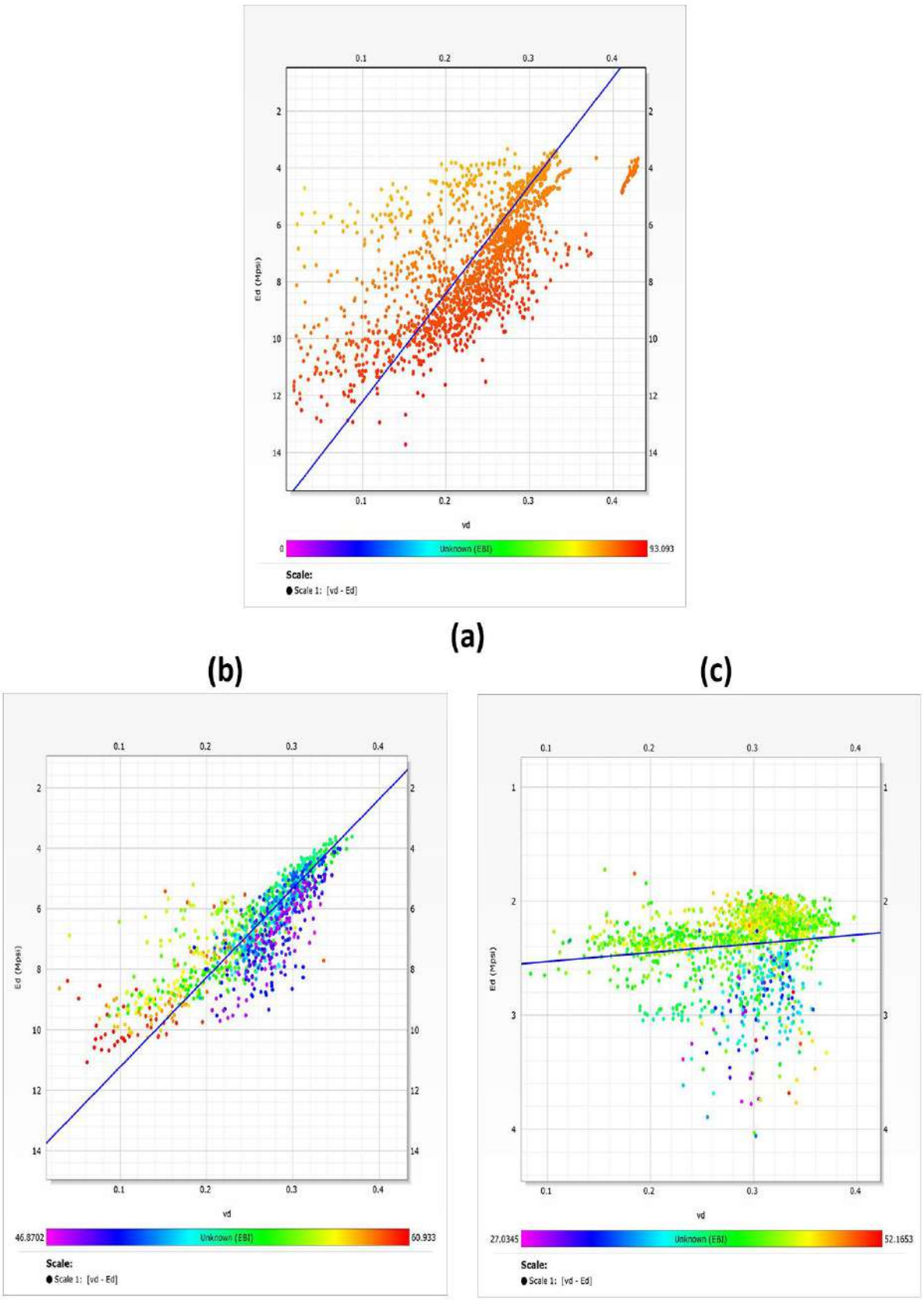

Fig. 83: *Only shales cross plots of Poisson ratio versus Young modulus with EBI as a reference;(a) well X1, (b) well X2, (c) well X3.*

The cross-plot of well X1 (Fig. 83a) shows no change compared to the previous chart built based on the available data. This is related to the data used in both cross-plots shown in Figure 76, where the whole data used belongs to the rock intervals where GR is above 100 API. The data scattering follows a logical trend linking Young's modulus and Poisson ratio, indicating that the EBI increases when Young's modulus becomes larger, and the Poisson ratio is lower. The Young's modulus was found between 3 and 13 MPsi, corresponding to the Poisson ratio ranging from 0.1 to 0.38. Nevertheless, the EBI varies along a narrow high range comprised between 80 and 90%.

For the second well X2, the cross-plot presented in Figure 83b shows a slight difference compared to that presented in Figure 79. The range of Young's modulus and Poisson ratio seems to be the same, even the scattering point's trend. On the other hand, there is a slight decrease in terms of EBI magnitude; the maximum EBI noted in Figure 83b is around 60 %, while it was around 74% when the whole data were used (Fig. 79). A narrow EBI range was obtained for this case, and it was evaluated between 45 and 60%.

The cross-plot of well X3 shown in Figure 83c illustrates a part of the data shown in Figure 82; the data scattering is mainly comprised within a narrow range of Young's modulus from 2 to 3 MPsi. The Poisson ratio ranges between 0.1 and 0.38. The trend of EBI in the function of Young's modulus and Poisson ratio seems to follow the same trend revealed in wells X1 and X2, with less consistency. The highest EBI was estimated at around 50%, with the EBI range between 27 and 52%.

The EBI trend shown in Figure 83a perfectly agrees with all conclusions indicated previously and supports even the idea that stiffer rocks tend to be more brittle. The comparison of the obtained EBI of the three wells could obviously result that the EBI of well X1 is significantly larger than that estimated for wells X2 and X3. The EBI of well X3 seems to be the lowest EBI potential of the three studied wells.

From the EBI point of view, this will undoubtedly give an immense potential for fracking well X1 rather than wells X2 and X3. This relationship is crucial for understanding the fracturing potential of the Frasnian shale formation and provides a vital insight into the geomechanical properties.

2.2. Mineralogy-based Brittleness

Before beginning the Mineralogy-Based Brittleness (MBI) analysis, it's more important to analyze the mineralogy rock components. In our case, the mineralogy analysis has been done based on ternary diagrams from mineral laboratory data. These triangular diagrams configuration gives the ability to identify the type of lithology by using the percentage of three main known minerals in nature: quartz, clay, and carbonate. Lithology is well presented in the diagrams illustrated in this section. These diagrams aim to identify the mineralogical domination part of the mixture.

The mineralogical data used in this section are obtained from laboratory XRD analyses. The ternary mineralogical diagrams established on the three wells are presented below. It is noticeable that there is an apparent mineralogical difference between the three studied wells in terms of mineral dominance and type.

The MBI profiles are plotted only along the rock intervals where the data are available (see Table 10). The data covered non-clay, clay, and organic minerals (TOC). The results obtained from this analysis are depicted as follows.

2.2.1. Well (X1)

Using the available data between 1520 and 1975 m, the mineralogical ternary diagram of the well X1 displays a range of mineralogical compositions and a varied mineral distribution with a larger presence of silica-rich minerals. Specifically, the majority of the points fall within the "Silica-dominated lithotype", and a few points are located in the "Carbonate-dominated lithotype" and the "Clay-dominated lithotype'' with more tendency to carbonates. Furthermore, this mineralogical ternary diagram clearly shows that the most analyzed samples have less than 50% of clay part. Overall, the clay part in the total tested samples comprises between 20 and 60 %.

As stated, most points fall within the silica rock-rich lithotype, where the lithotype argillaceous/siliceous mudstone is the most predominant part. The particularity of this rock interval is that it's predominated by a silica-rich tendency; at the same time, it has some tendency to carbonate lithotype. Based on this latter, this rock interval could have some geomechanical features and characteristics regarding strength and resistance to both stress and failure (Fig. 84).

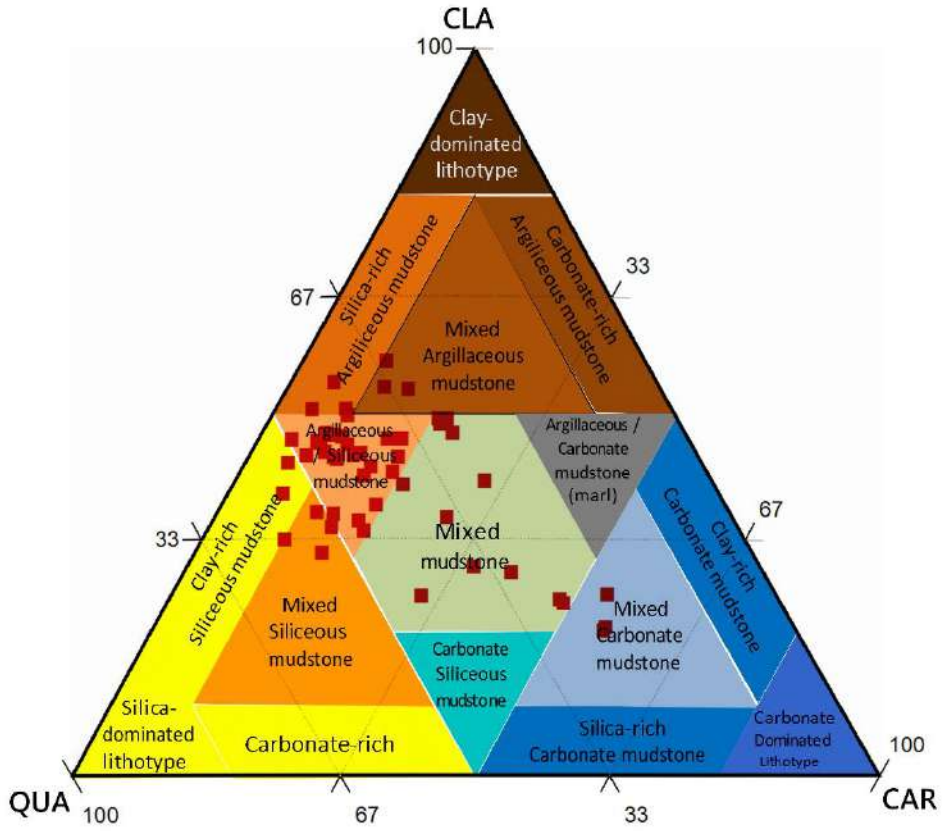

Fig .84: *Ternary plot showing the mineralogy composition for well X1.*

Buller et al. (2010) model provides a higher MBI than the other models. However, in terms of evolution, it could be noted that the three MBI models used follow the same BI trend along the entire evaluated rock depth interval (Fig. 85). Wang and Gale (2009) and Jarvie et al. (2007), MBIs follow relatively the same trend compared to Buller et al. (2010) MBI, except some tiny rock intervals of the entire evaluated rock, which could be related to a lack of data. However, Buller et al. (2010) MBI oscillates between 50 and 80%, and Jarvie et al. (2007) and Wang and Gale (2009) MBIs were respectively found between 28 and 59 % and 32 to 68%. If we base our analysis on Buller et al. (2010) MBI model, which exhibits a higher brittleness compared to the two other BI models, the first MBI magnitude level along the well X1 is the highest, comprised between 1520 and 1570 m, with MBI comprised between 60 and 80%. The second MBI level spreads between 1840 and 1980 m; it has a moderate MBI value compared to the first level, which mainly comprises between 55 and 70%. The last one is the lower MBI magnitude, which belongs to the depth interval 1570 and 1840 m, where the MBI was principally evaluated from 50 to 65%.

Above the depth of 1730 m, the MBI profiles estimated by the two models, Wang and Gale (2009) and Jarvie et al. (2007), follow perfectly the same magnitude trend. However, when the depth exceeds 1730 m, the MBI profiles of Wang and Gale (2009) and Jarvie et al. (2007) models start to separate slightly in terms of magnitude and trend. Below the depth of 1730 m, it is noticeable that the MBI of the model of Wang and Gale (2009) starts to get higher and closer to the MBI estimated by the model of Buller et al. (2010).

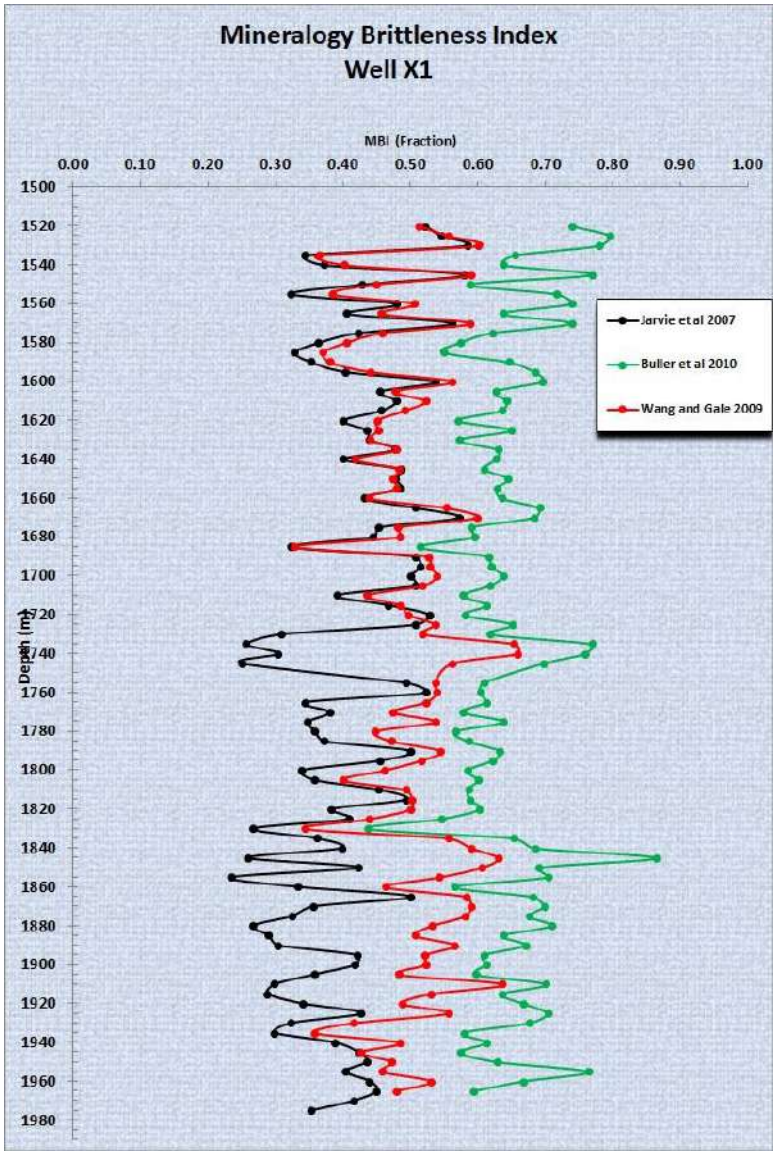

Fig .85: *Well X1, MBI versus depth.*

This phenomenon could relate to the diagenesis effect, which is sometimes associated with mineral domination and the high or low presence of organic and clay matter. In order to

understand this behavior, the mineralogy components' proportions have been plotted along the depth and presented in Figure 86. It is clear that the quartz mineral, clay mineral, and TOC have relatively stable representativeness in the rock material along the thoroughly evaluated depth; otherwise, the carbonates have a variable frequency, significantly below the depth of 1730 m. The clay portion was estimated between 10 and 35%, and the TOC showed low values.

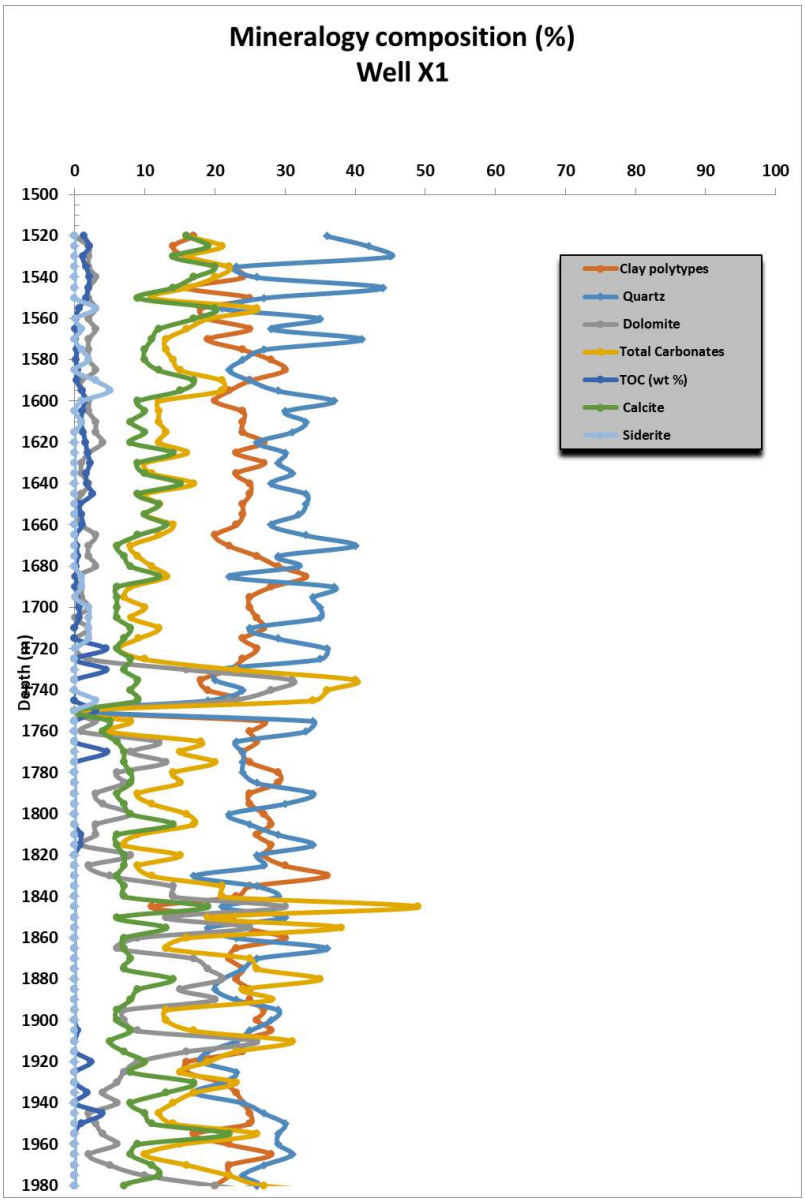

Fig .86: *Well X1, mineralogy composition versus depth.*

The representativeness of carbonates below this depth is higher than above, which has, without any doubt, a direct effect on the magnitude of MBI. However, the carbonates in this lower part are dominated by the dolomite mineral, where its proportion goes higher below the

depth of 1730 m. In some cases, it is more dominant than calcite compared to rock intervals above 1730 m, where the calcite is more dominant. Based on this latter, it could be concluded that the dolomite representativeness in the rock affects carbonates dominance in the rock, also on the MBI estimated by both models Wang and Gale (2009) and Buller et al. (2010), but more importantly on the model of Wang and Gale (2009).

2.2.2. Well (X2)

The tested samples taken from well X2 belong to the rock interval 1561 to 1662 m. The results of the data obtained have been presented in the mineralogical ternary diagram as the well X1. From a lithotypes perspective, there are principally three more representative lithotypes in this interval: argillaceous/siliceous mudstone, mixed mudstone, and mixed argillaceous mudstone. This diagram shows two noticeable mineralogical features: low carbonate presence and more clay part in the mineralogical mixture of this tested rock interval. The clay presence in this rock interval is between 33 and 67%. The silica-rich minerals are more representative than carbonate-rich minerals. The most mineralogical composition is mainly found between clay and silica prone, but this latter is the most dominant part. The more clay representative in the rock interval of this well could have little influence on its geomechanical behavior (Fig. 87).

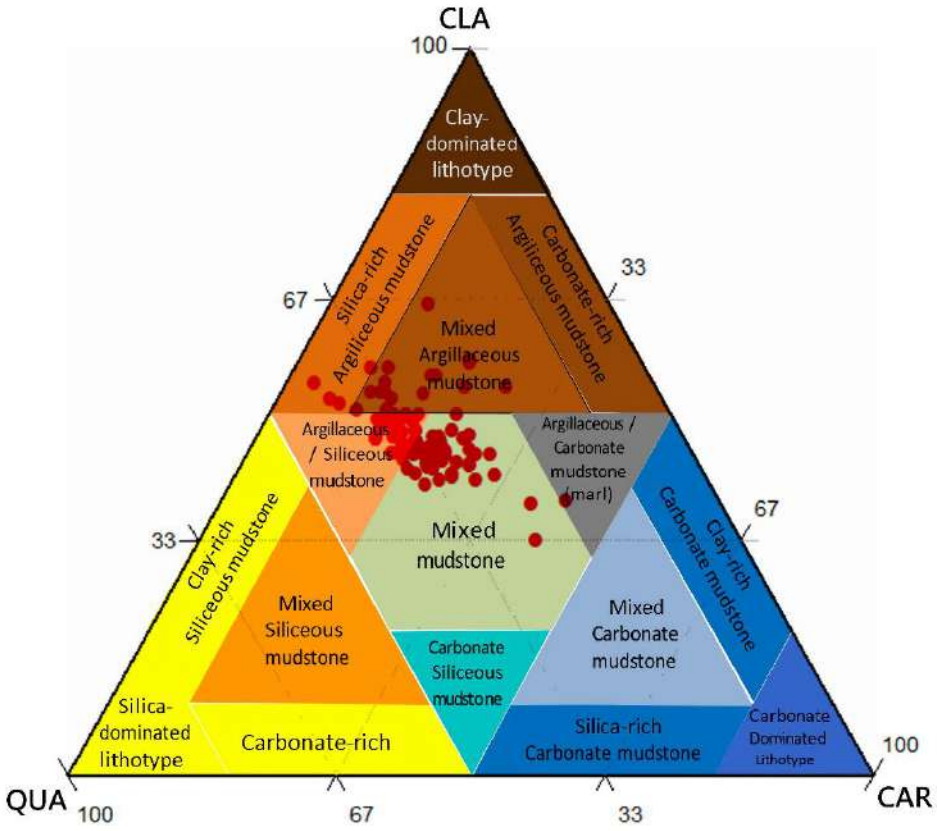

Fig .87: *Ternary plot showing the mineralogy composition for well X2.*

The MBI evaluated on the well X2 (Fig. 88) shows that the Buller et al. (2010) model provides a higher MBI compared to the other models by Wang and Gale (2009) and Jarvie et al. (2007). Buller et al. (2010) MBI was found to comprise between 40 and 73%; however, Jarvie et al. (2007) and Wang and Gale (2009) MBIs have been estimated between 22-50% and 32-70%, respectively. In terms of trend, Buller et al. (2010) and Wang and Gale (2009) MBIs follow the same evolution along the entire rock depth interval. The Jarvie et al. (2007) MBI observed almost the same trend except for some points, which obviously show distinct values compared to the two other models. Overall, if we concentrate on the Buller et al. (2010) method, there are mainly two MBI levels along the analyzed depth interval of the well X2. The first one is spread over 8 meters, from 1560 to 1568 m, where all the MBI values are less than 50%, more precisely between 32 and 50%. The second MBI level is between 1568 and 1665 m, the most evaluated points showing an MBI above 50%.

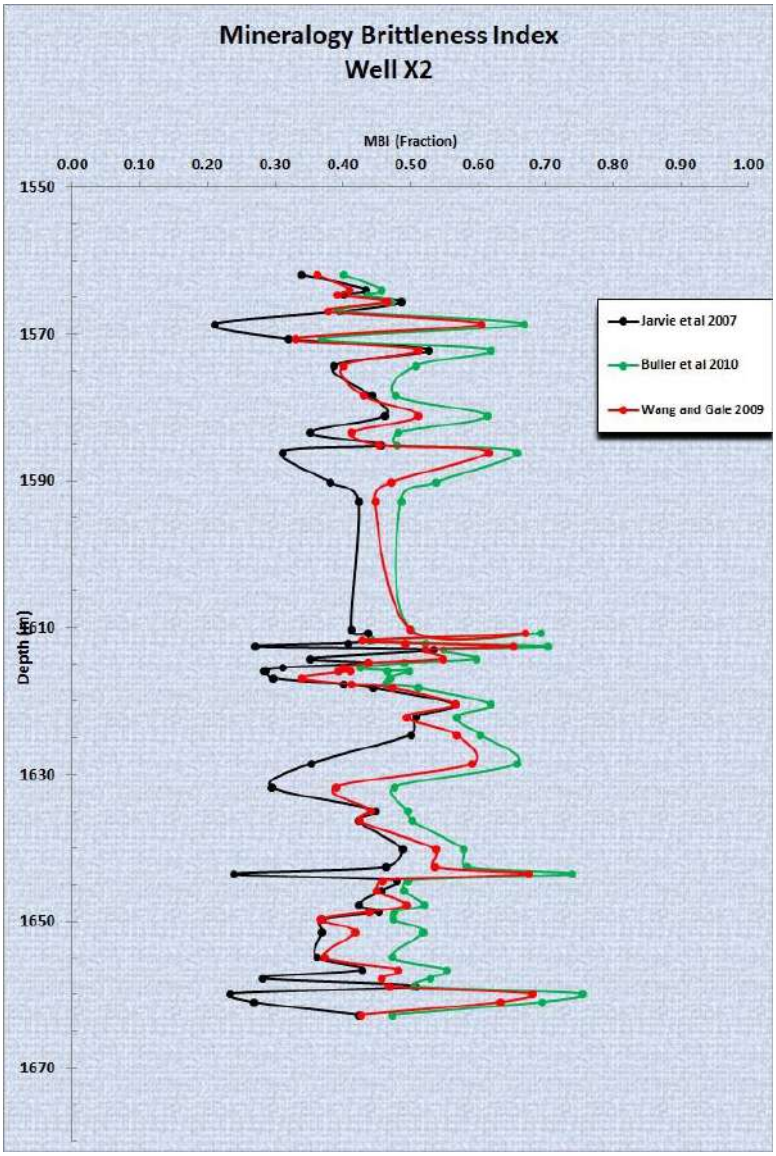

Fig .88: *Well X2, MBI versus depth.*

The trend of MBI could be correlated to different mineral proportion variations, where the proportions were more stable along the evaluated rock depth interval of the well X2. We could note that the quartz and clay proportions (between 20 and 40%) are more comparable in percentage. The TOC is more accentuated in this well with a proportion spectrum between 5 and 10%, and finally, the carbonates are dominated by calcite and dolomite with a comparative proportion. This latter could be the reason why the MBI evaluated by Buller et al. (2010) and Wang and Gale (2009) models are relatively close in terms of magnitude and trend. The graph gathering all analyzed mineral elements is presented in Figure 89.

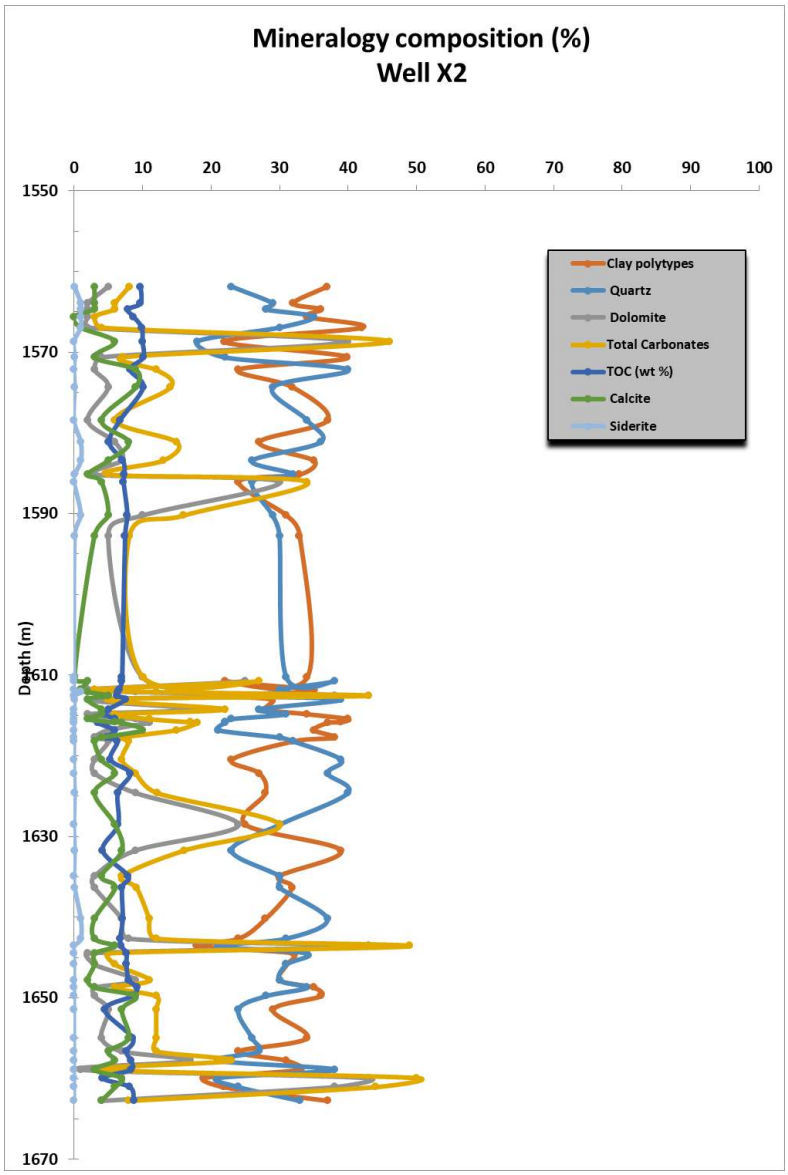

Fig .89: *Well X2, mineralogy composition versus depth.*

2.2.3. Well (X3)

The mineralogical ternary diagram for well X3, as it's done for wells X1 and X2, illustrates a lithotypes distribution dominated by clay part except for some points that have a carbonate tendency (Fig. 90). This dominance of clay reaches in some cases 80% and is mainly presented over two lithotypes, which are almost equally distributed. These latter are named Silica-rich argillaceous mudstone and mixed argillaceous mudstone, where the silica seems to have more contribution than carbonates to the mineralogical composition of the tested samples for this well. The few carbonates-rich samples are spread on three carbonate lithotypes: argillaceous/carbonate mudstone, mixed carbonate mudstone, and clay-rich carbonate mudstone.

Undoubtedly, the geomechanical behavior of this rock interval of the well X3 could be affected by the clay percentage dominance.

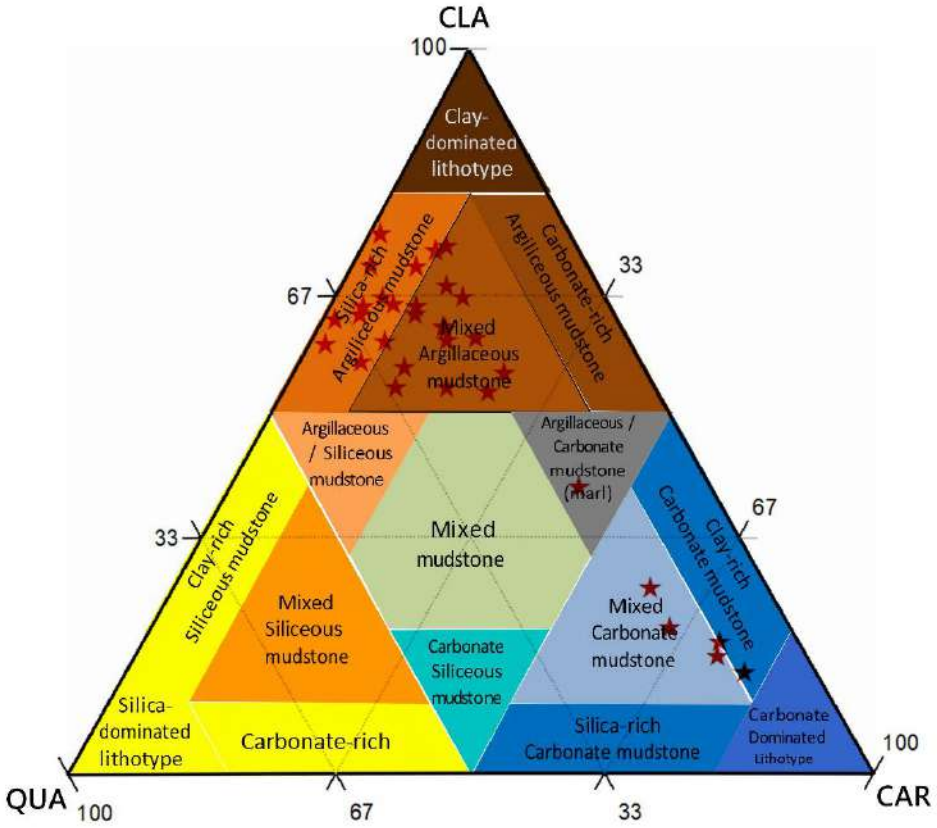

Fig .90: *Ternary plot showing the mineralogy composition for well X3.*

Regarding the MBI of the well X3, the Buller et al. (2010) model showed a higher MBI compared to Wang and Gale (2009) and Jarvie et al. (2007). The MBIs estimated by Buller et al. (2010) and Wang and Gale (2009) models are closer to each other in terms of magnitude and trend. Buller et al. (2010) model showed a wide range of MBI, which oscillated between 20 and 82%, almost the same MBI range observed in the model of Wang and Gale (2009). However, the model of Jarvie et al. (2007) showed an MBI between 10 and 40% (Fig. 91).

Overall, two MBI levels are observed in this well; the first and lower one is from 1570 to 1675 m, where most MBI values are less than 45%. Below the depth of 1675 m, a slight increase in MBI magnitude, primarily that evaluated by the two models, Buller et al. (2010) and Wang and Gale (2009), where the lower values are around 30%. Below the depth of 1675 m, Jarvie et al. (2007) showed controversial MBI values, which are relatively low.

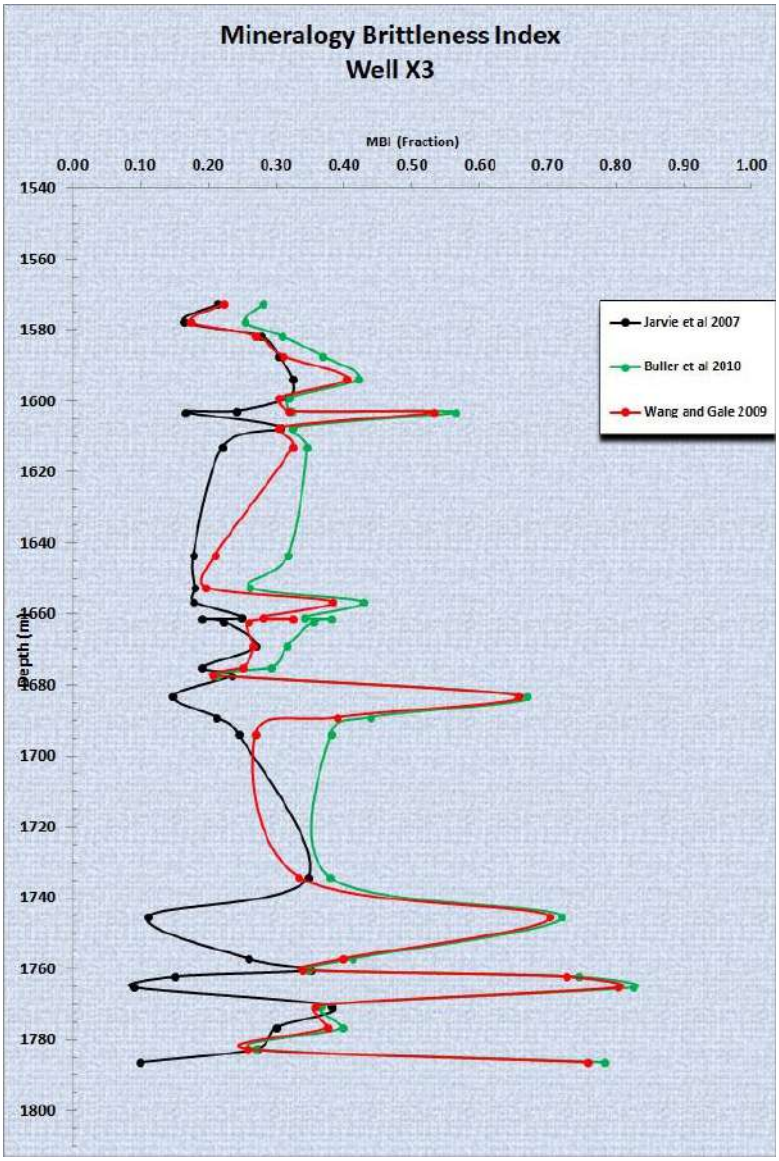

Fig .91: *Well X3, MBI versus depth.*

The mineralogy variation profile showed that the studied rock interval in well X3 (Fig. 92) has a high percentage of clay; most of the analyzed samples contain a clay percentage between 40 and 70%. A low amount of quartz has been observed compared to the previous wells. For carbonates, a low percentage has also been observed above the depth of 1675 m. However, below this depth, the carbonate proportion in the rock is higher and potentially dominated by dolomite. In some depths, the carbonate proportion exceeds 50%. However, the TOC is estimated to be between 2 and 12%. This mineralogy mixture of this well provides a low MBI magnitude compared to the wells X1 and X2; the effect of the presence of clay is highly remarkable on the magnitude of MBI.

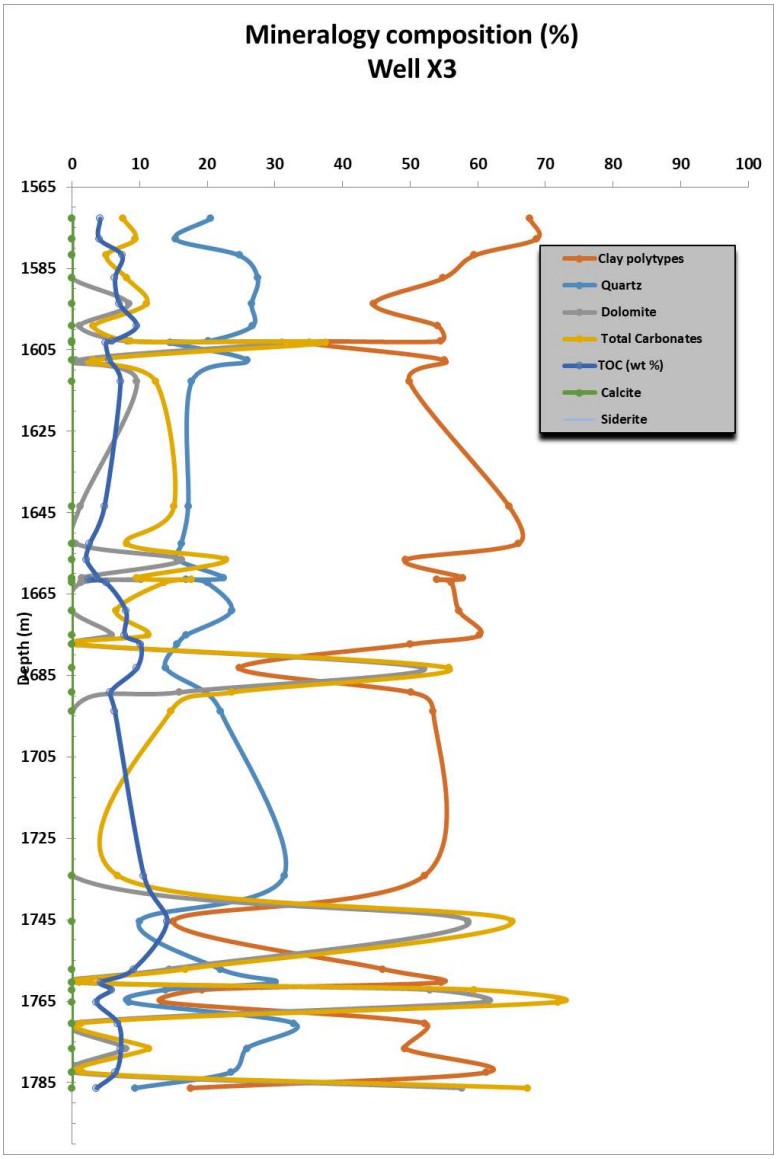

Fig .92: *Well X3, mineralogy composition versus depth.*

3. Comparison between EBI and MBI

Based on the EBI and MBI results presented previously and from a comparative perspective, it has been decided to focus only on the following comparison rock intervals:

Table 11: *Frasnian comparison intervals on both wells depending on available data.*

Wells	Frasnian Thickness		
	EBI Data	**MBI Data**	**EBI vs MBI**
X1	1315-1651 (336m)	1520-1975 (455m)	1520-1651 (131m)
X2	1501-1845 (344m)	1561-1662 (101m)	1561-1662 (101m)
X3	1378-1724 (346m)	1572-1786 (214m)	1572-1724 (148m)

From the GR response perspective, the selected rock depth intervals are characterized by the following features:

- Well X1: From 1520 to 1651 m, the GR oscillates between 116 and 230 API,
- Well X2: From 1561 to 1662 m, the GR response shows values from 110 to 775 API,
- Well X3: From 1572 to 1724 m, the GR is relatively comprised of between 100 and 300 API.

Based on this latter, all the selected intervals for the BI comparison perspective along the three wells are characterized by a very high gamma-ray response, which exceeds 100 API and is a good indicator of shale formations prone. This means that the BI comparison will be performed only on the shale-prone rock interval where both data from EBI and MBI are available.

Figures 93, 94, and 95 present the EBI and MBI profiles obtained from the available data along the selected rock interval depths of the three studied wells. These graphs give a clear insight and a general overview of the EBI and MBI comparison approach.

Focusing on Figure 93, it can be seen that the EBI and MBI obtained along the comparison selected formation interval of the well X1 show relatively good concordance in terms of tendency. Overall, the trend of MBI follows that of EBI relatively closely. Therefore, from a depth of 1520 to 1600 m, both EBI and MBI show the highest values along the entire evaluated rock interval. From a depth of 1600 m (between 1600 and 1651 m), both BIs decrease slightly. However, the EBI appears to be more stable than the MBI, which exhibits notable variations in terms of magnitude. This variation could be related to some reasons that will be discussed later. The Buller et al. (2010) MBI is the closest to EBI in terms of magnitude compared to the MBIs calculated from the two other models, Wang and Gale (2009) and Jarvie et al. (2007). Both EBI

and MBI obtained along this whole rock depth interval show the highest degree of Brittleness for this well.

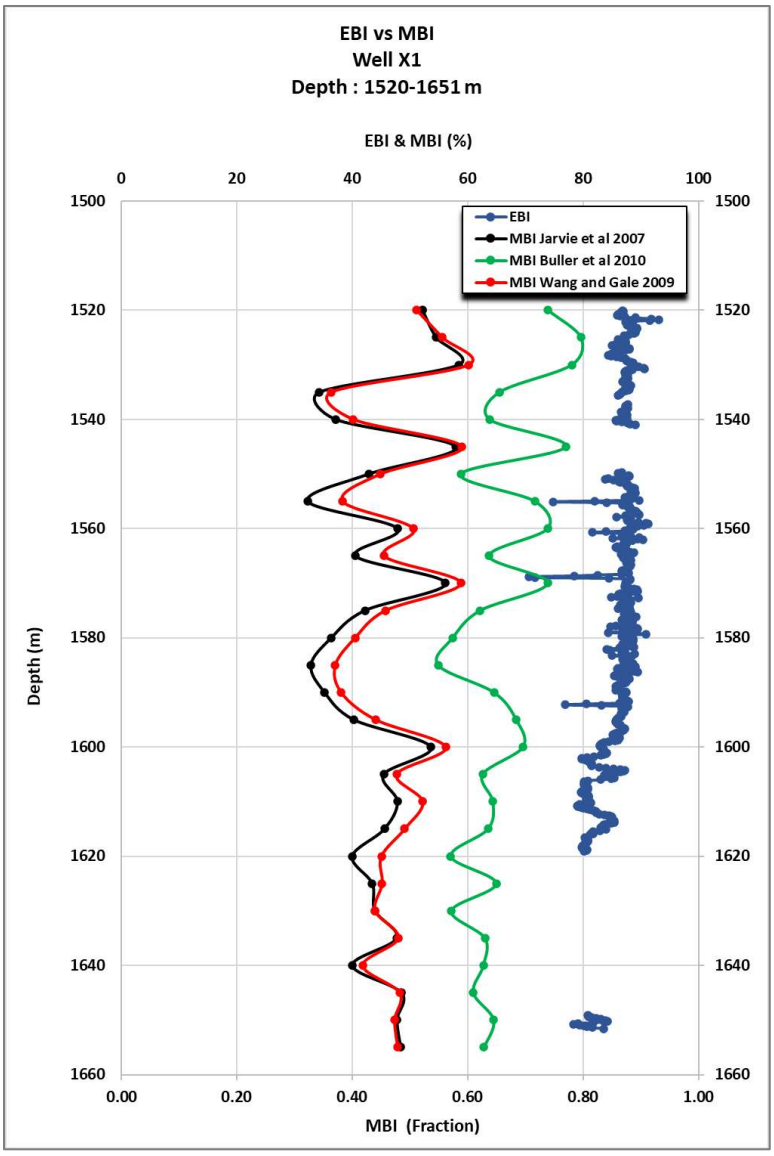

Fig .93: *Well X1, EBI and MBI profiles comparison versus depth.*

Figure 94 shows the EBI versus MBI evaluated profiles obtained from the available data of well X2. Notably, the EBI and the MBI are more comparable to the well X1, and the EBI seems even less stable. In general, the EBI and MBI values obtained from the three calculation models used are relatively close in magnitude along the rock interval from 1561 to 1662 m, especially those obtained by the model of Buller et al. (2010). This also has a reasonable

tendency with the EBI profile. For the majority of this rock depth interval, the EBI shows higher values than the MBI, especially within the interval from 1561 to 1610 m. Behind the depth of 1610 m, it's noteworthy that in some cases, MBI is higher than EBI.

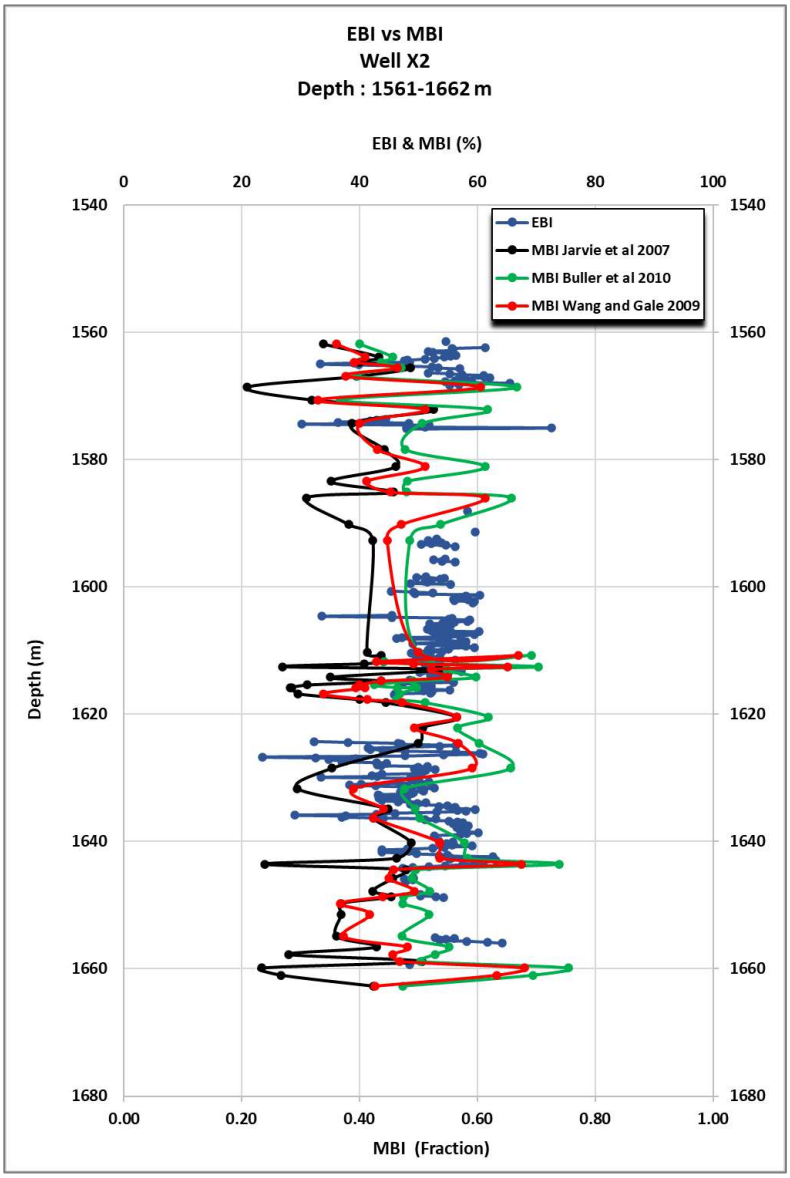

Fig .94: *Well X2, EBI and MBI profiles comparison versus depth.*

For the well X3, the EBI and MBI comparison is shown in Figure 95. In terms of magnitude, EBI appears to have a higher magnitude than MBI along the evaluated formation interval, except for some MBI-calculated points, particularly from depths of 1572 to 1680 m. As

noted for wells X1 and X2, the MBI model by Buller et al. (2010) is the most comparable model to EBI among the two other MBI models. Below the depth of 1680 m, EBI and MBI both show unstable behavior in terms of tendency; however, the MBI obtained by Buller et al. (2010) model is more comparable to the EBI than Wang and Gale (2009) and Jarvie et al. (2007) MBI models.

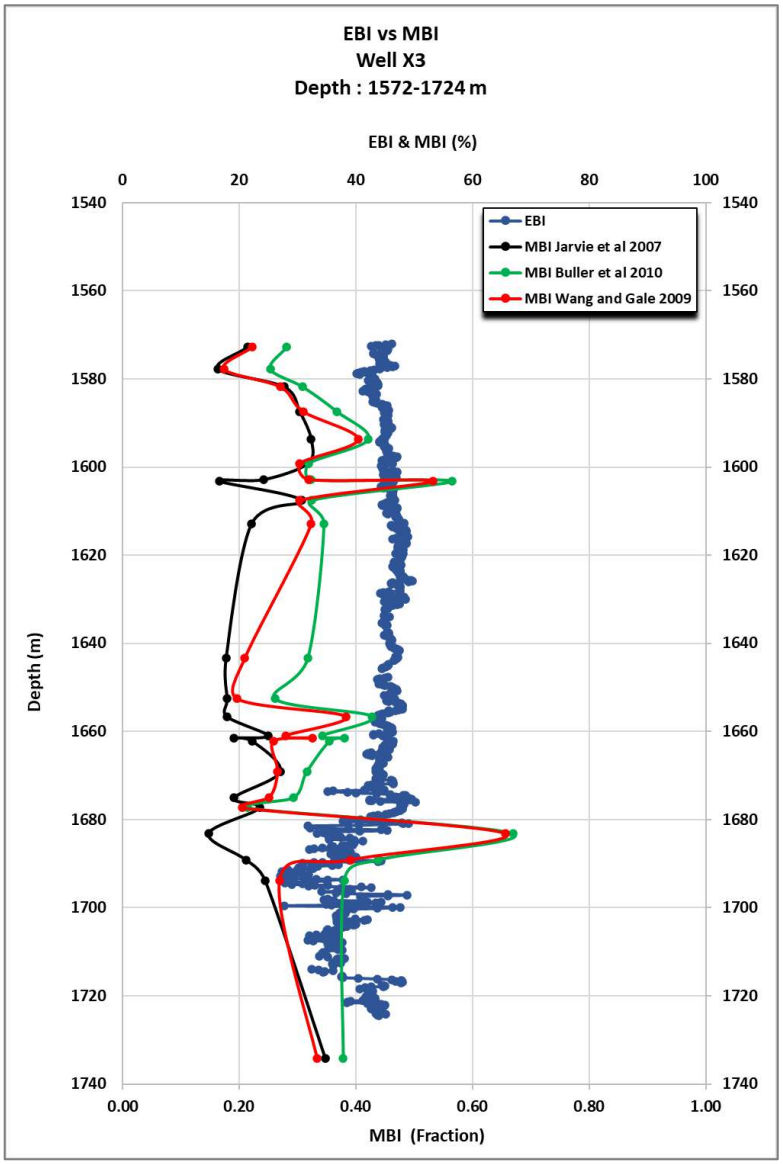

Fig .95: *Well X3, EBI and MBI profiles comparison versus depth.*

Finally, the following deductions could be distinguished from the EBI and MBI comparison approach performed on our three wells:

- The EBI and MBI of well X1 are the highest, while those of well X2 are even greater than those of well X3.
- The EBI is relatively higher than the MBI.
- The most comparable MBI calculation model to EBI is the model developed by Buller et al. (2010).
- The EBI is more stable than the MBI; this may be related to the resolution of the available data, the specificity of certain MBI calculation models, and the presence of a high percentage of clay. Additionally, the mechanical properties (Young's modulus and Poisson's ratio) are heavily dependent on petrophysical and mineralogical characteristics. Accordingly, the difference in magnitude between EBI and MBI could be significantly related to the mineralogical data in terms of composition and percentage. This fact can be observed in our case, where the MBI appears unstable (variable) from one calculation model to another and along the evaluated depth, whereas the EBI appears relatively stable. The difference in data resolution scale between mechanical properties and mineralogical data could correspondingly impact this difference and stability. Furthermore, the sampling depth of mineralogical analysis may also affect this aspect.

Conclusion

This chapter enabled us to study the Frasnian rock Brittleness along the three studied wells, X1, X2, and X3, using the available data. This BI evaluation has primarily focused on two calculation methods based on mechanical elastic properties and mineralogical data, which are referred to as EBI and MBI, respectively. Several data sets, including density, compressional, and shear slowness, have been used as input to calculate mechanical elastic properties and subsequently determine the EBI. Other data are also used to calculate the MBI. GR data were also used to analyze the main lithology of the rock facies, where different shale-rich zones were distinguished along the studied Frasnian interval of each well. Regarding the mineralogical aspect, the mineral proportion composition was the primary data used to analyze the types, dominance, and contribution of minerals, on the one hand, and to evaluate MBI, on the other hand.

The correlation of EBI with depth, GR, and mechanical elastic properties reveals that the EBI of well X1 is the highest among wells X1, X2, and X3, and that of well X3 is the lowest. The well X1 shows EBI relatively comprising between 80 and 90%. Well X2 exhibits EBI that oscillates relatively between 40 and 70%, and well X3 illustrates EBI ranging from 30 to 60%. For the shale-rich zones, well X1 have a narrower EBI window. For wells X2 and X3, EBI is relatively comprised of between 40 and 60%, 30 and 50%, respectively, for both wells.

From a rock-rich lithotype perspective, well X1 was found to be dominated by a single lithotype, characterized as silica-dominated, corresponding to quartz and clay dominance minerals, which range between 25 and 45%, 15 and 30%, respectively. The well X2 is characterized by three lithotypes: argillaceous/siliceous mudstone, mixed mudstone, and mixed argillaceous mudstone. Quartz and clay are the two main representative minerals, with proportions varying between 25 and 40%, 20 and 40%, correspondingly. Regarding well X3, two main rock-rich lithotypes have been distinguished: the silica-rich argillaceous mudstone and the mixed argillaceous mudstone. The main dominant mineral is clay, with a proportion ranging from 30 to 70%.

The MBI has been evaluated by three models, with the model of Buller et al. (2010) yielding the highest results. The MBI values of the three wells, as reported by Buller et al. (2010), vary as follows: well X1 ranges from 50 to 80%, while well X2 ranges from 40 to 73%. The MBI value of well X3 ranges between 20 and 82%. However, the EBI calculated using the model Jarvie et al. (2007) is less than that obtained from the model Wang and Gale (2009).

Finally, the comparisons made between EBI and MBI were primarily based on the available data and the results of EBI and MBI, as well as the comparative perspective and the shale rock-prone aspect. These comparisons have revealed that the EBI and MBI obtained from well X1 are the highest compared to those of wells X2 and X3; in turn, those of well X2 are even greater than those from well X3. In terms of magnitude, the EBI appears to be greater than the MBI in all studied wells, and the MBI model by Buller et al. (2010) is the most comparable to the EBI. The difference in terms of magnitude is notably lower in well X2 than in wells X1 and X3; however, the EBI stability of well X2 is less compared to the two other wells. The EBI and MBI seem to have relatively the same trend along the three studied wells.

NB:

All these deductions could be related to many reasons, such as the resolution of data, the specificity of the MBI calculation models used, the presence of a high percentage of clay, the features controlling mechanical properties (Young's modulus and Poisson ratio) as the petrophysical and mineralogical properties, the difference in data resolution scale between mechanical and mineralogical properties, and also the sampling depth of mineralogical analysis.

The MBI model should be applied in a manner that considers the available mineralogical data to prevent underestimating MBI, as the data used directly influences the MBI results.

GENERAL CONCLUSION

GENERAL CONCLUSION

1. Synthesis

The Ahnet Basin is situated in the southwestern part of the Algerian Sahara, within the western province of the Saharan Platform. This region is characterized by relatively intense brittle tectonics, which is manifested by the presence of the predominant N-S to NNW-SSE trending faults. One of the essential reservoirs in the sector is the Upper Devonian shaly deposits, where the reservoir rocks comprise the middle series of the Paleozoic. They are marked by marine sedimentation that develops along the basin. In this unconventional reservoir, three primary sequences can be distinguished, namely Frasnian, Famennian, and Strunian.

The Frasnian unconventional reservoir, known for its Black and radioactive basal shales, represents the study area and the objective of this thesis, which focuses on the application of direct and indirect methods (geochemical and geomechanical) to provide information on the shale's thermal maturity, organic richness, and hydrocarbon potential. Offering insights into the depositional environment, the source of the organic matter, and the conditions under which the organic matter was preserved, even regarding the type, abundance, and preservation state of the organic matter. Additionally, to identify hydrocarbon fluid types, the gas-oil contact (GOC) and the oil-water contact (OWC) are also taken into consideration. Furthermore, the Brittleness indices are calculated using both mechanical elastic properties and mineralogical elements to assess hydraulic-fracturing suitability, also known as sweet spots. At the end of this thesis, the main distinguished results are:

1.1. Geochemical characterization of Frasnian Hot shales

The laboratory geochemical analysis of core samples from wells X1, X2, and X3 in the Ahnet basin allows for an evaluation of the Frasnian hydrocarbon potential of these wells as follows:

Beginning at well X1, the core samples reveal moderate to excellent Total Organic Carbon (TOC) levels, indicating possible hydrocarbon sources. Nevertheless, the lack of free hydrocarbons and minimal amounts of potential hydrocarbons present challenges. The maturity indicators recorded suggest that wet gas condensate production is likely, with signs of progression towards the dry gas phase.

Well X2 exhibits good to excellent TOC contents, indicating a strong organic presence with potential for hydrocarbon generation. Like well X1, there are no free hydrocarbons, and the potential hydrocarbon volumes are low. However, maturity indicators point to a more advanced state, especially in the dry gas phase. Consequently, well X2 is more likely to produce dry gas resources compared to well X1. The rich organic material and high maturity hint at a more promising hydrocarbon potential for well X2.

In contrast, well X3 displays core samples rich in organic matter, with an average TOC content of 7%. However, this richness does not translate into high petroleum potential, as both free and residual hydrocarbon potentials are low. The primary organic composition is marine type II (proximal). Maturity analysis indicates that the organic matter has reached an advanced stage, suggesting potential for gas or dry gas, as evidenced by a thermal alteration index (TAI) ranging from 3.5 to 4.5. Although the organic matter appears rich, its usability as a source rock is restricted due to its decayed condition, likely resulting from high heat flux associated with deep magmatic activity (Takherist and Hamdi, 1995).

1.2. Geochemical evaluation of Frasnian Hot shales

The gas ratio method used in the Mud-logging chromatography technique for wells X1, X2, and X3 has revealed a significant deduction:

According to the interpretation provided by Haworth et al. (1984), and regarding the gas phase as a transitional state between the dry gas phase and the wet gas phase (condensate). Well X1 indicates the presence of two fluid types: wet gas and dry gas. In contrast, well X2 contains only one fluid type: dry gas. Similarly, well X3 encompasses two fluid intervals consistent with those found in well X1: wet gas and dry gas.

The above results align with 92% of the findings from the geochemical characterisation chapter. This suggests that the Gas ratio method is the most effective way to determine the maturity stages of the Ahnet Frasnian shales following laboratory analysis. Additionally, the use of this method is strongly recommended, particularly for saving time and money.

1.3. Geomechanical Characterization of Frasnian Hot Shales

This chapter examined Frasnian rock brittleness in wells X1, X2, and X3 using two calculation methods: Elastic Brittleness Index (EBI) based on mechanical properties and

Mineralogical Brittleness Index (MBI) based on mineral data. Various datasets, including density, compressional, and shear slowness, were used for EBI calculations, while mineral composition data were used for MBI. GR data helped analyze lithology and identify shale-rich zones across the wells.

Well X1 showed the highest EBI (80-90%) among the three wells, followed by well X2 (40-70%), with well X3 having the lowest values (30-60%). In shale-rich zones, X1 had a narrower EBI range, whereas wells X2 and X3 exhibited EBI ranges of 40-60% and 30-50%, respectively. Mineralogically, X1 was dominated by a silica-rich lithotype comprising quartz (25-45%) and clay (15-30%). Well X2 contained three distinct lithotypes with quartz (25-40%) and clay (20-40%). Well X3 presented two main lithotypes with clay as the dominant mineral (30-70%).

Three models were used to evaluate MBI, with Buller et al. (2010) serving the highest results. X1 (50-80%), X2 (40-73%), and X3 (20-82%). The Jarvie et al. (2007) model produced lower values than the Wang and Gale (2009) model. Comparisons between EBI and MBI revealed that well X1 had the highest values of both indices, followed by X2, then X3. EBI consistently exceeded MBI across all wells, with the Buller et al. (2010) model yielding results the most comparable to those of EBI. Well X2 showed the slightest EBI-MBI difference but displayed less EBI stability compared to the other wells. Overall, EBI and MBI exhibited similar trends across all three wells.

2. Perspectives

After gathering all the results obtained from the analysis made mainly on two disciplines, geochemistry and geomechanics, the following deductions could be made in order to come up with the specific conclusions regarding the best treated sweet spots along the three studied wells. However, from the reliability point of view, some of the data used in this study were correlated to the available core data, as well as the volume of shale, the TOC, and the Tmax. Nevertheless, a good match was noted between the correlated log and core data. Only the rock interval showed a shale prone, which was taken into consideration in this final analysis and evaluation, distinguished by the GR response magnitude when exceeding 100 API.

The composite logs data presented in Figures (96, 97, and 98) give, on the one hand, an overview and a quick look at the evaluated sweet spots along the studied Frasnian interval and

distinguish, on the other hand, the best rock interval of interest in terms of potential and suitability for hydraulic fracturing.

Regarding the well X1, two interesting intervals could be distinguished along the studied Frasnian interval (Fig. 96), the first and the shallower interval comprises between 1520 m and 1550 m, and the second one is located between 1595 m and 1650 m. The first interval has a moderate TOC comprises relatively between 1 and 2.5% which is a mature rich rock if we consequently consider the other geochemical parameters value (Tmax and TAI), relatively low percentage of clay and a high Brittleness Index with the presence of Gas. The second rock interval is located between 1595 m and 1650 m, where relatively good sweet spots are distinguished by a TOC of above 1%, mature organic matter and the presence of two fluids located above and below the depth 1630 m, the upper side is gas rich and the lower part is condensate rich. A slight decrease in the Brittleness Index is observed in this rock interval compared to the first one; however, its magnitude is still high. The volume of shale is even relatively low for most parts of this rock depth interval, except for two narrow parts from a depth of 1616 m to 1630 m, and from 1639 m to 1648 m.

Along the studied depth of the well X2, whose composite data is shown in Figure 97, a good stability in terms of sweet spots is relatively noted along the whole evaluated rock depth interval. The TOC was found to comprise between 4 and 10%, which could be qualified as a very rich rock with a mature nature, referring to Tmax and TAI results. From a BI point of view, this rock section has shown a moderate BI that still could be interesting values for fracking. The Vsh exhibits a relatively low percentage except for the rock interval between 1590 m and 1612 m, where the Vsh exceeds 50%. Therefore, except for this latter interval, the entire rock depth interval of the well X2 could be an interesting shale reservoir.

Finally, well X3 exhibited different features compared to wells X1 and X2, which made their unconventional petroleum interest less important and less promising. Indeed, on the one hand an excellent TOC has been evaluated along the studied rock interval comprising relatively between 2 and 10%, however, this organic matter has shown an immature nature making this organic matter poor of hydrocarbon potential where only five measuring points had a Tmax above 435 °C, the overwhelming majority of the measuring points are below the lower bound of the temperature defining the organic matter maturity (435°C) (Kracha, 2011). This immaturity makes the hydrocarbon potential of this shale source rock poor, especially regarding the adsorption and

absorption gas potential, which are the primary gas production source for shale gas rock. Furthermore, the Vsh seems high compared to the two other wells, especially for the rock intervals located between 1572 m and 1598 m, and 1624 m and 1672 m. The rest of the whole rock interval (where the Vsh is lower) is paralyzed on the one hand by the immature nature of organic matter and on the other hand by the low BI evaluated lower than 50% for the entire studied rock interval and significantly below a depth of 1680 m.

Overall, the characterization and evaluation study has been made on the available data of the three studied wells, X1, X2, and X3, which allowed us to conclude that wells X1 and X2 are better than well X3 in terms of petroleum potential and fracking suitability. This conclusion could give a general vision and insight into the exploitation and development of the Frasnian reservoir in the Ahnet region of these three wells. However, a deep investigation and study should be considered before any prior strategic decision.

The characterization and evaluation presented in this thesis are based only on some sweet spots where the data have been within our reach. The best way to conduct a shale gas characterization and evaluation study is to take into account not only the data used in our work; other useful data should also be considered to covert other important aspects and potentially strengthen, on the one hand, the quality of the study and, on the other hand, the decision-making.

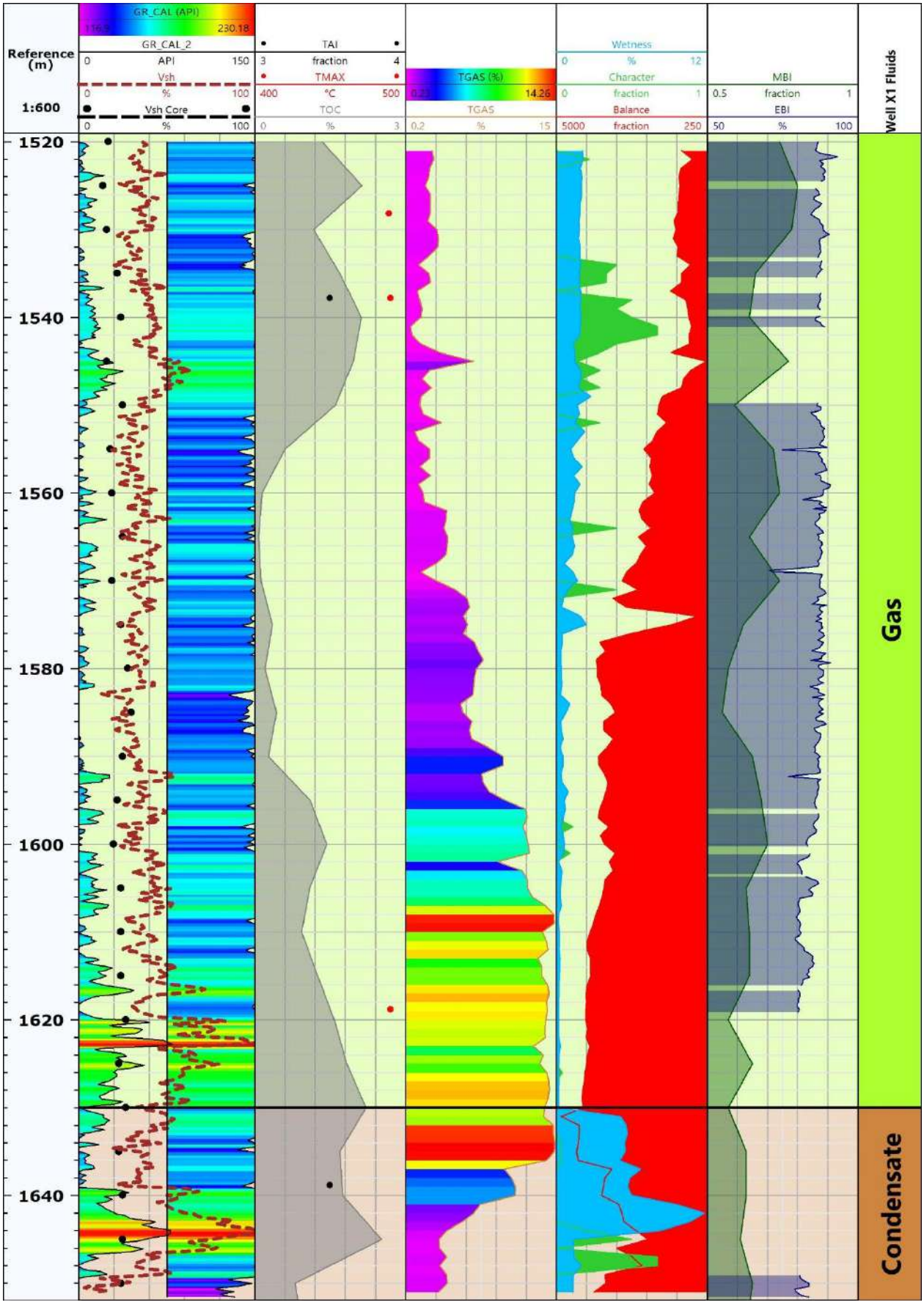

Fig .96: *Well X1, composite log versus depth.*

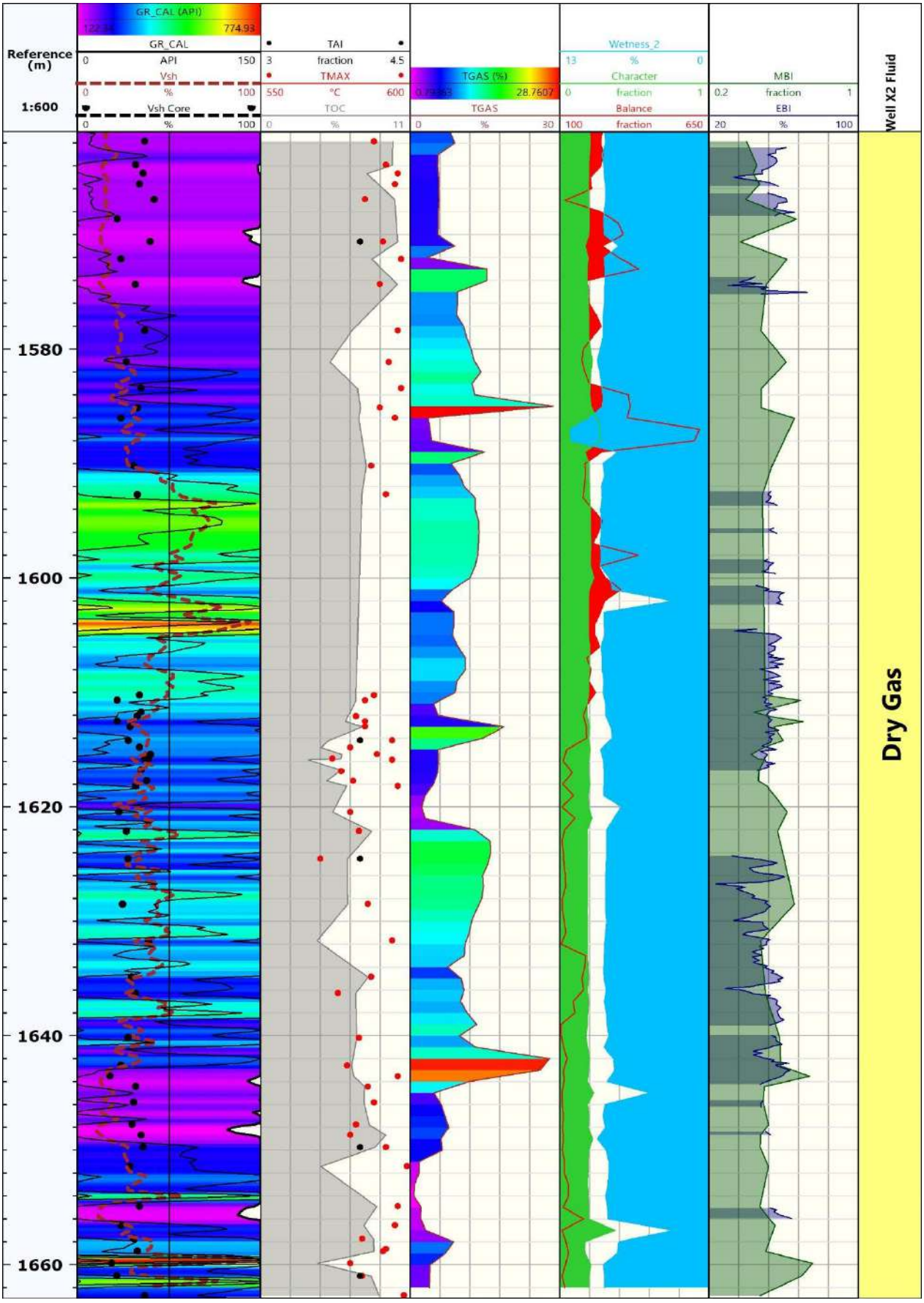

Fig .97: *Well X2, composite log versus depth.*

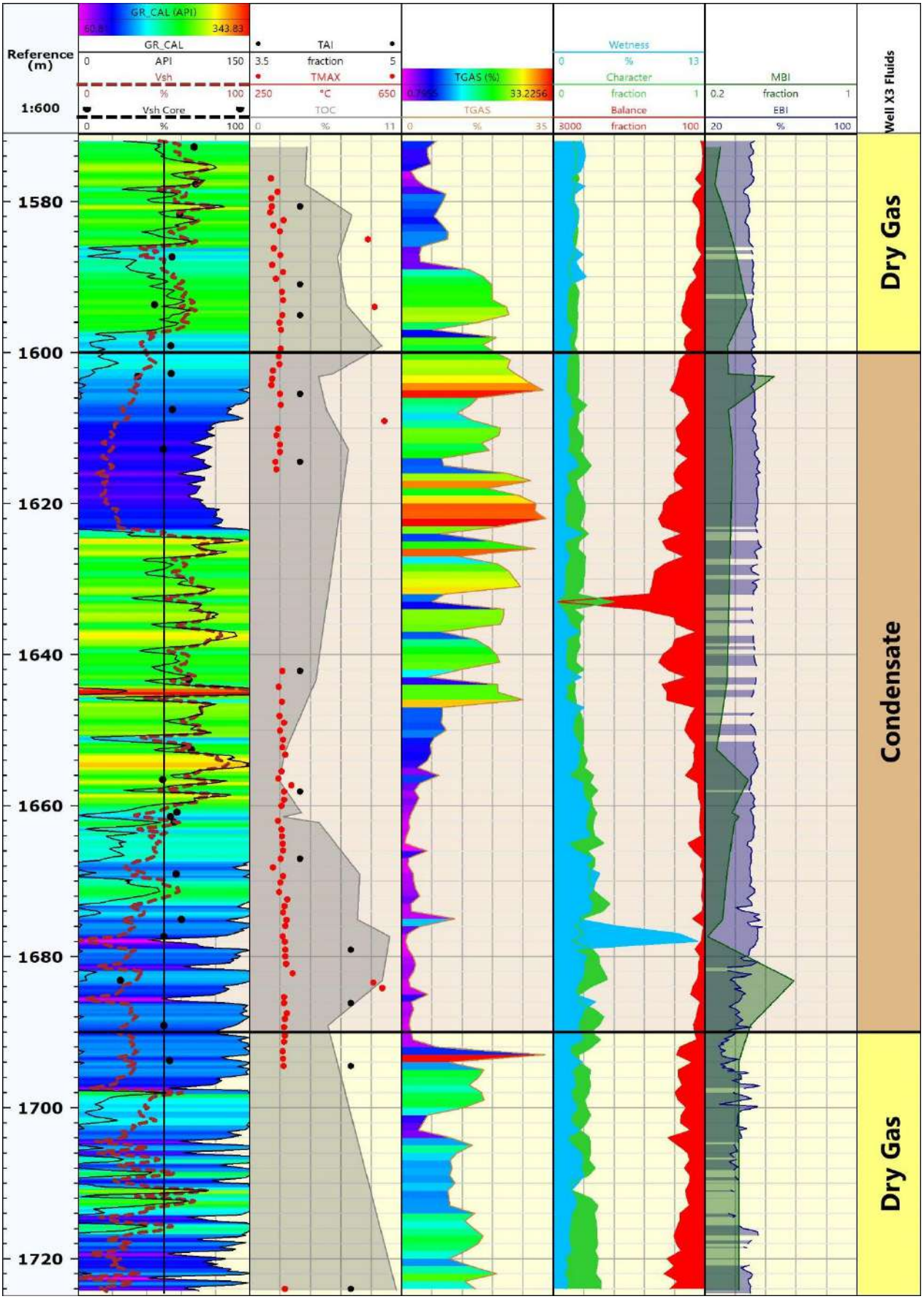

Fig. 98: *Well X3, composite log versus depth.*

3. Recommendations

The following Sweet Spots are the most targeted in the unconventional development field, especially in shale reservoirs:

- High TOC (mature organic matter),
- Low clay percentage,
- High porosity and high permeability,
- High fracture concentration or density,
- Low minimum horizontal stress,
- High Brittleness index.

Based on the available data, three sweet spots were the subject elements of this thesis, which will help evaluate the potential of the Frasnian reservoir of Ahnet Basin. The evaluation made mainly concerning the following properties Vsh, TOC, GR and BI, and based on results obtained from this study, the following recommendations should be taken into account in order to enrich more the consistence and the purpose of the evaluation and the assessment of the potential of Frasnian reservoir in the region of Ahnet:

- The GR core should be used to correlate the GR well Log and any available core data with logging data.
- To strengthen and improve the reliability of any shale gas prone formation evaluation, all the evaluation methods presented in this thesis should be used when the data are available.
- Any evaluation should be correlated to data obtained from direct resources or measurements.
- The results obtained and presented in this thesis regarding the Frasnian formation of Ahnet Basin should be completed and enhanced with other evaluations concerning the rest of the sweet spots presented previously to improve the petroleum potential assessment of this formation.

REFERENCES

REFERENCES

Achour, K. (2008). Etude de la fracturation dans les réservoirs de l'ordovicien du gisement de gaz de Garet El Gueffoul-bassin d'Ahnet Algerie. *Ingénieur d'Etat en Géologie Pétrolière BOUMERDES P*, *80*, 2-18.

Ai, C., Zhang, J., Li, Y. W., Zeng, J., Yang, X. L., & Wang, J. G. (2016). Estimation criteria for rock brittleness based on energy analysis during the rupturing process. *Rock Mechanics and Rock Engineering*, *49*, 4681-4698.

Al-Atroshi, S.J., Sherwani, G.H., and Al-Naqshbandi, S.F., 2020. Assessment the hydrocarbon potentiality of the Middle Jurassic Sargelu Formation, Northern Iraq. The Iraqi Geological Journal, 53(1A), 1-15.

Altindag, R. (2002). The evaluation of rock brittleness concept on rotary blast hold drills. *Journal of the Southern African Institute of Mining and Metallurgy*, *102*(1), 61-66.

Altındağ, R., & Güney, A. (2010). Predicting the relationships between brittleness and mechanical properties (UCS, TS and SH) of rocks.

Andreev, G. E. (1995). Brittle failure of rock materials. CRC press.

Badsi, M. (1998). Fracturation naturelle des roches: application au bassin de l'Ahnet (Algérie) (Doctoral dissertation, Paris 6).

Baudin, F., Tribovillard, N., and Trichet, J., 2007. Géologie de la matière organique dans les bassins sédimentaires : 263p.

Behar, F., Beaumont, V. D. E. B., & Penteado, H. D. B. (2001). Rock-Eval 6 technology: performances and developments. *Oil & Gas Science and Technology*, *56*(2), 111-134.

BENNACEF, A., ATTAR, A., FROUKHI, R., BEUF, S., PHILIPPE, G., & SCHMERBER, G. (1974). ILLIZI.

Bennacef, A., Beuf, S., Biju-Duval, B., De Charpal, O., Gariel, O., & Rognon, P. (1971). Example of cratonic sedimentation: lower Paleozoic of Algerian Sahara. *AAPG Bulletin*, *55*(12), 2225-2245.

Beuf, S. (1971). *Grès du Paléozoïque inférieur au Sahara (Les)* (Vol. 18). Editions Technip.

Bieniawski, Z. T. (1979, September). The geomechanics classification in rock engineering applications. In *ISRM Congress* (pp. ISRM-4CONGRESS). ISRM.

Blanton, T. L. (1981, February). Effect of strain rates from 10-2 to 10 sec-1 in triaxial compression tests on three rocks. In *International Journal of Rock Mechanics and Mining Sciences & Geomechanics Abstracts* (Vol. 18, No. 1, pp. 47-62). Pergamon.

Boote., D., R.D., Daniel, ClarkLowes, D., Traut,M.W., 1998. Palaeozoic petroleum systems of North Africa. Geological Society, London, Special Publications 132(1), 7-68.

Bordenave, M.L., Espitalié, J., Leplat, P.O.J. L., Oudin, J.L., and Vandenbroucke, M., 1993. Screening techniques for source rock evaluation. Applied petroleum geochemistry, 217-278.

Bose, D., Arora, D., Mekala, A., 2015. On the effect of hydrothermal pretreatment of biomass and catalytic conversion mechanism in pyrolysis process with a review of flash pyrolysis of lignocellulosic biomass using effective catalyst. World Scientific News, (4), 140-152.

Boudjema, A. (1987). *Évolution structurale du bassin pétrolier" triasique" du Sahara Nord oriental (Algérie)* (Doctoral dissertation, Paris 11).

Bowker, K.A., 2007. Barnett shale gas production, Fort Worth Basin: Issues and discussion. AAPG Bulletin, 91(4), 523-533.

Brace, W. F., Paulding Jr, B. W., & Scholz, C. H. (1966). Dilatancy in the fracture of crystalline rocks. *Journal of geophysical research*, *71*(16), 3939-3953.

Buller, D., Hughes, S., Market, J., Petre, E., Spain, D., & Odumosu, T. (2010, September). Petrophysical evaluation for enhancing hydraulic stimulation in horizontal shale gas wells. In *SPE Annual Technical Conference and Exhibition?* (pp. SPE-132990). SPE.

Burnaman, M.D. and Shelton, J., 2009. Shale gas play screening and evaluation criteria. 中国石油勘探, 14(3), 51p.

Caby, R., Dostal, J., & Dupuy, C. (1977). Upper Proterozoic volcanic graywackes from northwestern Hoggar (Algeria)—geology and geochemistry. *Precambrian Research*, *5*(3), 283-297.

Cai, M. (2008). Influence of intermediate principal stress on rock fracturing and strength near excavation boundaries—insight from numerical modeling. *International Journal of Rock Mechanics and Mining Sciences*, *45*(5), 763-772.

Carr, I. D. (2002). Second-order sequence stratigraphy of the Palaeozoic of North Africa. *Journal of Petroleum Geology*, *25*(3), 259-280.

Chang, C., Zoback, M. D., & Khaksar, A. (2006). Empirical relations between rock strength and physical properties in sedimentary rocks. *Journal of Petroleum Science and Engineering*, *51*(3-4), 223-237.

Close, D., Cho, D., Horn, F., & Edmundson, H. (2009). The sound of sonic: A historical perspective and introduction to acoustic logging. *CSEG Recorder*, *34*(5), 34-43.

Cotter, E. (1977). The evolution of fluvial style, with special reference to the central Appalachian Paleozoic.

Cotter, E. (1983). Shelf, paralic, and fluvial environments and eustatic sea-level fluctuations in the origin of the Tuscarora Formation (Lower Silurian) of central Pennsylvania. *Journal of Sedimentary Research*, *53*(1), 25-49.

Daoudi.M., Sadeg.K et Haddoum.H (1999). Rapport de mission effectuée dans le Bled El Mass et l'Ahnet occidental (du 27-10-1999 au 13-11-1999)- Sonatrach Exploration.

Dardour, A.M., Boote, D.R.D., Baird A.W., 2004. Stratigraphic controls on Palaeozoic petroleum systems, Ghadames basin, Libya. Journal of petroleum Geology 27(2), 141-162.

Donzeau, M., & Fabre, J. (1981). Comportement de la dalle saharienne et orogenèse Varisque: essai d'interprétation.

Durand-Delga, M. (2004). Le 19e Congrès géologique international-Alger, 1952. Travaux du Comité français d'Histoire de la Géologie, 3(tome 18), 165-180.

Echikh, K., 1998. Geology and hydrocarbon occurrences in the Ghadames basin, Algeria, Tunisia, Libya. Geological Society, London, Special Publications, 132(1), 109-129.

Economides, M.J.; Nolte, K.G. Reservoir Stimulation, 3rd ed.; John Wiley & Sons Press: New York, NY, USA, 2000.

Emeis, K.C. and Kvenvolden, K.A., 1986. Shipboard organic geochemistry on JOIDES Resolution. Ocean Drilling Program, Texas A & M University.

Espitalié, J., Deroo, G., Marquis, F., 1986. La pyrolyse Rock-Eval et ses applications. Troisième partie. Revue de l'Institut français du Pétrole 41(1), 73-89.

Ettensohn., Frank, R., Woodrow, D.L., Sevon, W.D., 1985. The Catskill delta complex and the Acadian orogeny: A model. The Catskill delta: Geological Society of America Special Paper 201, 39-49.

Euzen, T., Eschard, R., Cacas, M. C., Callot, J. P., & Deschamps, R. (2005). Field survey of the M'Sari area: Sedimentology, structural geology, and fracturing. IFP (Institut Français du Pétrole).

Fabre, J., Kaci, A. A., Bouima, T., & Moussine-Pouchkine, A. (1988). Le cycle molassique dans le Rameau trans-saharien de la chaîne panafricaine. *Journal of African Earth Sciences (and the Middle East)*, *7*(1), 41-55.

Fu, H., Wang, X., Zhang, L., Gao, R., Li, Z., Zhu, X., ... & Xu, T. (2015). Geological controls on artificial fracture networks in continental shale and its fracability evaluation: A case study in the Yanchang Formation, Ordos Basin, China. *Journal of Natural Gas Science and Engineering*, *26*, 1285-1293.

Gautier, E. F. (1908). Sahara algérien (Vol. 2). Librairie A. Colin.

Gong, W., Peng, Y., Wang, H., He, M., Ribeiro e Sousa, L., & Wang, J. (2015). Fracture angle analysis of rock burst faulting planes based on true-triaxial experiment. *Rock Mechanics and Rock Engineering*, *48*, 1017-1039.

Grady, D. E. (1996, May). Shock-wave properties of brittle solids. In *AIP conference proceedings CONF-950846* (Vol. 370, No. 1, pp. 9-20). American Institute of Physics.

Guanghui, Z., Jinyu, X., Peng, W., Shi, L., & Haoyu, W. (2017). Research on Strain Rate Effects of Red-sandstone under Water-rock Coupling. Chinese Journal of Underground Space and Engineering, 13(1), 79-85.

Guo, J. C., Zhao, Z. H., He, S. G., Liang, H., & Liu, Y. X. (2015). A new method for shale brittleness evaluation. *Environmental Earth Sciences*, *73*, 5855-5865.

Guo, X., Xu, S., Chen, G., Yan, X., & Cao, Q. (2021). Fracture criterion and control plan on CO2 pipelines: Theory analysis and full-bore rupture (FBR) experimental study. Journal of Loss Prevention in the Process Industries, 69, 104394.

Guo, Z. Q., Chapman, M., & Li, X. Y. (2012, June). Correlation of brittleness index with fractures and microstructure in the Barnett Shale. In *74th EAGE Conference and Exhibition incorporating EUROPEC 2012* (pp. cp-293). European Association of Geoscientists & Engineers.

Haddadi, A. (1996). The influence of basement fabrics on the development of structural highs in the Timimoun basin, Algeria. *Basin evolution and dynamics*, 26.

Haddoum, H. (2009). Les structures hercyniennes dans la couverture sédimentaire paléozoïque de l'Ahnet occidental et de Bled el Mass (NO du Hoggar, Algérie): une conséquence du rejeu des failles panafricaines. *Bulletin du Service Géologique de l'Algérie*, *20*(3), 221-243.

Hakimi, M.H., Abdullah, W.H., Sia, S.G., Makeen, Y.M., 2013. Organic geochemical and petrographic characteristics of Tertiary coals in the northwest Sarawak, Malaysia: implications for palaeoenvironmental conditions and hydrocarbon generation potential. Marine and Petroleum Geology, 48, 31-46.

HAMDI, L., & TAKHERIST, D. (1992). Considérations générales sur l'Atlas Saharien et les Hauts Plateaux à partir des données géophysiques. In *Séminaire national des Sciences de la Terre*.

Haworth, J. H., Sellens, M., & Whittaker, A. (1985). Interpretation of hydrocarbon shows using light (C1-C5) hydrocarbon gases from mud-log data. *AAPG Bulletin*, *69*(8), 1305-1310.

Heidari, M., Khanlari, G. R., Torabi-Kaveh, M., Kargarian, S., & Saneie, S. (2014). Effect of porosity on rock brittleness. *Rock mechanics and rock engineering*, *47*, 785-790.

Hill, J. and Whiteley, S., 2011. Shale Gas Potential of Selected Countries in Europe, North Africa and the Near East.

Honda, H., & Sanada, Y. (1956). Hardness of coal. *Fuel*, *35*(4), 451-461.

Hood, A. C. C. M., Gutjahr, C. C. M., & Heacock, R. L. (1975). Organic metamorphism and the generation of petroleum. *AAPG Bulletin*, *59*(6), 986-996.

Hoş-Çebi, F., Korkmaz, S., 2013. Organic geochemistry and depositional environments of Eocene coals in northern Anatolia, Turkey. Fuel, 113, 481-496.

Hucka, V., & Das, B. (1974, October). Brittleness determination of rocks by different methods. In *International Journal of Rock Mechanics and Mining Sciences & Geomechanics Abstracts* (Vol. 11, No. 10, pp. 389-392). Pergamon.

Hunt, J.M., 1967. The origin of petroleum in carbonate Rocks. In Developments in sedimentology, 9, 25-25, Elsevier.

Hunt, J.M., 1991. Generation of gas and oil from coal and other terrestrial organic matter. Organic geochemistry, 17(6), 673-680.

Hunt, J.M., 1996. Petroleum Geochemistry and Geology. Second Ed. Freeman, New York.

Jacobs, T. (2014). The shale evolution: Zipper fracture takes hold. *Journal of Petroleum Technology*, *66*(10), 60-67.

Jahandideh, A., & Jafarpour, B. (2016). Optimization of hydraulic fracturing design under spatially variable shale fracability. *Journal of Petroleum Science and Engineering*, *138*, 174-188.

Jarvie, D. M., Hill, R. J., Ruble, T. E., & Pollastro, R. M. (2007). Unconventional shale-gas systems: The Mississippian Barnett Shale of north-central Texas as one model for thermogenic shale-gas assessment. *AAPG Bulletin*, *91*(4), 475-499.

Jin, X., Shah, S. N., Roegiers, J. C., & Zhang, B. (2015). An integrated petrophysics and geomechanics approach for fracability evaluation in shale reservoirs. SPE Journal, 20(03), 518-526.

Jin, X., Shah, S., Truax, J., & Roegiers, J. C. (2014, October). A practical petrophysical approach for brittleness prediction from porosity and sonic logging in shale reservoirs. In *SPE Annual Technical Conference and Exhibition?* (pp. SPE-170972). SPE.

Kadri, M.M. and Hacini, M., 2017. Evaluation of Frasnian Shale reservoir, case studywell DAK-1, Ahnet Basin, southern Algeria. Journal of Fundamental and Applied Sciences 9(1), 542-552.

Kahraman, S. A. İ. R., Toraman, O. Y., & Cayirli, S. (2018). Predicting the strength and brittleness of rocks from a crushability index. *Bulletin of Engineering geology and the Environment*, *77*, 1639-1645.

Kipp, M. E., Grady, D. E., & Chen, E. P. (1980). Strain-rate dependent fracture initiation. *International Journal of Fracture*, *16*, 471-478.

Kivi, I. R., Ameri, M., & Molladavoodi, H. (2018). Shale brittleness evaluation based on energy balance analysis of stress-strain curves. *Journal of Petroleum Science and Engineering*, *167*, 1-19.

Kracha, N. (2011). *Relations entre sédimentologie, fracturation naturelle, et diagenèse d'un réservoir à faible perméabilité: application aux réservoirs de l'Ordovicien du bassin de l'Ahnet, Sahara central, Algérie* (Doctoral dissertation, Lille 1).

Kundert, D., & Mullen, M. (2009, April). Proper evaluation of shale gas reservoirs leads to a more effective hydraulic-fracture stimulation. In *SPE Rocky Mountain Petroleum Technology Conference/Low-Permeability Reservoirs Symposium* (pp. SPE-123586). SPE.

Langford, F. F., & Blanc-Valleron, M. M. (1990). Interpreting Rock-Eval pyrolysis data using graphs of pyrolizable hydrocarbons vs. total organic carbon. *AAPG Bulletin*, *74*(6), 799-804.

Li, D., Sun, Z., Xie, T., Li, X., & Ranjith, P. G. (2017). Energy evolution characteristics of hard rock during triaxial failure with different loading and unloading paths. *Engineering Geology*, *228*, 270-281.

Li, M. (2014). Research on rupture mechanisms of coal measures sandstone under high temperature and impact load. *China Univ Min Technol China, Xuzhou (Chinese)*.

Li, X. B., Lok, T. S., & Zhao, J. (2005). Dynamic characteristics of granite subjected to intermediate loading rate. *Rock Mechanics and Rock Engineering*, *38*, 21-39.

Li, Z., Li, L., Li, M., Zhang, L., Zhang, Z., Huang, B., & Tang, C. A. (2018). A numerical investigation on the effects of rock brittleness on the hydraulic fractures in the shale reservoir. *Journal of Natural Gas Science and Engineering*, *50*, 22-32.

Liang, L., Liu, X., Xiong*, J., Wu, T., & Ding, Y. (2017, April). New model to evaluate the Brittleness in shale formation. In Global Meeting Abstracts (pp. 1248-1251). Society of Exploration Geophysicists.

Liu, J., Xu, J., Lu, X., Zhang, L., & Wang, Z. (2009). Experimental study on dynamic mechanical properties of amphibolites under impact compressive loading. *Chinese Journal of Rock Mechanics and Engineering*, *28*(10), 2113-2120.

Lüning, S., Adamson, K., Craig, J., 2003. Frasnian organic-rich shales in North Africa: regional distribution and depositional model. Geological Society, London, Special Publications, 207(1), 165-184.

Macgregor, D.S., 1998. Giant fields, petroleum systems and exploration maturity of Algeria. Geological Society, London, Special Publications, 132(1), 79-96.

Mamaseni, W.J. J., Al-Juboury, A.I., Omar, N., Sherwani, G., 2022. Petroleum Potentiality and Petrophysical Evaluation of Late Triassic Baluti Formation, Northern Iraq. The Iraqi Geological Journal, 55(2B), 121-138.

Mamaseni, W.J., Naqshabandi, S.F., Al-Jaboury, F.K., 2019. Palynofacies and paleoenvironment of Late Jurassic-Early Cretaceous Formations at Duhok Basin, Northern Iraq. The Iraqi Geological Journal, 61-82.

Mansour, A., Tahoun, S.S., 2018. Palynological and palaeoenvironmental analyses of the upper Albian-Cenomanian succession in Gindi Basin, Egypt: Implication for transgressive/regressive systems tracts. Journal of African Earth Sciences, 147, 603-622.

Mendonça Filho, J.G., Chagas, R.B.A., Menezes, T.R., Mendonça, J.O., Da Silva, F.S., Sabadini-Santos, E., 2010. Organic facies of the Oligocene lacustrine system in the Cenozoic Taubaté basin, Southern Brazil. International Journal of Coal Geology, 84(3-4), 166-178.

Meng, F., Zhou, H., Zhang, C., Xu, R., & Lu, J. (2015). Evaluation methodology of brittleness of rock based on post-peak stress–strain curves. *Rock Mechanics and Rock Engineering*, *48*, 1787-1805.

Mercier, J., & Vergely, P. (1992). Tectonique (Collection Geosciences). *Paris: Dunod*, 1-214.

Merrill, R.K., 1991. Source and migration processes and evaluation techniques.

Mishra, S., Meena, H., Parashar, V., Khetwal, A., Chakraborty, T., Matsagar, V., ... & Singh, M. (2018). High strain rate response of rocks under dynamic loading using split Hopkinson pressure bar. *Geotechnical and Geological Engineering*, *36*, 531-549.

Mohamed, O., Mahdy, F., Tahoun, S.S., 2020. Palynofacies analysis and source rock evaluation of the Upper Cretaceous-Oligocene succession in the Drazia-1 well, Alamein Basin, Egypt. Arabian Journal of Geosciences, 13, 1-17.

Mohamed, O., Mansour, A., Tahoun, S.S., Elewa, A.M., Mekkey, M.A., 2018. Palynology of the cenomanian Raha Formation, Gulf of Suez, Egypt: biostratigraphical, palaeoenvironmental and palaeobiogeographical implications. Austrian Journal of Earth Sciences, 111(1), 135-154.

Mullen, M., & Enderlin, M. (2012, October). Fracability index–more than just calculating rock properties. In *SPE Annual Technical Conference and Exhibition?* (pp. SPE-159755). SPE.

Mullen, M., Roundtree, R., & Barree, B. (2007, April). A composite determination of mechanical rock properties for stimulation design (what to do when you don't have a sonic log). In *SPE Rocky Mountain Petroleum Technology Conference/Low-Permeability Reservoirs Symposium* (pp. SPE-108139). SPE.

Nejati, H. R., & Moosavi, S. A. (2017). A new brittleness index for estimation of rock fracture toughness. *Journal of Mining and Environment*, *8*(1), 83-91.

Perez, R., & Marfurt, K. (2013, September). Brittleness estimation from seismic measurements in unconventional reservoirs: Application to the Barnett Shale. In *SEG International Exposition and Annual Meeting* (pp. SEG-2013). SEG.

Peters, K. E., Walters, C. C., & Moldowan, J. M. (2005). *The biomarker guide* (Vol. 1). Cambridge university press.

Peters, K.E., 1986. Guidelines for evaluating petroleum source rock using programmed pyrolysis. AAPG Bulletin, 70(3), 318-329.

Peters, K.E., Cassa, M.R., 1994. Applied source rock geochemistry: Chapter 5: Part II. Essential elements, 93-120.

Pisarzowska, A., Sobstel, M., Racki, G., 2006. Conodont-based event stratigraphy of the Early-Middle Frasnian transition on the South Polish carbonate shelf. Acta Palaeontologica Polonica, 51(4), 609-646.

Rabaute, A. (1998). Obtenir une représentation en continu de la lithologie et de la minéralogie. Exemples d'application du traitement statistique de données de diagraphie aux structures sédimentaires en régime de convergence de plaques (Leg ODP 134, 156 et 160) (Doctoral dissertation, Université Montpellier II-Sciences et Techniques du Languedoc).

Racki, G., 2005. Toward understanding Late Devonian global events: few answers, many questions. In Developments in Palaeontology and Stratigraphy, Vol. 20, 5-36. Elsevier.

Rickman, R., Mullen, M., Petre, E., Grieser, B., & Kundert, D. (2008, September). A practical use of shale petrophysics for stimulation design optimization: All shale plays are not clones of the Barnett Shale. In *SPE Annual Technical Conference and Exhibition?* (pp. SPE-115258). SPE.

Rybacki, E., Meier, T., & Dresen, G. (2016). What controls the mechanical properties of shale rocks?–Part II: Brittleness. *Journal of Petroleum Science and Engineering*, *144*, 39-58.

Rybacki, E., Reinicke, A., Meier, T., Makasi, M., & Dresen, G. (2015). What controls the mechanical properties of shale rocks?–Part I: Strength and Young's modulus. *Journal of Petroleum Science and Engineering*, *135*, 702-722.

Schmoker, J.W., 2005. US Geological Survey assessment concepts for continuous petroleum accumulations. US Geological Survey digital data series DDS-69-D, 1-7.

Sia, S. G., & Abdullah, W. H. (2012). Geochemical and petrographical characteristics of low-rank Balingian coal from Sarawak, Malaysia: its implications on depositional conditions and thermal maturity. International Journal of Coal Geology, 96, 22-38.

Soliman, M. Y., East, L., & Augustine, J. (2010, June). Fracturing design aimed at enhancing fracture complexity. In *SPE Europec featured at EAGE Conference and Exhibition?* (pp. SPE-130043). SPE.

Sondergeld, C. H. (2020). Application of Interpretable Machine-Learning Workflows To Identify Brittle, Fracturable, and Producible Rock in Horizontal Wells Using Surface Drilling Data.

Suárez-Ruiz, I., Flores, D., Mendonça Filho, J.G., Hackley, P.C., 2012. Review and update of the applications of organic petrology: Part 1, geological applications. International Journal of Coal Geology, 99, 54-112.

Sykes, R. and Snowdon, L.R., 2002. Guidelines for assessing the petroleum potential of coaly source rocks using Rock-Eval pyrolysis. Organic geochemistry 33(12), 1441-1455.

Takherist, D., & Hamdi, L. (1995). Thermal anomaly at In Salah: possible consequences for petroleum potential. In *Well Conference Evaluation Algerie 1995* (pp. II-7). Schlumberger.

Tang, S. (2018). The effects of water on the strength of black sandstone in a brittle regime. *Engineering Geology*, *239*, 167-178.

TANG, S. H., ZHU, B. C., & YAN, Z. F. (2011). Effect of crustal stress on hydraulic fracturing in coalbed methane wells. *Journal of China Coal Society*, *36*(1), 65-69.

Tapponnier, P., & Brace, W. F. (1976, April). Development of stress-induced microcracks in Westerly granite. In *International Journal of Rock Mechanics and Mining Sciences & Geomechanics Abstracts* (Vol. 13, No. 4, pp. 103-112). Pergamon.

Tissot, B.P. and Welte, D.H., 1978. Petroleum formation and occurrence: a new approach to oil and gas exploration.

Tobia, F.H., Mustafa, R.K., 2022. Geochemical and Clay Mineralogical Characteristics of the Black Shale and Constrains on Diagenesis and Maturation, Chia Gara Formation, Kurdistan Region, Iraq. The Iraqi Geological Journal, 23-37.

Tyson, R.V., 1993. Palynofacies analysis. In Applied micropalaeontology (pp. 153-191). Dordrecht: Springer Netherlands.

Tyson, R.V., 1995. Palynological kerogen classification. Sedimentary Organic Matter. Springer, Dordrecht, 341-365.

Tyson, R.V., 1996. Sequence-stratigraphical interpretation of organic facies variations in marine siliciclastic systems: general principles and application to the onshore Kimmeridge Clay Formation, UK. Geological Society, London, Special Publications, 103(1), 75-96.

Wang, D., Ge, H., Wang, X., Wang, J., Meng, F., Suo, Y., & Han, P. (2015). A novel experimental approach for fracability evaluation in tight-gas reservoirs. *Journal of Natural gas science and engineering*, *23*, 239-249.

Wang, F. P., & Gale, J. F. (2009). Screening criteria for shale-gas systems.

Weibull, W. (1951). A statistical distribution function of wide applicability. *Journal of applied mechanics*.

WELL EVALUATION CONFERENCE ALGERIA, Sonatrach and Schlumberger., 1995.

WELL EVALUATION CONFERENCE ALGERIA, Sonatrach and Schlumberger., 2007.

Welte. D.H., 1965. Relation between petroleum and source rock. AAPG Bulletin 49(12), 2246-2268.

Willis, R. B., Fontaine, J., Paugh, L., & Griffin, L. (2005, September). Geology and geometry: A review of factors affecting the effectiveness of hydraulic fractures. In SPE Eastern Regional Meeting (pp. SPE-97993). SPE.

Wong, L. N. Y., Guo, T. Y., Wu, Z., & Xiao, X. (2021). How do thermally induced microcracks alter microcracking mechanisms in Hong Kong granite?. *Engineering Geology*, *292*, 106268.

Wood, S.E., Tyson, R.V., 1996. An integrated palynological-palynofacies approach to the zonation of the Paleogene in the Forties-Montrose Ridge area, central North Sea. Geological Society, London, Special Publications, 101(1), 121-128.

Yagiz, S. (2009). Assessment of brittleness using rock strength and density with punch penetration test. *Tunnelling and underground space technology*, *24*(1), 66-74.

Yang, X. L., & Huang, F. (2013). Three-dimensional failure mechanism of a rectangular cavity in a Hoek–Brown rock medium. *International Journal of Rock Mechanics and Mining Sciences*, *61*, 189-195.

Yang, X., Ge, Z., Sun, Q., & Zhang, W. (2021). Effect of Temperature and Strain Rate on the Brittleness of China Sandstone. *Geofluids*, *2021*(1), 6782146.

Yarali, O., & Soyer, E. (2011). The effect of mechanical rock properties and brittleness on drillability. *Scientific research and Essays*, *6*(5), 1077-1088.

Yasar, S. (2020). Cutting characteristics of a ductile rock. GeoScience Engineering, 66(2), 76-83.

Ye, Y., Tang, S., & Xi, Z. (2020). Brittleness evaluation in shale gas reservoirs and its influence on fracability. *Energies*, *13*(2), 388.

Zhang, B., Zhao, T., Jin, X., & Marfurt, K. J. (2015). Brittleness evaluation of resource plays by integrating petrophysical and seismic data analysis. *Interpretation*, *3*(2), T81-T92.

Zhao, J. (2008). Mécanique des roches, Course Lectures 2008 2ème partie – mécanique et propriétés des massifs rocheux, Laboratoire de Mécanique des Roches – LMR

Zhishui, L. I. U., & Zandong, S. U. N. (2015). New brittleness indexes and their application in shale/clay gas reservoir prediction. *Petroleum exploration and development*, *42*(1), 129-137.

Zhu, X., & Wang, S. Q. (2013). Mechanisms for different failure modes in startup uniaxial extension: Tensile (rupture-like) failure and necking. *Journal of Rheology*, *57*(1), 223-248.